Geometrical Frustration in Jahn-Teller Active Spinel Pyrochlores

A Thesis Submitted to
Indian Institute of Technology Guwahati
for the degree of

Doctor of Philosophy

By

Suchit Kumar Jena

Adm. No: 186121027

Department of Physics
Indian Institute of Technology Guwahati
Guwahati-781039, Assam (India)

Dedicated to

My Grandfather, Grandmother

& Our Family

INDIAN INSTITUTE OF TECHNOLOGY GUWAHATI
Department of Physics
Guwahati – 781039

Declaration

"*Geometrical Frustration in Jahn-Teller Active Spinel Pyrochlores*" is the result of my own doctoral research work. This work was carried out under the supervision of Prof. Subhash Thota at the Department of Physics, Indian Institute of Technology Guwahati. To the best of my knowledge, the work presented in this thesis has not been submitted to any other Institute/University for the award of any degree.

Suchit Kumar Jena
Research Scholar (Adm. No: 186121027)
Department of Physics
Indian Institute of Technology Guwahati
Guwahati-781039, India

INDIAN INSTITUTE OF TECHNOLOGY GUWAHATI
Department of Physics
Guwahati – 781039

Certificate

It is certified that the work described in this thesis, entitled “*Geometrical Frustration in Jahn-Teller Active Spinel Pyrochlores*”, done by Mr. Suchit Kumar Jena, a Ph.D. student of the Department of Physics, Indian Institute of Technology Guwahati, for the award of degree of Doctor of Philosophy has been carried out under my supervision. This work has not been submitted elsewhere for the award of any degree.

Prof. Subhash Thota
Professor
Department of Physics
Indian Institute of Technology Guwahati
Guwahati-781039, India

Acknowledgements

I am delighted to have the opportunity to express my sincere gratitude towards a number of people whose support helped me to complete the work presented in this thesis. First and foremost, I owe enormous thanks to my supervisor Prof. Subhash Thota sir for providing me an opportunity to work under his supervision. He has always been energetic and enthusiastic regarding research work which inspired me to actively carry out my research. After joining his lab, I have gained extensive knowledge on developing new ideas, how to approach and execute them, several important analyses, and expertise on various experimental skills. His timely cooperation, guidance and suggestions helped me to learn a lot. Apart from research work, he always tries to keep alive the sense of humour to maintain a friendly environment, for which I could seldom feel the work pressure. I am also thankful to Mrs. Revathi Thota mam, Veda Samhitha Thota and Avantika Chandra Thota for their support and encouragement.

I would like to express my deepest gratitude to my doctoral committee members, Prof. Ashwini Kumar Sharma (DC Chairman) sir, Prof. Tapan Mishra sir, Prof. Padma Kumar Padmanabhan sir and Prof. Ravindranath Adda sir for examining the progress of my work, and providing insightful comments and valuable suggestions, which helped to improve the quality of this dissertation work. I also wish to thank the present HoD, Prof. Perumal Alagarsamy and the former HoD, Prof. Subhradip Ghosh for their immense support in providing me with all the necessary facilities to ensure smooth execution of my work. I would like to extend my sincere thanks to Prof. Tapan Mishra sir, Prof. Pankaj Kumar Mishra sir and Prof. Kanhaiya Pandey sir for always motivating me to carry out good research work. I am also grateful to all the faculty members of the Physics Department, IIT Guwahati.

I would like to extend my sincere gratitude to Prof. Mohindar Singh Seehra, an Eberly distinguished Professor Emeritus at the Department of Physics & Astronomy, West Virginia University, USA, for his priceless guidance, opinions, and conversation related to Physics. I feel lucky that I could learn from him about several physical concepts which are used to solve complicated problems by dealing with the basics. Thank you Sir for sharing your valuable time and knowledge with me. My sincere thanks to Prof. Tapati Sarkar for performing extensive SQUID magnetic measurements without which this work would not have acquired what it has achieved. I take this opportunity to thank Prof. Bruno Weise for providing me with the heat-capacity data and Prof. Manfred Reehuis for performing the neutron-diffraction measurements, which are reported in this thesis. I also thank Prof. Yajun Qi and Prof. Rohit Medwal for helping me to get data from x-ray photoelectron spectroscopy measurements. A special thanks to Dr. Md. Kamal Warshi, for guiding me in the set up and repairment of the dielectric instruments in our lab. I would like to acknowledge Dr. Sidananda Sarma and Mr. Aditya Kalita for helping me in the technical aspects. I would also like to thank my institutional, departmental and hostel administrative staffs, scientific officers and staff members for their kind cooperation. I acknowledge the funding programs DST FIST-I (XRD) and FIST-II (PPMS) and the Central Instruments Facility (CIF), IIT Guwahati for providing an outstanding platform for research, offering sophisticated instruments for various scientific experiments. Also, I am grateful to IIT Guwahati, and Ministry of Education, Govt. of India for the financial support.

I am fortunate enough to have had caring seniors: Dr. Deep Chandra Joshi, Dr. Prativa Pramanik, Dr. Sayandeep Ghosh and Dr. Priyanka Tiwari, who helped me in various ways throughout my research work. I sincerely thank all of them for their selfless assistance. My special thanks to Sayandeep Bhaiya and Prativa Didi for always being there and helping me out at times of need. I feel lucky to have my juniors: Mouli, Harshita, Arpita, Arjyama, Joya, Arijit and Vedant, who had a great contribution in maintaining a healthy and happy working environment in the lab. Also, they were always there to help me in all kinds of circumstances. I acknowledge my present and former lab fellows and project students: Atyant, Soumya, Swati, Mahender, Bhupesh, Akshit, Mahesh, Ayush, Srinitha, Debjyoti, Rana, Shashank, Shourya, Aryan, Sweta, Soham, Shalini, Maruthi, for their support and pleasant company. I thank all of them for the wonderful times we shared together at IIT Guwahati.

I am thankful from the fathoms of my heart to Pushpesh Pathak and Manisha Srivastava, who always readily helped me in both academic and non-academic aspects, without a second thought, whenever I sought for their help. I am extremely fortunate to have special friends: Pushpesh, Sudeshna, Pushpanjali, Shilpa, who were always there for me; I cannot thank you all enough for all the cherishable memories and all that you have done for me. I thank from the bottom of my heart to my departmental Cricket team-mates and the IITG Cricket fraternity for the memorable moments which helped me to focus on my research work more effectively. I also want to thank my hostel-mates Rajnandan, Debabrata, Akanshu, Monu, Gajendra and Prantik for the quality times we spent together. A special note of thanks to Kamal Basumatary Bhaiya, Manoj Kumar Mohanta Bhai, Utkalika family, and my MSc mates at IIT Guwahati: Amalesh and Neda. Thank you for being so much understanding and cooperative to me. My special regards to all of my teachers who taught me not only at the educational institutes but also at different stages of my life by various means. I thank to all my dear friends and well-wishers for their encouragement and support.

I wish to offer my greatest gratitude towards the sacrifices made for me by my family members. Without their contribution, I could not have come up to this stage of life to complete my PhD. My grandfather, grandmother, parents, uncles, aunts, brother, sister, cousins; I thank everyone for the love, support and mental strength you have given to me, for the encouragement and motivation you have provided me, and for the sacrifices you have made to make my life a lot easier. I am blessed to have my FAMILY as my backbone. This last word of acknowledgement I have saved for the almighty Lord Jagannath, Subhadra and Balabhadra. From my deepest, I would like to express my heartfelt thanks to THEM for everything.

Suchit Kumar Jena
Research Scholar (Adm. No: 186121027)
Indian Institute of Technology Guwahati
Assam, India
22nd March 2023

List of Publications:

Peer Reviewed Journals:

[1] "Spin-liquid state with precursor ferromagnetic clusters interacting antiferromagnetically in frustrated glassy tetragonal spinel $Zn_{0.8}Cu_{0.2}FeMnO_4$",

S. K. Jena, M. S. Seehra, T. Sarkar, M. Reehuis, A. Hoser, B. Weise, and S. Thota,

Journal of Physics: Condensed Matter **–** accepted (2023).

[2] "Slow spin dynamics of cluster-glass spinel $Zn(Fe_{1-x}Ru_x)_2O_4$: Role of Jahn-Teller active spin-1/2 Cu^{2+} ions at *B*-sites",

S. K. Jena, T. Sarkar, M. RoyChowdhury, B. Weise, Y. Qi, and S. Thota,

Journal of Physics: Condensed Matter **34**, 405801 (2022).

[3] "Dynamical response of localized electron hopping and dipole relaxation in $Cu_{1-x}Zn_xFe_2O_4$ magnetoceramics",

S. K. Jena, D. C. Joshi, S. Ghosh, K. Dasari, and S. Thota,

Journal of Physics D: Applied Physics **54**, 425303 (2021).

[4] "Electronic structure and magnetic exchange interactions in Zn diluted $CuFe_2O_4$ magnetoceramics",

S. K. Jena, D. C. Joshi, Z. Yan, Y. Qi, S. Ghosh, and S. Thota,

Journal of Applied Physics **128**, 073908 (2020).

[5] "Unraveling the nature of ferrimagnetism and associated exchange interactions in distorted honeycomb $Ni_4Nb_2O_9$",

S. Thota, M. S. Seehra, M. RoyChowdhury, H. Singh, S. Ghosh, **S. K. Jena**, P. Pramanik, T. Sarkar, R. S. Rawat, R. Medwal, and B. Weise,

Phys. Rev. B. **106**, 134418 (2022).

[6] "The role of Zn and Ru substitution on the structural, magnetic and dielectric properties of ferrite Cuprospinels",

M. RoyChowdhury, **S. K. Jena**, V. P. Khadse, D. C. Joshi, and S. Thota,

Journal of Physics D: Applied Physics **–** accepted (2023).

[7] "Antiferromagnetism, spin-glass state, *H*–*T* phase diagram, and inverse magnetocaloric effect in Co_2RuO_4",

S. Ghosh, D. C. Joshi, P. Pramanik, **S. K. Jena**, S. Pittala, T. Sarkar, M. S. Seehra, and S. Thota,

Journal of Physics: Condensed Matter **32**, 485806 (2020).

[8] "Magnetic exchange interactions and band gap bowing in $Ni_xMg_{1-x}O$ $(0.0 \leq x \leq 1.0)$: A GGA+U density functional study",

S. Ghosh, **S. K. Jena**, P. K. Mishra, M. S. Seehra, and S. Thota,

Journal of Applied Physics **126**, 233904 (2019).

Works presented in international/national conferences:

[1] "Magnetic Relaxation Dynamics of Frustrated Glassy Tetragonal Spinel $Cu_{0.2}Zn_{0.8}FeMnO_4$",

S. K. Jena, T. Sarkar, B. Weise, and S. Thota,

MMM 2022, Minneapolis, MN, USA, 31st Oct-04th Nov, 2022.

[2] "Coexistence of Ferrimagnetic Ordering and Spin-glass state in Spinel $Zn(Fe_{1-x}Ru_x)_2O_4$: Role of Jahn-Teller active spin-1/2 Cu^{2+} ions at *B*-sites",

S. K. Jena, S. Ghosh, and S. Thota,

Q-MAT 2021, TIFR, Mumbai, INDIA, 8-11th December, 2021.

[3] "Elemental and Magnetization studies of Cu, Ru co-doped $ZnFe_2O_4$",

S. K. Jena, A. K. Hota, S. Singh, M. RoyChowdhury, R. Medwal, and S. Thota,

ICPN 2021, Mangalore University, Mangaluru, INDIA, 27-29th October, 2021.

[4] "Structural and Magnetization Studies of Cu, Mn co-doped Franklinite",

S. K. Jena, A. K. Hota, S. Ghosh, M. RoyChowdhury, and S. Thota,

CCMP 2021, PRL, Ahmedabad, INDIA, 16-18th August, 2021.

[5] "High Temperature Magnetization Studies of Mixed Spinel $Cu_{1-x}Zn_xFe_2O_4$",

S. K. Jena, S. Ghosh, S. Kushwaha, S. Sharma, D. C. Joshi, and S. Thota,

PMSR 2020, Dibrugarh University, Dibrugarh, INDIA, 4-6th February, 2020.

[6] “Dipole relaxation behaviour and dynamical response of Zn substituted $CuFe_2O_4$: Role of Polar Nanoregions”,

S. K. Jena, S. Mehta, A. K. Hota, S. Ratha, Md. K. Warshi, and S. Thota,

ICNAN’19, VIT, Vellore, INDIA, 29th Nov-01st Dec, 2019.

[7] “Synthesis, Structural and Magnetic Properties of $Ni_{1-x}Mg_xO$ Nanostructures”,

S. K. Jena, S. Mohapatra, S. Singh, P. Pramanik, D. C. Joshi, and S. Thota,

RC’19, IIT Guwahati, Guwahati, INDIA, 14-17th March, 2019.

[8] “Crystal Structural and Micro Raman Studies of $Ni_{1-x}Mg_xO$ Solid Solutions”,

S. K. Jena, S. Singh, S. Ghosh, A. Keelu, P. Pramanik, and S. Thota,

NCHSCMP-2019, Tezpur University, Tezpur, INDIA, 4-6th March, 2019.

Contents

List of Figures

Figure No.	Figure Description	Page No.

Chapter 1

Chapter 2

Chapter 3

Chapter 4

Chapter 5

Chapter 6

Chapter 7

List of Tables

Table No. **Table Description** **Page No.**

Chapter 1

Chapter 3

Chapter 4

Chapter 5

Chapter 6

List of Abbreviations and Symbols

MF − magnetic frustration
SL − spin liquid
SG − spin glass
T_{FiM} – Ferrimagnetic Néel temperature
T_{N} – Antiferromagnetic Néel temperature
FM − Ferromagnetic
AT − de Almeida Thouless
GT − Gabay Toulouse
JT − Jahn Teller
MCW − modified Curie Weiss
XRD − x ray diffraction
XPS − x ray photoelectron spectroscopy
ND − neutron diffraction
ZFC − zero field cooled
FC − field cooled
HTSE − high temperature series expansion method
S_M − magnetic entropy
MCE − magnetocaloric effect
TRM − thermoremanent
ϵ_{R} − dielectric permittivity
tan δ − Dielectric loss or Loss tangent
JPL − Jonscher's power law
VRH − variable range hopping
Å − Angstrom
K − Kelvin
pm − picometer
nm − nanometer
T − temperature
M − dc magnetization
χ − magnetic susceptibility
H − dc magnetic field
h_{ac} − ac magnetic field
μ_{B} − Bohr magneton

Chapter 1
Introduction: Geometrical Frustration in Spinels

A brief general introduction to the spinels and their importance in the scientific community is discoursed here. Spinels are the gemstones which have been used in ornaments for centuries and have drawn the attention of the scientific community since the middle of 18th century. The spinel crystal structure can accommodate variety of cations in the periodic table such as alkali, alkaline-earth, transition metals, and rare-earth elements. Such combination of solid solutions offers condensed matter physicists with one of the richest families of magnetic materials [1]. Owing to their noteworthy structural, magnetic and electrical properties, spinels have greater importance in terms of practical applications in a wide variety of industrial and scientific fields. Some of the key properties that spinels exhibit are: Ferrimagnetism, large magneto-crystalline anisotropy, higher saturation magnetization and squareness ratio [2], negative magnetization with magnetic compensation, bipolar-exchange-bias [3], much higher electrical permeability and resistivity [4], low loss of eddy current [5], and mechanical hardness [6]. Generally, spinel-ferrites are easily magnetized under small external magnetic fields because of which they find a unique place in the field of magnetic data storage, magneto-electronic devices, key elements in renewable energy sectors, and microwave relaxor ferroelectrics [7-10]. In addition, site specific substitution of spinel compounds with either magnetic or non-magnetic elements lead to some remarkable magneto-electric properties by introducing ordered/disordered states. Such disorderness is very sensitive to the temperature and external magnetic field, especially at ultra-low temperatures and triggers some important features such as quantum-spin ice/liquid state etc [11-13].

In this chapter, first we elucidate in detail the basic crystal structure of spinel oxides along with the foundation concepts of magnetic frustration arising from the crystal geometry of the chosen compounds for this doctoral thesis. These fundamentals are followed by a detailed description on few novel magnetic phenomena discovered in the recent past, which are linked to the current topic of research work discussed meticulously in the remaining chapters of the thesis. This chapter also provides a detailed description of some of the mathematical relations linking the underlying physics of the spin-glass, spin-liquid states including different types of exchange interactions. Further, we provide a brief information on the applications of spinel oxides including different type of dielectric relaxation and electrical conduction mechanisms of the systems under consideration. In the end, we provide a clear and vivid description of the undertaken research problem and our approach to achieve the key objectives of the proposed research work.

1.1. Spinel Oxides (AB_2O_4):

The general formula for spinel compounds is AB_2X_4. where the anion X is any divalent chalcogenide element: O^{2-}, S^{2-}, Se^{2-} or Te^{2-}. With oxygen as X, the form AB_2O_4 is regarded as the spinel oxide system. In typical spinel oxides, the anion O^{2-} forms a closely packed pseudo face centred cubic unit cell stabilized with the metal cations at two different coordination environments A and B. Here the divalent metal ions situated

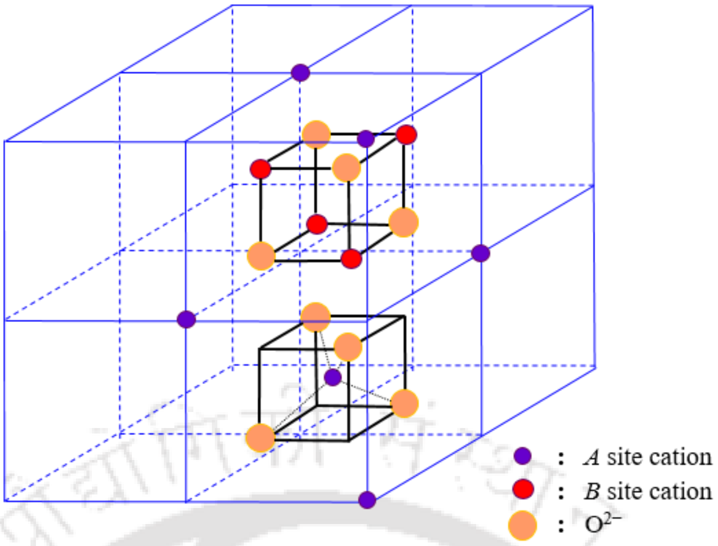

Figure 1.1: Schematic diagram of the spinel crystal structure.

at the tetrahedrally coordinated *A*-sites, along with the *B*-sites occupied by trivalent cations having octahedral coordination, is called a normal spinel [14]. Yet, the inversion parameter (u) among *A* and *B* sites plays a crucial role in determining the extent of deviation from the ideal case. For instance, in the spinel configuration $(A_uB_{1-u})[A_{1-u}B_{1+u}]O_4$, u can take values as (*i*) 1: normal spinel, (*ii*) 0: inverse spinel and (*iii*) $0 < u < 1$: mixed spinel. Further, the spinel lattice turns out to be like the zinc-blende structure in the absence of octahedral sites and fully occupied tetrahedral sites. Instead, if one considers only *B* sites, then the structure converges to that of a rock-salt-type crystal. Consequently, the spinel lattice can be imagined as an ordered-mixture of the rock-salt and zinc-blende unit cells [15]. Two independent works by Bragg [16] and Nishikawa [17] could reveal the crystal structure details of a spinel showing that four number of primitive unit cells are combined to form the conventional cubic spinel unit cell. It is worth mentioning that the primitive unit cell is comprised of two octants in the pseudo-cubic unit cell of the spinel lattice. As shown in figure 1.1, one octant is the cubic cell A_2O_4 (two *A* sites in tetrahedral coordination) and the other one is the cubic B_4O_4 cell (four *B* sites in octahedral coordination). There are in total 96 interstices available between the anions. Nonetheless, only 8 *A* and 16 *B* interstices are occupied out of the available 64 *A* and 32 *B* interstices, respectively, for cations. The choice of origin can be made with either an occupied site or a vacant site which results in two different equi-points (popularly known as the Wyckoff notations) each of them having both $\bar{3}m$ and $\bar{4}3m$ type point symmetries [18].

However, the anion O^{2-} may possess deficiency (δ) in the $AB_2O_{4-\delta}$ lattice depending on the sample preparation techniques which triggers the disruption of the conventional magnetic and electrical properties [19,20]. At some instincts the cubic spinel becomes a defect ABO_3 type of structure with uncompensated magnetic ions on *B* sites (taking charge neutrality into account) [21]. In view of the inter-sublattice and intra-sublattice exchange interactions (J_{AA}, J_{BB} and J_{AB}) between the magnetic and non-magnetic cations, spinels are capable of producing higher degree of magnetic frustration as a result of competing exchange interactions. In the below sections and coming chapters we give emphasis to the magnetic frustration exhibited in some Pyrochlore spinel lattices.

1.2. Pyrochlore Spinels and Their Crystal Geometry:

Ternary oxides isometric with $M_2N_2O_7$ are usually observed to exhibit the Pyrochlore structure [22,23]. The speciality of this structure is that they contain a corner shared tetrahedra geometry as depicted in figure 1.2. Typically, the M (a rare earth element) and N (a transition metal / p−block element) site accommodates 3+ (or 2+) and 4+ (or 5+) state cations, respectively [24]. The general formula of Pyrochlores can be alternatively expressed as $M_2N_2O_6O'$ with the space group ($Fd\bar{3}m$) and the number of molecules per unit cell (Z = 8) like in the case of spinels. In 1993, Subramanian and Sleight pointed out about the four different choices of origin, shown in Table 1.1 [25]. It is noticed that if we fix the origin to be on the N site (at 16c), then the other atoms M, O, and O′ occupy the Wyckoff positions 16d, 48f, and 8b, respectively. Here, the M and N site ions form a face-centred-cubic array with its ordered rows along <110> directions. Furthermore, the six O-atoms (48f) are surrounded by two numbers each from M and N cations, nevertheless, O′ is surrounded by four M site cations and the remaining unoccupied anion sites are surrounded by N cations. It is to be noted that, the positional parameter (x) indicates the extent of shift of 48f O-atoms towards the smaller sized ions N [22]. The only positional parameter for O-atoms at 48f provides two key inferences from the above discussed structural details: (a) concerning the topology of M and N sites and (b) co-ordination geometry at M and N sites with respect to O-atoms. As a result, the corner-sharing-tetrahedra formed at both the M and N sites gives rise to canonical geometrical frustration in the $M_2N_2O_7$ lattice [24]. However, a corner sharing tetrahera network is also realized in several AB_2O_4 minerals. It is interesting to note that contrary to $M_2N_2O_7$, in AB_2O_4, only the octahedral B site formulates a Pyrochlore lattice-type geometry while the A site frames a diamond lattice [15].

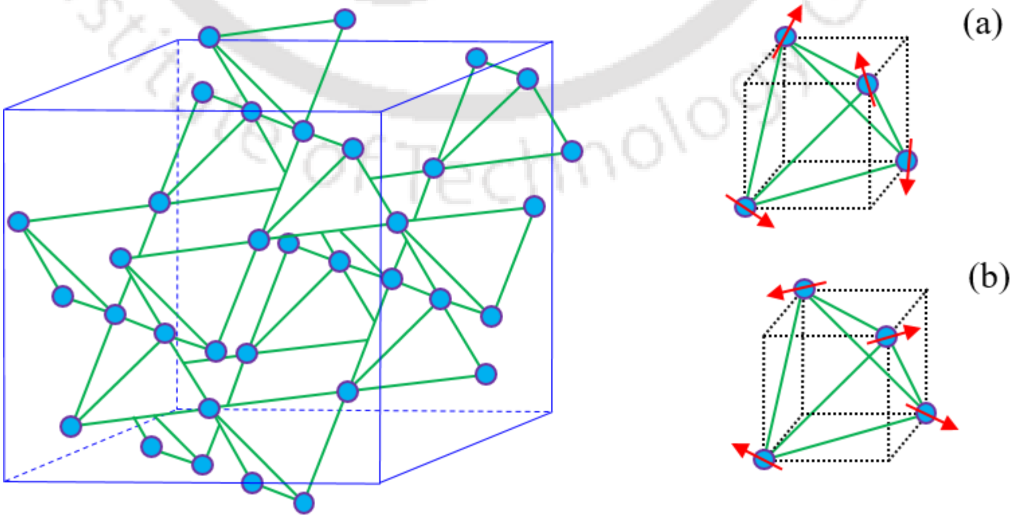

Figure 1.2: Schematic representation of the cubic Pyrochlore lattice which consists of tetrahedral shapes, connected with each other at the corners.

Table 1.1: Lattice sites of a Pyrochlore structure along the cubic body diagonal in the ideal conventional unit cell of spinel, by considering four possible choices of the origin.

Atom	Equipoint	Minimal coordinates (along body diagonal of the unit cell)	Point symmetry
M	16*d*	½, ½, ½	$\bar{3}m$ (D_{3d})
N	16*c*	0, 0, 0	$\bar{3}m$ (D_{3d})
O	48*f*	*x*, ⅛, ⅛	*mm* (C_{2v})
O′	8*b*	⅜, ⅜, ⅜	$\bar{4}3m$ (T_d)

1.3. Geometrical and Magnetic Frustration:

Frustration in magnets is defined by the inability of the system to stabilize in a unique ground state, rather it inhibits degeneracy. Magnetic frustration (MF) is realized when the lattice geometry is discordant to the interaction exhibited among the magnetic degrees of freedom giving rise to peculiar magnetic properties such as spin-ice and spin-liquid states [27]. The simplest form of MF can be understood with antiferromagnetically coupled spins occupying the triangular-lattice points (as shown in figure 1.3(a)). In such case, the magnetic-moments/spins of nearest neighbor atoms prefer antiferromagnetic (AFM) alignment, yet no defined pattern in the lattice satisfies the interaction between all the atoms. In 2D-case, an array of edge-sharing triangular-lattice leads to a Kagomé structure (kagome means a bamboo-basket (Kago) woven pattern (me)), while in 3D, the edge- or corner-sharing tetrahedral geometry results in a Pyrochlore structure. Nevertheless, the origin of MF is two-fold; irregular arrangement of the crystal lattice is the essential requirement while the second-most important one is the type of non-magnetic/magnetic ions occupying the lattice sites. For instance, in spinel-Pyrochlores, non-magnetic *A* site cation together with magnetic *B* site ions show higher degree of MF in comparison to the systems having magnetic ions on both *A* and *B* sites [24,28].

Previous studies reveal that the Heisenberg model established for the spinel-Pyrochlores considering AFM-type nearest neighbor exchange coupling exhibits an extensive number of degenerate ground states [30,31]. Apparently, such robust ground state in magnetically frustrated systems leads to the absence of magnetic long-range (LR) order since it averts minimization of all the interaction energies. The only feasible magnetic ordering is expected to arise from the existing exchange interactions among the magnetic species that may extend beyond the nearest neighbor ions, or from the possible dipole coupling [32]. Specifically, when the system is cooled to very low temperatures ($T \rightarrow 0$ K), the role of exchange interaction becomes clearly evident. With suppression of the conventional order, the magnetic moments revisit paramagnetic (PM)-type ordering (below the spin-freezing temperature, T_g) in a region which lies much below the disordered paramagnetic region than that predicted by the classical theory [30,33]. Drastic reduction of the ordering temperature often measures the degree/index of MF which is given as: $f = |\theta|/T_N$, where θ is the Curie-Weiss temperature and T_N is the AFM Néel temperature. It is well known that in general, to remove the robust spin-degeneracy, at times, the lattice may undergo structural phase transition to a lower structural symmetry associated with a magnetic transition to an ordered AFM state [34]. Having such peculiarities,

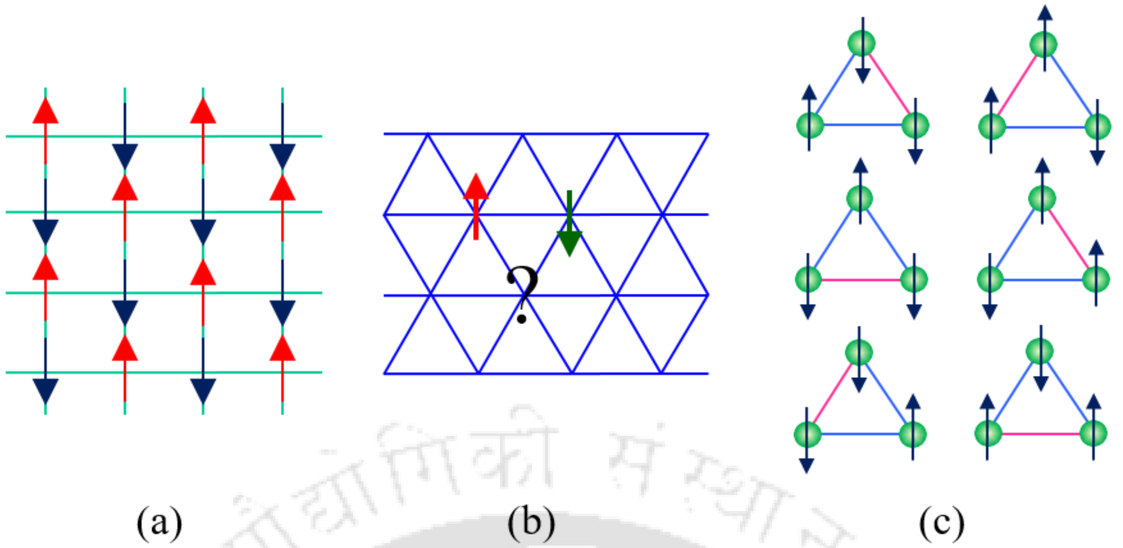

Figure 1.3: (a) An unfrustrated square lattice having AFM alignment among the neighboring spins. (b) Similar AFM alignment is not possible on a triangular lattice. (c) The six possible ground states in a triangular lattice instead of two ground states as directed by the Ising symmetry [27,29].

geometrically frustrated spinels and Pyrochlores are observed to exhibit certain novel magnetic phenomena such as spin-liquid (SL) state [35], spin-ice state [36,37], spin-Jahn−Teller state [38,39] etc., having practical applications in the areas of microelectronics and drug delivery.

1.4. Few Novel Magnetic Phenomena Exhibited by Spinel Pyrochlores:

1.4.1. Spin-Liquid Phenomena:

1.4.1.1. Quantum and Classical Spin-Liquids:

A possible classical model solution for stability of the frustrated AFM triangular lattice is suggested by Bernu *et al.* by assuming the spins on each corner at an angle of 120 ° with each other [40]. However, in 1973, P. W. Anderson proposed the probability of a more unusual ground state of the frustrated AFM configuration in the triangular 2D lattice governing quantum entangled spins and this prescribed model is popularly called as the resonating valence bond (RVB) model [41]. As per this model, two anti-parallel spins combine to form a spin-singlet with zero net moment (**S** = 0). Quantum fluctuations exhibiting in the frustrated lattice destroys the possibility of a particular arrangement for these singlets, consequently, the wavefunction of a RVB spin-singlet can be treated as linear superposition of all the possible configurations of the spin-singlet. Therefore, no LR magnetic ordering could be developed even up to $T = 0$. The spin pattern for such a system resembles a liquid, without breaking spontaneous translational and rotational symmetry of the lattice points, which leads to the nomenclature of this Quantum state as Quantum-Spin-Liquid (QSL) state. Nevertheless, LR entanglement between the spins is feasible in these cases (as illustrated in figure 1.4) which leads to fractional spin excitations [42].

On the other hand, in a classical spin liquid state (CSL), thermal fluctuation energy ($k_B T$) dominates over the superexchange interaction parameter (J) at high temperatures, hence the magnetic order could not be

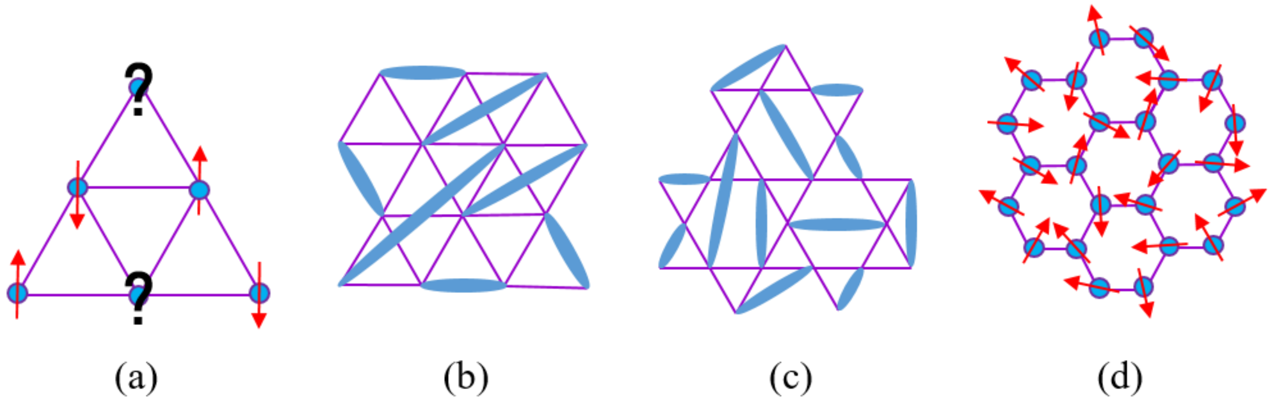

Figure 1.4: Schematic of few typical 2D crystal structures for (a) and (b) triangular, (c) Kagomé, and (d) Honeycomb lattices. The red arrows represent spins and question marks denote undetermined spin configurations resulting from geometrical frustration. The light-blue shades in (b) and (c) demonstrate the spin singlets mandated by the RVB model [42].

established. As a result, in contrast to QSL, CSL lacks LR quantum entanglement and fractional spin excitation. Such spin dynamics comes into picture over the static mechanism and the low-temperature (k_BT << J) quantum mechanical formulations like the spin-spin correlation starts to exhibit remarkable outcomes at high temperatures [42].

1.4.1.2. Gapless and Gapped Spin-Liquids:

Quantization of fractionalized excitation is a spinon (fermion or boson), which carries spin=1/2 but no charge. Now, SLs can be categorized into two sub-classes: gapless and gapped SLs. In gapless SL, excitation occurs across the Fermi surface (Dirac nodes) formed by fermionic spinons [43]. This is identified from the magnitude of the coefficient γ which is obtained by fitting the low temperature specific-heat ($C_p(T)$) data to the relation:

$$C_p = A\mathrm{T}^{-2} + \gamma\mathrm{T} + \beta\mathrm{T}^3 \qquad (1.1)$$

Here, the linear term in temperature i.e. "γT" is related to the finite excitation density of states. In case of metals γ usually remains unaffected by the external magnetic field [44]. Conversely, the theoretical prediction of $\mathrm{T}^{2/3}$ dependence of the above linear-T term is not quite evident in experimental observations so far [45]. Linear-T dependence of thermal conductivity is another vital signature for this kind of excitation [46]. One more type of gapless SL can possibly exist, wherein the spinons are gapless only at certain nodal points of the Fermi surface around which they display linear spectrum. Considering the presence/absence of gauge fields, formulated on the mean-field-theory, there exists two cases: U(1) or Z_2. In U(1), the gauge fluctuations may lead to the modification of the T-power laws, however, in Z_2, the density of states vary linearly with energy while both heat-capacity, C_p and the NMR spin-lattice relaxation rate ($1/T_1$ estimated over a finite temperature range using nuclear-magnetic-resonance) follow T^2 dependence [47].

In what follows a detailed discussion pertaining to the gapped SL which are considered as the Bosonic spinons combined with gapped visons (i.e. specific vortices in the Z_2 gauge fields), also commonly recognized as Z_2 –SLs (Z_2–spin liquids) [48,49]. Detailed studies by Kivelson *et al.* [50] and Baskaran *et al.* [51] have shown that Fermionic spinon based mean-field-theory can also bring about a Z_2 state, however, the fact that Fermionic spinons are formed when a Bosonic spinon binds with a vison (Z_2 vortices) and this situation is directing through the identical situation applicable to the Bosonic spinons, as discussed above. Furthermore, the case of U(1) gapped SL is forbidden in 2D since compactness leads to confinement.

Another important gapped system that are under intense investigation in recent times is the "Spin-Chirality"; ever since it was proposed by Kalmeyer and Laughlin in 1989 the concept of 'Chiral spin liquids' are under extensive study. Chiral spin liquid (ChSL) is a unique spin singlet state formed in the triangular Heisenberg AFM lattices [52,53]. Figure 1.5 shows the proposed schematic diagram for a ChSL usually formed from a Honeycomb lattice by replacing each of its site with a triangular geometry. This ChSL state often exhibits fractionalized excitations with notable properties like Kerr-Rotation, Quantized-Thermal-Hall conductivity and Chiral spin-edge modes [45]. Also, in ChSL the translational and spin-rotational symmetries are strictly maintained [54], still breaking of time-reversal and parity symmetries makes its candidature dubious to be categorized as a gapped spin liquid system [55]. Therefore, based on the gauge field theory, only Z_2 type gapped spin liquids have been evident so far although other exotic possibilities can't be denied without breaking the symmetry. The above discussion also concludes that the method to distinguish between the Dirac spin liquid, the U(1), Z_2 spin liquid and the chiral spin liquid systems is indeed debatable. Very low excitation energy is a typical character of all these systems as these systems do not show any significant difference in the excitation energy among them which makes it very tedious to differentiate between them.

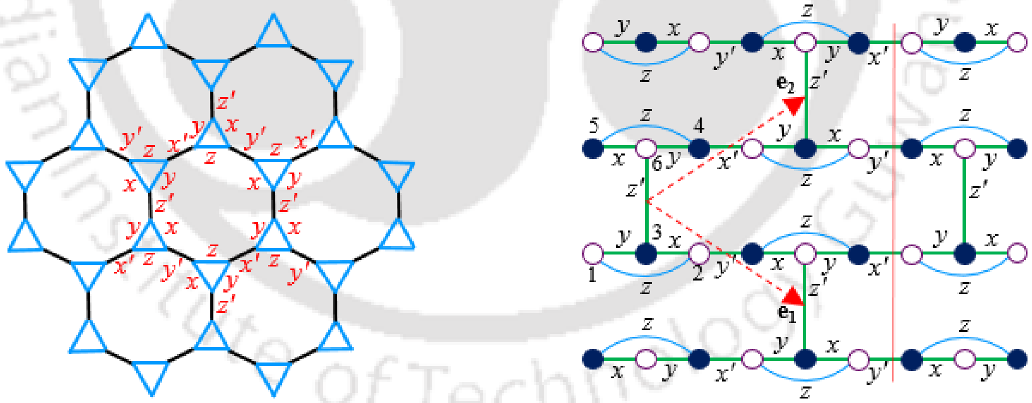

(a) (b)

Figure 1.5: (a) Diagram of the triangular-Honeycomb lattice of a Chiral spin liquid (ChSL) that is constructed by replacing each site of the Honeycomb with a triangle; thus 6 sites per unit cell is obtained. (b) These 6 sites are labelled in the topologically equivalent schematic representation, while the red dotted line is the vertical boundary of the unit cell [54].

1.4.2. Spin-Ice State:

1.4.2.1. Structure and Mechanism:

Spin-Ice, a rather strange yet exciting physical phenomenon is mainly governed by frustrated ferromagnetic (FM) alignment, not the frustrated AFM phenomena [56]. The nomenclature "Spin-Ice" came from its ferromagnetic analogue with Linus Pauling's model on the residual entropy of Water-Ice [57]. Experimental finding of spin-ice state was noticed for the first time in 1997 by Harris *et al.* in the Pyrochlore $Ho_2Ti_2O_7$ and was confirmed later by Ramirez *et al.* in its sister-compound $Dy_2Ti_2O_7$. The later compound displays an unusual residual entropy of magnitude approximately $(1/2)\,Ln(3/2)$ for $T \rightarrow 0$, which is associated with its ground state degeneracy and is in consonance with the Pauling's estimation of water ice [36,58].

Analogy between Water-Ice and Spin-Ice systems is illustrated in figure 1.6. It elucidates that the spin orientation in a spin-ice plays an equivalent role similar to the position of H^+ atom (proton) in the Water-Ice theory. In the H_2O molecule, an analogous tetrahedra motif is formed considering the mid-point of O−O lines as the corners sharing a tetrahedra. Following similar analogy of the direction of proton displacement in H_2O, the magnetic spins in a Spin-Ice follows the constraints that (*i*) all the four spins at the corners must point either outward (→) or inward (←) to the center of the tetrahedral, and (*ii*) in each tetrahedra two spins must point inward (←) while the rest two must point outward (→), which are usually symbolized as a 2:2 vertices. However, general interpretation of degeneracy in a 'Spin-Ice' system is explained by virtue of a 16-vertex model that includes six 2:2 vertices, eight 3:1 and two 4:0 vertices. It is to be noted that the energies of 4:0 vertices are higher than the 3:1 vertices, while 2:2 vertices exhibit the lowest energy. The statistical (Boltzmann) weights of all these 16-vertices can be tuned by the application of external fields (both electric and magnetic) [59,60], pressure [61], strain [62], by quantum effects [63], with change in temperature and substitution of elements as well [64]. At higher temperatures, all the 16-vertices carry equal statistical

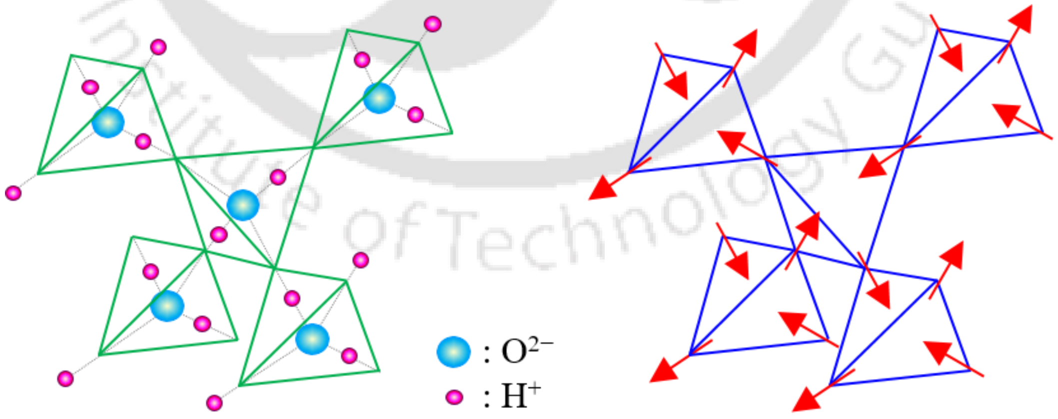

(a) : Water-Ice (b) : Spin-Ice

Figure 1.6: A schematic analogue between the (a) Water-Ice and (b) Spin-Ice systems. In Water-Ice, each hydrogen ion is close to one or the other of its two oxygen neighbors, and each oxygen must have two hydrogen ions closer to it than to its neighboring oxygen ions. In Spin-Ice, the spins point either directly toward or away from the centres of the tetrahedra, and each tetrahedron is constrained to have two spins pointing in and two pointing out [66].

weights, consequently the system attains a paramagnetic state. Nonetheless, with lowering of temperature, vertices with higher energy get frozen out first. Ultimately, the six 2:2 vertices remain to form the spin-ice state as per the Pauling's model at very low temperatures ($T < 1$ K) [56]. Surprisingly, there are evidences of unique properties like crossover from Debye spin relaxation to Quantum mechanical tunneling dynamics in 'Spin-Ice' systems at much greater temperatures $T = 15$ K, which requires further investigation [65].

1.4.2.2. Dipolar Interaction and Magnetic Monopoles:

The compounds (e.g. $Dy_2Ti_2O_7$ and $Ho_2Ti_2O_7$) exhibiting Spin-Ice property possess an easy axis anisotropy along <111> plane that points towards the centre of the tetrahedra, as a result the FM alignment behaves as a pseudo-spin AFM at much lower temperatures (well below the strength of anisotropy) [67]. Here, the existing local crystal field is able to spilt the free ion state so that the Ising-like doublet energy is lowered by few hundreds of Kelvins, which results in a local Ising symmetry. Further, the nearest neighbor FM interaction between Ising spins is the dipole-dipole interaction that is less likely to be a weaker AFM [37]. However, beyond the nearest neighbor, the dipolar interaction can be FM/AFM or even multiple-valued, which is dependent on the distance of neighboring spins [68]. For negative value of effective exchange interaction (J_{eff}) being the coupling energy corresponding to an 'in-out pair' of spins and positive J_{eff} to that of an 'in-in pair' or 'out-out pair', energies (E) of the different possible states are obtained to be $E(4{:}0) = 6J_{\text{eff}}$, $E(3{:}1) = 0$ and $E(2{:}2) = -2J_{\text{eff}}$. An abbreviated version of the dipolar spin-ice (DSI) model is the near-neighbor spin-ice model that gives a microscopic explanation to the phenomenological FM coupling in the Spin-Ice. This phenomenon can be understood according to the Hamiltonian as given below:

$$H = \frac{\mu_0 g^2 \mu_B^2}{4\pi} \sum_{i>j} \frac{S_i \cdot S_j - 3(\hat{r}_{ij} \cdot S_i)(\hat{r}_{ij} \cdot S_j)}{r_{ij}^3} - \sum_{<i,j>} J_{ij}\, S_i \cdot S_j \qquad (1.2)$$

where S_i is the spin, μ_0 and μ_B are the vacuum permeability and Bohr magneton, respectively. The dipolar term (first term on the right-hand-side in equation (1.2)) comes out to be much stronger (20.7eV) in comparison to the near-neighbor exchange term (−10.7 eV in $Dy_2Ti_2O_7$ and −4.5 eV in $Ho_2Ti_2O_7$) [37]. Nevertheless, the dipolar interaction energy in Spin-Ice could be considered as self-screened, and is distinctly irrelevant to the Pauling's manifold theory [58,69].

Unlike particles carrying electrical charge, no elementary particle carrying a net magnetic charge has been observed in the history even after intense research activities. Initially, a rare case of quasiparticle was considered to be the only one having fractional electric charge ($e/3$) exhibited in Quantum-Hall effect [70]. Later, existence of the magnetic monopole (MM) term emerged from the mysterious first-order type liquid−gas phase transition (i.e., from Kagomé-Ice to 3:1 ordered state). Such transition occurs as the temperature is lowered while simultaneously increasing the applied field along the crystallographic direction <111>, with a critical end-point in the Spin-Ice systems [71]. Suppose the Ising spins are assumed to be in dumbbell shape with opposite magnetic charges at their two extremities, then the magnetic charge at the centre of the tetrahedron emerges which is termed as a MM, that produces a non-zero divergence of the local magnetization [72]. It is only after the discovery of MM model that the 3:1 Spin-Ice defects could be believed to follow similar analogy of the ionic defects in Water-Ice, and this concept also helped in handling the dipolar interactions in the Hamiltonian for the excited states [13,56,73]. Additionally, the monopoles appearing in the work that is reported based on the anomalous Hall effect in highly anisotropic FM $SrRuO_3$ perovskite possess unresolved excitations since no magnetic field is involved here [13,74]. Furthermore, the MMs present rare cases of high-dimensional fractionalization and are of high interest in the fields like topological quantum computing and fields involving highly correlated electron systems [75].

1.4.3. Spin-Glass State:

Another peculiar yet popular phenomenon that arises in disordered magnets is the spin-glass (SG) state having multiple ground states. The origin of such a state can be understood by realizing isolated magnetic impurities situated at random lattice sites being able to interact with each other. The interactions between the impurity magnetic moments can be FM or AFM depending on the distance between them [76]. Because of such features the terms spin (magnetic moment) and glass (disorder) were introduced following the analogy that in real glasses/amorphous solids, the atoms are irregularly ordered in the lattice sites. As we lower the system temperature, competing exchange interaction between the random site moments and the bond-randomness (figure 1.7(a)) increase magnetic frustration. LR order is destroyed below a certain temperature in which the impurity moments are frozen in random directions (shown in figure 1.7(b) and 1.7(c)), called as the spin-glass/freezing temperature T_{SG}. In the SG state, spatial average of magnetic moments over all the lattice sites is zero, simultaneously the time average of a particular spin orientation will be non-zero; in contrast to the PM state where both the averages are zero with fluctuating spin orientation. A characteristic feature of SG state is that it follows non-ergodicity. In such state the system may fluctuate between a number of equilibrium states of equivalent energies, however it cannot make transition to the other states. In other words, the system is trapped in the deep minima of the hierarchically disordered energy-landscape [77,78]. As a result, different ground states may be attained by the system when it is cooled below T_{SG} after rising the temperature again to the PM region each time. Such nonergodic systems with rugged energy-landscapes have great applications in understanding the trends of neural networks for instance Hopfield networks, and also in genetics and for computer science optimization purpose [79-81].

In order to realize SG systems, an obvious and typical way is to incorporate magnetic ions into a non-magnetic matrix/lattice. Yet, the amount of substitution must be within a specified percolation limit/threshold (p_C). 'Percolation limit' is defined as the atomic percentage of substitution for which each magnetic site gets at least one nearest neighbor magnetic atom/ion. Ultimately, a macroscopic connection is established extending from one end to the other end of the crystal. With the doped magnetic ions exceeding the p_C, SG features may vanish concurrently setting up LR order [82]. In addition, with increase in the content of the magnetic impurities (below the p_C), the impurities may form pairs or eventually clusters. Different types of SG systems (canonical SG, cluster SG and others) are determined based on the scaling and power laws, and the fitting parameters are described in detail in Chapters 3 and 4.

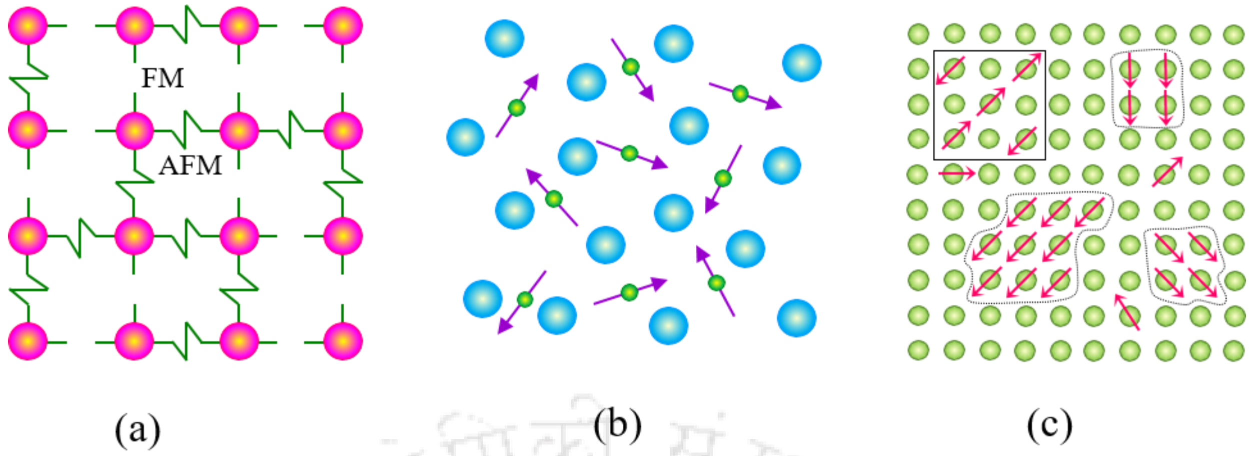

Figure 1.7: Illustration of the (a) bond randomness in a spin-glass state in which the zig-zag and dashed lines represent the antiferromagnetic (AFM) and ferromagnetic (FM) couplings, respectively, (b) disordered lattice sites occupied by magnetic ions, and (c) cluster spin-glass state.

1.4.3.1. de Almeida−Thouless and Gabay−Toulouse Lines:

The stability of SG state was questionable and assumed to be unstable under the application of dc magnetic field (*H*) until de Almeida and Thouless proposed the theory that the replica symmetry breaking can take place even under the external applied magnetic field (*H*) [83]. They also formulated a relation (specifically for low *H* values), that defines variation of $T_{SG}(H)$ with *H* which reveals decrease in T_{SG} with rise in *H* and is expressed mathematically as below:

$$H^2 = A_1\left(1 - \frac{T_{SG}(H)}{T_{SG}(0)}\right)^3 \tag{1.3}$$

In the above relation, A_1 is a characteristic constant. Additionally, the field variation of T_{SG} represented by de Almeida−Thouless (AT)−line may be extrapolated to the zero-field value ($T_{SG}(0)$) which determines the spin freezing temperature T_{SG} accurately. Such interesting field dependent trend in T_{SG} has got many experimental evidences soon after the invention of the AT theory [84-86]. On the other hand, although works by Gabay and Toulouse on disordered Heisenberg systems agreed on the characteristic AT−line behavior of T_{SG}, yet they claimed two transitions in the *H*−*T* plane pertaining to the breaking of ergodic and replica symmetries. According to the Gabay and Toulouse the field dependency of T_{SG} follows the equation given below.

$$H^2 = A_2\left(1 - \frac{T_{SG}(H)}{T_{SG}(0)}\right) \tag{1.4}$$

Here A_2 is a constant. Equation (1.4) is known as the Gabay−Toulouse (GT)−line. Later, Sherrington *et al.* suggested that both the symmetry breakings (replica and ergodic) occur at the same transition simultaneously. Nevertheless, the other transition at lower temperatures may not correspond to a thermodynamic phase change, giving rise to the GT− and AT−lines in the *H*−*T* plane [87]. A small (+ve) single-ion anisotropy may present in these systems, which would lead to the appearance of the lower temperature GT−line in comparison to higher temperature AT–line. Conversely, a small magnitude of –ve single-ion anisotropy results in the AT−line preceded by the GT−line at higher temperatures in the H−T phase diagram [88]. Moreover, the exchange anisotropy (even if it is not adequately weak) is also capable of driving the system to exhibit both the AT− and GT−lines [89]. Additionally, the GT−line critical behavior arises only when the external field perfectly aligns along the internal field. Nonetheless, the AT−line feature is more robust and common [90] feature noticed in many spin-glasses including the cluster-glass and canonical SG systems.

1.4.3.2. Hamiltonian Models for a Spin-Glass State:

- **Edwards−Anderson (EA) Model:**

For the first time, in 1975, S. F. Edwards and P. W. Anderson together proposed a solvable Hamiltonian model for the SG systems considering that there is no mean FM or AFM ordering present in the system. The reason they provided is that in the ground state, each of the magnetic spin is oriented in a specific direction, although the individual spins appear random to one another [91]. For spins arranged on a d-dimensional lattice having only nearest neighbor interactions (similar to the Ising model), the proposed model can be exactly solved for the critical temperatures for $T \leq T_{SG}$. The Hamiltonian based on the mean-field-theory under zero external field can be expressed as:

$$H = -\sum_{<ij>} J_{ij} S_i S_j \tag{1.5}$$

Here in equation (1.5), S_i takes Ising-like values = ±1 and J_{ij} corresponds to the interaction between independently distributed spins. A typical Gaussian model with the probability density distribution ($P(J_{ij})$) is given by:

$$P(J_{ij}) = \frac{1}{\sqrt{2\pi J^2}} \exp\left\{-\frac{(J_{ij} - J_0)^2}{2J^2}\right\} = p\delta(J_{ij} - J) + (1-p)\delta(J_{ij} + J) \tag{1.6}$$

In equation (1.6), J_0 is the mean with variance J^2, while J_{ij} is either +ve J (with probability 'p') or –ve J (with probability '$1-p$'). With use of the replica method the above problem can be solved below a certain temperature which provide the evidence for the glassy phase present in the system [92].

- **Sherrington−Kirkpatrick (SK) Model:**

A modified solution for SG systems was given by David Sherrington and Scott Kirkpatrick in the same year 1975, considering infinite-ranged random interactions of the coupled spins in the EA model [93]. The model is analogous to the Ising model with LR frustrated FM as well as AFM couplings which focuses mainly on competing exchange interactions between the FM and SG phases along with the type of order present in the system. Overall The Hamiltonian for the SK model is therefore given by,

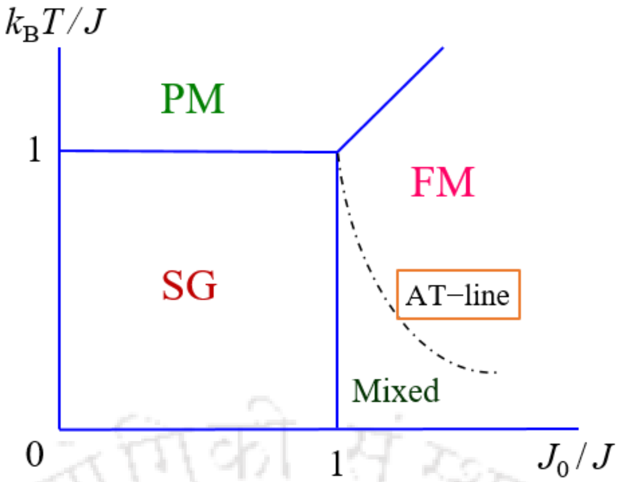

Figure 1.8: Phase diagram of the SK model. The solid blue lines are boundaries between different phases. As the replica-symmetric solution is unstable below the dash-dotted AT−line, a Mixed phase emerges between the spin-glass (SG) and ferromagnetic (FM) phases. At high temperatures, the system enters in to the paramagnetic (PM) region.

$$H = -\sum_{i<j} J_{ij} S_i S_j - h \sum_i S_i \tag{1.7}$$

The first summation term on the right-hand-side of equation (1.7) includes $N(N-1)/2$ number of distinct pairs of spins and the coupling J_{ij} is related to Quenched disorder. Then the probability distribution function becomes:

$$P(J_{ij}) = \frac{1}{J}\sqrt{\frac{N}{2\pi}}\ \exp\left\{-\frac{N}{2J^2}\left(J_{ij} - \frac{J_0}{N}\right)^2\right\} \tag{1.8}$$

where, the mean and the variance both varies as inverse of N as given below.

$$[J_{ij}] = \frac{J_0}{N}\,, \quad \text{and} \quad \left[(\Delta J_{ij})^2\right] = \frac{J^2}{N} \tag{1.9}$$

We note that such normalization is necessary since extensive properties like the specific heat and energy are found proportional to N for the above normalization of interactions. Further calculations based on the replica symmetry solution yielded the phase diagram given below. Later, the equilibrium mathematical solution was established by Giorgio Parisi in 1979, regarded as the Parisi solution [94]. Needless to say that several attempts have been made to the solve the above problem by introducing the cavity method which provide exactly solvable models of SG state Hamiltonian problem without the use of replicas [95].

1.5. Dielectric Relaxation and Conduction Mechanism:

It is well known that any dielectric material is treated as an electrical insulator at room temperature, yet it can store charge because of its polarizability and capacitive effect. Dielectric materials have always been on demand due to their applicability in microwave electronic industry especially their utility is quite noteworthy in the field of low-loss electrical components, low-κ/high-κ gate electrodes in semiconductor devices, batteries, supercapacitors, sensors and transducers [96-99]. Interaction with externally applied ac-electric field reveal abundant information related to the type of polarization and ac-conductivity including many other intrinsic features of broadband dielectric spectroscopy in which the fundamental physical properties are mostly driven by the grain and grain boundary response for various frequencies and temperatures. In general, the externally applied ac-signal (V_{ac}) covering a wide range of frequencies separates out the contributions among various polarization phenomena of the sample, most common mechanism that we usually notice in many High-κ dielectrics being electronic, ionic, dipolar/orientation and space charge etc. Impedance Spectroscopy is an important technique through which one can easily probe such popular polarization mechanism in terms of the capacitive and inductive properties of a system [100]. Under an external electric field, the localized electrons can hop between two charge defect states and the induced/permanent dipoles reorient with respect to the frequency of ac-signal. Also, the Polarons can hop or tunnel across the grains and gives rise to finite electrical conduction. At some particular frequencies, a momentary lag occurs in the response of the dipoles/charge carriers, which is referred to as relaxation. A note to be added is that the dielectric relaxation mechanisms should not be confused with molecular vibrations or the resonant electronic transitions for the fact that the former are much slower as compared to the later (frequency is greater than 10^{12} Hz). All these phenomena are systematically elaborated in Chapter 6 which deals with the dielectric properties of Cu-Zn spinel oxides. This chapter also provide clarity on different types of polarization, charge conduction mechanisms and various relaxation phenomena along with the underlying physics.

1.6. Description of the Research Problem and Our Approach:

Among the various classes of spinel-Pyrochlores, the franklinite, $ZnFe_2O_4$ (ZFO) manifests high MF index (f = 12) with very low T_N ~ 10 K and θ around 120 K. Such high degree of MF in ZFO with suitable magnetic or non-magnetic element substitution at the *B* site is expected to result in novel magnetic phenomena, such detailed study was rarely available in the literature when this problem was undertaken. Additionally, substitution of Jahn−Teller (*JT*) active element at *B* site in the spinel lattice is expected to enhance the MF by introducing structural distortion to lower symmetry. Aiming at such concept, we substituted *JT* active Mn^{3+} and Cu^{2+} in the bulk ZFO and the results are clearly discussed in Chapter 3. We adapted the approach to bring the solution to this problem by probing the plausible exchange coupling strength (J) of the ZFO system where a drastic alteration in J may take place due to the substitution of above mentioned *JT* active elements and a weakly magnetic Ruthenium (Ru^{3+}) at *B* site. Hence, a detailed magnetization study (both dc and ac) is required on the above proposed systems to determine the exact magnetic nature in terms of short-range (SR) and LR magnetic orderings and to map the relevant parameters in the field-temperature (H−T) plane. Extensive results on such study is discussed in Chapter 4. On the other hand, complete substitution at the *A* site in ZFO with *JT* active Cu^{2+} hosts significant degree of tetragonality in the crystal structure, changing its magnetic properties from AFM to ferrimagnetic (FiM) ordering, and all together leads to a mixed spinel configuration owing to the complex site distribution of divalent Cu. Although few reports are available on the magnetic and structural properties of the intermediate compositions (x) of $Cu_{1-x}Zn_xFe_2O_4$, there is no systematic study available in the literature pertaining to their magnetic, dielectric and structural properties. Hence an attempt has been made in the Chapter 5 of this thesis to study the magnetic behavior of $Cu_{1-x}Zn_xFe_2O_4$ bulk polycrystals in detail and to probe the variations of exchange interaction along with the change in crystal structure across the p_C. Finally, a systematic correlation between the magnetic and impedance spectroscopy parameters of $Cu_{1-x}Zn_xFe_2O_4$ systems are studied (Chapter 6) in consonance with its magnetic counterpart which are expected to be useful for the microwave applications.

1.7. Organization of the Thesis Work:

The organization of the remainder of this thesis work is as follows:

(i) The Chapter 2 elucidates the synthesis procedure and different characterization techniques carried out on the proposed systems.

(ii) In Chapter 3, a detailed dc and ac magnetic measurements are performed along with the heat capacity and neutron diffraction measurements on the bulk $Zn_{0.8}Cu_{0.2}FeMnO_4$ system to probe the coexisting SL and SG states.

(iii) The investigation in Chapter 4 is focused on the *B* site substitution effect of weakly magnetic Ru in ZFO. Additionally, dilution effect of *JT* active Cu^{2+} is also probed in the light of several short- and long-range magnetic orderings that arise from the exchange coupling among the weakly magnetic moment ions.

(iv) The Chapter 5 contains a detailed crystal structural and magnetic analysis on the intermediate compositions where the two end compounds are ZFO and $CuFe_2O_4$. Study of the $M\text{−}H$ hysteresis loop results provide a better insight in to the varying exchange coupling as we deviate from the Pyrochlore ZFO, and also across the structural transition that appears on approaching $CuFe_2O_4$.

(v) A comprehensive study of the dielectric parameters, acquired from the impedance spectroscopy measurements, is executed in Chapter 6 on the $Cu_{1-x}Zn_xFe_2O_4$ series of systems in consonance with the magnetic results attained in Chapter 5.

(vi) Lastly, Chapter 7 highlights all the key results obtained in this thesis work and its future scopes.

Chapter 2

Experimental Details and Methodology

This chapter describes all the experiments carried out during the PhD work along with the methodology and work plan. First section of this chapter deals with the synthesis procedure of bulk spinel samples, meticulously. In the later sections, we discuss various characterization techniques employed to study the crystal and electronic structure, magnetic (along with neutron diffraction and heat-capacity measurements), and dielectric properties of Zn-Cu-based spinel oxides. The precursors used here for synthesis purpose were procured from Alfa-Aesar GmbH and Sigma-Aldrich Chemicals.

2.1. Synthesis by Solid State Reaction Method:

In the current study we prepared bulk grain sized spinel ferrite samples using the standard solid-state reaction (SSR) method. The SSR method involves multiple steps such as Ball-Milling (BM) (an alternate way is to grind with an agate mortar and pestle) and calcination, which lead to volatilization of the crystallizing water resulting in formation of dry-precursor. This technique is one of the easiest, cost-effective and thermodynamically stable method to synthesize the ceramic systems [101]. One of the main advantage of this technique is that one can choose a wider spectrum of precursors like oxides and carbonates, which are mostly in their solid form. The precursors should be mixed thoroughly to obtain a homogeneous mixture, and then must be heated as the solids will not react with each other at room temperature. In the following sections, different steps involved in the SSR technique is discussed in detail along with the flow-chart (figure 2.1).

For our work, stoichiometric amounts of ZnO, Fe_2O_3, MnO_2, RuO_2 and CuO were chosen as the starting compounds (precursors). To attain the high degree of homogeneity and to avail higher surface area for reactants, these stoichiometric amounts of precursors were mixed and ground together in an agate mortar for 4−5 hours, or ball-milled for the required time duration. Such mixture was first calcined in air for 4 h between 600 °C and 900 °C to remove the volatile substances. This mixture was pelletized using both 13 mm (and 15 mm) diameter KBr die-set and hydraulic-press to form compact cylindrical pellets. These pellets were finally sintered in the temperature range 900−1200 °C for 4−8 hours in air with heating rate 5 °C/min which led to chemical decomposition and resulted in the formation of the desired dense ceramic compound. The final sintering temperature and pre-sintering conditions were varied depending on the nature of the composition.

2.1.1. Homogenization of the Precursors using Ball-Milling:

Using the planetary BM all the precursors are homogenized/mixed uniformly. The schematic diagram of the planetary Ball-Mill that is shown in figure 2.2 which is used for mechanical alloying or for mixing and perfect homogenization of emulsions and pastes. In the present case, we employed the Planetary Mono Mill model PULVERISETTE 6 classic line from FRITSCH GmbH. This is a high-performance Planetary Ball Mill with a single grinding bowl mount and practical easily adjustable imbalance compensation. This instrument has high-energy effect of up to 650 rpm. This ensures a constantly high grinding performance

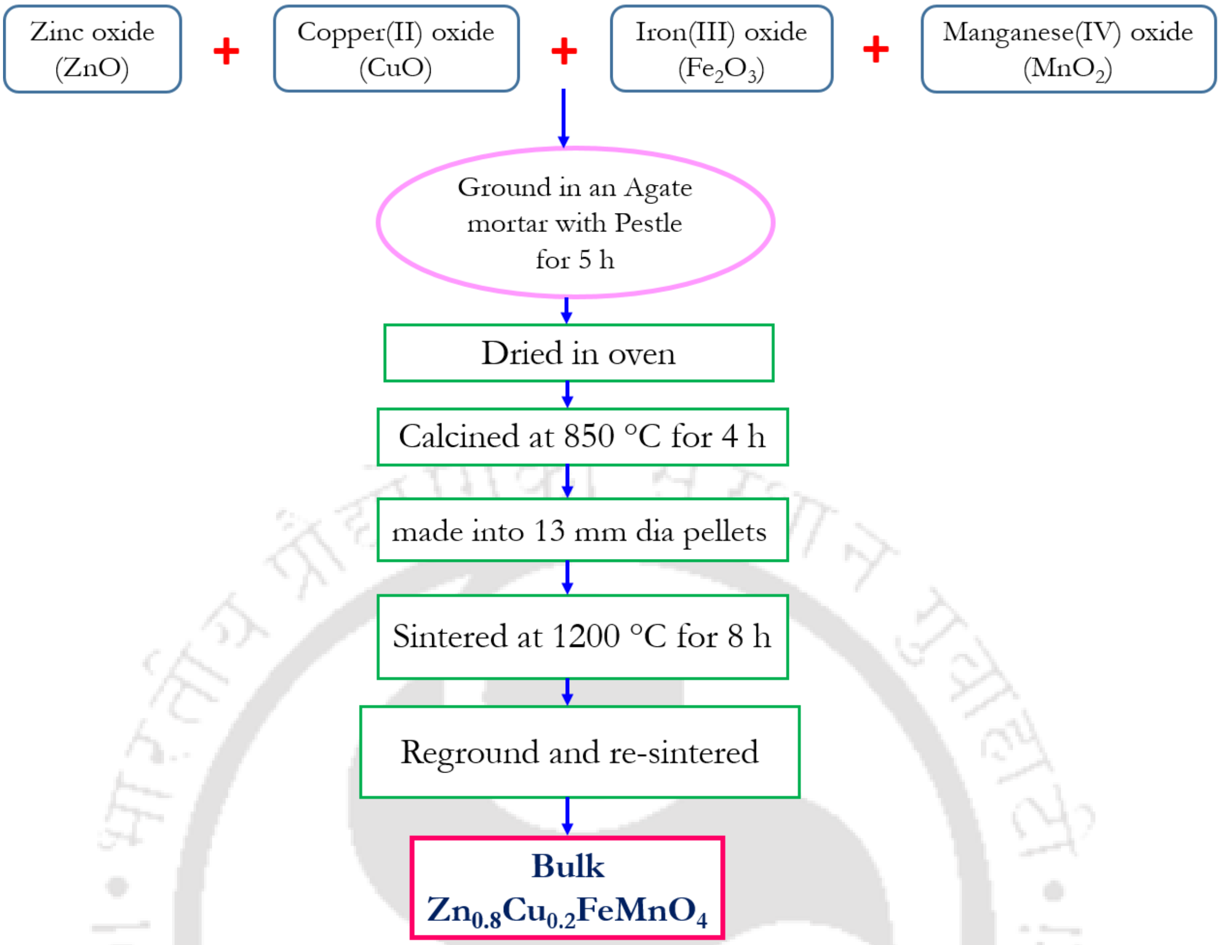

Figure 2.1: Flow-Chart for Solid-State Reaction technique followed to synthesize bulk $Zn_{0.8}Cu_{0.2}FeMnO_4$.

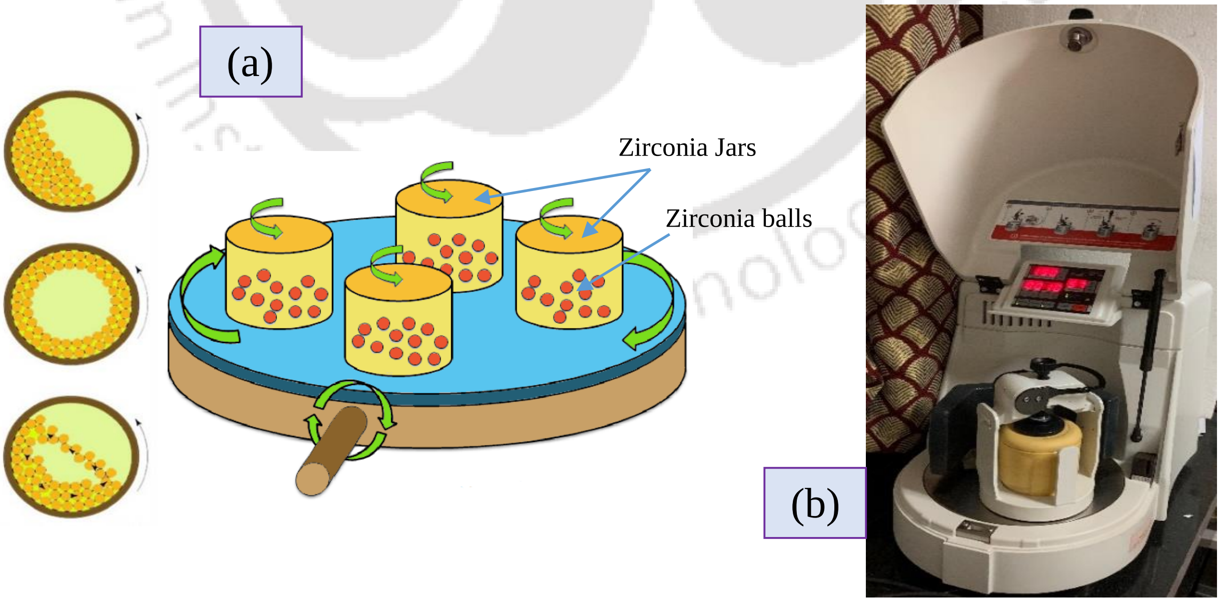

Figure 2.2: Schematic representation of how a planetary Ball-Mill works. Image on the left (a) shows the cascade action that happens inside the zirconia jar during the operation and the image on the right (b) shows the photograph of the Ball-Mill that was used in this work.

with extremely low space requirements for loss-free grinding results for the formation of hard, medium-hard, brittle and moist materials which is dry in suspension or in inert gas. Its arrangement consists of a hollow cylinder with zirconia balls placed in it. These balls can be occupying about 35−45% of the milling medium. Generally, BM is executed by placing the precursors in the jar made of high-dense ceramic materials such as zirconia or alumina (or tungsten carbide) with tiny balls made of same material as that of the jar, which weighs about 3−5 g each and of 10 mm diameter. The chemical composition of Mg stabilized zirconium oxide grinding bowl (250 ml volume) and balls should be between 94.2% and 95.2% of zirconium oxide (ZrO_2), 1−2% of hafnium oxide (HfO_2), 3.5% magnesium oxide (MgO), 0.1% of silicon dioxide (SiO_2) and 0.1% aluminium oxide. The fact behind using different sized balls is that the larger balls helps to breakdown the coarse feed material and the smaller balls helps to produce finer powder by reducing void space between the larger ones. Since, smaller particles offer larger area (greater surface to volume ratio) compared to larger particles, this improves the reaction probability. Another advantage of BM is that it can improve the density of the ceramics during sintering due to the reduced particle size. To synthesize the Cu-Zn spinel-ferrites, we carried out BM with ethanol as the milling medium, maintaining a speed of 150 rpm for 8 hours and a periodic break of 2 minutes. The slurry thus formed was heated in oven at 120 °C in air to remove the water content. This slurry is from what one obtains the parent Cu-Zn ferrites after the heat treatment as discussed below.

2.1.2. Calcination:

The IUPAC definition for calcination is ‘heating to high temperature in atmosphere or in the presence of air or oxygen [102]. Calcination is a pre-heating treatment prior to sintering (Section 2.1.4) which is carried out at a much lower temperature than the melting point of the material in a controlled environment. This is the step where decomposition of the precursors occurs by the elimination of carbonates as carbon dioxide (CO_2), sulphates as sulphur dioxide (SO_2), moisture, water of hydrates. Also, in the case of metallurgy, calcination removes organic matter from the ore. Calcination is also known to provide better thermal and weather stability. The duration of calcination, gas ambience (either air, Ar, N_2 or O_2) and the temperature also plays an important role for the phase formation. Calcination temperature or the phase formation temperature is generally decided from the differential scanning calorimetry (DSC) technique [103].

2.1.3. Densification or Pelletization:

After calcination, phase formation of Cu-$ZnFe_2O_4$ ceramics is complete which can be confirmed by x-ray diffraction technique (discussed in Section 2.2.1) by verifying the presence of any secondary phases (or impurities). Desired amount of the sample (obtained after calcination) is weighed accurately to the third decimal and mixed using an agate mortar and pestle for 1 h in a dust free environment, simultaneously adding appropriate amount of poly-vinyl alcohol (PVA). This is executed to further ensure uniform and homogeneous mixing of the sample, before pelletizing. With rise in temperature, the added PVA evaporates at around T = 250 °C, much below the calcination/sintering temperature. This mixture of the sample and PVA is then transferred part by part into the die as per requirement to prepare the pellets one after another.

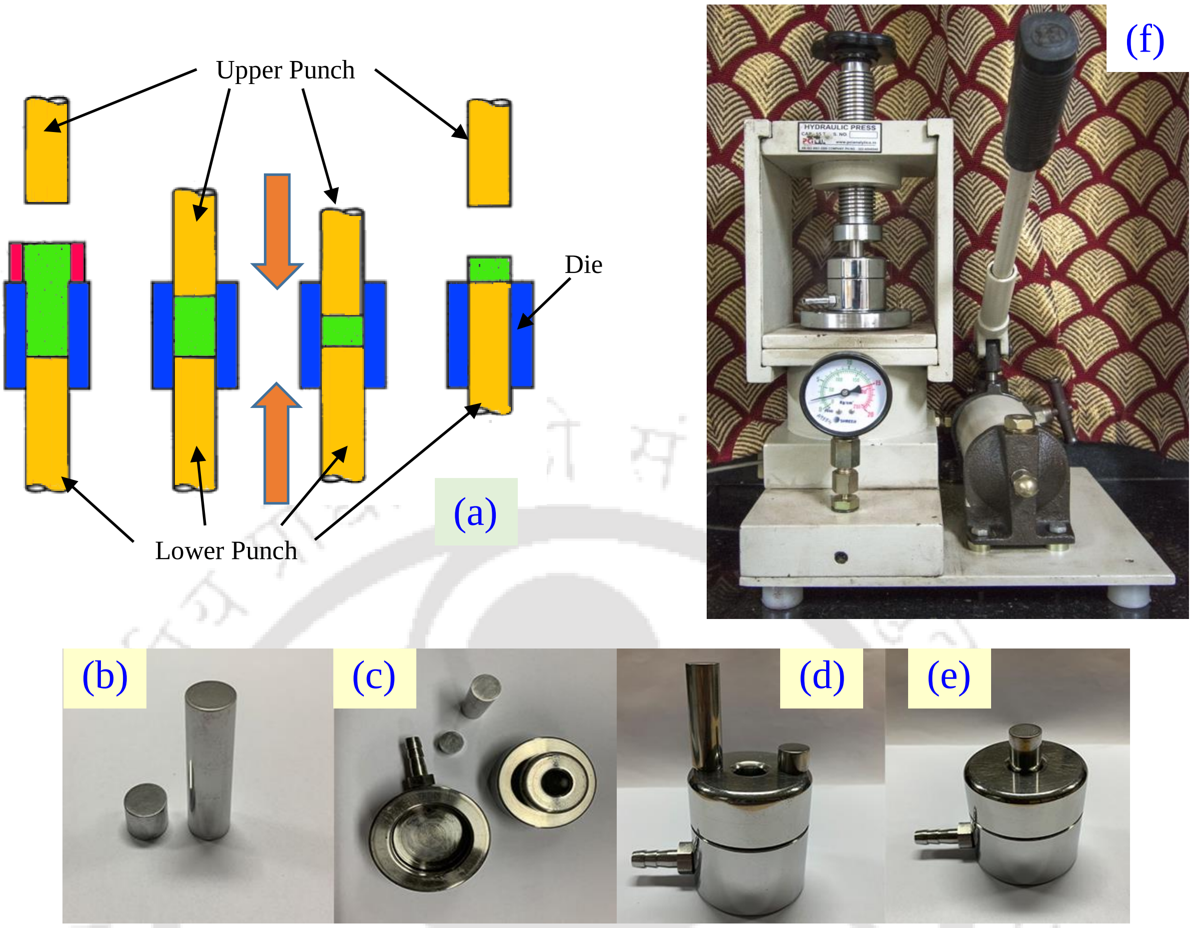

Figure 2.3: (a) Schematic representation of Pelletization of sample using a die-set, (b) Picture of upper and lower punch, (c) Top view of the complete die set, (d) Lateral view of the die set, and (e) View of how a die set appears after sample loading and ready to be installed in a hydraulic press, and (f) the Hydraulic press that we used for Pelletization of the samples with loaded die.

The die filled with adequate sample is then placed on a hydraulic press. It is made sure that the pressure is applied at a slow rate to allow the escape of the trapped air. If the applied pressure is P_a, then the gradient of pressure P_z at the top of the pellet dies out exponentially as per the below relation.

$$P_z = P_a \, exp\left(-\frac{4\mu\xi l}{d}\right) \tag{2.1}$$

In the above equation, μ is the coefficient of friction along the die wall, ξ is an arbitrary constant that accounts for the particle friction, l and d are the length and diameter of the pellet, respectively. Using of binder can reduce the coefficient of friction between the walls of the die during the application of uniaxial pressure. Figure 2.3 shows the process of Pelletization and the die used for this work. The green compact, or the homogeneous mixture lack mechanical strength to withstand even small physical stress, also it possesses high porosity. Hence one can proceed for further heat treatments, commonly referred as ‘sintering’, which is discussed in the following section.

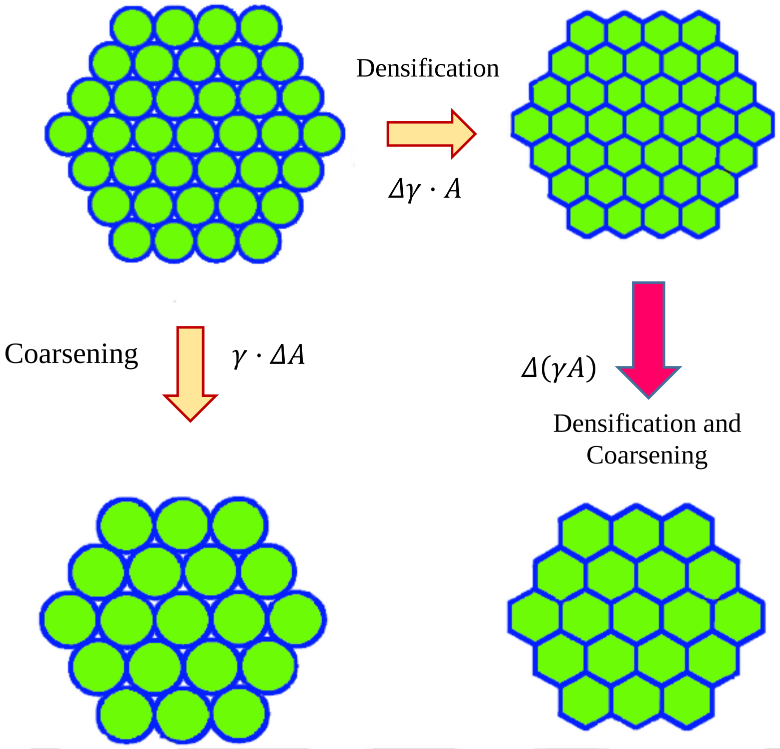

Figure 2.4: Schematic diagram showing the variation in the interfacial energy parameters γ and A with sintering.

2.1.4. Sintering:

Consolidation of the powder compacts by application of heat is known as sintering. On supplying the thermal energy close to its melting point (usually 3/4th of melting point), inter-particle bonding occurs by the process of inter-particle diffusion due to which the powder densifies and average grain size increases. This common phenomenon that occurs during sintering is called as densification and grain growth [104]. There are basically, two types of sintering: (*i*) Liquid-phase sintering and (*ii*) Solid-state sintering. As the name suggest, when the thermal treatment is done entirely to a solid content, it is called solid-state sintering. If the temperature of sintering exceeds the melting temperature of one of the chemical constituent, then it is commonly known as liquid-phase sintering. Along with the temperature, the atmosphere also plays a vital role on densification. One of the driving force for researchers to do sintering is the fact of reducing the surface area. The green compact consists of many individual particles itself, each possessing its own surface area. By controlled supply of heat energy, one can facilitate good amount of grain growth which results in decrease in the surface area. It is this reduction in the surface area that results in densification, or in other words, we can say that larger the surface to volume ratio, larger is the driving force for agglomeration. During a conventional sintering, following processes are known to occur to the powder compact: (*i*) Particle bonding via necking, (*ii*) neck growth, (*iii*) pore channel closure and (*iv*) pore shrinkage. All these processes can be accounted for by the total interfacial energy represented as γA, where γ is the specific energy of the interface and A is the total interfacial surface area of the powder compact. Reduction in the total interfacial energy can be written as,

$$\Delta(\gamma A) = (\Delta\gamma \cdot A) + (\gamma \cdot \Delta A) \tag{2.2}$$

In the above equation, $\Delta\gamma$ is due to densification and ΔA is due to grain growth [105]. Figure 2.4 shows the variation of interfacial energy or the driving force during sintering. Grain growth and lattice diffusion are the important aspects for eliminating porosity. This elimination in one way is important in the increase of overall density. Sintering temperature is thus an important factor to obtain highly dense material.

2.2. Characterization Techniques:

2.2.1. Crystal Structure and Morphology:

In the present thesis, the crystal structure and phase purity of the synthesized samples were determined by using the X-ray diffraction (XRD) analysis. The XRD is an important non-destructive technique primarily used for the phase identification of a crystalline material and provides detailed information on the unit cell dimensions and inter-axial angles. This technique also provides useful information of various structural properties of crystalline compounds such as the micro-strain, grain-size, phase composition, and defect structure. The XRD analysis is based on constructive interference of monochromatic x-rays after being reflected from the crystalline sample. When an x-ray beam, generated by a cathode ray tube, is radiated/incident upon a crystal, the beam undergoes diffraction from the set of planes (Miller indices (*hkl*)), once the geometrical condition satisfies the Bragg's law given below [106]:

$$2d_{hkl}\sin\theta = n\lambda \tag{2.3}$$

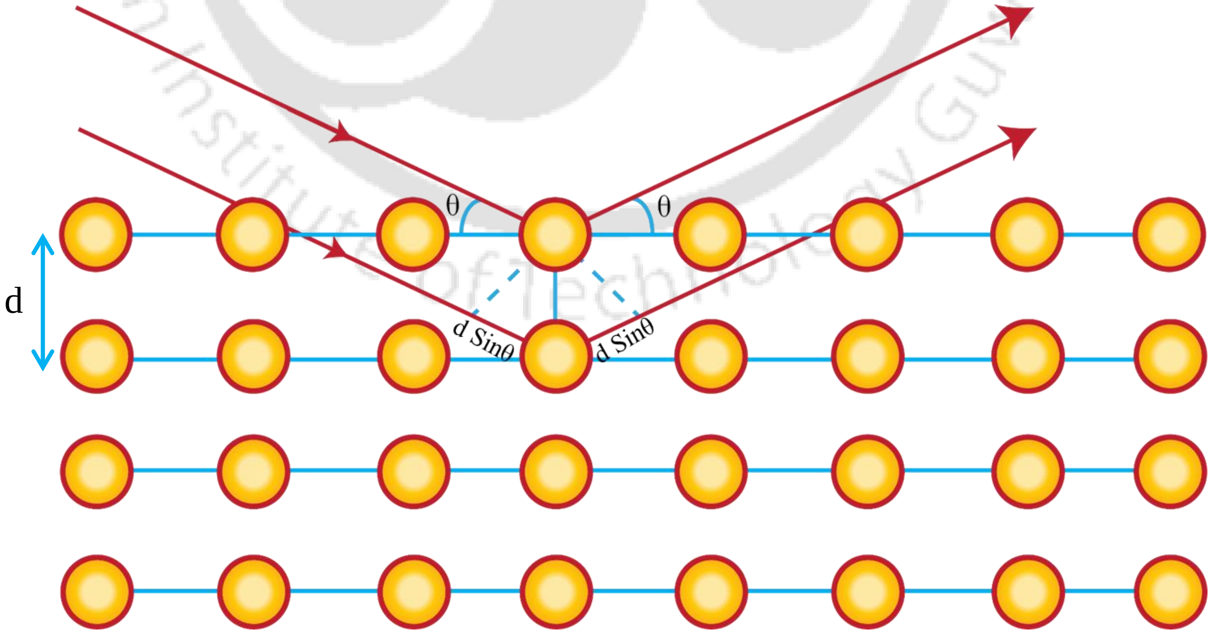

Figure 2.5: Schematic diagram for Bragg's law of diffraction.

In the above equation 'd_{hkl}' is the inter-planer spacing between the set of (hkl) planes, θ is the Bragg's angle or Diffraction angle, n is an integer and λ is the wavelength of x-ray radiation. Figure 2.5 shows the geometry of the Bragg's law for the XRD from a set of crystallographic planes. The locus of the diffracted beams taken together from the different set of planes is collectively known as the diffraction pattern of the crystal. For the present work, the XRD from Rigaku Smartlab (model: TTRAX-III) diffractometer (18 kW rotating anode x-ray source) with Cu-Kα as the radiation source (λ = 0.15406 nm) was used to study the crystal structure and phase purity. This XRD instrument works under the Bragg−Brentano reflection geometry with a specific arrangement where the sample stage is fixed at the centre of the circle, and both the x-ray source and detector rotates using a goniometer assembly. In order to extract the detailed crystallographic information from the obtained diffraction pattern we have also performed the Rietveld refinement using the open source programs *FullProf* Suite and *Powder-cell* [107,108]. On the other hand, to probe the surface morphology and microstructure of the samples investigated in the present work we employed a scanning electron microscope (SEM, M/s LEO, 1430vp) working under secondary-electron (SE) mode. This instrument is also equipped with energy dispersive x-ray spectrometer (EDS/EDAX) which is used to trace the elements present in the samples.

2.2.2. Elemental Analysis using the X-ray Photoelectron Spectroscopy:

In the present thesis, X-ray photoelectron spectroscopy (XPS) was employed to probe the composition and chemical states of the investigated samples. This technique is one of the most powerful non-destructive surface sensitive technique to study the chemical and physical phenomenon occurring at the surfaces of various materials such as metals, oxides, semiconductors, glasses, polymers etc. The XPS was first developed by Prof. Kai Siegbahn and co-workers at Uppsala University, Sweden between 1940 and 1950 and later awarded Nobel Prize in 1981. This spectroscopy technique has gained attention by the scientific community due to the following important reasons: (*i*) It can provide the quantifications of elemental composition from the solid surface up to a thickness of ≤ 10 nm, (*ii*) it can also provide an insight to the chemical and atomic environment of the elements present in the compound, (*iii*) using XPS, one can obtain the above information

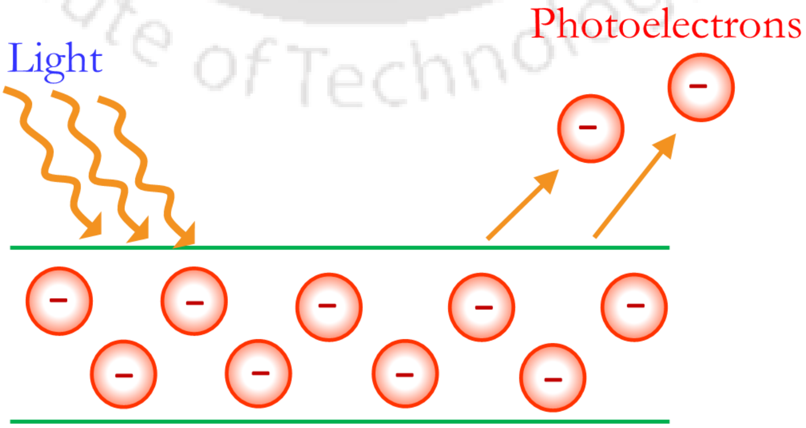

Figure 2.6: Schematic diagram for Photoelectric effect.

with relative ease and minimal sample preparation, (*iv*) the ability to explore first few atomic layers and assign chemical states to the detected atom, and (*v*) since the mean free path of the electrons in any solid is very small, the detected electrons originating from the top few atomic layers provide important information which makes XPS a unique surface-sensitive technique for the chemical analysis. In XPS, a monochromatic beam of soft x-rays (Mg-Kα (1253.6 eV) and Al-Kα (1486.6 eV)) are exposed to the sample which interact with the core-level electron and transfer its energy to the electron leading to emission of the core-level electrons (Photoelectric effect). The XPS spectrum is recorded between the variations of the number of detected core-level photoelectrons per energy interval versus their kinetic energy or binding energy. Each element has a unique XPS characteristic spectrum. For the system containing different set of elements, the spectrum is comprised of intermixture of the individual peaks of the constituent elements.

Basic principle behind the XPS is the Photoelectric effect in which electrically charged particles are released from or within (core) of a material when it absorbs electromagnetic radiation as shown in figure 2.6. In the case of XPS, the interaction of soft x-rays with the specimen leads to photoemission process and its energy is analyzed by the spectrometer. Generally, the x-ray radiation (usually, Mg-Kα and Al-Kα) is capable of inducing electrons not only from the outer shells but also from the core levels. Emission of an electron from the 1*s* shell of an atom is schematically represented in figure 2.7. The kinetic energy of an incident photoelectron (E_K) is equivalent to the difference between the x-ray photon energy ($h\nu$) and the binding energy of core-level electron (E_b). Relation between these parameters and the work function of the instrument (Φ_s) is given by the below equation [109-111]:

$$E_b = h\nu - E_K - \Phi_s \tag{2.4}$$

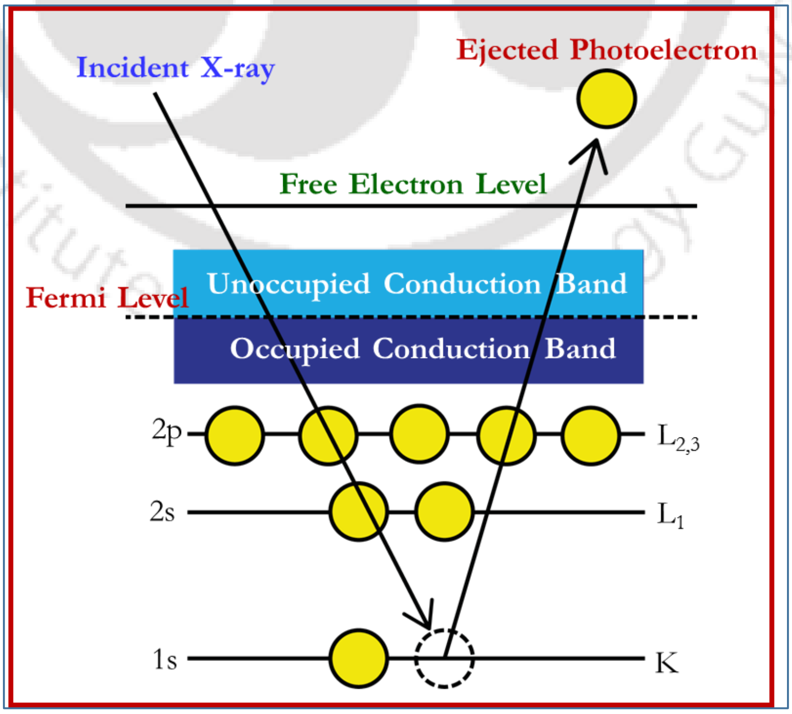

Figure 2.7: Energy level diagram for the emission of core-level photoelectron.

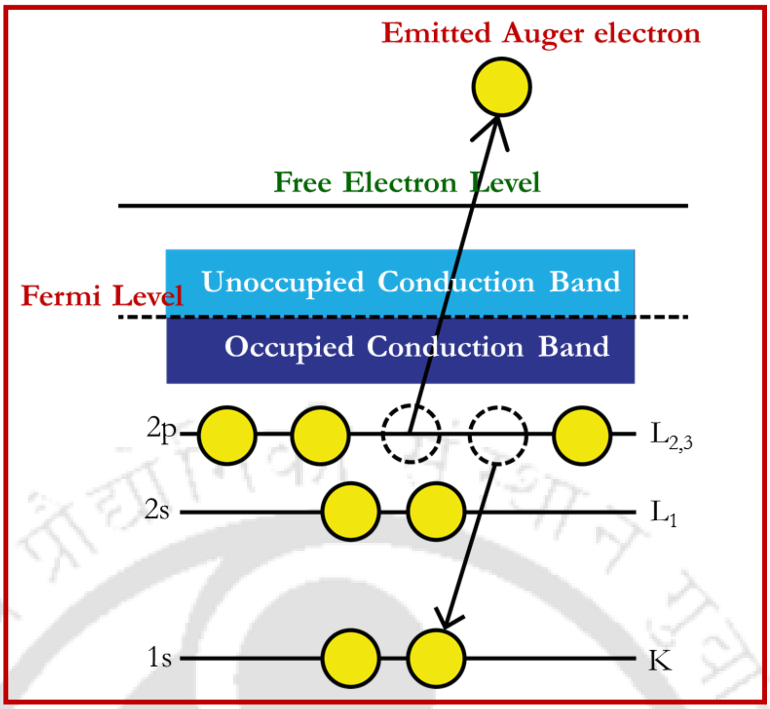

Figure 2.8: Energy level diagram for the emission of Auger electron.

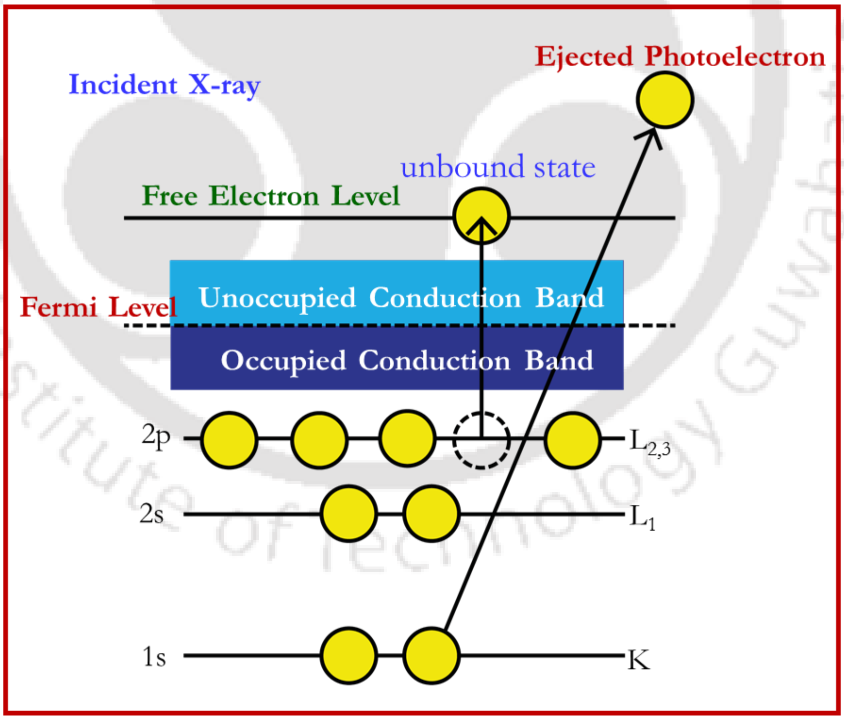

Figure 2.9: Energy level diagram to understand the Shake-up/Shake-off process.

Besides, the work function of the instrument (Φ_s) is defined as the difference between the energy of the fermi level (E_F) and the energy of the vacuum level (E_V), with E_V being the zero point of the electron energy scale:

$$\Phi_s = E_F - E_V \tag{2.5}$$

Usually, Φ_s will be determined from a detailed calibration of the spectrometer used. From equation (2.5) it is clear that only binding energies lower than the excitation radiation (in the present case it is 1486.6 eV for Al-Kα and 1253.6 eV for Mg-Kα) are probed. In addition to the photoelectric process, relaxation of the excited ion may occur by the emission of Auger electrons (figure 2.8). The Auger emission dominates for elements having low atomic numbers ($Z < 30$). When an electron is emitted from a core level, another electron from a higher level falls to occupy the core level vacancy [109-111]. In order to conserve the total energy of the system, a third electron is emitted during this process, which is known as Auger electron (figure 2.8) [109-111]. Auger emission is independent of the photon energy and therefore the x-ray source. Another important relaxation process, which can significantly contribute to the XPS spectrum, is the "Shake-up"/"Shake-down" process in which electrons from the valence levels are excited to the bound/unbound states (figure 2.9). Moreover, 'multiplet' splitting of the XPS peaks can also occur when atoms having unpaired electrons couple with other unpaired electrons in the atoms giving rise to several possible final state configurations, consequently peaks shift to higher binding energy from the principle peak [109-111]. Some less intense Plasmon peaks also appear at higher binding energies from the principle peak at equal spacing due to specific amounts of energy losses when the photoelectron excites free electrons in a material.

2.3. Magnetic Characterization:

In this section we present a detailed description related to the magnetic characterization employed in the present work. The magnetic properties of most of the polycrystalline compounds in the current thesis are investigated by both superconducting-quantum-interference-device (SQUID) based magnetometer (magnetic property measurement system, MPMS-XL5 from Quantum-Design) and physical property measurement system (PPMS) with vibrating-sample-magnetometer (VSM) accessory for high field (± 9 T) and low-temperature (1.9 K) measurements [112,113]. For selected compounds we used the neutron diffraction measurements. It is well known that the SQUID magnetometer is most effective and sensitive tool which can detect low magnetic moments with very high resolution ($> 10^{-7}$ emu) and very small magnetic field (10^{-18} T) using the Josephson junctions [114,115]. Usually, SQUID consists of two superconductors separated by a thin insulating layer to form two parallel Josephson junctions as shown in figure 2.10(a). These Josephson junctions act as a magnetic flux-to-voltage transducer. The basic principle governing the operation of a SQUID device is based on the flux-quantization in superconducting (SC) loops and the Josephson-effect [116]. In 1962, Josephson showed that the electrical current density through a weak electric contact between two superconductors depends on the phase difference $\Delta\varphi$ of the two SC wave functions [112,115]. Following subsections deals with the instrumentation, basic principles, relevant units to SQUID magnetometry, and also with the sensitivity and detection limits of the instrument.

2.3.1. DC Magnetization:

In this section we present the particulars of extraction of DC magnetization and the working principle of a SQUID. Typically, in a SQUID when the current enters at the terminal 1, it gets divided into two parts,

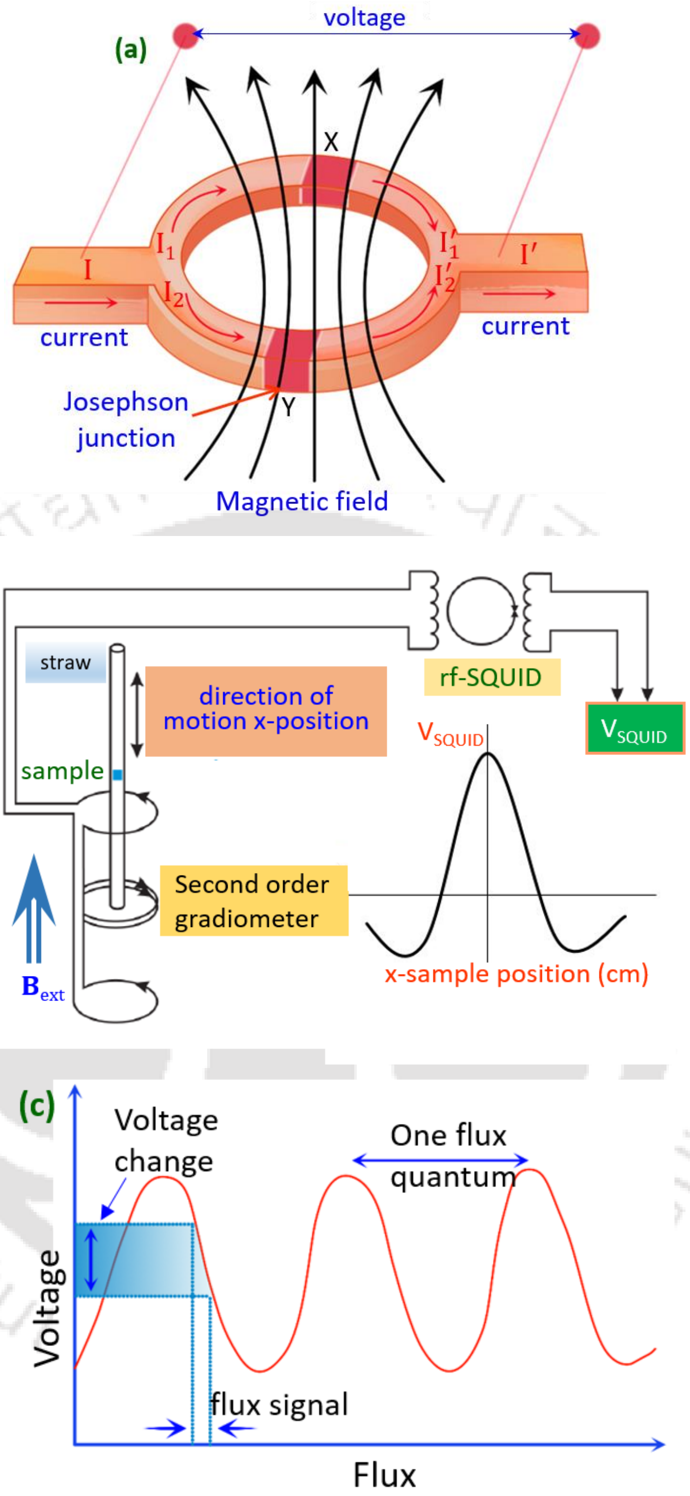

Figure 2.10: (a) Schematic diagram of a SC ring that consists of two Josephson junctions inside the DC SQUID magnetometer. (b) The SC pick-up coil with second order gradiometer (four circular rings). Inset shows the SQUID response V_{SQUID} versus sample position (*x*-pos.). (c) The output voltage plotted as a function of applied flux, here a small change in flux corresponds to the measurable voltage change across the SQUID.

namely I_1 and I_2 which experience a phase shift while passing through the two Josephson junctions X and Y (see figure 2.10(a)). The two phase shifted currents (I_1' and I_2') interfere at the terminal 2 and the resultant current oscillates between a maximum and a minimum value. The magnetic flux (φ) inside any SC ring is quantized and defined as $\varphi = nhc/2e = n\varphi_0$, where n is an integer and φ_0 is the magnetic flux quantum = $hc/2e$ = 2.07×10^{-7} G cm^2. The maximum value of the current occurs when the magnetic flux inside reaches an integral number of flux quantum, whereas, the minimum corresponds to the half integral of the flux quantum. The voltage which also oscillates depending on the change in magnetic flux is measured across the two terminals 1 and 2. Thus SQUID acts as a transducer which converts magnetic flux into voltage. In the magnetometer, this SC loop is connected with the pickup coil which is also located inside the magnetic field. The pickup coil is made of SC wire with four windings (figure 2.10(b)). When a sample moves up and down inside the SC wires the magnetic moment of the sample induces an electric current in the coil which couples with magnetic flux through the coil with the SQUID sensor, as shown in figure 2.10(a). The SQUID sensor changes the magnetic flux to the output voltage which is proportional to the change in magnetic moment of the sample (figure 2.10(c)). The voltage is then magnified and read out by the magnetometer electronics. It is well known that SQUID can only detect magnetic flux φ (= $\int \boldsymbol{B} \cdot d\mathbf{A}$, magnetic flux density B times the area 'A' of the SQUID loop, and every SQUID magnetometer has to be calibrated with a sample of known magnetic moment such that one can obtain the fringing/stray field (since the actual area 'A' of every SQUID is not precisely known). However, commercially available SQUID magnetometers detect the change of magnetic flux created by mechanically moving the sample through a SC pick-up coil which is converted to a voltage V_{SQUID}.

In a typical MPMS, the position is denoted as the x-direction which is parallel to the external magnetic field H_{ext} so that one obtains the raw data, often called as "last scan," where V_{SQUID} is plotted against the sample position (x_{pos}), as demonstrated in figure 2.10(b). In order to suppress the influence of all kinds of external magnetic fields, the pick-up coil is made as a second order gradiometer (surveying instrument used for measuring the gradient). The entire detection system is sketched in figure 2.10(b) with a clear depiction of single SQUID scan in the inset where the maximum of V_{SQUID} at x_{pos} = 2 cm corresponds to the sample directly positioned in-between the double coil of the pick-up gradiometer. After mounting the sample, this center-position has to be determined using a long scan to accurately adjust the sample position with respect to the pickup coils (this procedure is popularly known as Centering). During the Centering process one has to record relatively long scans so that not only the maximum but also two minima should be included in the scan. In this process the sample can be imagined like an ideal point dipole which is exactly pinned on the axis of the magnetometer. Usually, the software allows one to execute the fit in two ways: First, it either assumes a fixed sample position and only fits the amplitude of the V_{SQUID} (x_{pos})-curve with a single fitting parameter, which is the magnetic moment of the assumed point dipole, often called as the linear-regression-mode in the MPMS. In the second method the sample position is fitted together with the amplitude by iterative regression mode which is very convenient method for measuring the temperature dependent magnetization. The iterative regression mode easily compensates for the thermal expansion of the sample holder assembly. To minimize errors in the fit due to the point dipole approximation in either fitting routine, the specimen size should be limited to a maximum of 5 mm along the scan direction. Whereas, the lateral size of sample is naturally limited to 5−6 mm depending upon the design of the sample holder.

In the present case we mounted the sample at the centre of a transparent plastic straw. But, for highly sensitive measurements, the following parameters turned out to be a good compromise between the accuracy and time: 4 cm of sample movement, average over 5 scans with 10 oscillations each at 1 Hz, and iterative regression mode for the fit routine. Concerning the units, magnetization (M) of a homogeneous sample of volume (V) is related to the magnetic moment (μ) with $M = \mu/\mathrm{V}$. Typically, magnetometry measurements are different from susceptometry measurements where the magnetic susceptibility tensor χ_{ij} is given by $\chi_{\mathrm{ij}} = \partial M_{\mathrm{i}}/\partial H_{\mathrm{j}}$. Here H represents the magnetic field intensity, which is not to be mistaken with B, the magnetic flux density (or magnetic induction). In the cgs unit, B is measured in Gauss (G), while H is measured in Oersted (Oe), and in vacuum both quantities are same. In the SI unit, B is measured in Tesla (T), whereas, H is measured in A/m, and in vacuum $B = \mu_0 H$; the conversion from cgs to SI is 10000 Oe = 1 T. The MPMS uses the cgs-unit emu for 'M', which can be easily converted into the SI-units. Usually, the measured magnetic moment from SQUID magnetometry is often given in emu/g which is easier to be measured and does not require the density of the material and this quantity can be easily representable in μ_{B}/atom (1 $\mu_{\mathrm{B}} = 9.274 \times 10^{-21}$ emu). The sensitivity of commercial SQUID magnetometers is usually provided in emu. For the MPMS-XL5, it is $< 10^{-8}$ emu below 250 mT field and less than 2×10^{-7} emu up to the full-field conferring to the manufacturers specifications, which is $\sim 2 \times 10^{-7}$ emu corresponding to the magnetic moment of a single atomic layer of nickel.

In the present study, fully automated "standard sequences" were used for the temperature dependence of magnetization and magnetic hysteresis loops performed using both SQUID magnetometer and VSM based PPMS (discussed in below sections). Throughout this work we used the standard MPMS/PPMS sequences for the $M{-}H$ and $M{-}T$ measurements under both zero-field-cooled (ZFC) and field-cooled (FC) conditions. For the $M{-}H$ curve we used the following experimental protocol. First, a full $M{-}H$ is measured at 300 K under five cycle hysteresis mode (0 → +5T → 0 → –5T → 0 → +5T) using the "no overshoot" mode (field is approaching the desired value from one side and exactly stabilizes the magnetic field at the requested value; magnet is in persistent mode during the actual measurement). Then the sample is cooled down in the presence of field H and no-field ($H = 0$ Oe) to 2 K and then a full $M(H)$ curve is recorded. We performed the $M(H)$ curve at 2 K under field-cooled conditions to see whether the investigated system exhibits exchange-bias effects or not. This procedure also allows us to probe the field imprinted magnetic phenomena like the uncompensated antiferromagnets or ferrimagnets.

On the other hand, temperature dependence (2 K to 300 K) of magnetization $M(T)$ was measured using the standard protocols, ZFC and FC by cooling the compound in the presence of field/no-field (≤ 500 Oe) and under sweep mode (no stabilization of the temperature). However, few measurements were performed under settle mode with small temperature interval. Before the beginning of sequence for low-field measurements, 3 kOe field is set using the "oscillation" mode and set to zero, such that one can minimize the residual/stray fields and ensure perfect virgin state. After this procedure, we performed the low-field $M(T)$ measurements in which field is applied with no-overshoot condition. The major components of the SQUID measurement system comprise the following major constituents: (*i*) Temperature control system which precisely control the temperature in the range 1.85 K to 400 K. (*ii*) Magnet control system which is the current from a power supply set to provide magnetic fields from zero to ±9 T. (*iii*) Superconducting SQUID amplifier system that is the DC SQUID detector and is the heart of the magnetic moment detection system; meant to provide reset circuitry, auto-ranging capability, a highly balanced second-derivative sample coil array. (*iv*) Sample handling system which has the ability to step and rotate the sample through the detection coils without transmitting undue mechanical vibration to the SQUID, hence is of primary importance. (*v*) Computer operating system that is all the operating features of the MPMS are automated and computer controlled. The user interface at the PC console provides the option of working under standard sequence control or diagnostic control which will invoke the individual functions.

2.3.2. AC Magnetic Susceptibility:

In this subsection we discuss the theory and experimental methods related to dynamic magnetic susceptibility under time varying magnetic field together with the measurement technique. In the ac susceptometer, the sample is mounted in the center within the pick-up coil and a small time varying sinusoidal magnetic field $h = h_0 \sin(\omega t)$ is applied on the sample. Here ω $(= 2\pi f)$ is the angular frequency of the oscillating magnetic field. The frequency (f) is typically varied between 0.1 kHz and 10 kHz. The response of the magnetization is recorded, $M_{ac} = \frac{\mathrm{dM}}{\mathrm{dH}} h_0 \sin(\omega t)$; where the ac susceptibility is defined by the relation: $\chi_{ac} = M_{ac} / h$. Usually, the frequency of the oscillating magnetic field is comparable to the timescale of the magnetic dipole relaxation of the system. It is possible that there may be some phase lag (consequently,

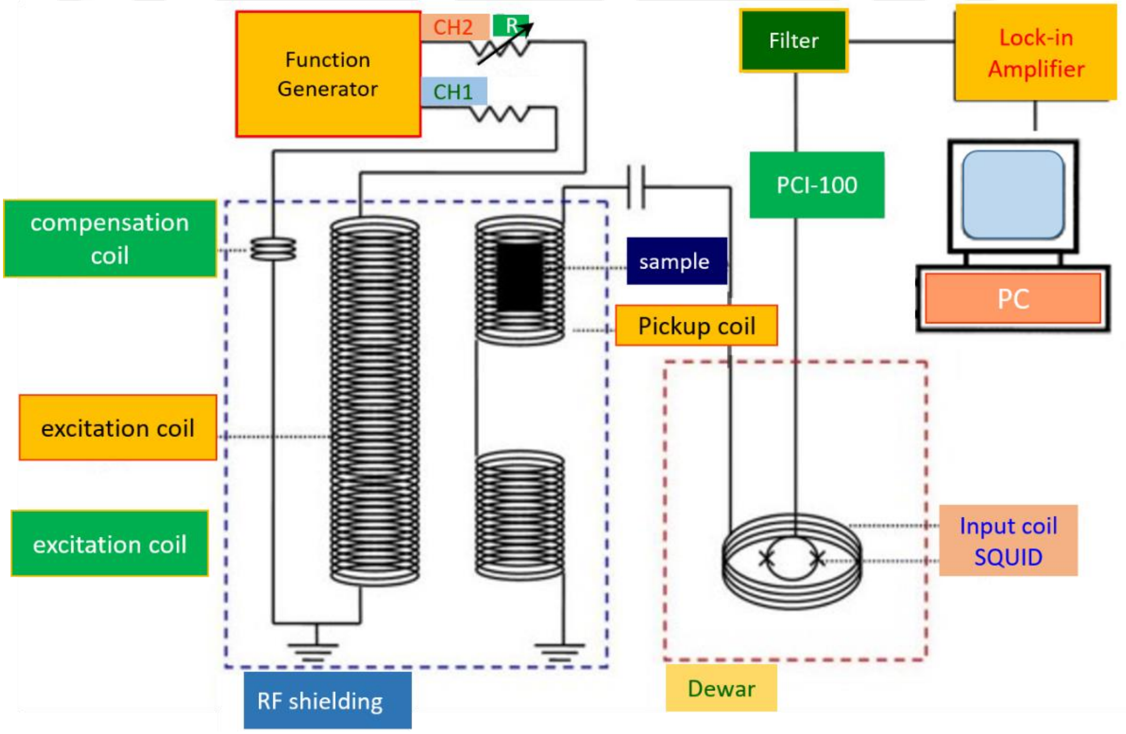

Figure 2.11: Schematic setup of a SQUID-based ac susceptometer [117].

dissipation takes place) when the perturbation is slightly faster or slower than the natural frequency of the system. Thus, the response is reported in two parts: the in-phase or real component (χ') and out-of-phase or imaginary component (χ''). Here, the imaginary component (χ'') relates to dissipation/loss in the system. Thus, the ac susceptibility may be written as a complex quantity: $\chi_{ac} = \chi' + \chi''$. Here,

$$\chi' = \mathrm{Re}[\chi_{ac}] = \chi_0 \cos\varphi = \frac{\chi_0}{1 + (\omega\tau_{eff})^2} \tag{2.6}$$

$$\chi'' = \mathrm{Im}[\chi_{ac}] = \chi_0 \sin\varphi = \frac{\chi_0}{1 + (\omega\tau_{eff})^2}\,\omega\tau_{eff} \tag{2.7}$$

and $\chi' / \chi'' = \tan\varphi = \omega\tau_{eff}$. In the above equations, φ represents the phase delay of the time-varying magnetization ($M(t)$) relative to the applied ac magnetic field ($h(t)$) and τ_{eff} is the effective relaxation rate which characterizes the ability to retain magnetization after the dc field is removed. As compared with the dc magnetic susceptibility, the temperature dependence of ac susceptibility $\chi_{ac}(T)$ gives sharp transitions and the ac data clearly separates out the order−disorder transitions from the local short-range magnetic orderings [118]. In this work we employed the same SQUID magnetometer as discussed above for the temperature and frequency dependence of ac susceptibility data. However, ac measurements are performed using a PPMS (Quantum Design) along with the ac measurement system (ACMS) accessory. In general, any home-made ac magnetic system contains sensing coils including the excitation coil, pick-up coil and compensation coil. First, the excitation coil was excited with a certain frequency of ac signals where the pickup coil is used in gradient configuration and the compensation coil is used to recover the balance of the pickup coil. By means of a lock-in amplifier the real (χ') and imaginary (χ'') components of ac susceptibility can be detected. Figure 2.11 shows a schematic of the detection process of ac susceptibility.

2.3.3. Specific Heat:

For selected compounds we performed the temperature dependence of specific heat ($C_p(T)$) using the PPMS (from Quantum Design) with heat capacity accessory in which heat added and removed from a sample by monitoring the resulting change in temperature [119]. It is well known that heat capacity 'C' is defined as the amount of heat, Q required to effect a corresponding change in temperature T at a constant volume; $C = dQ/dT$. At low temperatures, the heat capacity of material may be written as the sum of electron and phonon contribution: $C = \gamma T + AT^3$, where γ and A are the constants which are characteristics of the material under investigation. The contribution from the electronic part is linear with T and is dominant at very low temperature. In each measurement cycle, a known amount of heat is supplied to the sample at constant power for a fixed time, then this heating period is followed by a cooling period of the same duration. After each cycle, the software option fits the temperature response of the sample stage to an appropriate mathematical model. It is possible that weak thermal contact between the sample and sample-platform causes thermal relaxation. Hence, the model considers the thermal relaxation of the sample stage to the thermal bath and also the relaxation between the sample-platform and the sample itself, which offers the accurate value of C_p of

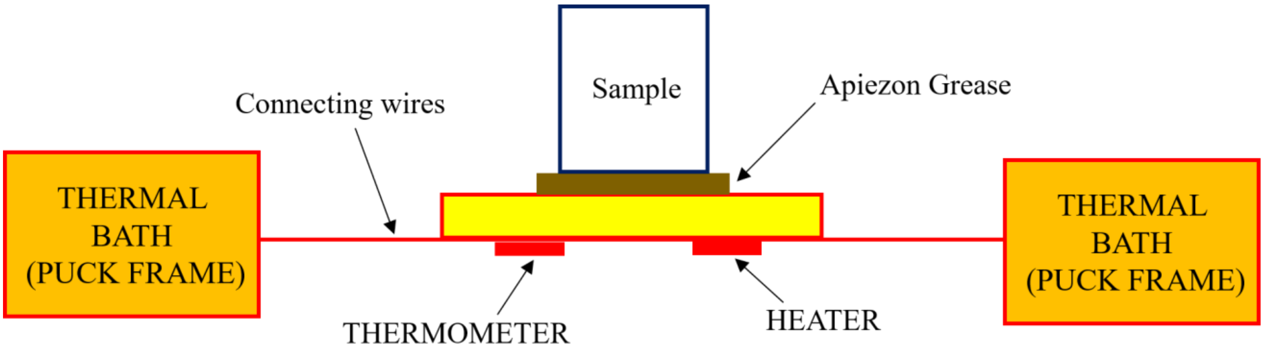

Figure 2.12: Schematic of the specific heat measurement assembly and connections adopted from Quantum Design PPMS.

the sample [120]. Figure 2.12 illustrates the schematic of thermal connections to the sample and sample platform in the PPMS heat capacity accessory. A heater and a thermometer are attached at the bottom of the sample stage. The sample is attached on the stage by thin layer of Apiezon N Grease which helps to make thermal contact between sample and the sample-platform. Highly sensitive wiring system is connected with the heater and thermometer to provide electrical and thermal connections. Usually, the additional measurements are performed before the $C_p(T)$ measurement of the sample, which consists of measuring the C_p of the sample holder. In the additional run, a thin layer of Apiezon N Grease is placed on the sample stage and the measurement is taken. After the completion of additional run, the sample is carefully attached with the grease without disturbing it. The measurement is performed once more and the correct value of the C_p of the sample is determined by subtracting the C_p of the sample holder from the total magnitude. Next section explains methodology of the neutron diffraction technique, we have used to investigate the structure and magnetic behavior of the complex spinel oxide $Zn_{0.8}Cu_{0.2}FeMnO_4$.

2.3.4. Neutron Diffraction Technique:

For the specific system $Zn_{0.8}Cu_{0.2}FeMnO_4$, we performed low-temperature neutron diffraction (ND) experiments at the Helmholtz Zentrum Berlin (HZB), Germany. These measurements are aimed to probe the site dependent magnetic moment, magnetic ground state and details about the crystal structure at various temperatures below the T_{FiM}/T_N. In principle, the powder ND uses a similar method as that of XRD where x-rays interact with the electron cloud, but neutron scattering occurs at the atom nuclei since the neutrons carry magnetic moment. This principle makes neutrons excellent candidates to probe the magnetic properties of materials. Using this method one can accurately determine the magnitude of the magnetic moment. Below we discuss some of the basic understanding of the ND technique. It is well known that the neutrons are uncharged particles, hence, it experiences very weak or no Coulombic barrier and penetrate deeply into materials and interact directly with the atomic nucleus. On the other hand, a neutron consists of quarks and gluons and possesses spin=1/2 with magnetic moment $\mu_n = -1.913\,\mu_N$, where $\mu_N = \frac{e\hbar}{2m_p}$ is the nuclear magnetic moment. Thus, the neutron's magnetic moment interacts with the unpaired electron spins of magnetic atoms with a comparable strength and gives the magnetic structure of the compounds. Furthermore, due to large mass (1.675 × 10^{-27} kg), neutrons lead to a thermal-neutron de-Broglie wavelength [$\lambda = \frac{h}{mv}$] of about 1.8 Å, which is of the order of the interatomic distances, generating possible interference patterns which gives the structural information about the system. Consequently, ND technique is a powerful tool to probe the crystal and magnetic structure of crystalline samples under elastic and inelastic scattering conditions [120-122].

For the scattering measurements the neutron beam is typically produced using two mechanisms: The first one is 'fission process' in which a steady flux of neutrons is produced inside a nuclear reactor and the second mechanism is 'spallation source' where neutrons are produced by bombarding heavy metal atoms with energetic protons from accelerators [123]. The neutrons generated from the two sources usually possess very high energy, thus their energy can be categorized in different ranges; Cold neutrons and Thermal/hot neutrons depending on the temperature/energy range. In the present case we performed the ND measurements at HZB using the BER II reactor as source along with a fine resolution powder diffractometer (E9). We also used the focusing powder diffractometer (E6) with a 2D detector, and a flat-Cone diffractometer (E2). A detailed description about all these three diffractometers can be found in some other reports [123].

2.4. Impedance Spectroscopy:

In order to investigate the dielectric properties and ac electrical conductivity of the investigated samples we employed the high precision RF Impedance analyzer. This instrument is an important characterization

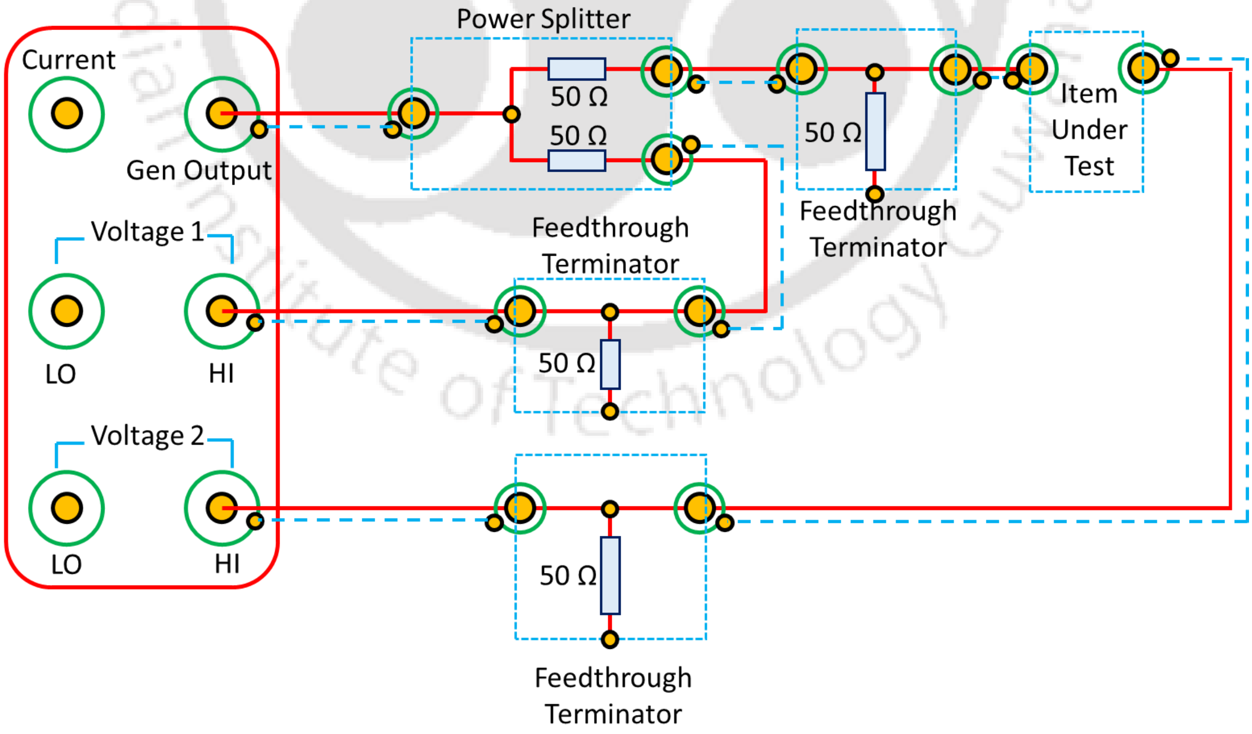

Figure 2.13: Typical connections for high frequency voltage measurements.

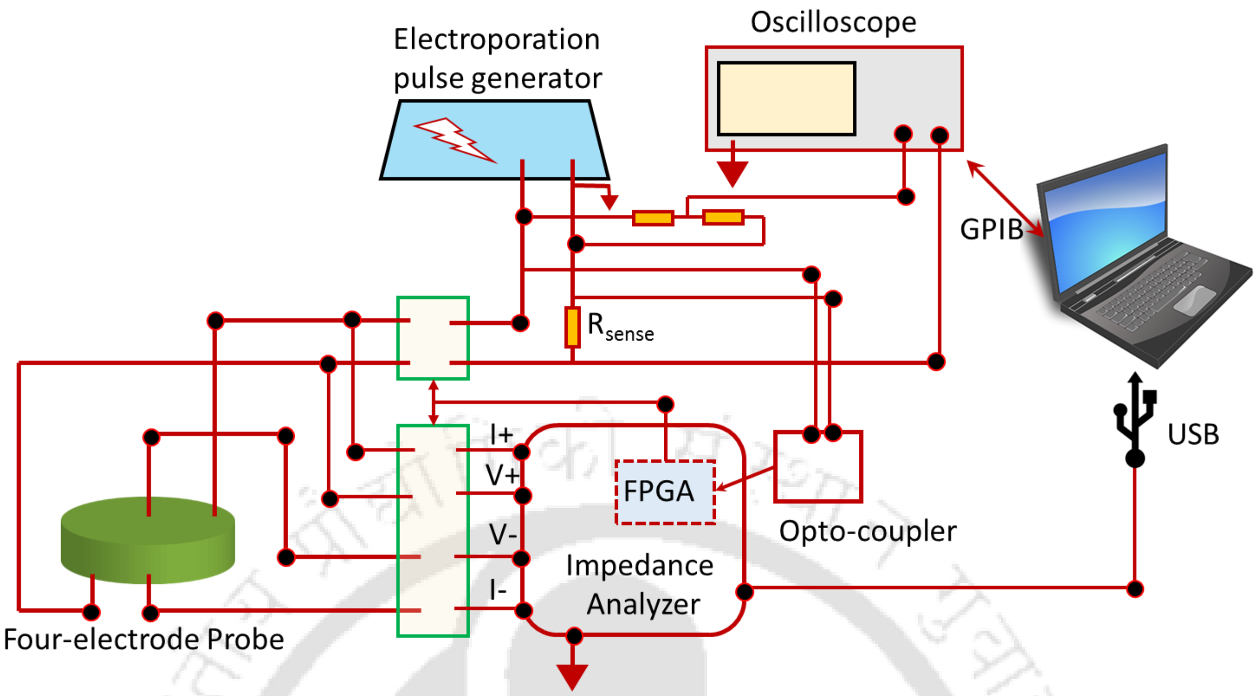

Figure 2.14: Schematic representation of an Impedance Analyzer.

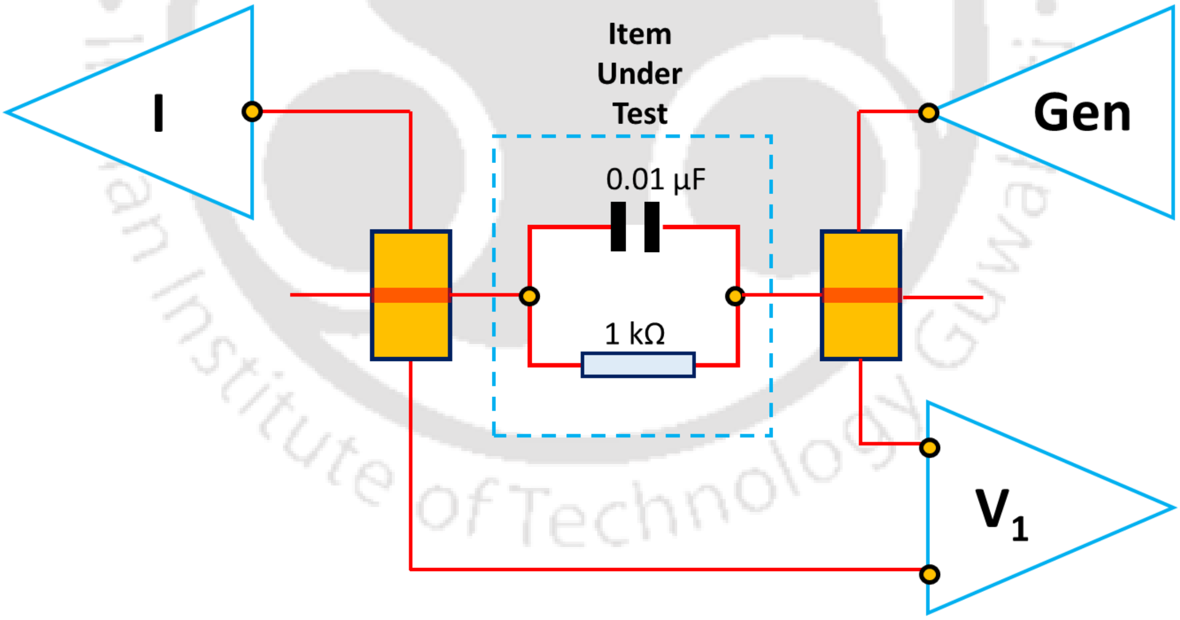

Figure 2.15: Connection for a simple impedance measurement.

tool used in the field of ferroelectrics and high-κ dielectrics using which one can probe the different relaxation mechanism and transition temperatures [124-126]. The frequency and temperature dependence of ac resistivity and dielectric permittivity of the bulk $Cu_{1-x}Zn_xFe_2O_4$ polycrystalline samples were measured using two different high precision RF Impedance analyzers; one from Solartron (SI1260A) and other from Wayne-

Kerr Electronics Pvt. Ltd. (model 1J6530B). Both these instruments are equipped with temperature controller (Eurotherm-2204 e) and a heater capable of reaching 600 °C. For these measurements, two sides of the sintered pellet were fashioned like parallel-plate electrode geometry using silver coating. Constant ac peak-to-peak sinusoidal driving potential of 100 mV (or 1 V during measurements in Wayne-Kerr Impedance anlyzer) with varying frequencies between 20 Hz and 20 MHz has been used as input signal. In order to match the input/output impedances of the instrument and investigating sample under high frequency limits, a 50 Ω feed-through terminator cable was connected at the input and simultaneously a 50 Ω power splitter was used at the output terminal as shown in figure 2.13. The most common and standard technique to measure impedance is by applying a single-frequency voltage (V) or current (I) to the interface and measuring the phase shift and amplitude (or the real and imaginary parts) of the resulting current at that frequency using either analog circuit or fast Fourier transform (FFT) analysis of the response [127-128].

Generally, three different types of electrical stimulations can be used: (*i*) For the transient measurements, a step function of voltage [$V(t) = V_0$ for $t > 0$, $V(t) = 0$ for $t < 0$] may be applied at $t = 0$ to the system and the resulting time-varying current $I(t)$ is measured. The ratio $V_0/I(t)$, often called as the indicial impedance or the time varying resistance, measures the impedance resulting from the step function voltage perturbation at the electrochemical interface. (*ii*) The second technique is to apply a signal $V(t)$ composed of random noise to the interface and measure the resulting current. Fourier-transformation of the results is required to pass into the frequency domain and obtain definite value of the impedance. This approach offers the advantage of fast data collection because only one signal is applied to the interface for a short time. The technique has the disadvantage of requiring true random noise. (*iii*) The third approach, the most common and standard one, is to measure impedance by applying a single-frequency voltage or current to the interface and measuring the phase shift and amplitude, or real and imaginary parts, of the resulting current. Figure 2.14 shows the general architecture of any commercial Impedance-Gain-Phase Analyzer. Figure 2.15 shows the simplest way of connecting the capacitance (C) and resistance (R) network of the measurement. The following are the four specific components that we extracted to study the dielectric behavior of bulk $Cu_{1-x}Zn_xFe_2O_4$: Capacitance (C), Dissipation factor (D), Impedance (Z), and Phase Angle (Φ).

Chapter 3

Spin-Liquid State in Frustrated Tetragonal Spinel (ZnCu)FeMnO$_4$

This chapter deals with the Spin-Liquid state below the glassy phase of tetragonally distorted frustrated spinel pyrochlore ZnFe$_2$O$_4$ with dilute dispersion of Cu at Zn sites. We also probed the role of Jahn−Teller active trivalent Mn substitution on the *B* site along with divalent Cu at *A* sites. First section of this chapter deals with the introduction on spinel pyrochlores along with a detailed literature review on the current status of ZnFe$_2$O$_4$ based spinels. The later sections provide motivation, experimental details and their results. In the discussion part we first discuss on the crystal structure and provide extensive analysis on the magnetization data to investigate the novel magnetic phenomena. Most importantly this chapter includes a unique approach to probe the novel spin-liquid state using both ac- and dc-magnetic susceptibility studies including the thermoremanent magnetization data. In the end, a brief summary of the important findings is highlighted.

3.1. Literature Review, Motivation and Objectives:

In this section, we mostly discuss about various properties of ZnFe$_2$O$_4$ based spinels and the frustration driven phenomena in other spinel pyrochlores. Frustrated magnetic materials as a special class of compounds different from ferromagnets, antiferromagnets, ferrimagnets and metamagnets was first noted in a review by Ramirez in 1994 [129]. A more recent review by Balents describes how magnetic frustration resulting from competing exchange interactions among nearest neighbors (*nn*) that cannot be simultaneously satisfied due to geometry of the lattice can lead to exotic states such as spin-liquids, spin-ice and magnetic monopoles [29]. Such geometrical frustration is easily visualized on a triangular lattice with spin on each lattice point coupled to *nn* antiferromagnetically. In this case, all three spins cannot be antiparallel, leading to large degeneracy of the ground state and absence of long-range (LR) order. Lattices in two-dimensions (2D) suitable for magnetic frustration are edge-sharing triangular lattice and corner-sharing Kagomé lattice with spins on each lattice point coupled with *nn* with AFM interaction [130-132]. In 3D, the corresponding lattices with magnetic frustration are edge sharing face-centred cubic (FCC) and corner-sharing Pyrochlore lattice [129].

Another class of materials with inherent magnetic frustration are spinels, AB_2O_4 with cations occupying the 8 tetrahedral *A* sites and 16 octahedral *B* sites. As first noted by Anderson [133], spinels containing magnetic ions only on the *B* sites (with *A* sites occupied by non-magnetic ions such as Zn^{2+}) should lack LR magnetic order due to magnetic frustration. This is so because magnetic ions on the *B* site are arranged on corner-sharing tetrahedra, with the tetrahedra forming the FCC structure. This situation resembles the Pyrochlore lattice leading to magnetic frustration.

The idea of magnetic frustration in the spinel structure has been thoroughly tested in the spinel ZnFe$_2$O$_4$ = $(Zn^{2+})_A[2Fe^{3+}]_BO_4$ if the magnetic Fe^{3+} ions only occupy the *B* site. An early report by Lotgering on the magnetic properties of an annealed polycrystalline sample of ZnFe$_2$O$_4$ (ZFO) showed a peak in the magnetic susceptibility χ *vs.* T at 15 K which was associated with the Néel temperature T_N, possibly resulting from site inversion involving the presence of a fraction of Fe^{3+} on the A site [134]. More recent detailed studies by Schiessel *et al.* on a polycrystalline ZFO employing neutron diffraction (ND), muon-spin rotation (µSR) and Mössbauer spectroscopy showed $T_N \simeq 10.5$ K with LR order, although short-range (SR) order was evident up to 10 T_N and even below T_N, up to 20% of sample had SR ordering [135]. In the recent χ *vs.* T studies in both polycrystalline [136] and single crystals of ZFO [137], a cusp has been reported near 11 K. The main conclusion from the neutron scattering experiments in the high-quality single crystal of ZFO was that there is no LR ordering in this system due to geometrical frustration and that ZFO is effectively a spin-liquid (SL) rather than a spin-glass (SG) [137]. The observed θ = 120 K from the Curie−Weiss variation: $\chi = C/(T - \theta)$ with C yielding effective magnetic moment $\mu_{\text{eff}} = 4.08\ \mu_B$ is due to dominant ferromagnetic *nn* exchange interaction [137], whereas the third-neighbor interaction J_3 is antiferromagnetic [138]. Further, the ratio of $|J_3/J_1|$ is temperature dependent tending towards zero for $T > 50$ K [138]. However, the density functional theory (DFT) calculations of Cheng reported all three exchange interactions J_1, J_2 and J_3 to be antiferromagnetic in both ZnFe$_2$O$_4$ and CdFe$_2$O$_4$ with J_2 being much weaker than J_1 and J_3 [139]. These calculations, however, do not explain why θ = 120 K in ZFO is positive.

It is noted that in the cubic spinel GeCo$_2$O$_4$ = $(\text{Ge}^{4+})_A[2\text{Co}^{2+}]_B\text{O}_4$ with the similar Pyrochlore lattice, where the A site occupied only by non-magnetic Ge^{4+}, recent DFT calculations showed J_1 to be ferromagnetic and considerably larger than antiferromagnetic J_2 and J_3 [140]. So a second look at the DFT calculations for ZFO is required. In addition, a recent report by Dey *et al.* on polycrystalline ZFO sample prepared using solid-state reaction technique discovered rhombohedral distortion near 110 K accompanied by spontaneous electric polarization [141]. So, all issues regarding the magnetic properties of ZFO are not yet resolved. Like ZFO, MgMnO$_3$ is also a cubic spinel but with the defect structure: 4 MgMnO$_3$ = $3(\text{Mg}^{2+})_A[\text{Mg}_{1/3}{}^{2+}\ \text{Mn}_{4/3}{}^{4+}\ \Delta_{1/3}]_B\text{O}_4$ and with magnetic Mn^{4+} ions only on the B site [21]. It also showed only SR ordering and absence of LR ordering, presumably due to similar magnetic frustration as in ZFO [21].

In contrast to cubic spinels ZnFe$_2$O$_4$ and MgMnO$_3$ without LR order, ZnMn$_2$O$_4$ is a tetragonal spinel because of the presence of the Jahn−Teller (*JT*) active Mn^{3+} ions on the B site [142,143] and specific heat C_p *vs.* T data in this system show a magnetic transition at $T_N \simeq 63$ K. Neutron diffraction and µSR measurements in this system for $T < T_N$ show 2D correlations with full development of ordered magnetic moment due to single-ion anisotropy [142,143].

In this chapter, we present results on a sample consisting of intermediate composition between ZnFe$_2$O$_4$ and ZnMn$_2$O$_4$ since results on such systems have not yet been reported. Specifically, the investigated sample has the composition Zn$_{0.8}$Cu$_{0.2}$FeMnO$_4$ in which we have also added *JT* active Cu^{2+} ions to see the effect of magnetic dilution in addition to the effect of *JT* distortions of Mn^{3+} and Cu^{2+} ions. After structural characterization of this sample using x-ray diffraction (XRD) and x-ray photoelectron spectroscopy (XPS), temperature dependence of the ac and dc magnetic susceptibilities, neutron diffraction and temperature dependence of specific heat studies were carried out. These studies show the absence of LR ordering in Zn$_{0.8}$Cu$_{0.2}$FeMnO$_4$, but presence of SR order combined with cluster SG state near 47 K followed by SL state below 9 K. Details of these results and their discussion are presented in the following pages. Below we provide details about the experimental synthesis of Zn$_{0.8}$Cu$_{0.2}$FeMnO$_4$ together with various characterization techniques including their methodology.

3.2. Materials and Methodology:

There are five important experimental parts in this work: (*i*) Growth of the bulk samples using standard solid-state-reaction method, (*ii*) Electronic and crystal-structure characterization, (*iii*) Magnetic characterization, (*iv*) low-temperature heat-capacity measurements and (*v*) Neutron diffraction studies. For the synthesis of polycrystalline bulk samples of Zn$_{0.8}$Cu$_{0.2}$FeMnO$_4$ (ZCFMO), we used high purity binary transition-metal oxides viz. zinc oxide (ZnO), copper oxide (CuO), ferric oxide (Fe$_2$O$_3$) and manganese (IV) oxide MnO$_2$ as precursors. As an initial step, stoichiometric quantities of these oxides were mixed (ground) in an agate mortar with pestle for five hours which were then made into 13 mm diameter cylindrical pellets using a hydraulic press followed by multiple times sintering at 1200 °C for 8 hours in air with 4 h rising time and natural cooling to room temperature. For crystal structure analysis and determination of the phase purity of the sample, we used the x-ray diffractometer from Rigaku (Model: TTRAX III) with Cu-Kα radiation (λ = 1.54056 Å). The corresponding x-ray diffraction (XRD) patterns and their analysis using Rietveld refinement are discussed in next section. To understand the electronic structure and cationic distribution analysis we made x-ray photoelectron spectroscopy (XPS) measurements using Thermo-Fisher Scientific 250Xi system. Detailed frequency and temperature dependence of dynamical magnetization studies were carried out using SQUID magnetometer, whereas for the dc magnetization measurements we employed a physical property measurement system (PPMS) from Quantum Design of Model DynaCool. The temperature dependent specific heat $C_p(T)$ measurements were performed by means of a Quantum Design PPMS system using the standard heat-pulse calorimetry in the presence of both H = 0 and 90 kOe from 4 K to 200 K. Powder ND experiments on the polycrystalline Zn$_{0.8}$Cu$_{0.2}$FeMnO$_4$ were carried out on the instrument E6 at the BER II reactor of the Helmholtz-Zentrum Berlin. This instrument uses a pyrolytic graphite monochromator selecting the neutron wavelength λ = 2.417 Å. Powder patterns were collected between the diffraction angles of 4.6° and 136°. The powder sample was placed in a cylindrical vanadium container with the dimensions d = 6 mm and h = 5 cm. Rietveld refinements were carried out with the program *FullProf* [144] using the nuclear scattering lengths b(O) = 5.805 fm, b(Mn) = −3.73 fm, b(Fe) = 9.54 fm, b(Cu) = 7.718 fm and b(Zn) = 5.68 fm [145]. In the next section we provide a detailed analysis of core experimental results on the crystal structure followed by the magnetic properties.

3.3. Results and Discussion:

3.3.1. Crystal Structure from Powder Neutron Scattering and XRD:

The structural characterization of the prepared sample of Zn$_{0.8}$Cu$_{0.2}$FeMnO$_4$ using x-ray and ND confirmed the monophasic nature of the sample. As evident in the x-ray pattern in figure 3.1, this compound, at room temperature (295 K), exhibits the tetragonal spinel structure with lattice parameters a = 5.745(3) Å

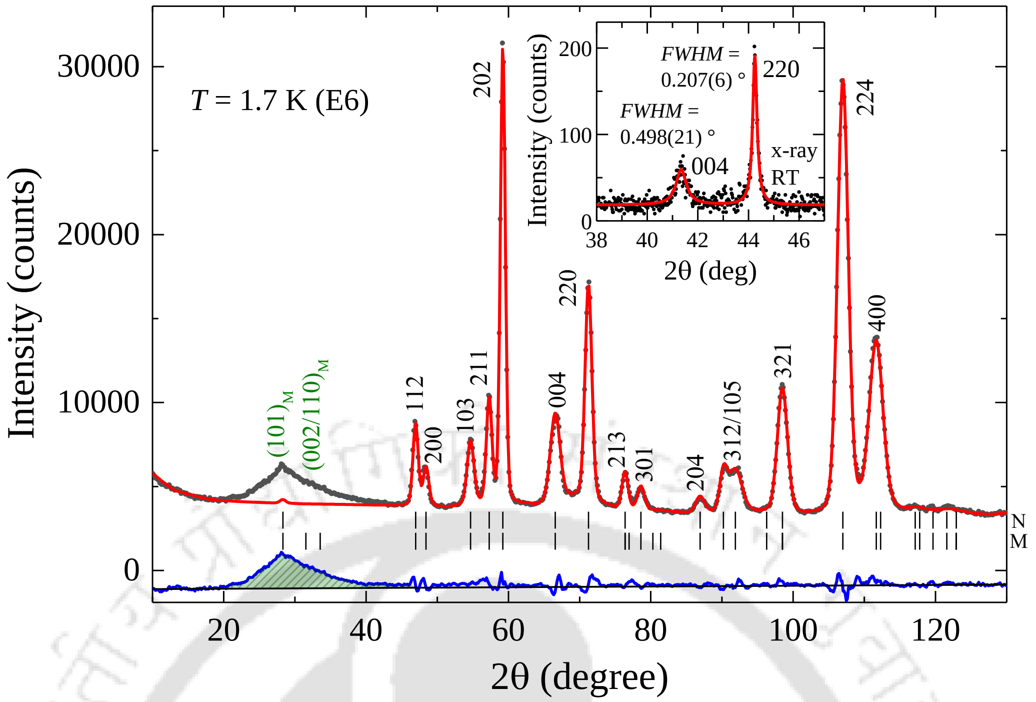

Figure 3.1: Rietveld refinement analysis of the x-ray and neutron powder diffraction pattern of bulk $Zn_{0.8}Cu_{0.2}FeMnO_4$ collected at 295 K and 1.7 K, respectively. Due to the better instrumental resolution of the x-ray pattern (inset) it is shown that the 004 reflection is broader than the 220. For both the reflections a satisfactory fit is obtained using a Lorentzian peak shape. The calculated patterns (red solid line) are compared with the observations (black-filled circles). The positions of the nuclear (N) (black bars) as well as the difference pattern of ($I_{obs} - I_{cal}$) (blue solid line) are also shown. Also shown are the positions of magnetic (M) reflections if long-range ordering is present. But in the difference pattern a strongly broaden magnetic reflection is observed in the 2θ range between 20° and 40° close to the positions of the reflections (101), (002) and (110).

and c = 9.059(3) Å giving a $c/a\sqrt{2}$ ratio of 1.115(3). For comparison, the parameter a = 8.52 Å was found for cubic $ZnFe_2O_4$ [137], and a = 5.72 Å and c = 9.245 Å has been reported for tetragonal $ZnMn_2O_4$ giving a $c/a\sqrt{2}$ ratio of 1.143 [143]. The elongation along the c direction results from the presence of *JT* active Mn^{3+} ions. However, this *JT* effect is also well established in $Zn_{0.8}Cu_{0.2}FeMnO_4$, where the tetragonal distortion is smaller but also strongly pronounced. Although, from our neutron data collected at 1.7 K it is found that the tetragonal splitting is somewhat reduced leading to a $c/a\sqrt{2}$ = 1.06054(10). Here, it is noted that no changes could be detected for $Zn_{0.8}Cu_{0.2}FeMnO_4$ concerning the structural part between 1.7 K and 79.4 K. Further, our refinements revealed anisotropic peak broadenings, especially for the reflections (220) and (004). The fit could be improved by using strain parameter implemented in the *FullProf* suite [144]. Due to the better instrumental resolution of the x-ray data, the half widths could be determined more precisely. Interestingly, the best fit of the integrated intensities (shown in the inset in figure 3.1) could be obtained by using a Lorentzian peak shape.

To obtain more information on the crystal structure properties we carried out Rietveld refinements of the powder pattern recorded at 1.7 K. Here, it is noted that the scattering power of oxygen is more pronounced in ND than in x-ray diffraction which allowed us to determine its positional parameters with higher accuracy. Further, we can get important information on the distribution of the metal atoms Mn, Fe, Cu and Zn in the

AO_4 tetrahedra and BO_6 octahedra since their neutron scattering lengths show considerable differences, whereas their x-ray form factors are very similar. A satisfactory fit can be obtained for refinements in the tetragonal space group $I4_1/amd$ (No. 141, cell choice 2). The metal ions at the *A* and *B* sites are located at the Wyckoff sites 4*b*(0,¼,⅜) and 8*c*(0,0,0), respectively, and the O atom at the site 16*h*(0,*y*,*z*). The refinements resulted in a residual factor R_F = 0.0155, where the occupancies of the *A* and *B* sites are initially allowed to vary using the constraints $occ(\mathrm{Cu}_A) + occ(\mathrm{Zn}_A) = 1$ and $occ(\mathrm{Fe}_B) + occ(\mathrm{Mn}_B)$. Here it has to be noted that the occupancies of the *B* site atoms Fe and Mn can be determined with much higher accuracy because of their strongly different neutron scattering lengths resulting in the values $occ(\mathrm{Fe}_B) = 0.4986(10)$ and $occ(\mathrm{Mn}_B) = 0.5014(10)$ which is very close to ratio of 1 : 1. Nonetheless, in the case of refinements of the occupancies at *A* site the difference of neutron scattering lengths of Cu and Zn are much smaller, resulting consequently in an enlarged standard deviation. This may also be the reasons that the occupancies are not in good agreement with the expected values as per the chemical stoichiometry, because of the dilute incorporation of Cu^{2+}, where for $occ(\mathrm{Zn}_A)$ and $occ(\mathrm{Cu}_A)$ the values 0.913(11) and 0.087(11) (instead of 0.8 and 0.2) are found, respectively. Therefore, we have inspected the possibility that Cu at the *A* site is fully or partially replaced either by Fe or Mn. In the next step we carried out a refinement, where Cu is partially replaced by Mn which has a negative neutron scattering length. In this refinement we have set $occ(\mathrm{Zn}_A) = 0.8$ and $occ(\mathrm{Fe}_B) = 0.5$ as well as the constraints $2\times occ(\mathrm{Cu}_B) = occ(\mathrm{Mn}_A)$ and $occ(\mathrm{Cu}_A) + occ(\mathrm{Mn}_A) = 0.2$. Finally, we obtained the stoichiometry $(\mathrm{Mn}_{0.0128(18)}\mathrm{Cu}_{0.1872(18)}\mathrm{Zn}_{0.8})_A\,[\mathrm{FeMn}_{0.9872(18)}\mathrm{Cu}_{0.0128(18)}]_B\mathrm{O}_4$. This would only give a replacement of Cu by Mn at the *A* site of 6.4 %, which does not support existence of Mn at the *A* site. At this point feasibility of either of the chemical formula $(\mathrm{Zn}_{0.8}\mathrm{Cu}_{0.2})_A[\mathrm{FeMn}]_B\mathrm{O}_4$ and $(\mathrm{Zn}_{0.8}\mathrm{Fe}_{0.2})_A[\mathrm{Cu}_{0.2}\mathrm{Fe}_{0.8}\mathrm{Mn}]_B\mathrm{O}_4$ cannot be ruled out. If both Cu and Fe occupy the *A* site along with Zn, the following constraints are used: $occ(\mathrm{Zn}_A) = 0.8$, $occ(\mathrm{Mn}_B) = 0.5$, $2\times occ(\mathrm{Cu}_B) = occ(\mathrm{Fe}_A)$ and $occ(\mathrm{Cu}_A) + occ(\mathrm{Fe}_A) = 0.2$. Finally, the refinements result in the occupancies $occ(\mathrm{Cu}_A) = 0.214(4)$ and $occ(\mathrm{Fe}_A) = -0.014$. This is a strong indication that the *A* site is fully occupied with Zn and Cu whereas the *B* site with Fe and Mn giving the chemical formula $(\mathrm{Zn}_{0.8}\mathrm{Cu}_{0.2})_A[\mathrm{FeMn}]_B\mathrm{O}_4$.

The refinement of the structural parameters of $\mathrm{Zn}_{0.8}\mathrm{Cu}_{0.2}\mathrm{FeMnO}_4$ (table 3.1) revealed a strong elongation of the $T_B\mathrm{O}_6$ octahedra, where the apical bond length $d_{ab}(T_B\text{-O}) = 2.1274(11)$ Å is somewhat larger than the equatorial one $d_c(T_B\text{-O}) = 1.9752(7)$ Å, which is finally the cause of the increase of the $c/a\sqrt{2}$. A similar trend was found recently for mixed spinel $\mathrm{Ti}_{0.6}\mathrm{Mn}_{0.4}\mathrm{Co}_2\mathrm{O}_4$, but weaker pronounced, having the bond lengths $d_c(T_B\text{-O}) = 2.025(4)$ Å and $d_{ab}(T_B\text{-O}) = 1.998(2)$ Å despite the fact that the $c/a\sqrt{2}$ ratio is very close to 1 [2]. The enlarged $c/a\sqrt{2}$ of $\mathrm{Zn}_{0.8}\mathrm{Cu}_{0.2}\mathrm{FeMnO}_4$ also leads to an elongation of the $T_A\mathrm{O}_4$ tetrahedra. Here the bond angle $\angle_c(\text{O-}A\text{-O}) = 107.76(8)$ °, having a bisector along the *c* axis, is slightly smaller than the ideal tetrahedron angle of 109.47 °. More information about cation distribution and valence states of the determined interatomic *T*-O distances of $\mathrm{Zn}_{0.8}\mathrm{Cu}_{0.2}\mathrm{FeMnO}_4$ are compared with those obtained from the ionic radii given by Shannon [146]. It is noted that the ionic radius of Cu^{2+} ($r_{\mathrm{Cu}2+} = 0.57$ Å) is closer to the value of Zn^{2+} ($r_{\mathrm{Zn}2+} = 0.6$ Å) than to that of Fe^{3+} ($r_{\mathrm{Fe}3+} = 0.49$ Å). If one assumes that iron occupies the *A* site instead of Cu^{2+} it is more likely that iron is in the valence state 2+ ($r_{\mathrm{Fe}2+} = 0.63$ Å, high spin). With this insight, the bond length in the

Table 3.1: Results of the Rietveld refinements of $Zn_{0.8}Cu_{0.2}FeMnO_4$ at 1.7 K using neutron powder diffraction data collected on the instrument E6. The refinements were carried out in the tetragonal space group $I4_1/amd$ (No. 141, cell choice 2). The metal ions at the *A* and *B* sites are located at the Wyckoff sites 4*b*(0,¼,⅜) and 8*c*(0,0,0), and the O atom at the site 16*h*(0,*y*,*z*). Listed are the positional parameters *y* and *z* of the O atom, lattice parameters and the overall isotropic thermal parameter B_{is}. The obtained residual (R_F = 0.0155) is defined as $R_F = ||F_{obs}| - |F_{calc}||/|F_{obs}|$. Further the bond distances and angles in the T_AO_4 tetrahedra (T_A = Cu_A, and Zn_A) and T_BO_6 octahedra (T_B = Mn_B, and Fe_B) are also given.

Structure parameters		Bond distances and angles	
y(O)	0.52219(16)	$d(T_A$-O) [Å]	1.9667(10)
z(O)	0.24257(13)	$d_a(T_B$-O) [Å]	1.9752(7)
B_{is} (Å^2)	0.55(4)	$d_c(T_B$-O) [Å]	2.1274(11)
a [Å]	5.8366(3)	$\angle_{ab}$(O-A-O) [°]	110.33(7)
c [Å]	8.754 (5)	$\angle_{c}$(O-A-O) [°]	107.76(8)
$c/a\sqrt{2}$	1.06054(10)*	$\angle_{ab}$(O-B-O) [°]	84.63(3)
V (Å^3)	298.21(7)	$\angle_{ac}$(O-B-O) [°]	85.54(6)

* 1.0676(3) x-ray data at 295 K.

T_AO_4 tetrahedron is found to be $d(T_A$-O) = 1.9667(10) Å. This value is somewhat smaller than the value 2.01 Å using the ionic radii of Shannon if the composition at the *A* site is $Zn_{0.8}^{2+}Fe_{0.2}^{2+}$. If the composition $Zn_{0.8}^{2+}Cu_{0.2}^{2+}$ ($Zn_{0.8}^{2+}Fe_{0.2}^{3+}$) is assumed the value 1.95 Å (1.87 Å) is obtained using the ionic radii of Shannon. Here, it is noted that the value 1.95 Å of the composition $Zn_{0.8}^{2+}Cu_{0.2}^{2+}$ is only slightly smaller than the refined bond distance $d(T_A$-O) = 1.9667(10) Å. All these aspects again strongly indicate the chemical formula is simply $(Zn_{0.8}Cu_{0.2})_A[FeMn]_BO_4$ for which the cationic and spin states of all the individual atoms are determined below.

We also compare the determined bond distance in the T_BO_6 octahedron with that obtained with the ionic radii given by Shannon. Assuming a high- or low-spin state of both Mn^{3+} and Fe^{3+} one obtains the values 2.045 Å and 1.965 Å, respectively. In our study we obtained the bond lengths $d_{ab}(T_B$-O) and $d_c(T_B$-O) (see table 3.1) giving an averaged value of 2.026 Å that is closer to the value given above for the high-spin states. Interestingly, the Fe^{3+} ions in $ZnFe_2O_4$ carry at the *B* site a magnetic moment in the ordered state of 3.9 μ_B [147]. In Mn_3O_4 the ordered moment at this site is μ_{tot} = 3.55 μ_B [148]. For $Zn_{0.8}Cu_{0.2}FeMnO_4$ no LR order occurs at 1.7 K as shown in the powder ND pattern (figure 3.1), where the magnetic reflection is strongly broadened indicating the presence of a SG state. Using the moment values of $ZnFe_2O_4$ and Mn_3O_4 we can estimate for $Zn_{0.8}Cu_{0.2}FeMnO_4$ a magnetic moment of 3.7 μ_B at the *B* site, which refers to a combination of both high- and low-spin states on the octahedral site.

3.3.2. Ionic Distribution using XPS:

To further confirm the electronic states and probe the elemental stoichiometry in detail, we performed the XPS measurements. The recorded XPS spectra for all the individual elements present in ZCFMO are plotted as a function of binding energy (in eV) as displayed in figure 3.2. Here the adventitious carbon (C-

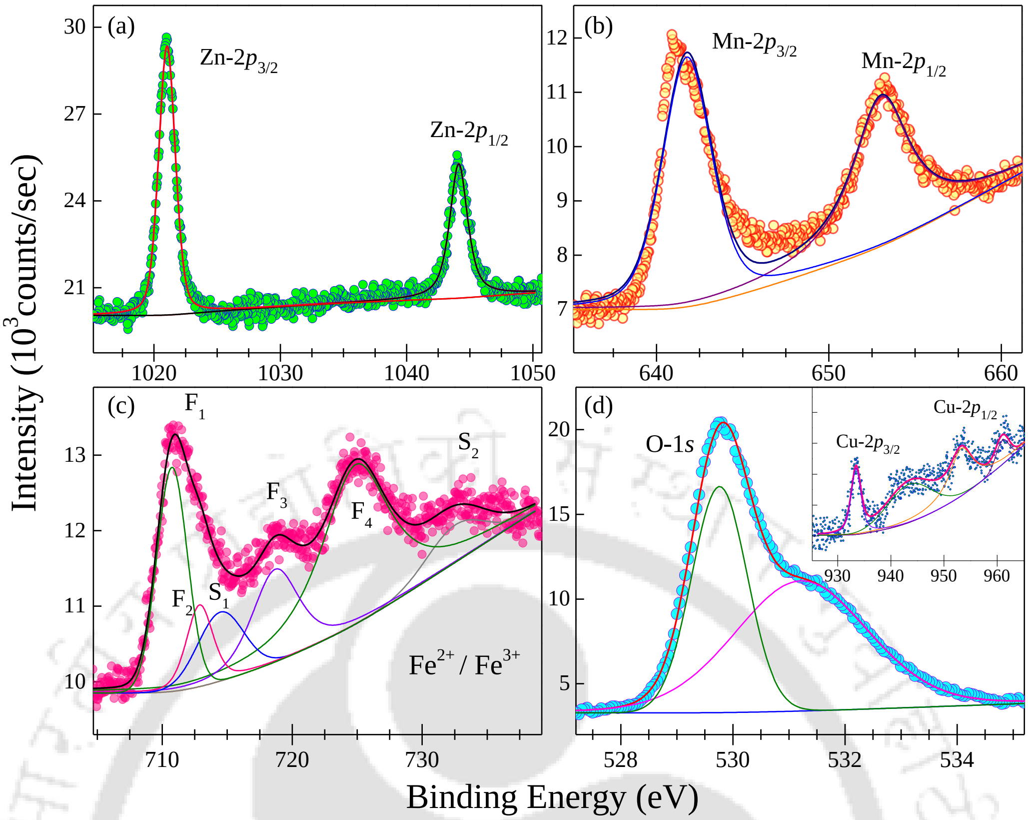

Figure 3.2: X-ray photoelectron spectra of bulk ZCFMO pellets sintered multiple times at 1200 °C for 8 h in air. The main panels of (a), (b), and (c) shows the 2*p* core level spectra of Zn, Mn, and Fe, respectively, whereas the inset in (d) shows that for Cu. The main panel of (d) represents the XPS spectrum of O-1*s*.

1*s*) peak at 284.8 eV was used as a charge reference to standardize the core level spectra of all the individual atoms namely: Cu-2*p*, Zn-2*p*, Fe-2*p*, O-1*s* and Mn-2*p*. Figure 3.2(a) shows the core level spectrum of Zn-2*p* which exhibits two sharp cusps centred across 1021 eV (2$p_{3/2}$) and 1044 eV (2$p_{1/2}$) with no signatures of additional satellite peaks. The energy difference between these two cusps (ΔZn-2$p_{(1/2-3/2)}$ ~ 23 eV) confirms the divalent character of Zn in ZCFMO [2,146]. Further, two humps are noticed in the core level XPS spectrum of Mn-2*p* (figure 3.2(b)) around 641.2 eV and 653.25 eV, associated with the 2$p_{3/2}$ and 2$p_{1/2}$, respectively, confirms the trivalent electronic state of Mn [147]. On the other hand, the XPS spectra of Fe-2*p*, depicted in figure 3.2(c), consists of at least four main peaks, which are deconvoluted into six number of peaks situated at 710.75 eV (F_1), 712.9 eV (F_2), 718.85 eV (F_3), 725.1 eV (F_4), 714.65 eV (S_1) and 733.1 eV (S_2). Here S_1 and S_2 are the satellite peaks corresponding to the shoulders noticed across the maximum intensity peaks of lower binding energies. The peak centred at F_1 is associated with the 2$p_{3/2}$ core level spectra of divalent Fe, while the peak located across F_2 belongs to Fe^{3+} [148,149]. Additionally, the spin-orbit splitting energy for these maxima are calculated to be $\Delta(F_3 - F_1)$ ~ 8.1 eV and $\Delta(F_4 - F_2)$ ~ 12.2 eV, which again confirms the mixed-valent character of Fe present in the ZCFMO system. The main panel data of figure 3.2(d) possesses a sharp peak across 529.75 eV pertaining to the O-1*s* spectra of ZCFMO. Whereas, the inset in figure 3.2(d) represents the XPS spectra of Cu which is comparatively weaker because of their dilute substitution in the spinel lattice. Nonetheless, we notice that the Cu-2*p* core level spectra has been

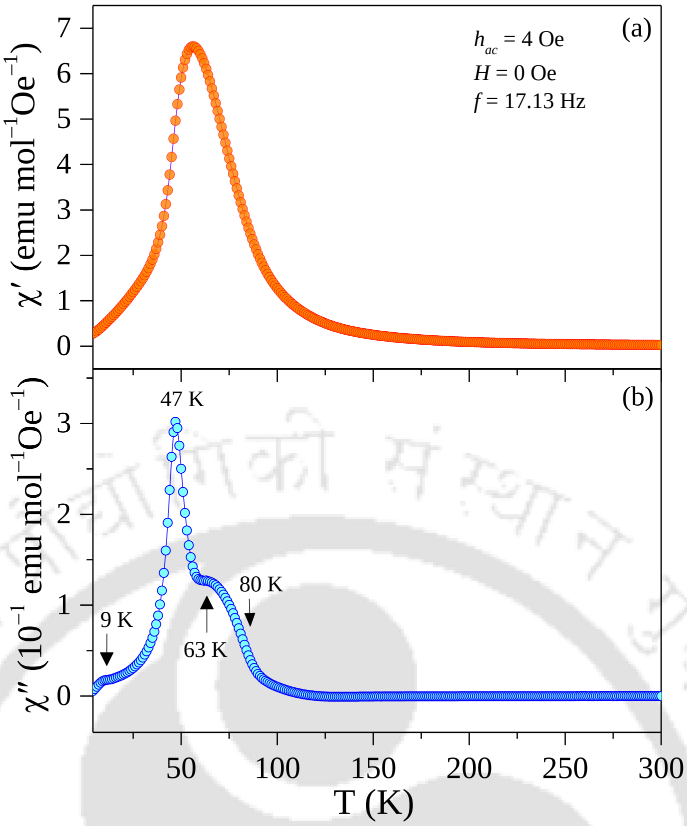

Figure 3.3: Temperature dependence of the ac susceptibilities χ' in (a) and χ'' in (b) measured at a fixed frequency of 17.13 Hz, h_{ac} = 4 Oe, and dc H = 0 Oe. The positions of the peaks observed in (b) are marked with additional discussion on them given in the text.

deconvoluted into total four number of peaks: C_1, C_2, C_3 and C_4, in which the main cusps C_1 and C_2 are located at 933.45 eV and 953.6 eV, respectively, while the other two are satellite peaks situated at C_3 ~ 943.05 eV and C_4 ~ 961.75 eV. The spin-orbit splitting energy (ΔC) between the two main peaks (C_1 and C_2) is obtained to be 20.15 eV confirms the presence of Cu^{2+}, which is further supported by the broad satellite peak across 943.05 eV [150,151]. In summary, the results from the analysis of XRD and XPS lead to the chemical formula for $Zn_{0.8}Cu_{0.2}FeMnO_4$ as $(Zn_{0.8}^{2+}Cu_{0.2}^{2+})_A[Fe_{0.4}^{2+}Fe_{0.6}^{3+}Mn^{3+}]_BO_{4-\delta}$, with δ = 0.2 for reason of charge balance; for brevity, this is listed simply as ZCFMO in the rest of the chapter.

3.3.3. Temperature and Frequency Dependence of AC Susceptibility:

In order to probe the magnetic properties, firstly the temperature dependence of ac susceptibilities, χ' and χ'', of ZCFMO were measured at several frequencies f = 0.17 Hz to 510 Hz under an ac field h_{ac} = 4 Oe and the dc field H = 0. For these measurements, the sample was cooled under H = 0 from 300 K to 4 K, known as the zero field cooled (ZFC) condition, followed by measuring χ' and χ'' with increasing temperature. In figure 3.3, results for a fixed frequency f = 17.13 Hz are presented which show only a single broad peak near 60 K for χ' *vs.* T whereas for χ'', there is a sharp peak near 47 K, with associated weaker broader peak near 63 K and a weaker peak near 9 K. In figure 3.4, temperature dependence of χ' and χ'' at various frequencies shows that with increase in frequency the peak position of the 47 K peak shifts to higher temperatures. The

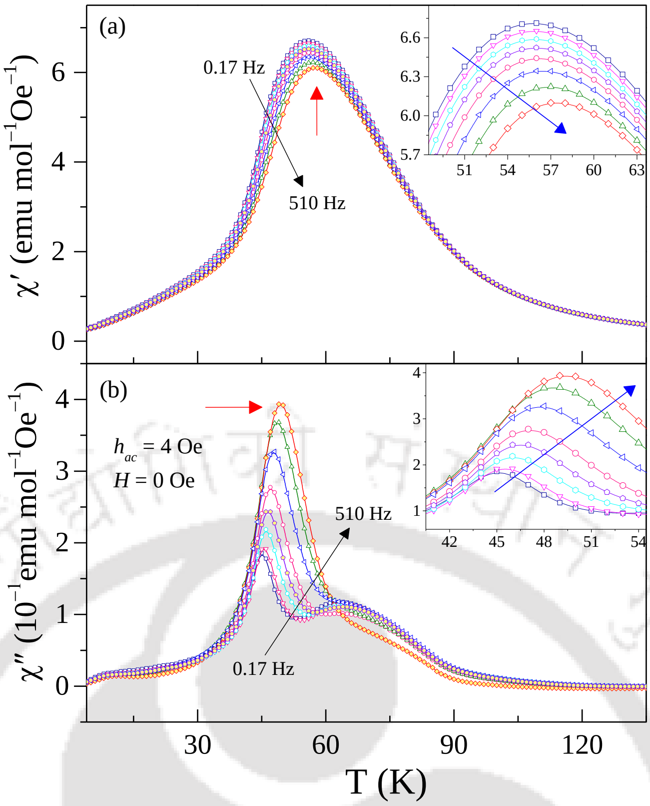

Figure 3.4: The temperature dependence (4 K ≤ T ≤ 135 K) of the ac magnetic susceptibilities χ' and χ'' for ZCFMO are shown in the panels (a) and (b), respectively, measured at several constant frequencies from 0.17 to 510 Hz in the presence of an applied 4 Oe ac magnetic field and zero dc bias. The insets show the zoomed images of the respective main panel data across the peak temperatures.

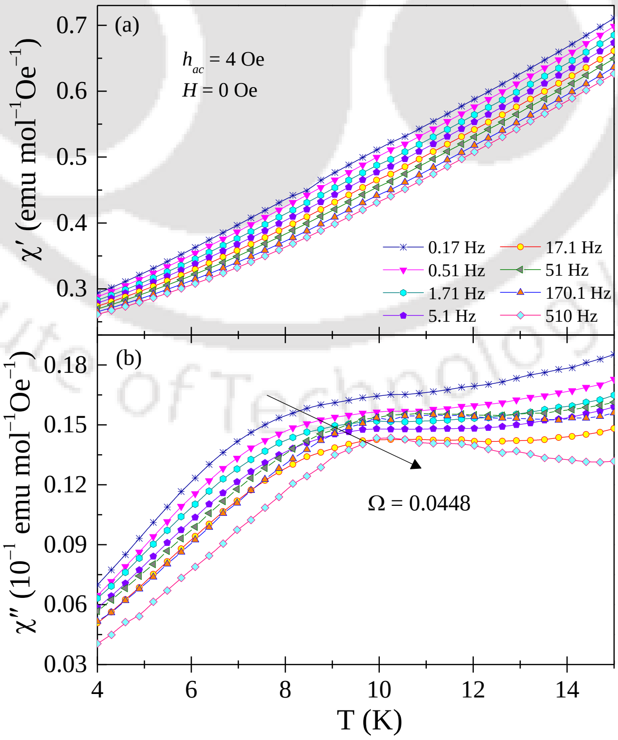

Figure 3.5: Temperature dependence of (a) $\chi'(T)$ and (b) $\chi''(T)$ data for ZCFMO measured with smaller temperature intervals in the range 4 K ≤ T ≤ 15 K under similar conditions as in figure 3.4 with the purpose to probe the nature of the anomaly across T = 9 K. The arrow indicates the direction of peak shift with increasing frequency.

temperature dependence of the peak near 9 K covering the temperature range from 4 K to 15 K for eight frequencies between 0.17 Hz and 510 Hz is shown in figure 3.5. From these results, the peak in the χ'' *vs.* T data is evident near 9 K, its peak position shifting to higher temperatures with increase in frequency. For the χ' *vs.* T data, there is a change in slope near 9 K, especially for higher frequencies.

To determine the origin of these peaks near 47 K and 9 K, the Mydosh parameter Ω given by [152,153]

$$\Omega = (T_{f2} - T_{f1})/T_{f1}(\log f_2 - \log f_1) \qquad (3.1)$$

is determined from the χ'' data using f_1 = 0.17 Hz and f_2 = 510 Hz with T_f being the position of the peak. For the peak near 47 K, this analysis gives Ω = 0.0246, and for the peak near 9 K, similar analysis gives Ω = 0.0448. These magnitudes are considerably larger than Ω = 0.005 observed in canonical spin glasses but close to the magnitudes for cluster spin glasses [154-156], especially for the peak near 47 K. So, this peak near 47 K is determined to be due to cluster SG transition. Additional discussion on the nature of the peak near 9 K is presented later.

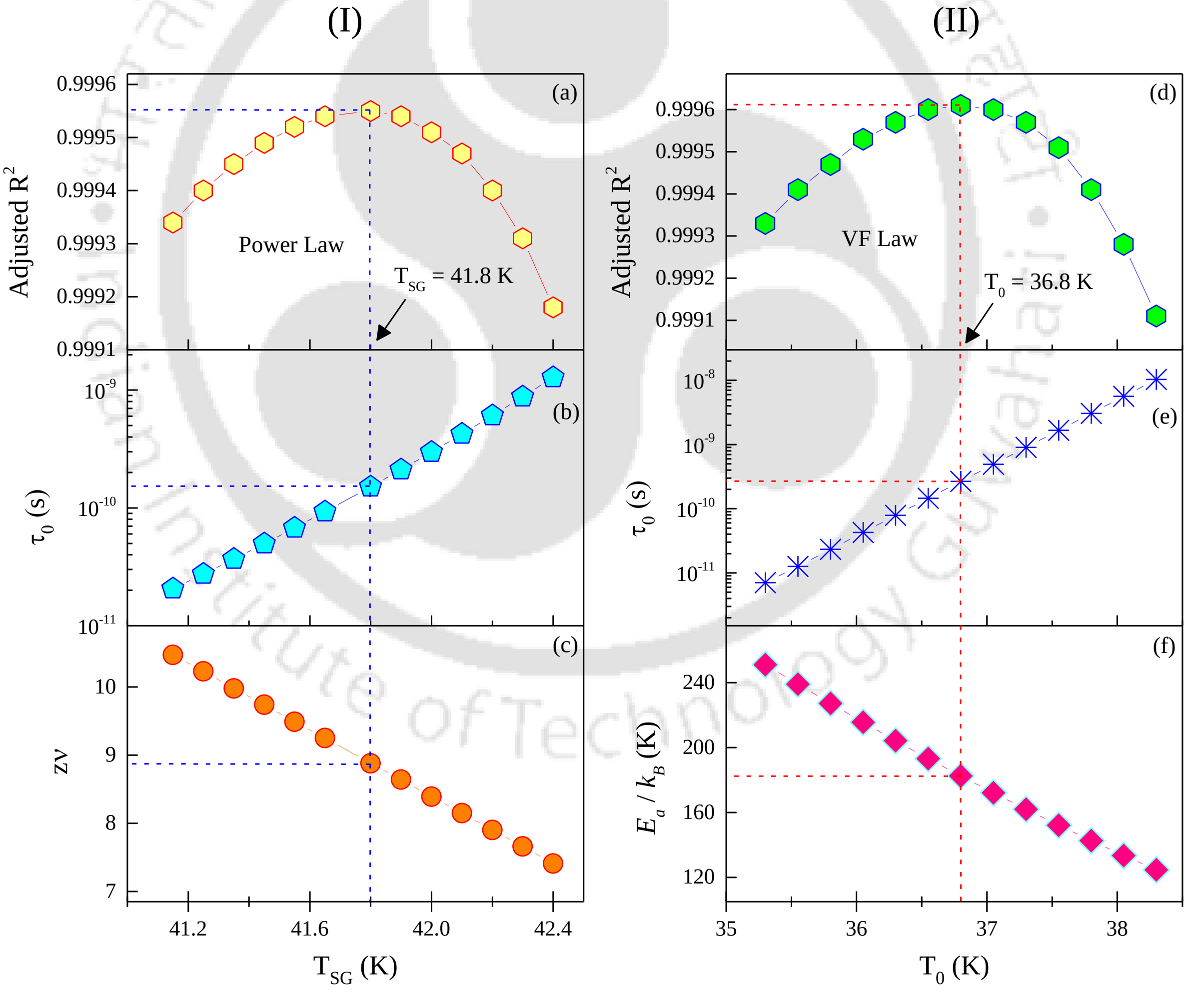

Figure 3.6: Fitting parameters: (a) Adjusted R^2, (b) characteristic relaxation time τ_0 and (c) the critical exponent $z\nu$, obtained for different selections of T_{SG} based on the Power Law, are given in the panel I. The panel II represents the fitting parameters: (d) Adjusted R^2, (e) τ_0 and (f) activation energy E_a/k_B, attained for different values of T_0 following the Vogel−Fulcher (VF) law. The dotted lines are visual guides connecting among the sub-panels across the local maxima in the Adjusted R^2 value.

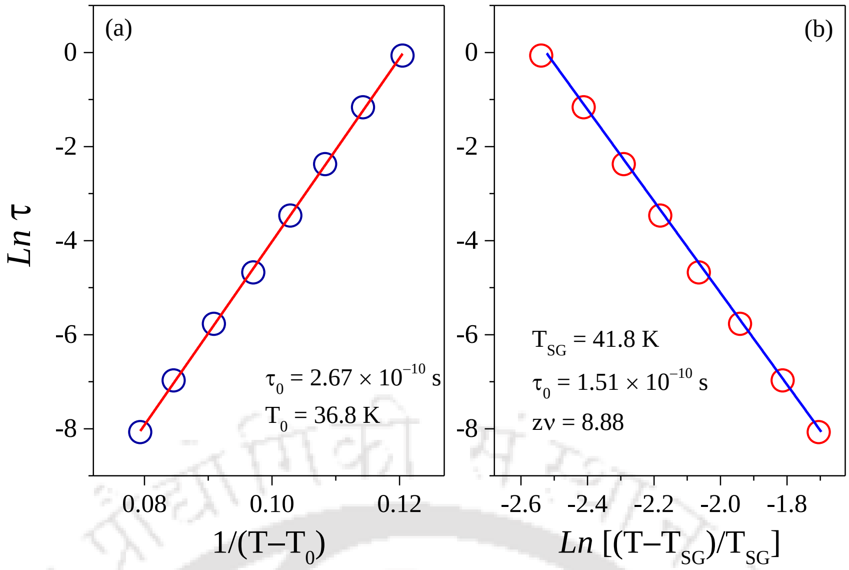

Figure 3.7: Variations of the relaxation time $Ln\ \tau$ against $1/(T - T_0)$ in (a) for the fit to the VFL and against $Ln\ [(T - T_{SG})/T_{SG}]$ for the fit to PL in (b). The circles represent experimental points for the optimum magnitudes of T_0 and T_{SG} determined in figure 3.6. The solid lines represent the least-squares fit to the data with the magnitudes of the determined parameters listed in the figures.

Another approach to verify the nature of SG transitions is to do scaling analysis using the Vogel-Fulcher law (VFL) given by equation (3.2) and the Power law (PL) given by equation (3.3) [154].

$$\tau = \tau_0\ exp[E_a/k_B(T - T_0)] \qquad (3.2)$$

$$\tau = \tau_0\ [(T - T_{SG})/T_{SG}]^{-z\nu} \qquad (3.3)$$

In these equations, $\tau = 1/(2\pi f)$ is determined from the positions of the peaks in the χ'' *vs.* T at different f, E_a is the activation energy, T_0 represents the strength of inter-cluster interaction, T_{SG} is the SG transition and $z\nu$ is the dynamical critical exponent [157]. From equation (3.2), plot of $Ln\ \tau$ *vs.* $1/(T - T_0)$ should yield a straight line with intercept $Ln\ \tau_0$ and slope E_a/k_B. Similarly, from equation (3.3), plot of $Ln\ \tau$ *vs.* $Ln\ [(T - T_{SG})/T_{SG}]$ should be linear with slope yielding $z\nu$. However, the optimum of T_0 and T_{SG} for such analysis is still not obvious.

In a recent work from our group [158], we have presented a procedure to determine optimum magnitudes of T_0 and T_{SG} using an adjusted R^2 method, noting that adjusted $R^2 = 1$ for optimum values. In figure 3.6, we show the results of this procedure for the peak near 47 K by plotting Adjusted R^2 *vs.* different choices of T_{SG} and T_0 and determining the corresponding magnitudes of τ_0, $z\nu$ and E_a/k_B. This analysis shows that the optimum T_{SG} = 41.8 K with $\tau_0 = 1.5 \times 10^{-10}$ s and $z\nu$ = 8.88 for the fit to the PL and T_0 = 36.8 K, $\tau_0 = 2.67 \times 10^{-10}$ s and E_a/k_B = 182.4 K for the fit to the VFL (figure 3.7). Since $k_BT_0/E_a = 36.8/182.4 \simeq 0.2$ is much less than unity, it shows that inter-cluster interaction is weaker than the energy barrier between clusters, leading to the cluster glass state without LR magnetic order. The magnitude of τ_0 and $z\nu$ are characteristic of SGs, although it is now realized that their magnitudes cannot be used to distinguish between cluster and canonical SGs [150,158]. In summary, the magnitude of $\Omega = 0.0246$, combined with $k_BT_0/E_a << 1$ establishes

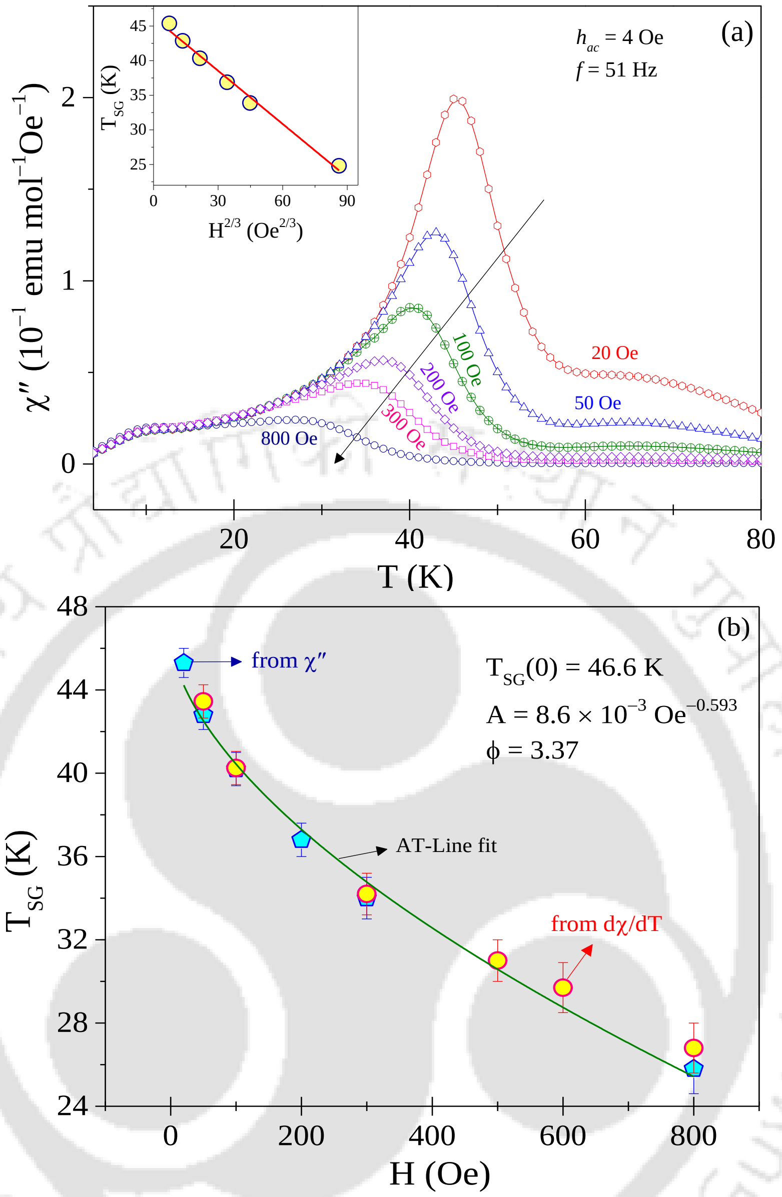

Figure 3.8: (a) Temperature dependence of $\chi''(T)$ measured at different dc applied fields 20 Oe ≤ H ≤ 800 Oe superimposed with h_{ac} = 4 Oe and a fixed f = 51 Hz. The arrow indicates the shifting of peak position towards lower temperature side with increase in H. (b) The field variation of T_{SG} obtained from the dc magnetic measurements is fit to the Eq.: $T_{SG}(H) = T_{SG}(0)\,[1 - AH^{2/\phi}]$ with the magnitudes of the parameters listed in the figure. In the inset of (a), the linear variation of $T_{SG}(H)$ against $H^{2/3}$ is shown.

this system as a cluster SG. The reason for the difference of $T_{SG} \simeq 41.8$ K obtained from this procedure from 47 K is not yet clear. Our attempts to do this analysis using T_{SG} near 47 K were not successful.

The shift in the peak position of χ'' at 47 K with applied dc field H = 20, 50, 100, 200, 300 and 800 Oe is shown in figure 3.8(a). This shift is analyzed with the help of non-mean field theory (AT−line analysis) described by the equation: $T_{SG}(\mathrm{H}) = T_{SG}(0)[1 - A\mathrm{H}^{2/\phi}]$, where $T_{SG}(\mathrm{H})$ is the position of the peak in χ'' *vs.* T data in applied dc field H. The exponent ϕ = 3 for the de Almeida−Thouless line (AT−line) pertains to the Ising system. Our fit in figure 3.8(b) yields ϕ = 3.37 not too different from the Ising case. In this plot, we have also plotted the shift in $T_{SG}(H)$ *vs.* H (figure 3.8(b)) determined from the inflection point in the plot of

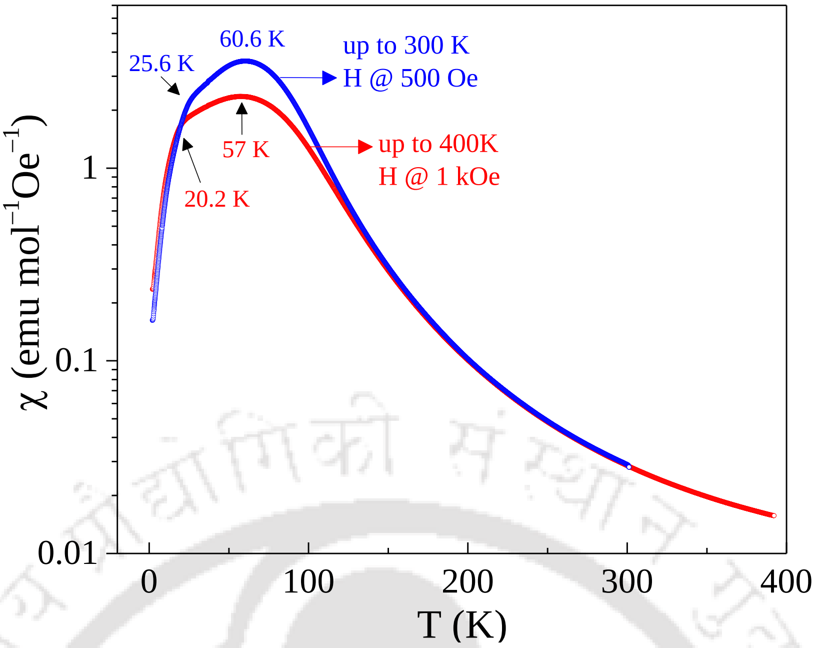

Figure 3.9: Temperature variation of dc magnetic susceptibility (χ) obtained for ZCFMO at H = 1 kOe (up to 400 K) and at H = 500 Oe (up to 300 K) along with the peak positions are indicated in both the curves.

$\partial\chi/\partial T$ *vs.* T where χ (= M/H) is the dc susceptibility measured in presence of different magnetic fields H. The details of these measurements and analysis are presented in the next section. It is noted that the broad peak near 63 K present in low H values in figure 3.8(a) effectively disappears in larger H values. So, this peak is likely due to some domain structure and no additional discussion is presented on this peak. Another notable point from the variation of T_{SG} *vs.* H in figure 3.8(b) is that for H = 800 Oe, T_{SG} is lowered to about 25 K. Additional discussions on this is presented in the next section on the temperature and magnetic field dependence of magnetization measured under various applied magnetic fields H.

3.3.4. Temperature and Magnetic Field Dependence of Magnetization:

The temperature dependence of the measured dc magnetic susceptibility (χ) for H = 500 Oe (up to 300 K) and H = 1 kOe (up to 400 K) is shown in figure 3.9. For T above ~ 125 K, the two measurements coincide but for T < 125 K, χ at H = 1 kOe is noticeably lower than that at H = 500 Oe. Both data show peak near 60 K and a second inflection near 25 K. The χ *vs.* T data was fit to the modified Curie−Weiss (MCW) law: $\chi = \chi_0 + C/(T-\theta)$, where $\chi_0 = -1.14 \times 10^{-4}$ emu mol^{-1}Oe^{-1} was determined as the diamagnetic contribution based on the Hartree−Fock theory [159]. The plot of $1/(\chi - \chi_0)$ *vs.* T is shown in figure 3.10. The data fits the MCW law for T > 250 K quite well with significant deviations observed for T < 250 K. The fit yields C = 3.29 emu K mol^{-1}Oe^{-1} and $\theta \simeq 185$ K. The positive θ signifies that the dominant exchange interaction in the system is ferromagnetic (FM). However, the magnitude of $1/(\chi - \chi_0)$ being higher than the MCW fit for T < 250 K signifies the presence of AFM interaction between the FM clusters. The magnitude of C = 3.29 emu K mol^{-1}Oe^{-1} is used to determine $\mu_{\text{eff}} = \sqrt{7.993C}\ \mu_B$ yielding μ_{eff} = 5.13 μ_B. Using this value of μ_{eff} and the relation $\mu_{\text{eff}}/\mu_B = g\,[S(S+1)]^{1/2}$, yields effective spin S = 2.11 for g = 2 for this system. This magnitude of

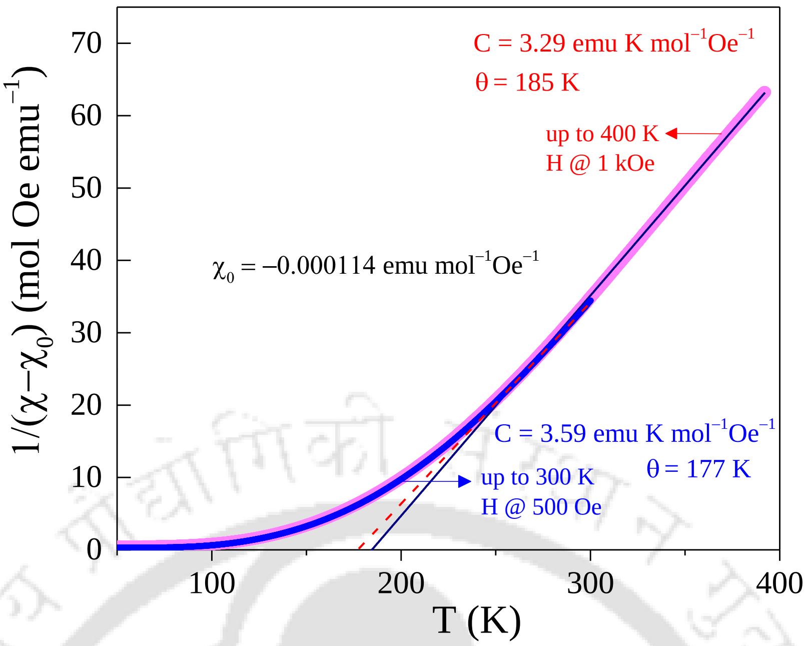

Figure 3.10: Temperature dependent inverse paramagnetic susceptibility $1/\chi_p = 1/(\chi - \chi_0)$ plotted between the range of T = 50 K to 400 K at H = 1 kOe and up to 300 K at H = 500 Oe for ZCFMO. The solid and dashed line are the linear fits to the modified Curie−Weiss law: $\chi = \chi_0 + C/(T - \theta)$ for the high temperature region with the magnitudes of C and θ listed in the figure.

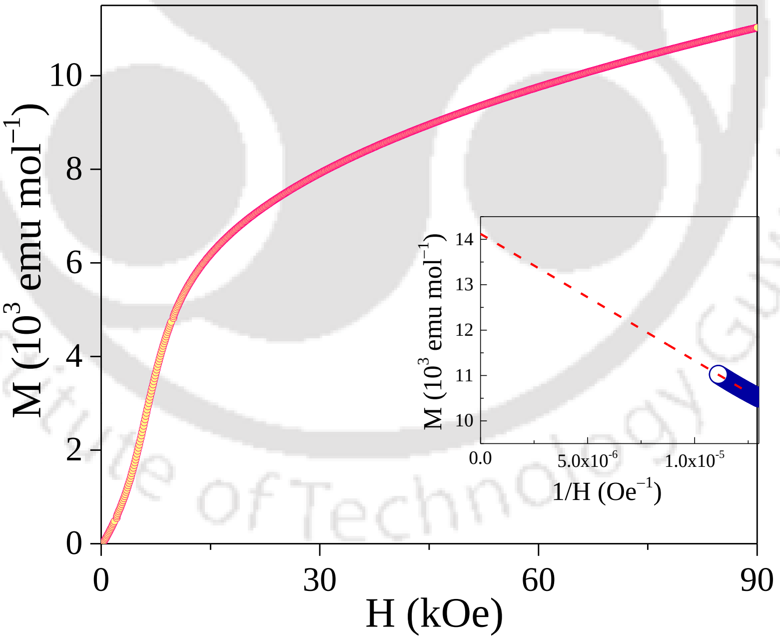

Figure 3.11: Plot of the measured magnetization M *vs.* applied field H with H up to 90 kOe at 2 K. The inset shows the high-field linear extrapolation of M to $1/H = 0$ to estimate the saturation magnetization M_S.

μ_{eff} can be explained if the B site Fe^{3+} and Mn^{3+} ions are in the low spin configuration with μ = 1.73 μ_B for Fe^{3+} and μ = 2.828 μ_B for Mn^{3+} ions with effective spins S = 1/2 and S = 1, respectively. Fe^{2+} in the high spin state has S = 2. This yields $(\mu_{eff}/\mu_B)^2 = 0.2(1.9)^2 + 0.4(4.9)^2 + 0.6(1.73)^2 + (2.828)^2 = 20.12$ or (μ_{eff}/μ_B)

= 4.49. Here the values of spin-only moments are used, and so this may be the reason that the resultant theoretical moment ($\mu_{\mathrm{eff}} \simeq 4.5\ \mu_{\mathrm{B}}$) is slightly smaller than the moment $\mu_{\mathrm{eff}} = 5.13\ \mu_{\mathrm{B}}$ obtained from our susceptibility measurement. This also yields the *B* site moment $\mu \simeq 4.4\ \mu_{\mathrm{B}}$ compared with $\mu \simeq 3.7\ \mu_{\mathrm{B}}$ determined from the ND results discussed above.

The second test on the correctness of this ionic arrangement is the measured *M vs. H* at 2 K, shown in figure 3.11, and the estimated saturation magnetization $M_{\mathrm{S}} \simeq 14{,}000$ emu/mol = 2.55 $\mu_{\mathrm{B}}/f.u.$ The measured moment for each ion is gS_{Z}. We take $g = 2.2$ for Cu^{2+} and $g = 2$ for Mn^{3+}, Fe^{2+} and Fe^{3+} ions. This calculation yields $\mu = 2.78\ \mu_{\mathrm{B}}$ for the arrangement $(\mathrm{Cu}^{2+}\downarrow)_A[\mathrm{Fe}^{2+}\uparrow, \mathrm{Fe}^{3+}\downarrow, \mathrm{Mn}^{3+}\uparrow]_B$ close to the experimental value. Except for low-spin Fe^{3+}, all the other magnetic ions located on the *B* site interact with dominant FM(↑) coupling, while the dilute Cu^{2+} on the *A* site couples antiferromagnetically. For $\mu_{\mathrm{eff}} = 5.13\ \mu_{\mathrm{B}}$, effective $S = 2.11$ and using $g = 2$ should yield $M_{\mathrm{S}} = gS\mu_{\mathrm{B}} = 4.22\mu_{\mathrm{B}}$, if all the moments are aligned parallel to each other. Our experimental value of $M_{\mathrm{S}} \simeq 2.55\ \mu_{\mathrm{B}}/f.u.$ indicates that all the moments are not aligned parallel to each other. Thus, this system is expected to have high degree of magnetic frustration as in the spinels ZnFe$_2$O$_4$ [135-138] and MgMnO$_3$ [21], which also have magnetic ions only on the *B* site. The above analysis shows that

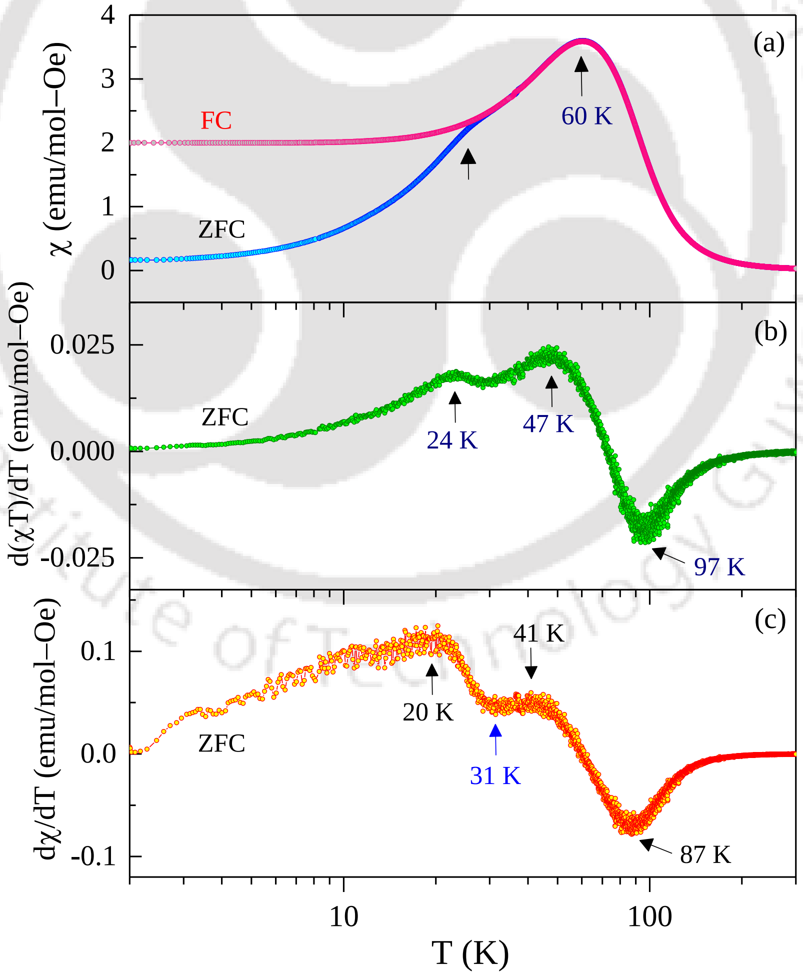

Figure 3.12: (a) DC magnetic susceptibility χ *vs. T* (log-scale) for H = 500 Oe under the zero-field-cooled (ZFC) and field-cooled (FC) protocols. (b) Plot of the computed $\partial(\chi T)/\partial T$ *vs. T*. (c) Plot of $\partial\chi/\partial T$ *vs. T*. The positions of the peaks are listed, and their significance is discussed in the text.

ferromagnetically aligned spins of Fe^{2+} and Mn^{3+} have antiferromagnetic interaction with the antiferromagnetically aligned spins of Fe^{3+} on the *B* site and dilute Cu^{2+} spins on the *A* site although the effect of Cu^{2+} is likely insignificant because of its low concentration. So, this system can be considered to have ferromagnetically aligned spin clusters mediated by antiferromagnetically aligned spins. With this insight, our measurements reported here on the ac and dc magnetic susceptibilities, ND and temperature dependence of the specific heat are interpreted in terms of SR ordering of ferromagnetic clusters interacting antiferromagnetically but without the presence of LR magnetic ordering. These considerations lead to complex magnetic ordering in ZCFMO including SG state near 47 K and SL state at lower temperatures, the latter discussed in more details later.

The temperature dependence of χ with H = 500 Oe and under the field cooled (FC) and ZFC protocols is shown in figure 3.12(a), clearly showing bifurcation of the two plots for $T < 24$ K along with a maximum across 60 K. It is known that in an antiferromagnet, the peak in χ *vs.* T does not represent magnetic ordering. Instead, it is the peak in $\partial(\chi T)/\partial T$ *vs.* T which corresponds to the Néel temperature as confirmed through peak in the specific heat versus temperature data [160,161]. In ferromagnets, the negative peak in $\partial\chi/\partial T$ *vs.* T is usually used as the magnetic ordering temperature [162,163]. Because of the presence of both ferromagnetic and antiferromagnetic couplings in ZCFMO, the plots of both $\partial(\chi T)/\partial T$ *vs.* T and $\partial\chi/\partial T$ *vs.* T are shown in figure 3.12(b) and figure 3.12(c), respectively. In figure 3.12(b), the peaks in $\partial(\chi T)/\partial T$ *vs.* T are observed at 97 K (negative peak), 47 K and 24 K whereas the positions of these peaks in $\partial\chi/\partial T$ *vs.* T in figure 3.12(c) are shifted to lower temperatures by a few degrees. The peak near 97 K is associated with local ferromagnetic ordering in clusters since its position shifts to higher temperatures with increase in applied H as expected in

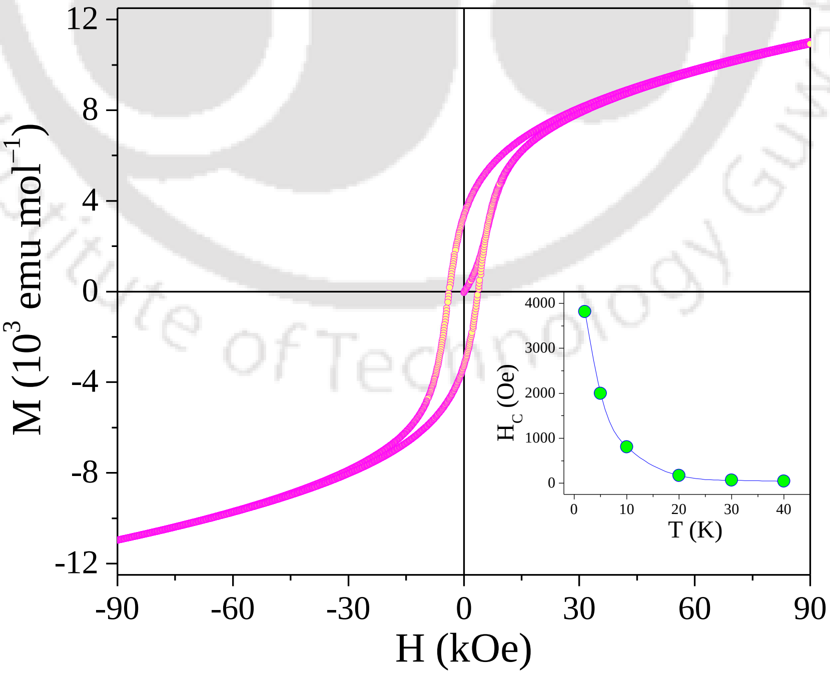

Figure 3.13: The *M−H* hysteresis loop obtained at T = 2 K for the sample of ZCFMO under ZFC conditions. The inset shows the temperature dependence of the coercivity (H_C) acquired from the *M−H* loops measured at different temperatures.

ferromagnets and ferrimagnets [85,164]. Though the peak near 47 K coincides with the SG transition T_{SG} observed in ac susceptibilities discussed in detail in Section 3.2, the maximum at 60 K in figure 3.12(a) likely appears due to the crossover dynamics of domains owing to the rotational processes or wall displacements in ferrimagnets/ferromagnets [165,166]. The peak near 24 K below which there is a bifurcation of χ(FC) and χ(ZFC) plots, is associated with the shift of T_{SG} with applied H = 500 Oe as shown previously in figure 3.8(b). Interestingly, if we consider the local minima or the inflection point between the peaks 24 K and 47 K as T_{SG}, which is obtained at 31 K based on the $\partial\chi/\partial T$ *vs.* T plot, the results perfectly agree with the ac susceptibility results in figure 3.8(b).

To understand the transition near 24 K below which $\chi(FC) > \chi(ZFC)$ in figure 3.12(a), we measured the temperature dependence of hysteresis loop parameters. The temperature dependence of the coercivity H_C in the inset of figure 3.13 shows that for $T > 24$ K, H_C goes to zero. This suggests that for $T < 24$ K, the system develops a partially ordered state in a magnetic field but without signatures of exchange-bias or loop shift like the situation in magnetically diluted system like Co$_x$Mg$_{1-x}$O [167].

3.3.5. Exchange Constant Calculation:

As noted earlier, the dominant exchange constant which governs the high temperature χ *vs.* T variation is ferromagnetic. To determine this dominant exchange interaction, we followed the high temperature series expansion method (HTSE), based on fitting the paramagnetic χ_P *vs.* T, prescribed for spinel structure following Heisenberg Hamiltonian [150,168,169]. This HTSE relation is given below:

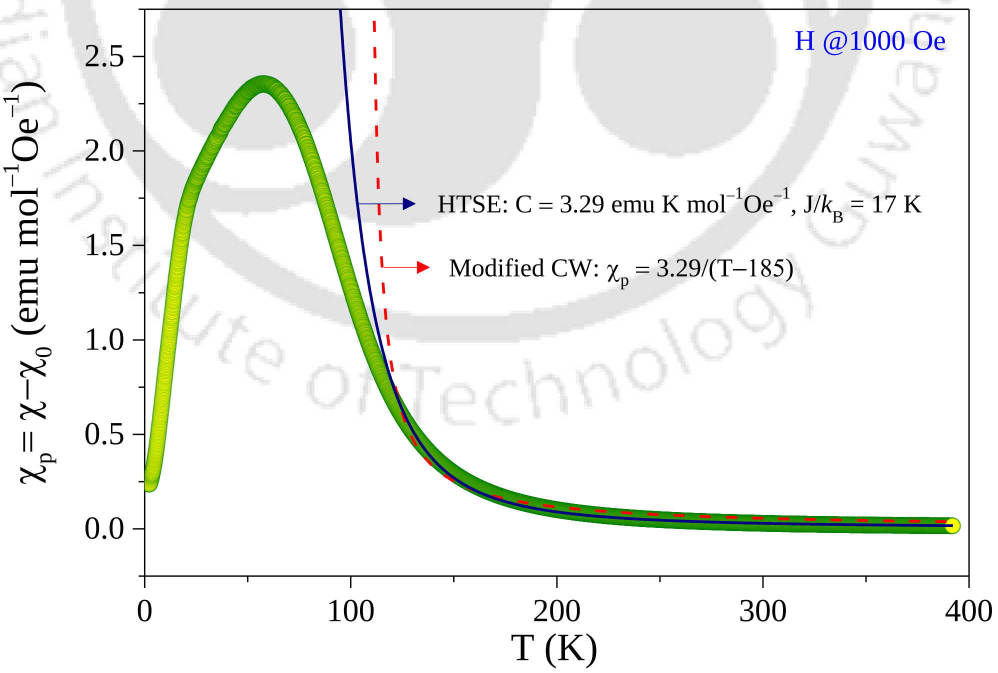

Figure 3.14: Temperature dependence of the dc paramagnetic susceptibility ($\chi_P = \chi - \chi_0$) measured under H = 1 kOe fitted to the High temperature series expansion (solid line) and the modified Curie−Weiss (dotted line) expressions. The magnitude of χ_0 used here is obtained from the Hartree−Fock theory whereas C = 3.29 emu K mol^{-1}Oe^{-1} and θ = 185 K are determined based on the analysis in figure 3.10.

$$\chi_{\mathrm{p}} = \frac{C}{T}\sum_{i=0}^{6} \mathrm{C}_i \left(\frac{-J}{k_{\mathrm{B}}T}\right)^{i} \tag{3.4}$$

Here, k_B is the Boltzmann's constant, $\chi_p = \chi - \chi_0$, C_i's are the normalized coefficients calculated up to 6th order as suggested by Schmidt *et al.* using the parameter "$r = \mu_{eff}^2/4$" in which $\mu_{eff} = 5.13\ \mu_B$ is used as determined previously from the fit to MCW law. The coefficients obtained using this procedure are: $C_0 = 1$, $C_1 = -13.2$, $C_2 = 141.25$, $C_3 = -1333.47$, $C_4 = 11872.9$, $C_5 = -104854.14$, $C_6 = 934662$. The fits of the χ *vs.* T data to equation (3.4) along with the fit to the MCW expression is shown in figure 3.14. The fit to HTSE represent only marginal improvement over the MCW fit and yield ferromagnetic $J/k_B = 17$ K. It is noted that retaining just the first two terms (C_0 and C_1) of the series yield the approximate MCW law and $J/k_B = 14$ K using $\theta = 185$ K. The departure of the fit from the experimental values at lower temperatures signifies the presence of antiferromagnetic exchange interactions among ferromagnetic clusters which are not considered in the above analysis because of the complexity of such calculations.

3.3.6. Temperature Dependence of Specific Heat:

To investigate the LR *vs.* SR magnetic ordering in ZCFMO, the thermal variation of its heat capacity C_p

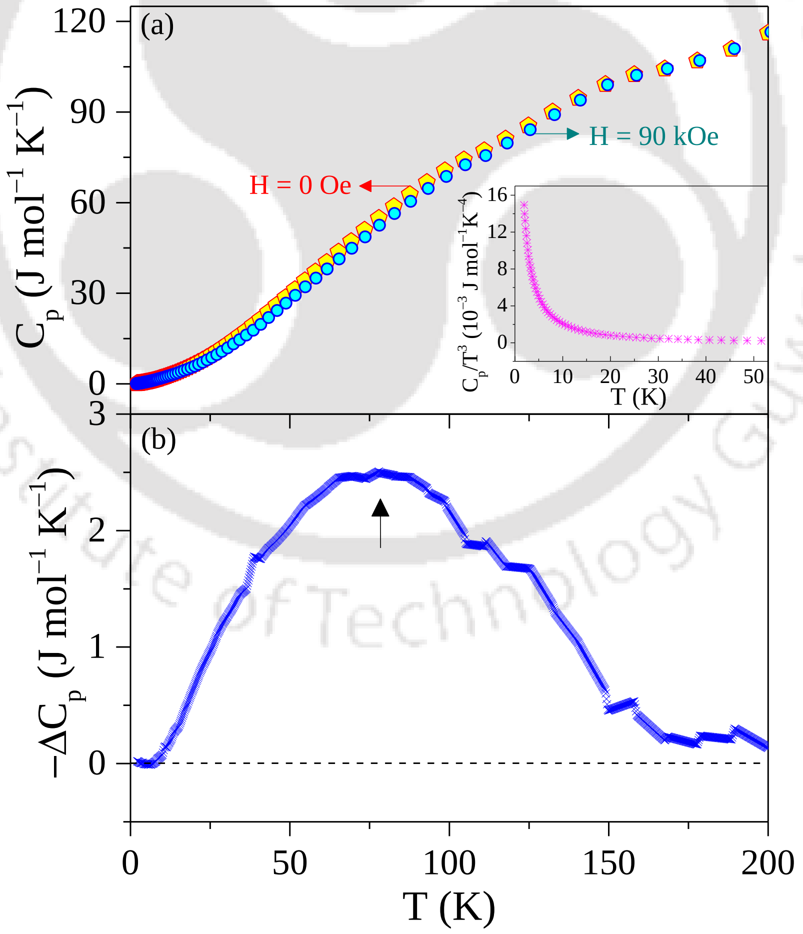

Figure 3.15: (a) Thermal variation of total specific heat (C_p) measured under the application of constant magnetic fields (H = 0 and 90 kOe) up to T = 200 K. The inset represents the temperature dependence of C_p/T^3 up to about 50 K. (b) The difference $-\Delta C_p = C_p(0) - C_p(90\text{ kOe})$ is plotted using same horizontal scale as of the upper panel.

was measured from 2 K to 200 K under ZFC conditions in applied $H = 0$ and 90 kOe. This variation of C_p *vs.* T is shown in figure 3.15 along with the plot of $-\Delta C_p = C_p(0) - C_p(90\text{ kOe})$ *vs.* T. Although the magnitude of $-\Delta C_p$ is comparatively small, it shows that applied H suppresses C_p with a peak in its magnitudes around 80 K. This variation is likely due to coupling of the FM clusters to the applied H. More importantly, in the $C_p(0)$ *vs.* T data, a λ−type anomaly characteristic of LR ordering is not observed as often reported for second order magnetic transitions [158,170]. However, lattice contribution to C_p must be first subtracted out from the measured C_p before any magnetic contribution to C_p can be ruled out. The Debye model of lattice specific heat C_L which usually work quite well at lower temperatures yields the following relation for C_L:

$$C_L = 9\,N\,R\,(T/\Theta_D)^3 \int_0^{\frac{\Theta_D}{T}} \frac{x^4 e^x}{(e^x-1)^2}\,dx \tag{3.5}$$

where Θ_D is the Debye temperature, usually determined from the fit to the data and $R = 8.314$ J mol^{-1}K^{-1} is the gas constant. For low temperatures when $T << \Theta_D$, so that the limit Θ_D/T in the integral in equation (3.5) can be replaced by infinity, $C_L = 216\,R\,(T/\Theta_D)^3$ is obtained for the lattice contribution. Therefore, in the case of only lattice contribution to C_p, C_p/T^3 should yield a constant value at lower temperatures. In the inset of figure 3.15, the plot of C_p/T^3 *vs.* T up to 45 K shows that below about 25 K, there is indeed some magnetic contribution to C_p whereas for higher temperatures C_p tends to become constant. This also shows that for $T > 45$ K, a good fit of the C_p *vs.* T to equation (3.5) can be expected for a specific choice of Θ_D. This fit of the C_p *vs.* T data for $H = 0$ Oe to equation (3.5) for $\Theta_D = (376.2\pm0.4)$ K is shown in figure 3.16 along with the

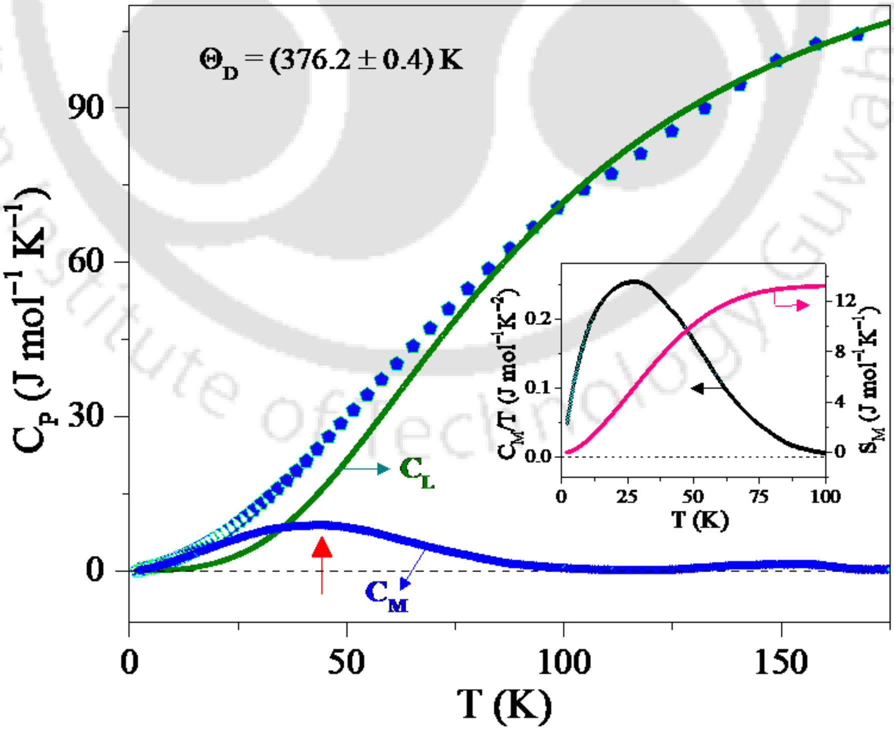

Figure 3.16: Temperature variation of the measured specific heat C_p for $H = 0$ Oe together with the temperature dependent contributions from the phonon contribution C_L derived based on the Debye model of specific heat and the magnetic contribution $C_M = C_p - C_L$. The inset shows the temperature variations of C_M/T and computed magnetic entropy (S_M).

temperature variation of the evaluated $C_M = C_p - C_L$, where C_M is the magnetic contribution. The temperature variation of C_M has a broad peak around 40 K which coincides with T_{SG} determined from the analysis of the ac susceptibilities. This analysis confirms the presence of SR magnetic order associated with the cluster SG state.

The variation of C_M *vs.* T is used to determine the change in temperature dependence of the magnetic entropy:

$$S_M = \int_0^T (C_M/T)\, dT \tag{3.6}$$

In the inset of figure 3.16, the thermal variation of C_M/T and computed S_M are shown. At 100 K, $S_M \simeq 13.1$ J mol^{-1}K^{-1} which effectively remains constant above 100 K. But with decrease in temperature, S_M begins to decrease due to the onset of SR magnetic ordering and S_M approaches zero below 4 K. Using $S_M = R\, Ln(2S + 1) = 13.1$ yields effective $S = 1.92$ to be compared with $S = 2.11$ determined earlier from the analysis of paramagnetic susceptibility. Our system ZCFMO contains magnetic ions with $S = 1/2$, 1, and 2. So these composite values of S obtained from the analysis of magnetic susceptibility and specific heat are quite reasonable.

3.3.7. Spin-Glass *vs.* Spin-Liquid State:

The temperature variation of C_p at liquid helium temperatures has been used to distinguish between spin-glass and spin-liquid states in magnetically diluted systems. In canonical glasses which contain only a few percent of magnetic ions, C_p is known to vary linearly with temperature [92]. However, in other diluted

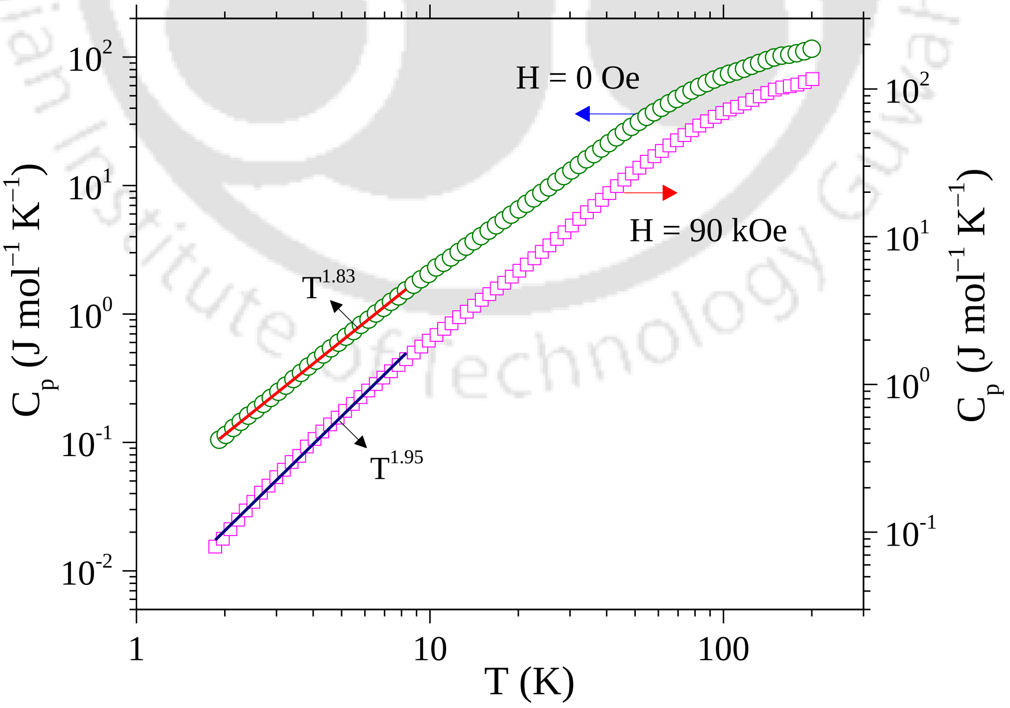

Figure 3.17: Log-Log plot of the temperature dependence of the measured $C_p(T)$ for both $H = 0$ and $H = 90$ kOe. The solid lines are linear fits to $C_p \sim AT^n$ below 9 K with $n = 1.83$ for $H = 0$ and $n = 1.95$ for $H = 90$ kOe.

systems with magnetic frustration such as $SrCr_8Ga_4O_{19}$ with Kagomé lattice [171,172], $NiGa_2S_4$ with triangular lattice [173], $CuCr_{0.7}V_{0.3}S_2$ [174], and even in Co based glassy systems Co_2TiO_4 and Co_2SnO_4 [175], C_p varying as T^2 at low temperatures has been reported. This T^2 variation of C_p is considered to be signature of SL state in which magnetic moments fluctuate dynamically at very low temperatures [92,171-175]. For the ZCFMO system, the variation of $C_p = AT^n$ is tested by plotting log C_p *vs.* log T in figure 3.17 for the data taken for both $H = 0$ and $H = 90$ kOe. For $T < 9$ K, the data fits straight line with $n = 1.83$ for $H = 0$ and $n = 1.95$ for $H = 90$ kOe, the slope becoming smaller at higher temperatures. This analysis suggests SG state for $T > 9$ K changes to SL like state for $T < 9$ K. The ND studies presented earlier in this work provide additional support for the dynamical fluctuations of the magnetic moment for $T < 9$ K. In the ac susceptibility measurements shown earlier in figure 3.3 and figure 3.5, there is a clear peak near 9 K in the plot of χ'' *vs.* T. These results provide sufficient proof for the transition to different magnetic phase below 9 K which has known signatures of a SL state.

Additional information on the nature of magnetic ordering can be obtained by evaluating the change in magnetic entropy $\Delta S_M = S(H) - S(0)$ with change in magnetic field H. This can be determined from the M *vs.* H isotherms such as the one shown in figure 3.11 at 2 K using the Maxwell equation [168]:

$$\Delta S_M = \int_0^H \left(\frac{\partial M}{\partial T}\right)_H dH' = \frac{\partial}{\partial T}\int_0^H M dH' \tag{3.7}$$

M *vs.* H isotherms were measured at many temperatures between 2 K and 200 K and the plot of $-(\Delta S_M)$ *vs.* T determined from these plots using 2nd part of equation (3.7) is shown in figure 3.18. This analysis is also used to determine the magnetocaloric effect (MCE) in materials. As seen in figure 3.18, a crossover from +ve

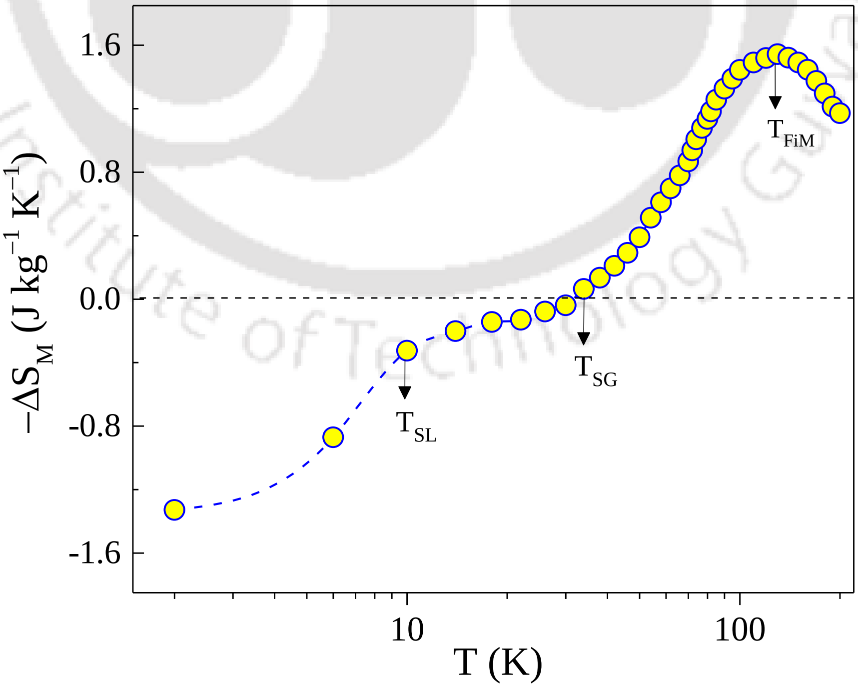

Figure 3.18: Temperature dependence of change in magnetic entropy i.e. $-\Delta S_M$ computed from the M−H isotherms measured for the range $0 \leq H \leq 90$ kOe and using equation (3.6). The arrows mark the positions of T_{FiM}, T_{SG} and T_{SL} discussed in the text.

(normal MCE) to −ve (inverse MCE) value of $-\Delta S_M$ is noticed across T_{SG} since with increase in *H*, magnetic disorder decreases in the paramagnetic region but increases in the SG regime. A further drop is observed below the SL transition T_{SL} = 9 K. This analysis provides additional support for the SL state below 9 K.

The time dependent behavior of frustrated systems in the SL region has rarely been reported in the literature. So, a detailed analysis of the thermo-remanent magnetization (TRM) studies on the ZCFMO system in the SL region is provided below, and is compared with that reported in literature for the SG region. For this purpose, the system was cooled to the required low temperature under *H* = 50 kOe, *H* was then set to zero and the magnetization (M_{TRM}) was measured for a time (*t*) duration of 7600 s. The data is represented in figure 3.19 for the M_{TRM} *vs*. *T* isotherm obtained at *T* = 5 K. The main panel data is analyzed by employing several typical scaling laws and/or power laws such as [176,177]:

$$M_{TRM} = M_0 - S\,Lnt \tag{3.8}$$

$$M_{TRM} = M_0\, t^{-\gamma} \tag{3.9}$$

$$M_{TRM} = M_0\, exp[-(\frac{t}{\tau})^{\alpha}] \tag{3.10}$$

$$M_{TRM} = M_0 - M_g\, exp[-(\frac{t}{\tau_p})^{\beta}] \tag{3.11}$$

In the above equations, M_0 is the initial remanent magnetization, *S* stands for the magnetic viscosity, M_g denotes the glassy component of magnetization, whereas, τ and τ_p are the characteristic relaxation time

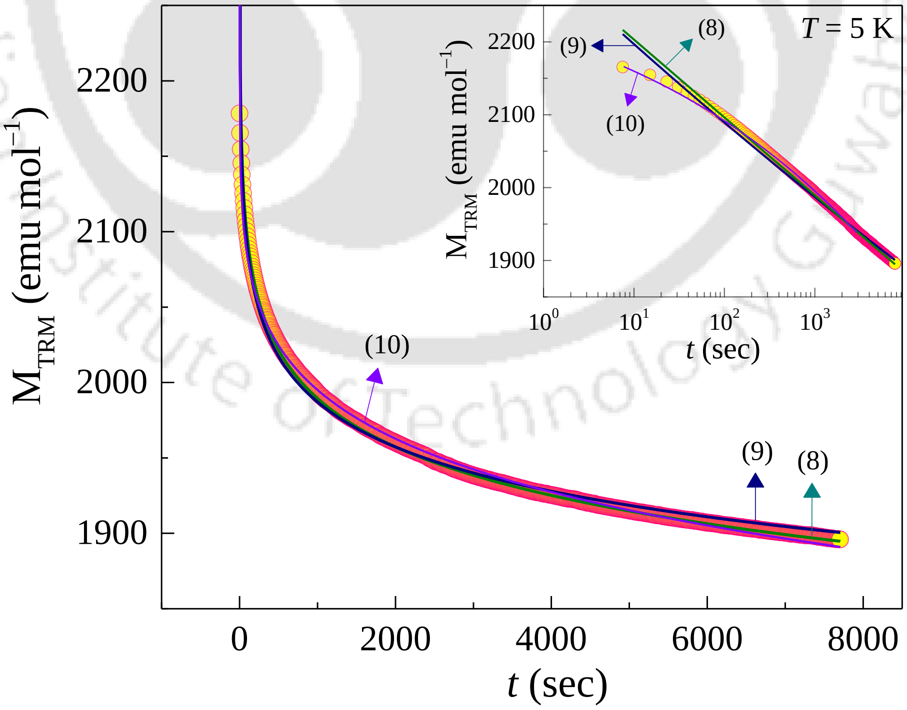

Figure 3.19: Relaxation of field-cooled (*H* = 50 kOe) magnetization of ZCFMO system measured for a duration of *t* = 7600 s at *T* = 5 K. The solid olive, navy and violet color lines represent fits of the experimental data to equation (3.8), (3.9) and (3.10), respectively. The inset shows the main panel data in a log-linear (*X*−*Y* axis) scale representation to identify the best fit to equation (3.10).

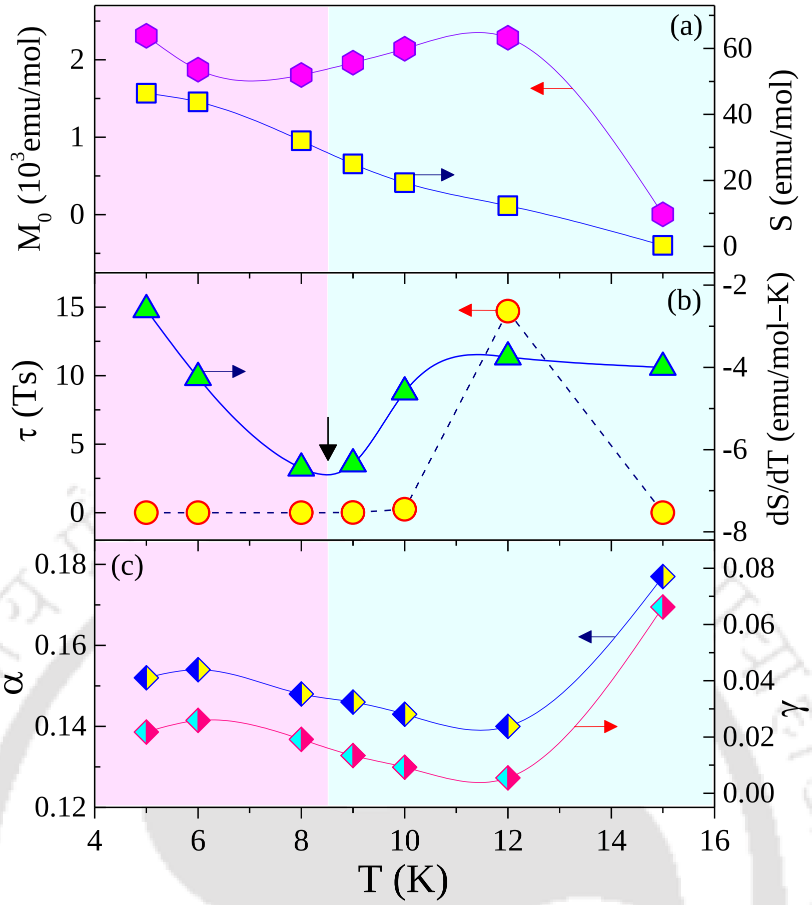

Figure 3.20: The parameters acquired based on the thermoremanent magnetization analysis, listed in table 3.2, are plotted against temperature. The left-hand-scales in (a), (b) and (c) shows the temperature variation of M_0, τ and α, and the right-hand-scales of the same show the temperature dependency of S, $\partial S/\partial T$ and γ, respectively. The shaded portions separate the spin-liquid region (light pink color) from the spin-glass region (light blue color).

constants. Here, the exponents α, β and γ are constants out of which the former two are known as the Kohlrausch−Williams−Watt (KWW) stretched exponents; usually these exponents are used to determine the strength of the dipolar interaction among the magnetic clusters [177-179]. The equations (3.8), (3.9), and (3.10) all appear to fit well with the main panel data in figure 3.19, although, the best fit to the experimental data till the lowest measured time is obtained with only equation (3.10), which is confirmed from the logarithmic-time scale representation (inset of figure 3.19). However, our data does not fit to equation (3.11) for the expected range of β ($0 \leq \beta \leq 1$). Similar analysis was also performed for the M_{TRM} *vs.* t isotherms obtained at T = 6 K, 8 K, 9 K, 10 K, 12 K and 15 K, and the extracted parameters are listed in table 3.2.

The fitting parameters are plotted against temperature in figure 3.20 for further analysis. Evidently, the magnitudes of M_0 and τ falls drastically for $T > 12$ K while the exponents α and γ increase. It is noted that the values of all the fitted parameters obtained at 15 K are quite comparable to that observed in other SG systems like Nd_5Ge_3, $PrRhSn_3$, U_2PdSi_3 etc. in the SG domain [180-182], probably because the system is in the SG state at 15 K. However, for $T < 12$ K when transition to SL state begins, we notice significant deviation both in the magnitudes and trend followed by these curves. In SG systems, with increase in temperature, α

Table 3.2: List of the scaling laws and corresponding fitted parameters obtained from the thermoremanent magnetization measurements across T_{SL}.

Scaling Laws	Fitting parameters	T = 5 K	T = 6 K	T = 8 K	T = 9 K	T = 10 K	T = 12 K	T = 15 K
$M_{TRM} = M_0 - S\, Lnt$	M_0 (emu/mol)	2310	1871	1802	1962	2141	2283	5.8
	S (emu/mol)	46.4	43.8	32	25	19.3	12.3	0.3
$M_{TRM} = M_0\, t^{-\gamma}$	γ	0.0218	0.0259	0.0192	0.0134	0.0093	0.0055	0.0662
$M_{TRM} = M_0 \exp[-(\frac{t}{\tau})^{\alpha}]$	τ (s)	2.92×10^{8}	8.43×10^{7}	9.67×10^{8}	1.37×10^{10}	2.4×10^{11}	1.47×10^{13}	1.15×10^{5}
	α	0.152	0.154	0.148	0.146	0.143	0.14	0.177

increases (τ decreases) monotonically throughout the SG domain and also beyond T_{SG} [180,183,184]. Similar pattern is exhibited by the ZCFMO system above ~ 11.4 K, yet opposite trend is noticed below this temperature. According to the observations by Chu *et al.* the slope change in the exponent may occur at a slightly higher temperature than where the change from the weak to strong irreversibility in magnetization takes place [184].

The large magnitude of M_0 in the SL region is likely due to the presence of ferromagnetic clusters or uncompensated spins [168]. Usually, for systems with a uniform energy barrier, α = 1 indicates that the system has a single relaxation time constant, whereas α = 0 corresponds to the absence of relaxation. For systems having a distribution of energy barriers, α ranges between 0 and 1. The value of α acquired in our case suggests that the ZCFMO system evolves through several intermediate metastable states, hence the activation occurs against multiple anisotropic energy barriers [154]. Additionally, contrary to SG systems, where increase in the value of the exponent (α or γ) with temperature in the SG region reflects the increase of magnetic inter-cluster interaction, we witness weakening of interaction between the clusters with rise in temperature in the SL region [179]. Typically, in the SG ordered region, the magnetic viscosity S increases with T as a signature of the thermally activated process. However, in ZCFMO, decrease in S with T reveals that the properties in the SL region are not governed by thermal activation [185]. In support of the above results, the differentiation analysis $\partial S/\partial T$ *vs.* T (figure 3.20(b)) exhibits a sharp minimum across 9 K, as the ZCFMO system undergoes SL to SG magnetic phase transition.

3.4. Concluding Remarks:

In this section we provide some key conclusions drawn from the results presented in this chapter. In particular, the structural and magnetic properties of $Zn_{0.8}Cu_{0.2}FeMnO_4$ spinel reveals the stable complex cationic distribution: $(Zn_{0.8}^{2+}Cu_{0.2}^{2+})_A[Fe_{0.4}^{2+}Fe_{0.6}^{3+}Mn^{3+}]_BO_{4-\delta}$. Detailed analysis on the magnetic characterization yields the main inferences such as: (*i*) The fit of the χ *vs.* T data to the CW law: $\chi = C/(T - \theta)$ from T = 250 K to 400 K with $\theta \simeq$ 185 K and its deviations from the CW law for T < 250 K suggests the presence of ferromagnetically-coupled clusters of spins interacting antiferromagnetically, with the ferromagnetic exchange constant J/k_B = 17 K. (*ii*) The temperature variation of the ac susceptibilities show spin-glass transition whose position shifts to lower temperatures with the applied field H following the equation: $T_{SG}(H) = T_{SG}(0)[1 - AH^{2/\phi}]$ with $T_{SG}(0) = 46.6$ K, $A = 8.6 \times 10^{-3}$ Oe$^{-0.593}$ and $\phi = 3.37$. (*iii*) The analysis of the spin relaxation time τ obtained from the temperature and frequency dependence of ac magnetic susceptibilities in terms of the Power law and Vogel─Fulcher laws shows the presence of a cluster spin-glass state at T_{SG}. (*iv*) Measurements of the specific heat C_p *vs.* T from 2 K to 200 K in $H = 0$ and $H = 90$ kOe do not show any peak characteristic of long-range order. However, after correcting for the lattice contribution, a broad weak peak typical of short-range ordering centred at ~ 40 K becomes evident. (*v*) The presence of a weak peak in the χ'' *vs.* T data at $T_{SL} = 9$ K and C_p varying as T^2 for $T < T_{SL}$ is used to conclude the presence of a spin-liquid state for $T < T_{SL}$. (*vi*) Comparison of the neutron diffraction measurements at 1.7 K and 79.4 K shows the absence of long-range ordering but presence of short-range ordering at 1.7 K, confirming the above results of T_{SG} and T_{SL}. (*vii*) The thermoremanent magnetization studies reveal that, unlike the spin-glass ordered region, the magnetic inter-cluster interaction weakens for $T < 9$ K as the properties do not obey thermal activation process in the spin-liquid region. (*viii*) These results show that in Zn$_{0.8}$Cu$_{0.2}$FeMnO$_4$, ferromagnetic clusters interact antiferromagnetically producing a cluster spin-glass state at T_{SG} followed by spin-liquid behavior below 9 K but without long-range magnetic order. These interesting magnetic states observed here are a result of the magnetic frustration inherently present in the spinel structure when magnetic ions are located primarily on the octahedral *B* sites as in Zn$_{0.8}$Cu$_{0.2}$FeMnO$_4$.

Chapter 4

Cluster Spin-Glass State and Slow-Spin Dynamics of $Zn(Fe_{1-x}Ru_x)_2O_4$

This chapter discloses a completely different approach to acquire information on the magnetic frustration in spinel ferrites by minimizing the interaction energy among the *A* and *B* site magnetic moments. To achieve this, Jahn−Teller active elements of very less magnetic moment such as Cu^{2+} (in dilute amount) and Ru^{3+} are substituted in $ZnFe_2O_4$. The experimental part that follows the introductory background provide details of the crystal structure, heat capacity as well as magnetic measurements to decipher the short-range and long-range behavior in the $H-T$ plane.

4.1. Introductory Background:

Here, reports on the geometrically frustrated pyrochlore $ZnFe_2O_4$ is presented first along with its probable future aspects that constitutes the motivational background for this work. Spinel-ferrites are well-studied systems in the scientific literature because of their unique electrical and magnetic properties which largely depend upon the nature of substituents at the tetrahedral (*A*) or octahedral (*B*) sites [186,187]. Consequently, a wide variety of ferrite families have been investigated since decades both from a theoretical and an experimental point of view and their full potential towards the applications in the fields of microwave devices, circulators/actuators, semi-transparent magnetic semiconductor with high Curie temperature, and sensors is being explored [4,188-190]. Enormous research activity is still in progress on the low-dimensional nanostructures of these compounds, especially focusing on their catalytical activity and role in fuel-cells, Li-ion batteries and in the renewable energy sectors [191-196]. On the other hand, research work related to the tunable magnetic properties in Zn-ferrites by altering the relative strengths of the inter-sublattice interactions (J_{AB}) and intra-sublattice interactions (J_{AA} and J_{BB}) with the substitution of either magnetic or non-magnetic elements is also under intense activity in order to explore their unique magnetic properties in microwave magnets [2,197,198]. In almost all spinels, the above mentioned three main exchange interactions are essentially negative and one cannot rule out the competition between the exchange interactions (intra-sublattice and inter-sublattice), which often leads to 'magnetic-frustration (MF)' [2,199,200]. In the two-dimensional case, the corner sharing of triangles results in the Kagomé lattice which is prone to the MF phenomena [201,202]. Whereas, in three-dimensional case, the network of shared tetrahedral corners of the spinel lattice results in pyrochlore structures/Laves phases, while that formed by triangular corners give rise to the family of garnets, all of which exhibit fascinating magnetic phenomena [11,203-205].

Usually the MF phenomena arises when the sublattice magnetization is unable to minimize its total ground-state energy by decreasing the bond energy of individual spin-spin interactions separately [206]. The spin network made up of basic units of triangular or tetrahedral geometry are considered as archetypal examples of geometrically frustrated systems in which all the spins are antiferromagnetically coupled [207-209]. As a result of MF phenomena, one can expect: (*i*) strong suppression of the local magnetic moment and drastic reduction of long-range (LR) ordering, (*ii*) spin-ice/liquid/vortices like fluctuations at low-temperatures along with the (*iii*) emergence of macroscopic degeneracy in spin positioning [133,210]. As a consequence of the above phenomena and spin fluctuations remarkable magnetic properties including superconductivity has been observed in the recent past [35,211-213]. Moreover, geometrical frustration usually gives rise to some unique magnetic phenomena such as re-entrant spin-glass (SG) behavior and exchange bias driven by the disorderness which is induced by site specific substitution of non-magnetic elements [214-217].

The nature of magnetic ordering in franklinite, $ZnFe_2O_4$ (ZFO) based spinel ferrites have received substantial scientific attention because their crystal structure can be realized in the form of pyrochlore-like lattice [139,218]. Previous studies reveal that ZFO system exhibits antiferromagnetic (AFM) character with its Néel temperature, T_N ~ 10 K and a very large Curie−Weiss (CW) temperature, θ ~ 120 K, demonstrating the presence of strong MF with index of frustration, $f = |\theta|/T_N$ (~ 12) [137,138,218]. These experimental results support the earlier theoretical predictions of Anderson who proposed that the interacting *B* site cations are capable enough to create topological frustration in ZFO [133,219]. Such unusual intrinsic magnetic behavior is driven by the AFM 3rd nearest neighbor spatial spin correlations corresponding to the exchange interaction ($J_3 < 0$) along the path Fe-O-Fe-O-Fe and the ferromagnetic (FM) character corresponds to the exchange interaction J_1 (> 0) along the path Fe-O-Zn-O-Fe [137,139]. Such studies were extended by Tomiyasu and Kamazawa who proposed a spin dodecamer model on the Kagomé plane in which the MF effects can be lifted by means of dissimilar exchange paths where orbital mixing is selectively enhanced in the dodecamer [213]. It is also possible that AFM ordering can be pushed to higher temperatures by strengthening the inter-sublattice *A*−*B* superexchange interaction, via mechanical activation [134,135,220,221]. Few reports suggested that bulk ZFO exhibits SG like behavior with freezing temperatures close to 21 K and short-range (SR) AFM correlations across 100 K along with the LR ordering below T_N due to the formation of tiny spin-clusters exhibiting ‘superantiferromagnetism’ [135,222].

Furthermore, recent studies revealed the coexistence of ferrimagnetic (FiM) and AFM states in ZFO while maintaining the inversion parameter δ between 0.14 and 0.27 [223]. On the other hand, Murata *et al.* observed SG behavior in the superlattices of ZFO and $ZnCr_2O_4$, driven by very high spin frustration caused by the random exchange field because of the local symmetry breaking across the interface [208]. Moreover, Suzuki *et al.* reported large magneto-capacitance (~ 10% at 14 T) and magnetization coupled dielectric relaxation in polycrystalline ZFO [224]. These results are further supported by very recent observations on ferroelectric behavior linked to the rhombohedral distortion (*R*3*m* space group) from the cubic structure, across 110 K, along with the glassy AFM character and magnetic memory effects below T_N in addition to a weak exchange bias effect [141]. Nevertheless, the high field susceptibility data and neutron scattering measurements of single crystalline ZFO by Kamazawa *et al.* reported the absence of LR order and diffuse magnetic scattering around the nuclear Bragg peaks which disappear under the application of an external magnetic field of magnitude ~ 30 kOe [225-227]. The x-ray absorption near edge structure calculations (of Zn-K and Fe-K) and the first principles studies revealed cation disordering in ZFO with cation distribution

$[Zn_{1-u}^{2+}Fe_u^{3+}]_A[Zn_u^{2+}Fe_{2-u}^{3+}]_BO_4$ ($u \sim 0.6$), due to which a cluster SG-like behavior emerges associated with the disordering of Zn^{2+} and Fe^{3+} ions in the spinel lattice [136,228,229].

In the past few years, researchers tried to investigate the site-dilution effects in bulk ZFO by replacing Zn with other transition metals such as Co, Mn, Ni, and Cu. Both Mn and Co substituted systems display FiM properties across room temperature with a proportional increase in magnetization and coercivity with the level of Mn/Co substitution [230,231]. The Mn substituted ZFO exhibits weakly coupled AFM type J_{AB} at low temperatures along with notable effects of the Griffiths mixed phases below the percolation threshold (p_C). While, the Ni and Cu substitution in ZFO strengthens the spin-spin interactions, increases the magnetic ordering temperature. These systems also exhibit interesting magnetocaloric features with a relative cooling power close to 161 (37.78) J kg^{-1} and the associated maximum entropy change ~ 1.15 (0.77) J kg^{-1}K^{-1} for a field change of ~ 25−30 kOe for $Zn_{0.5}Ni_{0.5}Fe_2O_4$($Zn_{0.8}Cu_{0.2}Fe_2O_4$), useful for the magnetic refrigeration [232,233]. Most of the today's research activity in the field of ferrites is largely focused on the low dimensional nanostructures and limited studies are available on the detailed magnetic properties of *B* site Fe substitution by the non-magnetic ions in ZFO [234-236]. Despite numerous experimental and theoretical reports on bulk ZFO system, a detailed magnetization study focusing on the dilution of *B* sites occupied by Fe with Ru atoms has not been initiated in the literature which is the main aim of the current work. In the present study, we also focus on the competing role of the Jahn−Teller (*JT*) active cation Cu^{2+} and weakly magnetic Ru^{3+} ions on the global moment orderings of the ZFO system. Since the divalent Cu ions usually prefer to occupy the *B* sites, their incorporation in the ZFO matrix is thus, expected to alter the cationic distribution (from normal/inverse to mixed spinel) and hence lead to a weak tetragonal distortion which may collectively affect the AFM ordering of the ZFO system.

4.2. Pertinent Experimental Methods:

In the similar line as discussed in Chapter 3, this experimental section provide details of the synthesis procedure and techniques used for the characterization of the proposed systems. There are four important experimental parts in this work: (*i*) growth of the bulk samples using standard solid-state reaction method, (*ii*) electronic and crystal structure characterization, (*iii*) magnetic characterization, and (*iv*) low-temperature heat-capacity measurements. For the synthesis of different compositions (for various levels x and y) of polycrystalline bulk samples of $Zn_{1-y}Cu_y(Fe_{1-x}Ru_x)_2O_4$ (y = 0 and 0.2; x = 0.5, 0.75) we used high purity binary transition-metal oxides such as copper oxide (CuO), zinc oxide (ZnO), ferric oxide (Fe_2O_3) and ruthenium dioxide (RuO_2) as precursors. As an initial step, stoichiometric quantities of these oxides were mixed (ground) in an agate mortar with pestle for 4 h which were then made into 15 mm diameter cylindrical pellets using a hydraulic press followed by sintering at 1200 °C for 8 h in air with 4 h rising time and natural-cooling to room temperature. For crystal structure analysis and determination of the phase purity of the compounds, we used the x-ray diffractometer from Rigaku (Model: Smartlab) with Cu-Kα radiation (λ = 1.54184 Å). The corresponding x-ray diffraction (XRD) patterns and their analysis using Rietveld refinement are discussed in the next section. To understand the electronic structure and cationic distribution analysis we

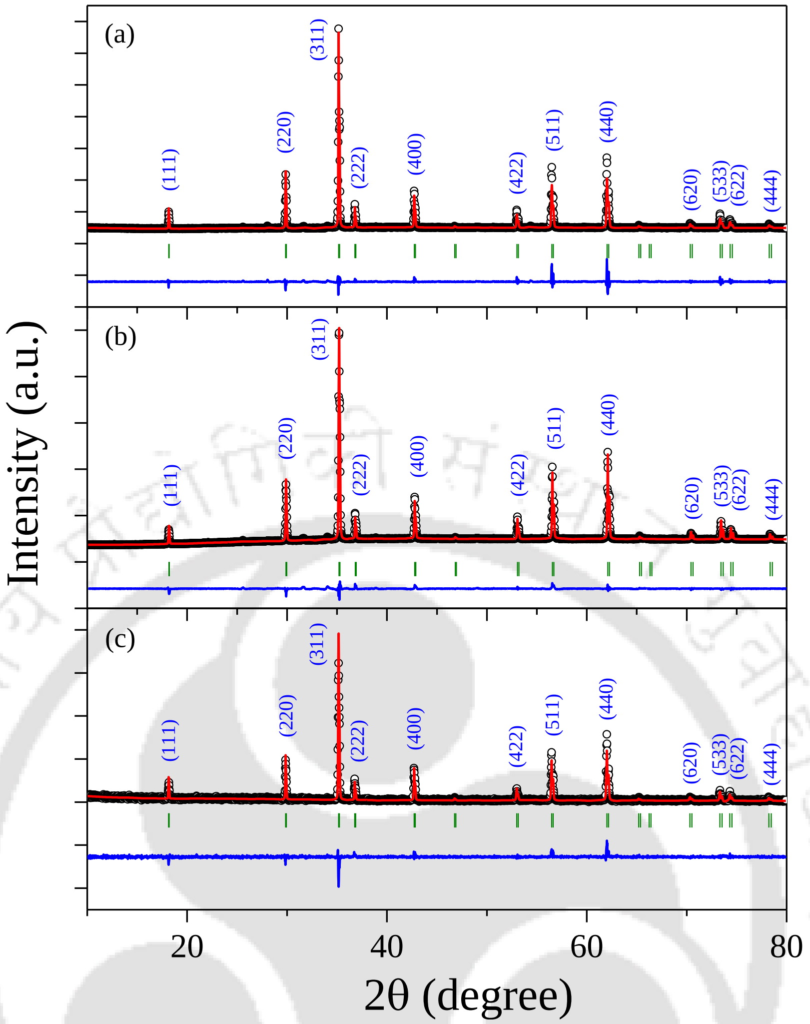

Figure 4.1: The Rietveld refinement patterns of the powder x-ray diffraction data for the compositions (a) ZFRO, (b) CZFRO, and (c) CZFR1.5O. The green marks indicate the Bragg positions, whereas blue lines are the difference between the observed virgin data points (black circles) and calculated ones (overlying red lines).

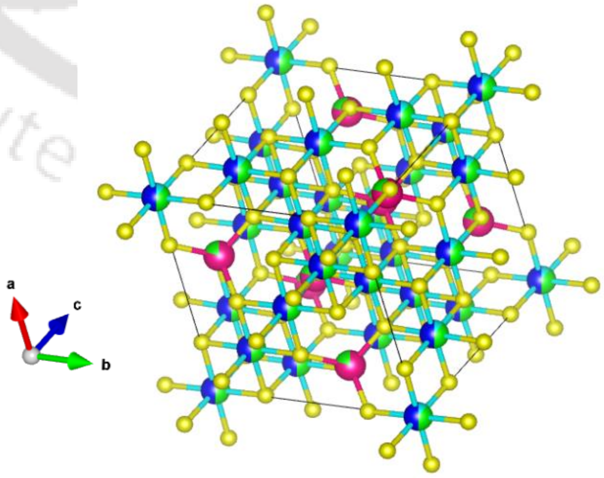

Figure 4.2: (a) Crystal structure of CZFRO. The tetrahedral (*A*) sites are occupied by divalent Zn and a fraction of trivalent Fe ions, while, Cu^{2+}, Ru^{3+} and a mixture of both divalent and trivalent Fe ions (Fe^{2+} and Fe^{3+}) occupy the octahedral (*B*) sites.

obtained x-ray photoelectron spectroscopy (XPS) measurements from Thermo Fisher Scientific 250Xi. Detailed frequency and temperature dependence of dynamical magnetization studies were carried out using a superconducting quantum interference device (SQUID) magnetometer, whereas for the dc magnetization measurements we employed a physical property measurement system (PPMS) from Quantum Design of Model: DynaCool. The temperature dependent specific heat $C_p(T)$ measurements were performed by means of a Quantum Design PPMS using the standard heat-pulse calorimetry in the presence of both H = 0 and 90 kOe from 4 K to 120 K [120]. Below we discuss the primary results obtained on the investigated systems which involve discussion on the XRD and XPS followed by the magnetic properties.

4.3. Experimental Results and Analysis:

4.3.1. Structural and Elemental Information:

The preliminary characterization data such as XRD pattern and XPS spectra confirms the monophasic nature of the synthesized compounds with significant changes in their lattice parameters, bond-angles and bond lengths. In particular, the three different compositions $ZnFeRuO_4$ (ZFRO), $Cu_{0.2}Zn_{0.8}FeRuO_4$ (CZFRO) and $Cu_{0.2}Zn_{0.8}Fe_{0.5}Ru_{1.5}O_4$ (CZFR1.5O) exhibit spinel cubic structure with lattice parameters a (= b = c) ~ 8.456 Å, 8.457 Å and 8.459 Å of $Fd{-}3m$ symmetry without any tetragonal distortion, respectively. All the relevant parameters obtained from the Rietveld refinement analysis of the XRD data (figure 4.1) carried out

Table 4.1: List of crystallographic parameters obtained by analyzing the XRD data with the help of Rietveld refinement and 3D visualization VESTA program analysis for the compositions ZFRO, CZFRO, and CZFR1.5O.

Composition →	ZFRO	CZFRO	CZFR1.5O
Crystal structure	Cubic	Cubic	Cubic
Space group	$Fd{-}3m$	$Fd{-}3m$	$Fd{-}3m$
Lattice constants (Å) $a = b = c$	8.456	8.457	8.459
Cell volume (Å^3)	604.64	604.852	605.281
Bond lengths A-O (Å) B-O (Å)	1.905 2.072	1.886 2.079	1.881 2.087
Bond angles B-O-B (°) A-O-B (°)	92.34 123.59	91.82 123.97	91.55 124.16
Formula weight	286.291	285.924	308.537
2θ range	10-80°	10-80°	10-80°
R_p	64%	77.6%	54.7%
R_{wp}	49.4%	54.2%	42.7%
R_{exp}	30.91%	32.73%	29.34%
R_{Bragg}	19.96%	23.67%	14.63%
R_F-factor	17.53%	29.13%	10.62%
χ^2	2.57	2.83	2.12
Cation distribution	$(Zn)_A$ $[Fe_{1.0}\,Ru_{1.0}]_BO_4$	$(Zn_{0.8}\,Fe_{0.2})_A$ $[Cu_{0.2}\,Fe_{0.8}\,Ru_{1.0}]_BO_4$	$(Zn_{0.8}\,Fe_{0.2})_A$ $[Cu_{0.2}\,Fe_{0.3}\,Ru_{1.5}]_BO_4$

using the *FullProf* Suite software are listed in table 4.1. In the present case the Wyckoff positions assigned to the *A* and *B* sites in these mixed spinels are 8*b*(0.375, 0.375, 0.375) and 16*c*(0, 0, 0), respectively, whereas, the Wyckoff positions of the oxygen atoms are at 32*e*(0.245, 0.245, 0.245), 32*e*(0.246, 0.246, 0.246) and 32*e*(0.247, 0.247, 0.247), respectively, for the compositions ZFRO, CZFRO and CZFR1.5O. The corresponding cationic distributions are given in table 4.1, moreover, a detailed site distribution of all the ions are analyzed meticulously below and deduced using the temperature and field dependent magnetization data. On the other hand, a significant shrinkage in the *A*-O bond length (1.881 Å) is noticed in comparison to the marginal increase of the *B*-O bond length (to 2.087 Å). Similar trend has been noticed in case of the *B*-O-*B* bond angle (92.34 ° → 91.55 °) as compared to the changes noticed in *A*-O-*B* bond angle (124.16 °). Such alterations in the crystal structure (figure 4.2, generated from the XRD data applied to the 3D visualization program VESTA) are associated with the different ionic radii of the Cu and Ru substituents as compared to the cations of the pristine compound [237].

To probe the electronic structure and for a detailed elemental analysis we performed the XPS measurements, the results of which are presented below. Figure 4.3 shows the XPS spectra plotted as a function of binding energy (BE in eV) for all the individual elements present in CZFRO. In this case the adventitious carbon, *C*-1*s* peak at 284.8 eV has been used as a charge reference to standardize the individual core level spectra of all the ions viz: Cu-2*p*, Zn-2*p*, Fe-2*p*, O-1*s* and Ru-3*d*. The 2*p* (3/2 and 1/2) character

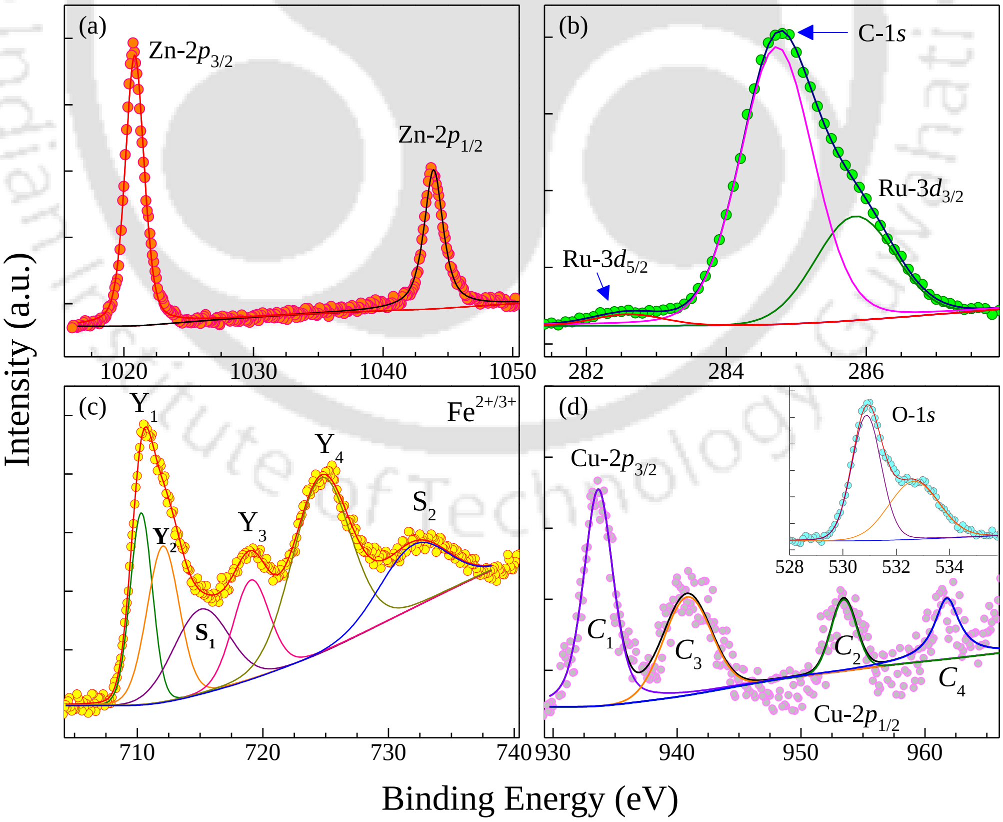

Figure 4.3: X-ray photoelectron spectra of bulk CZFRO pellets sintered at 1200 °C for 8 h in air. The main panels of (a), (c), and (d) shows the 2*p* core level spectra of Zn, Fe, and Cu, respectively, whereas (b) shows the XPS spectra for both Ru-3*d* and C-1*s*. The inset in figure (d) represents the XPS spectra of O-1*s*.

located across 1020.8 eV and 1043.9 eV, devoid of any weak intensity satellite peaks, while the energy of Zn core level spectrum is clearly evident from figure 4.3(a) which shows two sharp symmetrical cusps difference (ΔZn-2$p_{1/2-3/2}$) between these two cusps is ~ 23.1 eV which proves the divalent character of Zn [2,146]. The core level XPS spectra of Ru-3*d* and C-1*s* are closely spaced (figure 4.3(b)), yet the Ru-3*d* spectra are well resolved into two weak intensity humps across 282.6 eV and 285.85 eV which corresponds to the trivalent character of Ru associated with the 3$d_{5/2}$ and 3$d_{3/2}$, respectively [238]. On the other hand, the Fe-2*p* XPS core level spectrum depicted in figure 4.3(c) comprises of a minimum of four main peaks which are deconvoluted into a total of six number of peaks located at 710.7 eV (Y_1), 712.1 eV (Y_2), 719.15 eV (Y_3), 724.85 eV (Y_4), 715.24 eV (S_1) and 732.6 eV (S_2) out of which S_1 and S_2 are the satellite peaks corresponding to the shoulders noticed across the maximum intensity peaks of lower BEs. The cusp located across Y_1 is associated to the 2$p_{3/2}$ core level of divalent Fe, while the cusp centred at Y_2 is assigned to the trivalent Fe [148,149]. For these transitions, the spin-orbit splitting energy $\Delta(Y_3 - Y_1)$ ~ 8.45 eV and $\Delta(Y_4 - Y_2)$ ~ 12.75 eV further confirms the mixed valent character of Fe present in the CZFRO system. In case of Cu the intensity of XPS spectra is rather weak because of their dilute substitution in the spinel lattice. Nevertheless, in the present case the Cu-2*p* core level spectrum has been deconvoluted into four peaks: C_1, C_2, C_3 and C_4, in which the main peaks C_1 and C_2 are centred at 933.65 eV and 953.44 eV, respectively, and the other two are satellite peaks at C_3 ~ 940.84 eV and C_4 ~ 961.8 eV (figure 4.3(d)). The spin-orbit splitting energy (ΔC) observed between the two main peaks is about 19.79 eV confirms the divalent electronic state of Cu, which is further supported by the presence of broad satellite peak across 940.84 eV [151]. Alongside, the inset in figure 4.3(d) possesses a main sharp peak across 530.9 eV featuring the O-1*s* spectra of CZFRO.

4.3.2. Temperature Dependence of DC Magnetization:

To determine the magnetic structure of the synthesized compounds we performed both dc magnetization (M) measurements under different magnetic fields (H), at various temperatures, along with a detailed frequency (f) and temperature (T) dependence of the ac magnetic susceptibility $\chi_{ac}(f, T)$. Figure 4.4 illustrates the thermal variation of the dc magnetic susceptibility ($\chi = M/H$) measured under both zero-field-cooled (ZFC, blue symbols) and field-cooled (FC, red symbols) conditions from T = 1.9 K to 300 K in the presence of a constant H. The $\chi(T)$ variation is shown on the left-hand-side (LHS) scale of figure 4.4 where the corresponding data has been recorded under warming conditions. One can clearly notice the bifurcation in χ data between the ZFC and FC below the peak temperature representing the FiM character of the three systems due to the different magnetic moments of cations located at *A* and *B* sites of the spinel lattice. The magnitude of bifurcation is higher in case of CZFRO than that in the other compositions signifying the additional role of magnetocrystalline anisotropy, in-line with the previous reports, particularly on Cu-based ferrite systems exhibiting FiM ordering at low-temperatures [2,239]. On the right-hand-side (RHS) scale of figure 4.4, we have shown the temperature dependent behavior of effective magnetic moment ($\mu_{eff}(T)$) calculated from the Curie-law: $(\mu_{eff}/\mu_B)^2 = 3k_B\chi T/N_A\mu_B^2$, in which $\mu_{eff}(T)$ shows a sharp change in the slope across the peak temperature T_{FiM} which has been determined from the differential magnetic susceptibility data discussed

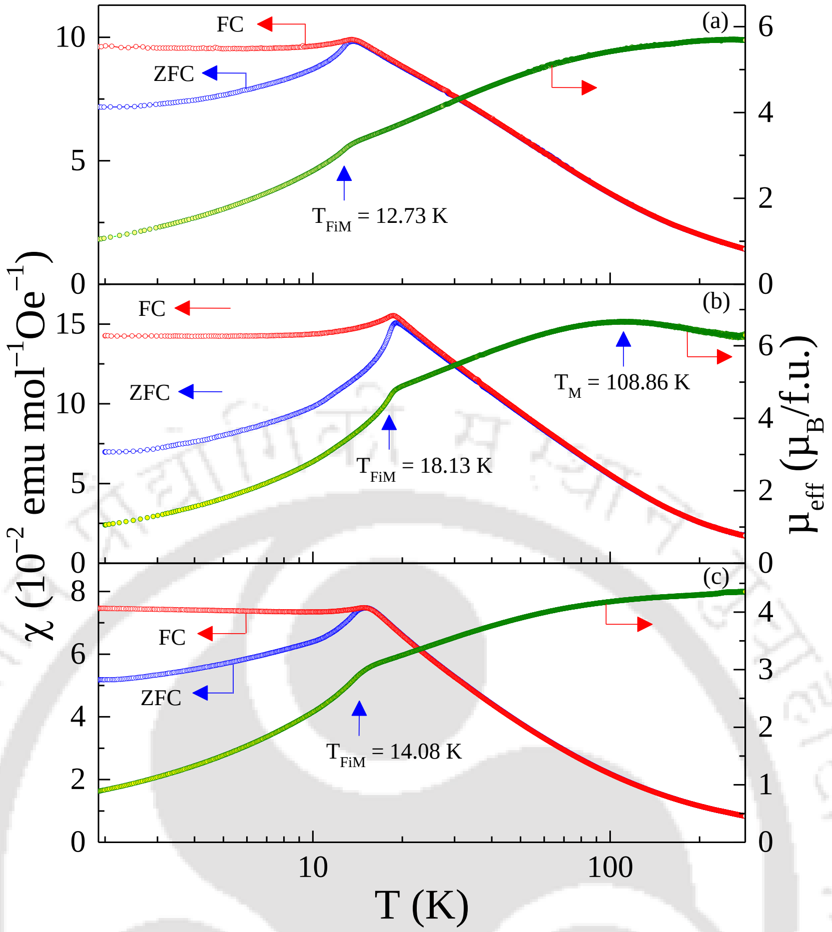

Figure 4.4: The low-temperature (1.9−300 K) dc magnetic susceptibility (χ) data obtained under H = 500 Oe for both zero-field-cooled (blue symbols) and field cooled (red symbols) modes are shown on the LHS for (a) ZFRO, (b) CZFRO, and (c) CZFR1.5O. The temperature variation of effective magnetic moments (μ_{eff}) are shown on the corresponding RHS.

below [240]. Moreover, it is interesting to notice an additional cusp-like feature in $\mu_{\mathrm{eff}}(T)$, labelled by T_{M}, in case of CZFRO across 108.86 K (nearly six times higher than T_{FiM}) due to the additional change in magnetic ordering owing to the intrasublattice exchange coupling among the B site cations which is mostly FM in nature, similar to that observed in other highly frustrated spinels such as $GeCo_2O_4$, where $\mu_{\mathrm{eff}}(T)$ shows a cusp like transition across five times of its AFM ordering temperature [240]. Moreover, $\mu_{\mathrm{eff}}(T)$ behavior noticed in the present system is in line with the previous studies on Co substituted ZFO systems which exhibits AFM ordering across 110 K followed by SR correlations in the range 110 K $\leq T \leq$ 260 K, nonetheless, the low-temperature region (below AFM region) is dominated by cluster SG like features [86,241]. Interestingly, Schiessl *et al*. reported SR AFM correlations at higher temperatures (nearly ten times above the T_{N}) in the parent ZFO bulk system which is attributed to the development of small magnetic clusters leading to a peculiar feature called ‘superantiferromagnetism’ [135].

For an accurate determination of ordering temperature, we have evaluated the differential ZFC magnetic susceptibility $\partial(\chi T)/\partial T$ and plotted the same as a function of temperature for all the three systems as shown in figure 4.3. This analysis provides a mathematical basis of relating the transition temperature obtained from

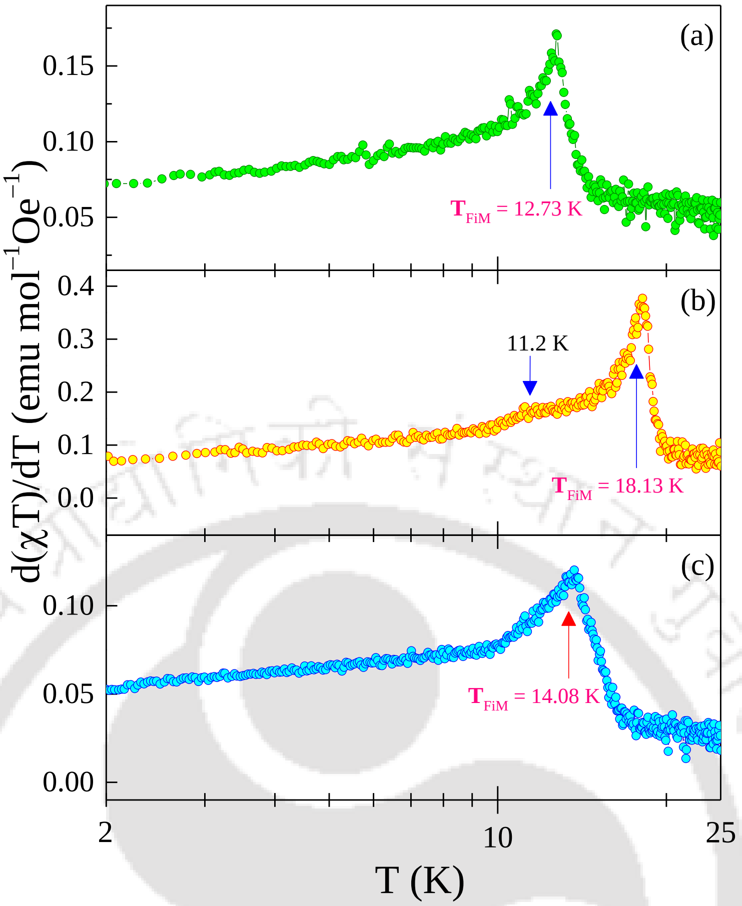

Figure 4.5: The plots of first order temperature derivatives of χT versus T of ZFRO, CZFRO, and CZFR1.5O samples attained in the presence of external magnetic field H = 500 Oe are illustrated in the panels (a), (b), and (c), respectively.

the magnetization measurements with the heat-capacity data following the relation ($C \simeq A\partial(\chi T)/\partial T$) reported by Fischer's reference [160]. Accordingly, we obtained the peak temperatures which are the FiM Néel temperatures (T_{FiM}) ~ 12.73 K, 18.13 K, and 14.08 K for the compositions ZFRO, CZFRO and CZFR1.5O, respectively (measured for H = 500 Oe under ZFC conditions). An additional weak hump noticed below T_{FiM} at ~ 11.2 K in figure 4.5(b) may be originating due to the progressive freezing of spin clusters in locally ordered states similar to the systems which exhibit Gabay−Toulouse type mixed phases [7,85,242-244]. Usually, such transitions are not so prominent under low-fields ($H \leq 1$ kOe) [158,168]. Since these magnitudes are sensitive to the strength of external applied field, such field (H) variation by virtue of both temperature and frequency dependent analysis of ac (and dc) magnetic susceptibility are discussed below in a detailed way.

4.3.3. Spin-Glass State:

Thus, in order to get more accurate insight into the dispersive nature of the transition and SR ordering, we performed a detailed temperature and frequency dependence of ac magnetic susceptibility $\chi_{\mathrm{ac}}(f, T)$ study for the two compositions. These measurements are performed using the SQUID magnetometer from 5 K to 76 K at several frequencies between 0.17 Hz and 1202 Hz with an ac peak-to-peak amplitude h_{ac} ~ 4 Oe,

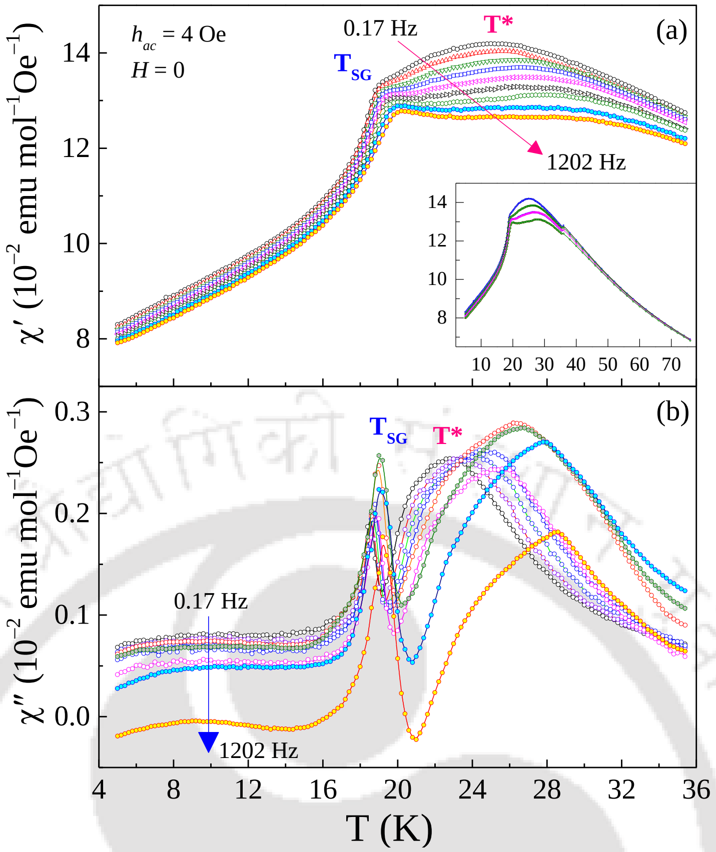

Figure 4.6: (a) Real and (b) imaginary components of the ac magnetic susceptibility (χ_{ac}) of CZFRO measured under warming conditions using an applied ac field (h_{ac}) of amplitude 4 Oe with H = 0 Oe, for several frequencies between 0.17 Hz and 1202 Hz. The inset in (a) shows the χ' versus T data up to 76 K.

along with and without the superimposition of H. Figures 4.6 and 4.7 shows the temperature variation of the in-phase ($\chi'(T)$) and out-of-phase ($\chi''(T)$) components of χ_{ac} for different magnitudes of f. The main panels of these figures contain data within the interval 5 K ≤ T ≤ 35 K and 5 K ≤ T ≤ 30 K for CZFRO and CZFR1.5O, respectively, whereas the inset of figure 4.6(a) shows the full temperature scale exhibiting a complete broad cusp revealing no further transition beyond ~ 30 K. The frequency dispersion across the main transition temperature (low temperature peak) in both the compositions is quite clearly evident from both $\chi'(T)$ and $\chi''(T)$ and shows the signatures of SG like features. The frequency dispersion is observed at temperatures very close to T_{FiM}, yet, the T_{FiM} may or may not exhibit SG-like features every so often, and the separation between the SG ordering temperature (T_{SG}) and T_{FiM} becomes noticeable only under higher applied fields (discussed in figure 4.11) [158,168]. Hence the low temperature peak noticed in both figures 4.6 and 4.7 are represented by T_{SG} with its H dependence, which is distinctly different from T_{FiM}, is discussed later in figure 4.11. The insets of figure 4.7 display the zoomed views of the ac data clearly showing the peak shift (of T_{SG}) towards the higher temperature side with increasing frequency. It is interesting to notice a second local maximum T* in $\chi''(T)$ above T_{SG} in CZFRO, on the contrary, the second composition CZFR1.5O does not exhibit T*. To unveil the SG like SR characteristics, present in the investigated systems, we employed the

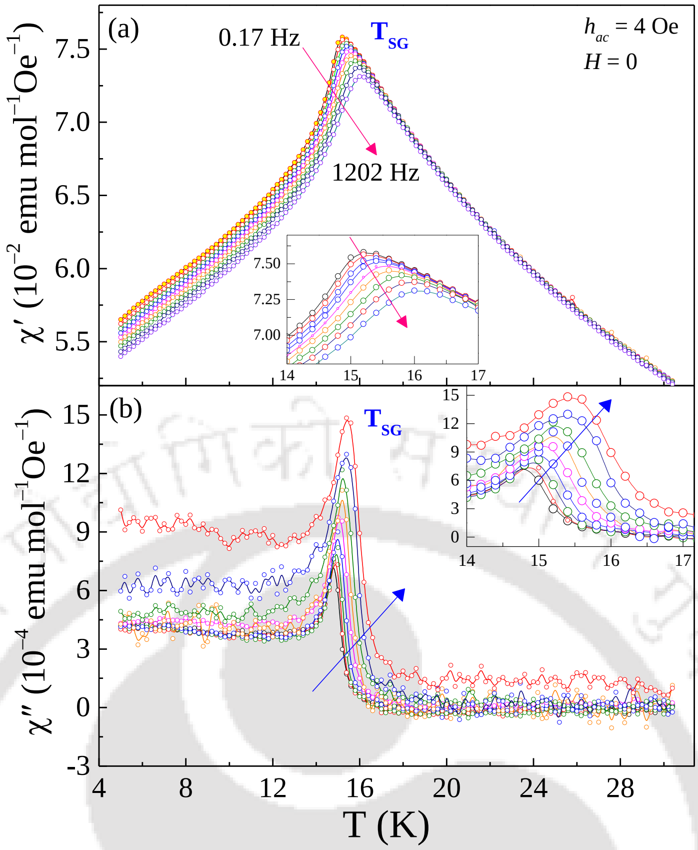

Figure 4.7: Temperature variations of (a) real and (b) imaginary components of the ac magnetic susceptibility χ_{ac} of CZFR1.5O recorded under h_{ac} = 4 Oe and without applying H, for several frequencies between 0.17 Hz and 1202 Hz. The zoomed images of the main panel data across the peak temperatures are shown in the respective insets of both (a) and (b).

analysis pertaining to two standard empirical scaling laws known as: the Vogel−Fulcher law (VFL) given by the equation (4.1) and the power law (PL) given by the equation (4.2), as listed below [154].

$$\tau = \tau_0 \, exp[E_a/k_B(T - T_0)] \tag{4.1}$$

$$\tau = \tau_0 \, [(T - T_{SG})/T_{SG}]^{-z\nu} \tag{4.2}$$

In the above equations, $\tau = 1/2\pi f$ is the relaxation time whose temperature dependence is usually determined from the peak position of the $\chi''(T)$ data at different f, τ_0 is associated with the relaxation of individual cluster magnetic moments, T_0 represents the strength of inter-cluster interactions, E_a is the activation energy and $z\nu$ is a dynamical critical exponent with values usually lying between 4 and 12 for SG systems [181]. Both the above equations contain three parameters each: τ_0, E_a and T_0 in equation (4.1) and τ_0, T_{SG} and $z\nu$ in equation (4.2). Figure 4.8 shows the logarithmic variations of the relaxation time $Ln\ \tau$ versus (a) $1/(T - T_0)$ and (b) $Ln\ [(T - T_{SG})/T_{SG}]$ corresponding to the equations (4.1) and (4.2) of the VFL and PL, respectively. For this purpose, the peaks in the real and imaginary components of χ_{ac} values of both CZFRO (two peaks) and CZFR1.5O (one peak) are considered. The solid lines shown in red color are the least square fits of the

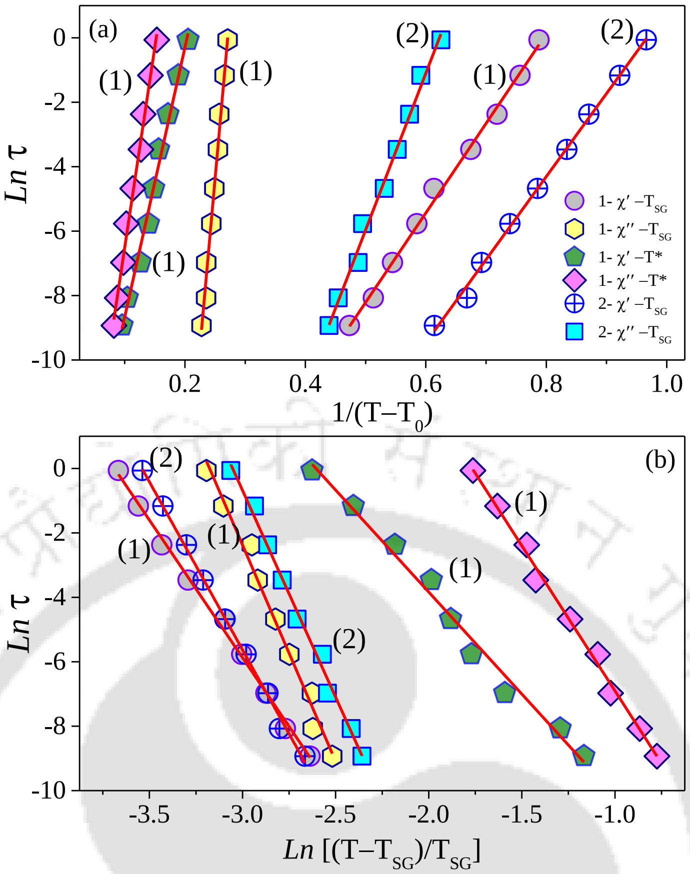

Figure 4.8: Logarithmic variations of the relaxation time *Ln* (τ) versus (a) 1/($T - T_0$) and (b) *Ln* (($T - T_{SG}$)/T_{SG}) based on the Vogel−Fulcher law and Power law, respectively. For this purpose, the peaks in the real and imaginary χ_{ac} values of both CZFRO (two peaks) and CZFR1.5O (one peak) are taken under consideration. The solid red lines are least square linear fits of the experimental data points (represented by scattered symbols).

Table 4.2: Parameters obtained by fitting the empirical scaling laws: equations (4.1) and (4.2), to the χ_{ac} (T) *vs.* T data of both CZFRO and CZFR1.5O.

Composition →		CZFRO	CZFRO	CZFRO	CZFRO	CZFR1.5O	CZFR1.5O
Scaling Laws	Fitting parameters	$\chi' - T_{SG}$	$\chi'' - T_{SG}$	$\chi' - T^*$	$\chi'' - T^*$	$\chi' - T_{SG}$	$\chi'' - T_{SG}$
Vogel−Fulcher Law	T_0 (K)	17.48	16.93	22.21	19.89	13.72	13.65
	τ_0 (s)	2.01×10^{-9}	6.73×10^{-10}	1.09×10^{-4}	1.35×10^{-4}	7.28×10^{-12}	2.88×10^{-8}
	E_a (meV)	2.26	2.89	2.24	2.37	2.89	1.67
Power Law	T_{SG} (K)	18.1	17.77	22.43	20.03	14.67	14
	τ_0 (s)	1.45×10^{-12}	2.5×10^{-12}	1.44×10^{-8}	5.22×10^{-7}	9.36×10^{-12}	2.48×10^{-11}
	$z\nu$	8.34	8.43	8.43	7.56	6.84	8.41
$z\nu$ values from: $Ln\left(\frac{40k_BT_0}{E_a}\right)\sim\frac{25}{z\nu}$		7.62	8.32	7.08	7.44	8.94	7.49

experimental data points represented by the hollow symbols. Both the scaling laws resulted in a straight line behavior with different fitting parameters as listed in table 4.2. The following fitting parameters are evaluated from PL for CZFRO (CZFR1.5O): $\tau_0 = 1.45 \times 10^{-12}$ s (9.36×10^{-12} s), T_{SG} = 18.1 K (14.67 K) and $z\nu$ = 8.34 (6.84), using the frequency variation of $\chi'(T)$ for T_{SG} (similarly using $\chi''(T)$ we obtained $\tau_0 = 2.5 \times 10^{-12}$ s (2.48×10^{-11} s), T_{SG} = 17.77 K (14 K) and $z\nu$ = 8.43 (8.41) for CZFRO (CZFR1.5O)). On the other hand, the mathematical fits corresponding to VFL for CZFRO (CZFR1.5O) yield the following parameters: E_a = 2.26 meV (2.89 meV), T_0 = 17.48 K (13.72 K) corresponding to $\chi'(T)$-T_{SG} and E_a = 2.89 meV (1.67 meV), T_0 = 16.93 K (13.65 K) corresponding to $\chi''(T)$-T_{SG}. By means of the fitting parameters acquired from VFL and the relation between VFL and PL: $Ln\left(\frac{40k_BT_0}{E_a}\right) \sim \frac{25}{z\nu}$, we have reevaluated the magnitudes of $z\nu$ which are in excellent agreement with that determined from PL (table 4.2) [154]. The τ_0 and $z\nu$ values in case of both CZFRO and CZFR1.5O lies well within the range valid for the cluster SG systems [7,78,154,158,180,245-248]. Yet, the confirmation of cluster SG state is relied more on the basis of the magnitudes of Mydosh parameter (Ω) which is calculated using the below relation [147,158,168]:

$$\Omega = \frac{T_{f2} - T_{f1}}{T_{f1}(\log f_2 - \log f_1)} \tag{4.3}$$

Here $T_{f\,2}$ and $T_{f\,1}$ are the temperatures corresponding to the peak values in χ'' for f_2 (highest measured frequency) and f_1 (lowest measured frequency), respectively. For both the systems, CZFRO and CZFR1.5O, we obtained Ω = 0.009 and 0.0119, respectively across T_{SG}, however, considerably higher value (Ω ~ 0.0579) is obtained in case of T^*. Usually low-dimensional magnetic nanostructures exhibit significantly higher Ω values between 0.05 and 0.13 which progressively increases with ceasing of inter-particle interaction [249,250]. The scale of Ω for typical cluster SG transitions is usually of magnitude comparable to or smaller

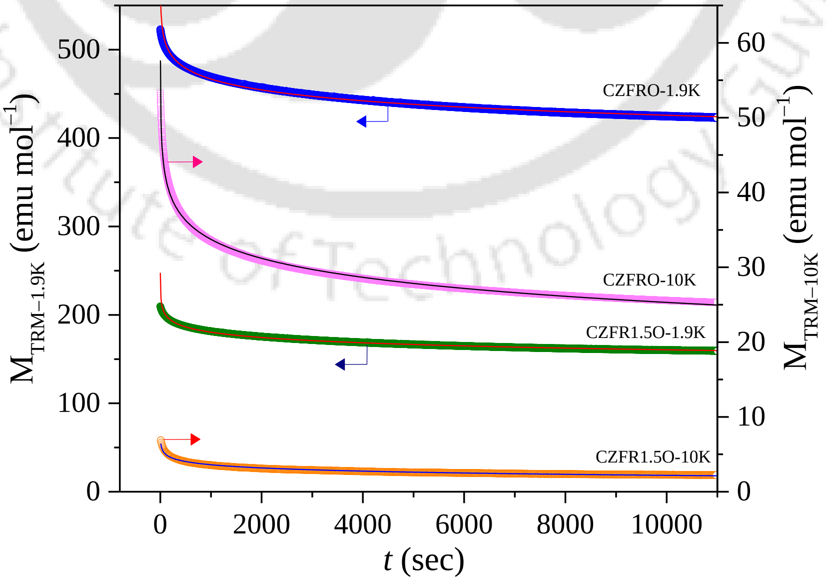

Figure 4.9: Time dependence of the thermoremanent magnetization (M_{TRM}) for both CZFRO and CZFR1.5O. LHS and RHS indicates the data points obtained immediately after switching off the cooling magnetic field of 90 kOe, at T = 1.9 K and 10 K, respectively. The solid lines are fits of the equation $M_{TRM}(t) = M_{TRM}(0) - S\ Ln\ t$ with the data points measured over 11000 seconds.

than 0.01 [250,251]. In case of canonical SG systems, the Mydosh parameter Ω is mostly one order less, for instance $\Omega = 0.0045-0.005$ for AuMn and CuMn systems [118,153]. Although, higher order (0.28) values are noticed in case of noninteracting superparamagnets [118].

Thus, in this work, the results obtained above collectively supports the prevalence of SR-ordered cluster SG state in both the systems below T_{SG} [154,155,252,253]. While, the broad cusp across T^* is rather related to the SR spin correlations as described below. Nonetheless, the frequency dispersion noticed in the imaginary component (figure 4.6(b)) of CZFRO system contains another broad hump in the lower temperature region ($T \sim 9.5$ K), which is not very prominent except at high frequencies. Also, the frequency variation of this peak position does not follow any specific (increasing or decreasing) trend, leading to negative value of Ω, which has no physical basis. It may be argued that this hump appears as a result of relaxation of the spins that are decoupled from the main clusters due to the increase of dilution of magnetic ions on the *B* sites [158].

The two peak (T_{SG} and T^*) behavior noticed in figure 4.6 is rare in the literature and is considered as an important finding of this study. T^* is related to the formation of slowly fluctuating spin clusters coexisting within the fast fluctuating paramagnetic (PM) region. As a result, SR ordering persists above T_{SG} (up to T_M, in consonance with the $\mu_{eff}(T)$ *vs.* T analysis discussed above) in the CZFRO [254]. Similar results are reported in multiferroic $Ba_3NbFe_3Si_2O_{14}$, perovskite systems such as $SrRuO_3$ and $Pr_{0.9}Ca_{0.1}MnO_3$, and nanoparticulated solid solutions of $(La_{0.7}Sr_{0.3}MnO_3)_{1-x}(BaTiO_3)_x$ [255-258]. Nevertheless, Baker *et al.* reported bidirectional frequency dependence in $\chi'(T)$ plots of layered-triangular-magnet $NaNiO_2$ and also similar type of results are reported by Pakhira *et al.* on a hexagonal intermetallic compound $Pr_2Ni_{0.95}Si_{2.95}$, in which the exchange interaction among the ions is dominated by the Ruderman−Kittel−Kasuya−Yosida-type interactions [254,259].

Further evidence for the existence of SG character is confirmed from the time (t) dependence of its magnetization measured well below the T_{SG}: at 1.9 K and 10 K, after cooling both the samples from room temperature in the presence of high magnetic field ($H \sim 90$ kOe). After the temperature became stable at set point, field was switched off and the magnetization was measured immediately as a function of time $M(t)$ up to ~ 3 h. To obtain data for the next temperature, the sample was warmed to 300 K and cooled back to the subsequent set temperature (10 K) under 90 kOe field and the data acquisition was repeated in the similar way. Figure 4.9 shows the time dependence of the thermoremanent magnetization, $M_{TRM}(t)$ for both the systems CZFRO and CZFR1.5O recorded at 1.9 K and 10 K. The solid lines are fits of experimental data points with the equation $M_{TRM}(t) = M_{TRM}(0) - S\,Lnt$, where S is the magnetic viscosity; in the present case it is determined from the fits and/or slope and $M(0)$ is the Y−intercept (figure 4.9). For both the systems CZFRO and CZFR1.5O at 1.9 K, the magnitudes of the fitting parameters are as follows: $S = 17.77$ emu mol^{-1} and 8.65 emu mol^{-1}, and $M(0) = 590$ emu mol^{-1} and 240 emu mol^{-1}, respectively. These magnitudes decrease monotonically with increase in temperature (at 10 K, $S = 3.66$ emu mol^{-1} and 0.62 emu mol^{-1}, and $M(0) =$ 59 emu mol^{-1} and 7.9 emu mol^{-1} for CZFRO and CZFR1.5O, respectively) and finally become negligible on approaching T_{FiM}. The large value of $M(0)$ at low temperatures specifies existence of spin-clusters [168,181].

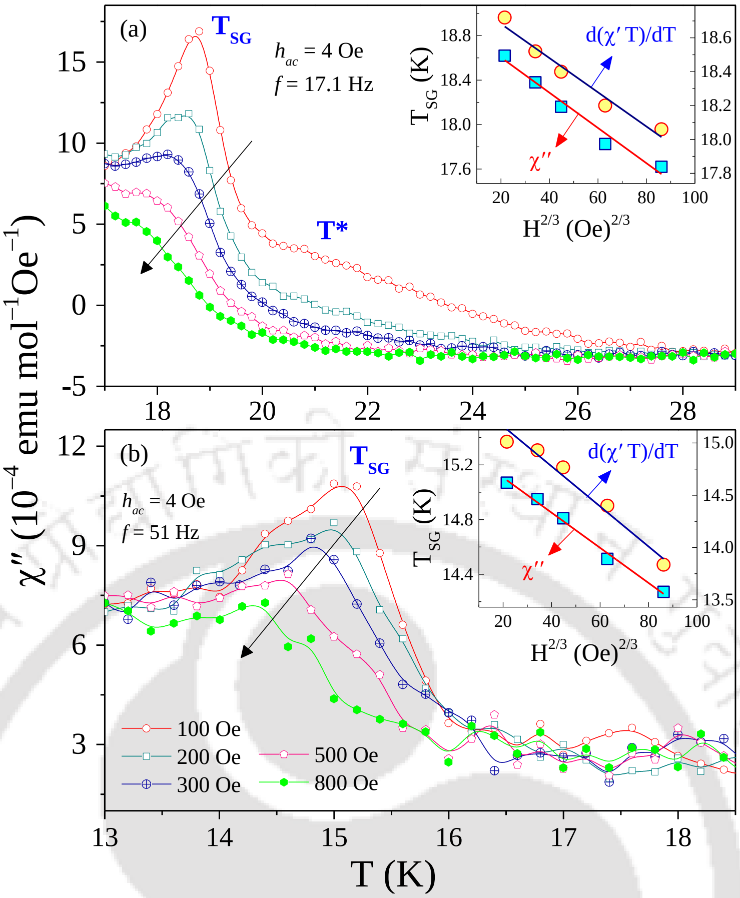

Figure 4.10: Temperature dependence of $\chi''(T)$ for the compositions (a) CZFRO and (b) CZFR1.5O measured at 17.1 Hz and 51 Hz frequencies, respectively, and h_{ac} = 4 Oe with superimposed dc bias fields ($100 \leq H \leq 800$ Oe). Insets show the AT-line (T_{SG} *vs.* $H^{2/3}$) linear fits of the experimentally obtained data points from the cusps in $\chi''(T)$ and $\partial(\chi'T)/\partial T$ on the LHS and RHS, respectively.

4.3.4. Field Dependence of AC Susceptibility and DC Magnetization:

In order to gain more insight on the glassy characteristics of the current system we performed the additional ac measurements in the presence of external dc magnetic field. Figures 4.10(a) and 4.10(b) shows the $\chi''(T)$ of CZFRO (and CZFR1.5O) system recorded at a constant driving frequency of 17.1 Hz (and 51 Hz) with peak-to-peak amplitude h_{ac} ~ 4 Oe by superimposing different dc bias-fields ($100 \leq H \leq 800$ Oe). For both the samples, the out-of-phase susceptibility curves exhibit cusp like behavior in which the peak maximum (T_{SG}) shift significantly towards low temperature side with increase in the magnitude of H. Additionally, in the case of CZFRO, the cusp across T^* (indicated in figure 4.6) is suppressed with increasing H suggesting that the slowly fluctuating FiM clusters lose their significance in the PM regime at higher applied dc magnetic fields. Such variation across T_{SG} is interpreted on the basis of non-mean field approach $T_{SG}(H) = T_{SG}(0)[1 - AH^{2/\phi}]$ commonly known as de Almeida−Thouless, AT−line analysis $\left(\text{or } H(T_{SG}) = A\left(1 - \frac{T_{SG}(H)}{T_{SG}(0)}\right)^{\phi}\right)$, where ϕ = 3 corresponds to the ideal case [260,261]. Accordingly, the variations of T_{SG} obtained from the cusps in both $\chi''(T)$ and $\partial(\chi'T)/\partial T$ are plotted as a function of $H^{2/3}$ on the LHS and RHS,

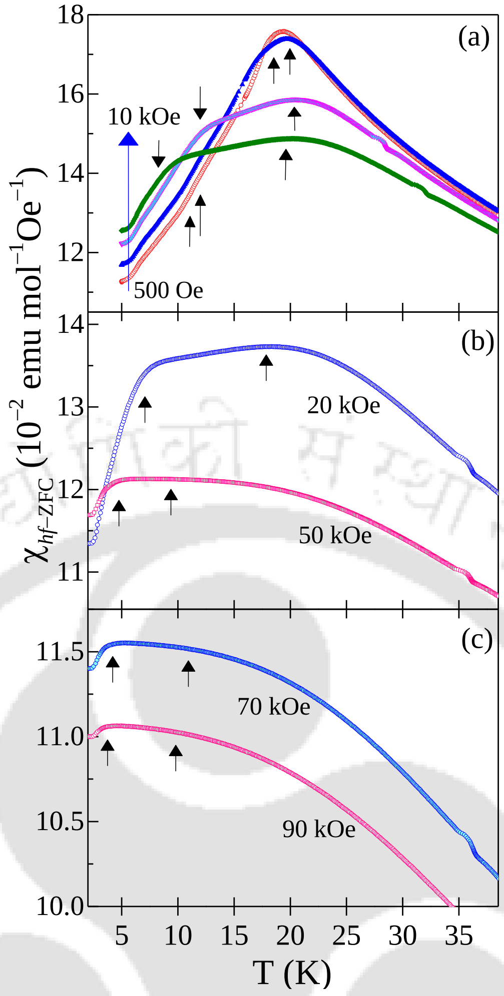

Figure 4.11: Temperature dependence of the dc susceptibility χ for the composition CZFRO measured at several constant H values between 500 Oe and 90 kOe under zero field cooling conditions. The small arrows mark the two peak positions corresponding to a higher and a lower temperature magnetic ordering transitions.

respectively, of the insets in figure 4.10 (scattered symbols) along with their corresponding mathematical least square fits, supporting the non-mean field approach of SR spin correlations, which slightly departs for the case obtained from $\partial(\chi' T)/\partial T$ in consonance with the literature reports [168]. Such AT-analysis has been frequently employed in the literature to explain the SG like disordered state in variety of compounds, and this criterion is often used to study the characteristic features of SG ordering, including the magnetic nanoparticles [262-264]. On the other hand, the temperature dependence of high field (2 kOe $\leq H \leq$ 20 kOe) dc susceptibility $\chi_{\mathrm{hf}}(T)$ analysis provides evidence for the Gabay−Toulouse type mixed-phase (i.e. coexistence of the SG and FiM behavior) present in the investigated system. Figure 4.11 shows the $\chi_{\mathrm{hf-ZFC}}(T)$ plots which clearly shows that the two-peak behavior visibly distinguishing between the FiM ordering temperature T_{FiM} and SG state T_{SG}, in which both the order parameters shift towards lower temperature side with rise in H. Both the order parameters are obtained from the differential susceptibility plots, i.e. $\partial(\chi_{\mathrm{hf-ZFC}} T)/\partial T$ versus T plots associated with the Fisher's relation discussed above and these parameters are further utilized in establishing the $H-T$ phase diagram (discussed below).

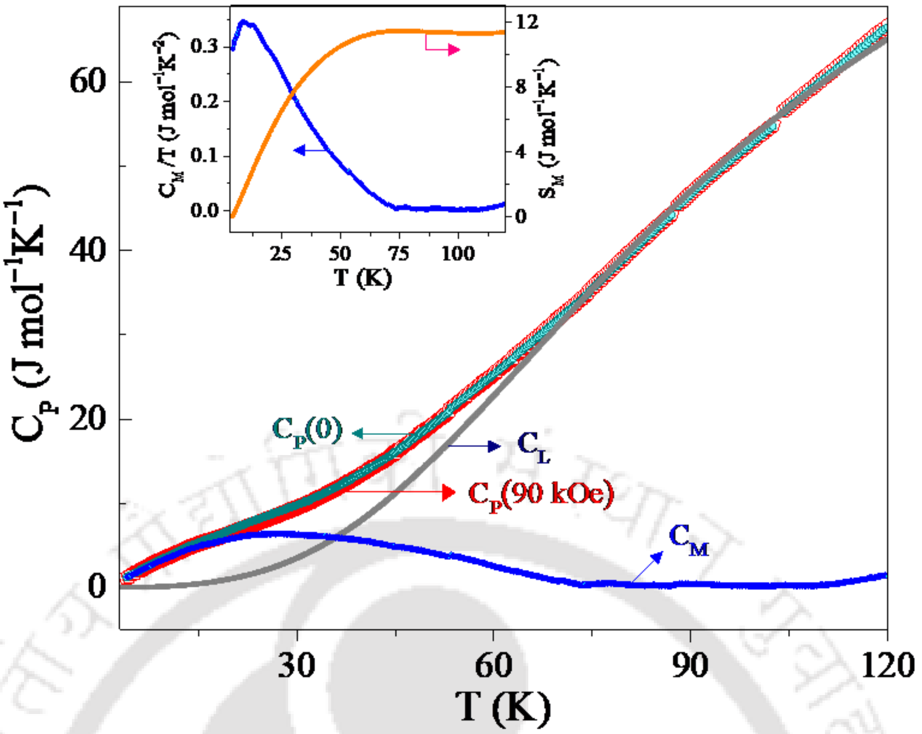

Figure 4.12: Thermal variation of total specific heat C_p data measured under both H = 0 and 90 kOe conditions for the bulk CZFRO system. Along with the $C_p(T)$ the individual contributions of magnetic C_M and phonon C_L parts and their temperature variations are also plotted, which are estimated from the Debye model of specific heat. The inset represents the temperature dependence of the C_M/T (depicted on left-hand-side-scale) in which the right-hand-side-scale shows the magnetic entropy $S_M(T)$ calculated using the numerical integration of C_M/T.

4.3.5. Temperature Dependence of Specific Heat:

The temperature dependent heat capacity measurements were carried out from 4 K to 120 K and plotted in figure 4.12. We observe that even higher field up to 90 kOe could not produce bifurcation between the specific-heat curves corresponding to H = 0 ($C_p(0)$) and 90 kOe (C_p(90 kOe)). Furthermore, the individual contributions to specific heat capacity from lattice (C_L) and magnetic (C_M) parts for CZFRO have been obtained from the total specific heat (C_p) data using the Debye formula,

$$C_L = N f_D(\Theta_D/T) = 9 N R (T/\Theta_D)^3 \int_0^{\frac{\Theta_D}{T}} \frac{x^4 e^x}{(e^x-1)^2} dx \qquad (4.4)$$

and $C_p = C_L + C_M$. In equation (4.4) the term $f_D(\Theta_D/T)$ defines the Debye function (= $9R\ (T/\Theta_D)^3 \int_0^{\frac{\Theta_D}{T}} \frac{x^4 e^x}{(e^x-1)^2} dx$), N is the number of cations per formula unit/unit cell, R is the universal gas constant (8.314 J mol^{-1}K^{-1}) and Θ_D represents the Debye temperature. Usually, the $C_p(0)$ curve is fitted to the Debye relation for $T \gg T_{FiM}$ to extract C_L, where the role of C_M is expected to be insignificant [175,263,264]. This analysis results in Θ_D = 400.6 K for CZFRO which is nearly 25 K lower than the Θ_D of AFM bulk ZFO (Θ_D = 425 K) [170,265]. The fitted data i.e. C_L has been extrapolated to 4 K and is shown as grey square symbols in figure 4.12 which apparently deviates from C_p at low temperatures. Whereas, for T < 35.9 K, C_M takes over C_L as the spin reorientation in preferred directions takes place while lattice vibrations collapse. However, the

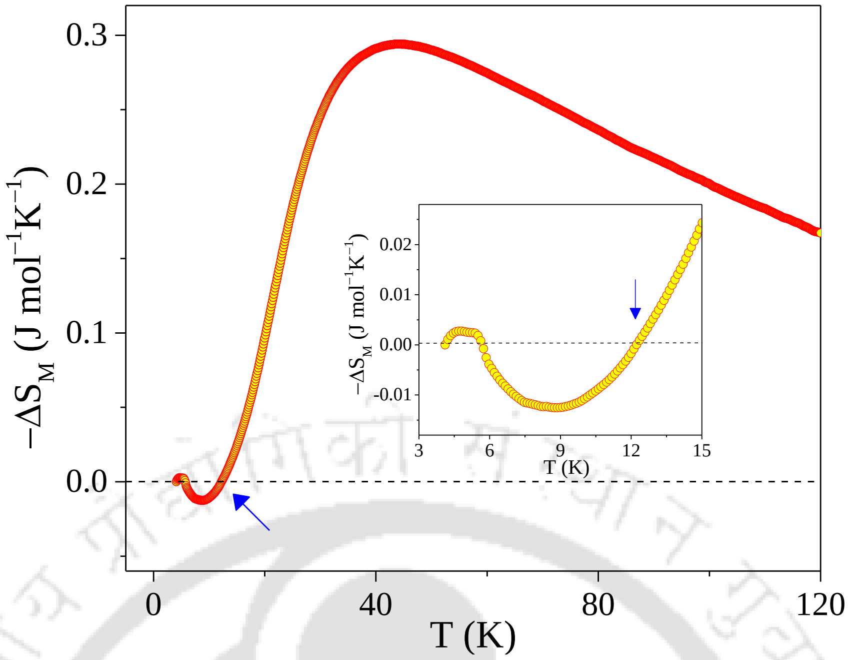

Figure 4.13: The magnetic entropy (ΔS_M) contribution at low temperatures derived from the specific heat data for CZFRO. The magnified image for the range $T \leq 15$ K is shown in the inset.

temperature dependence of C_M does not exhibit any λ−type anomaly across T_{FiM} except for the broad hump around 27 K which indicates the absence of LR ordering in CZFRO [158].

Upon numerical integration of C_M/T data the magnetic entropy (S_M) has been calculated and shown on the RHS scale of inset in figure 4.12. Across the T_{FiM}, S_M is about 4.4 J mol^{-1}K^{-1} and is significantly smaller than the expected theoretical value of ~ 14.75 J mol^{-1}K^{-1} (= $R\,Ln(2S + 1)$ for $S = 5/2$ ground state spin of Fe^{3+}). It is quite intriguing to notice that the saturation of the magnetic entropy occurs at a temperature close to 75 K (much higher than T_{FiM}) with a further residual magnetic gain to a total of 11.36 J mol^{-1}K^{-1} at 120 K. Nevertheless, the difference between the experimental and theoretical values are accounted for the slight deviation in the cationic distribution of the mixed spinel system in comparison to the ideal spinel configuration. Considering the mixed valence state of Fe and its dominant spin in comparison to spin-half states of Cu and Ru, both the experimental and calculated magnitudes of $S_M(T)$ are in excellent agreement with each other. The exact cationic distribution obtained from the inverse PM susceptibility analysis together with the structural data has been given in table 4.1. These signify the fact that no contribution of the spin entropy exists beyond the ground state of the magnetic entropy in the mixed valence states of transition metal ions present in the current CZFRO system. On the other hand, the temperature dependence of magnetic entropy change $(-\Delta S_M)(T)$ obtained from the heat-capacity data for a field change of 90 kOe is quite fascinating. In particular, the zero crossover of the entropy at low temperatures is in consonance with the transition region from SR FiM state to SG state (inset of figure 4.13). Nonetheless, the temperature variation of ac susceptibility is in congruence with the change in entropy trend in which both the quantities decrease above ~ 40 K.

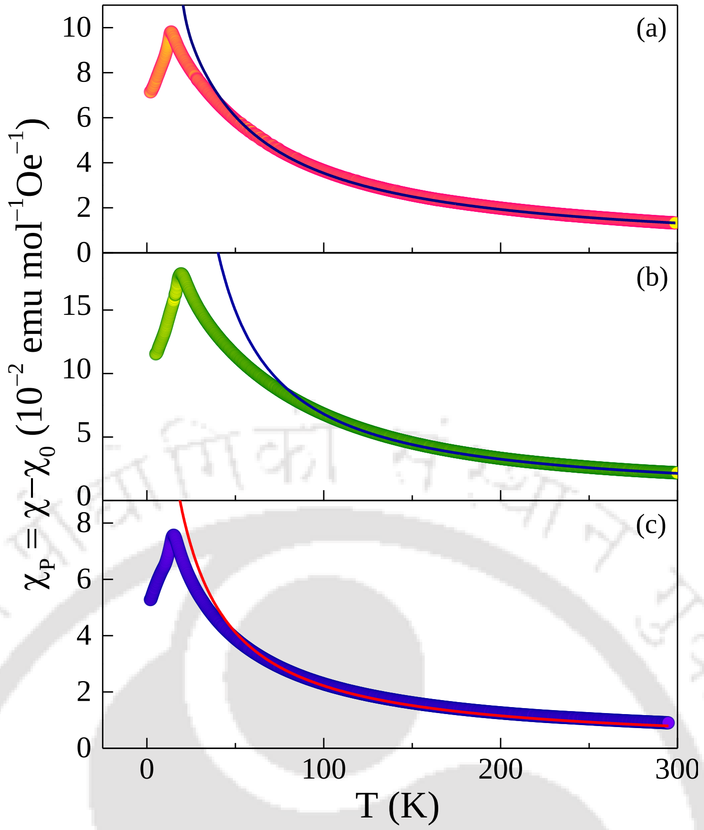

Figure 4.14: Temperature variation of the paramagnetic susceptibility ($\chi_P = (\chi - \chi_0)$) data obtained experimentally while the solid lines represent the best fits to the high temperature series expansion (HTSE) given in the equation (4.5).

4.3.6. Exchange Constants:

To determine the dominant exchange interaction in these systems we employed the high temperature series expansion (HTSE) method applicable to the spinel lattice based on the Heisenberg Hamiltonian and the corresponding susceptibility series expansion is given as follows [169].

$$\chi_\mathrm{p} = \frac{C}{T}\sum_{i=0}^{6} \mathrm{C}_i \left(\frac{-J}{k_\mathrm{B}T}\right)^i \tag{4.5}$$

In the present case, the systems under investigation contains multiple magnetic ions contributing to the total magnetic moment of each system separately. Accordingly, to calculate the normalized coefficients (C_i) up to 6th order the factor 'r' has been evaluated following the analysis employed by Schmidt *et al.* such that $r = \mu_{\mathrm{eff}}^2/4$ [168,169]. Here, μ_{eff} is calculated from the inverse of PM susceptibility analysis which is discussed later. In equation (4.5), the magnitudes of the coefficients C_i's for ZFRO being: $\mathrm{C}_0 = 1$, $\mathrm{C}_1 = -16.8$, $\mathrm{C}_2 = 231$, $\mathrm{C}_3 = -2808.77$, $\mathrm{C}_4 = 32\,266.39$, $\mathrm{C}_5 = -367\,268.15$, $\mathrm{C}_6 = 4211\,223.76$. Similarly, for CZFRO (CZFR1.5O): $\mathrm{C}_0 = 1$ (1), $\mathrm{C}_1 = -24.51$ (−11.23), $\mathrm{C}_2 = 494.48$ (102.09), $\mathrm{C}_3 = -8855.87$ (−814.41), $\mathrm{C}_4 = 150\,138.28$ (6118.19), $\mathrm{C}_5 = -2519\,522.84$ (−45 632.91), $\mathrm{C}_6 = 42\,508\,607.62$ (344 130.82). The solid lines shown in the figure 4.14 represents the best fits of the HTSE to the experimental data points for all the three compositions (a) ZFRO, (b) CZFRO and (c) CZFR1.5O which results in the dominant exchange constant

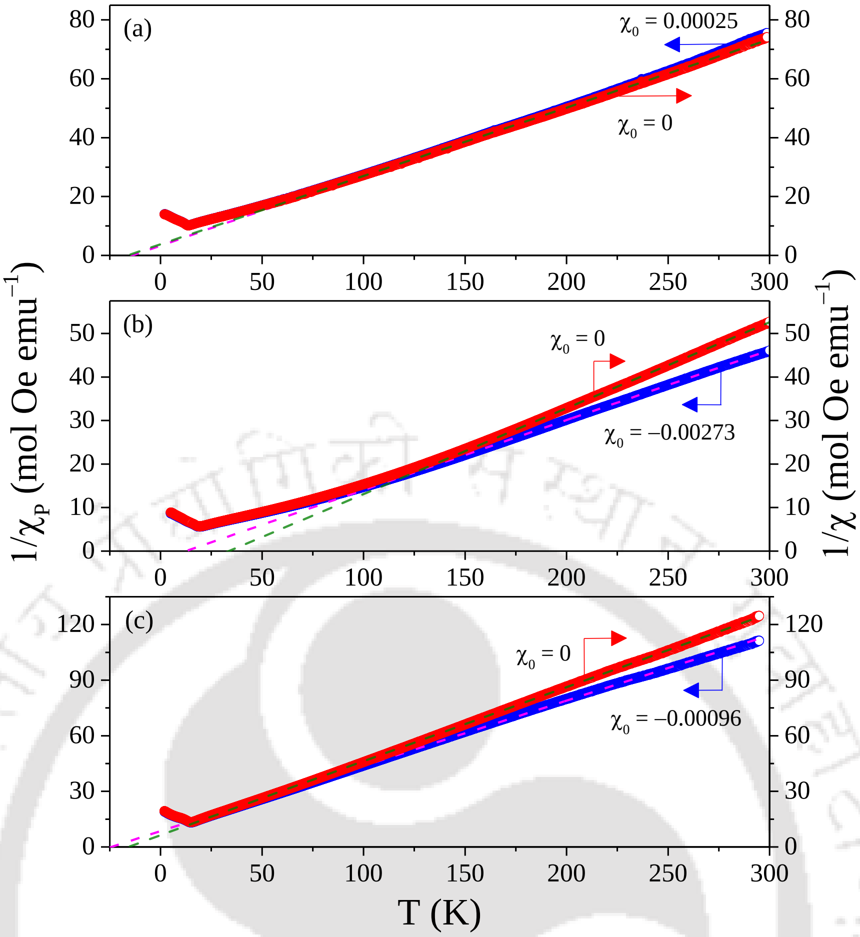

Figure 4.15: Temperature variation (1.9 K ≤ T ≤ 300 K) of the inverse dc magnetic susceptibility $\chi^{-1}(T)$ obtained at H = 500 Oe (scattered circles) with non-zero χ_0 (LHS) and for $\chi_0 = 0$ (RHS) along with the dotted lines (linear fits) to the CW law for the compositions (a) ZFRO, (b) CZFRO and (c) CZFR1.5O.

Table 4.3: The parameters obtained by fitting the modified Curie−Weiss law (for $\chi_0 = 0$ and $\chi_0 \neq 0$) to the temperature dependence of inverse dc magnetic susceptibility ($\chi^{-1}(T)$) curves for ZFRO, CZFRO and CZFR1.5O obtained at H = 500 Oe.

Composition →		ZFRO		CZFRO		CZFR1.5O	
Fitting Law ↓	Fitting parameters ↓	$\chi_0 = 0$	$\chi_0 = 0.00025$	$\chi_0 = 0$	$\chi_0 = -0.00273$	$\chi_0 = 0$	$\chi_0 = -0.00096$
Modified Curie−Weiss Fit	C (emu K mol^{-1} Oe^{-1})	4.31	4.21	5.07	6.23	2.5	2.84
	μ_{eff} (μ_B /$f.u$)	5.87	5.8	6.36	7.06	4.47	4.76
	θ (K)	−16.26	−13.97	33.68	12.37	−15.72	−24.29

J/k_B = −1.09 K (AFM), 0.35 K (FM) and −0.71 K (AFM), respectively. On the other hand, the modified CW ($\chi = \chi_0 + C/(T - \theta)$) analysis (figure 4.15) leads to the effective magnetic moment (μ_{eff}) = 5.8 μ_B/*f.u.*, 7.06 μ_B/*f.u.* and 4.76 μ_B/*f.u.*, and the CW temperature θ = −13.97 K, 12.37 K, and −24.29 K for the three compositions (a) ZFRO, (b) CZFRO, and (c) CZFR1.5O, respectively. Here the temperature independent diamagnetic susceptibility term (χ_0) is evaluated using the high-temperature extrapolation method ($\chi(1/T)$), also these magnitudes are comparable to that of the relativistic Hartree−Fock method. These magnitudes of μ_{eff} are consistent with the individual moments obtained for the ideal spin values in consonance with the cationic distribution acquired from the Rietveld refinement data. All the relevant parameters extracted (for both $\chi_0 = 0$ and non-zero χ_0) from this analysis has been listed in table 4.3.

4.3.7. *M*−*H* Hysteresis Loop and *H*−*T* Phase Diagram:

Furthermore, we performed the field dependence of magnetization (five cycle hysteresis, $M-H$) measurements at temperatures below the T_{SG} of all the three compositions. The main panel of figure 4.16 shows the $M-H$ hysteresis loops of (a) ZFRO, (b) CZFRO and (c) CZFR1.5O measured between −90 kOe and +90 kOe at $T = 1.9$ K under ZFC conditions. For all these compositions, we found the $M-H$ data to exhibit unsaturated loops with significant coercivity ($H_C \sim 3.6$ kOe). The inset of figure 4.16 illustrates the zoomed image of MH−loops at low fields less than 7 kOe clearly showing the H_C, remanent magnetization (M_R) and negligible loop-asymmetry exchange-bias field (H_{eb}). The magnitude of M_R (H_C) being 186 emu mol^{-1} (2254 Oe) for the composition ZFRO which increases by a considerable amount 127% (59%) due to the addition of Cu for CZFRO while H_C decreases monotonically with T and becomes negligible on approaching T_{FiM}. Based on the parameters extracted collectively from both the dc magnetization data and dynamical susceptibility measurements along with the heat capacity analysis, we established the magnetic phase diagram in $H-T$ plane for CZFRO as shown in figure 4.17. From this $H-T$ phase diagram one can clearly distinguish between the low temperature SG state (determined for $H > 2$ kOe from $\chi_{\mathrm{hf-ZFC}}$ (H, T) analysis) and the FiM state, but with SR ordering, FiM(SRO). Above these phases, a mixed phase (PM +

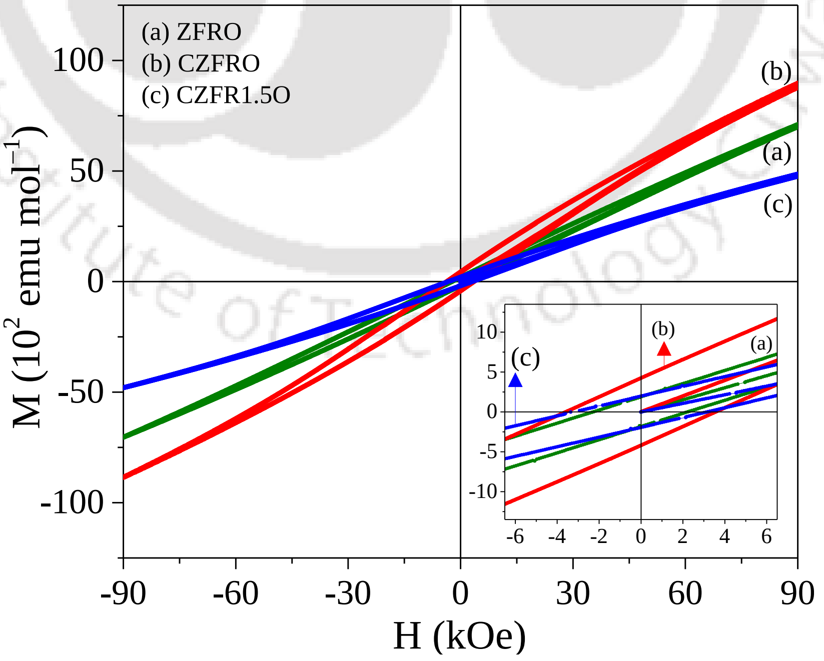

Figure 4.16: Magnetization (M) versus magnetic field (H) hysteresis loops of ZFRO, CZFRO, and CZFR1.5O recorded at 1.9 K under zero-field cooling conditions applying field up to ±90 kOe. The inset shows the zoomed view of the main panel loops near the coercive region.

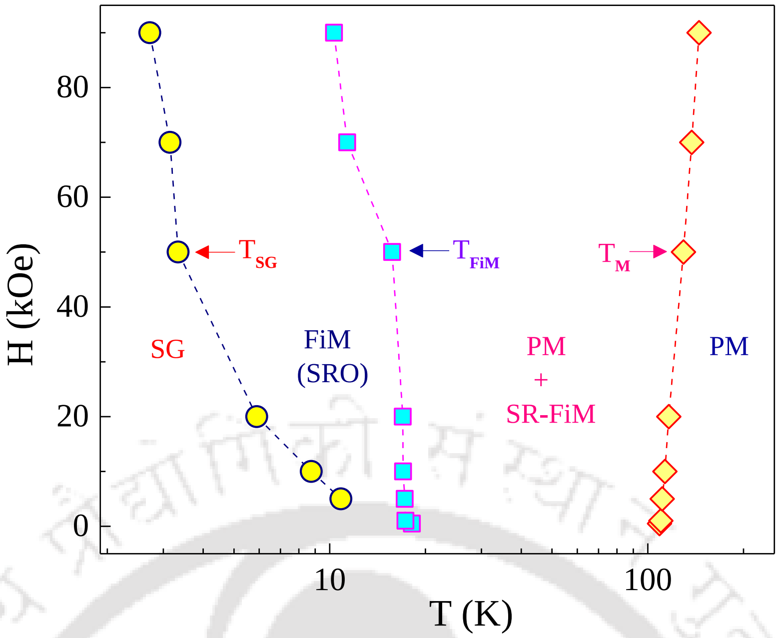

Figure 4.17: The *H−T* phase diagram established on the basis of various paramaters obtained from the dc and ac magnetization measurements for the composition CZFRO.

SR−FiM) region is mapped, corresponding to the slowly fluctuating FiM clusters having SR ordering (SR−FiM) coexisting within the fast-fluctuating PM regime, distinguished by T_M as obtained from $\mu_{eff}(T)$. For $T > T_M$, a completely PM state is prevalent without any additional magnetic ordering. It is quite obvious from these studies that the moderate presence of the *JT* active divalent Cu on *B* sites along with Fe and Ru significantly alters the FiM ordering by increasing the *A*−*A* and *B*−*B* FM interactions.

4.4. Conclusions:

Below we summarize the important results presented in this chapter. (*i*) We have successfully synthesized single phase polycrystalline bulk samples of mixed spinel $Zn(Fe_{1-x}Ru_x)_2O_4$ (x = 0.5, 0.75) with dilute (≤ 0.2) dispersion of the *JT* active Cu-atoms. Rietveld refinement of the XRD data reveals that the *B*-O bond length (2.072 Å → 2.087 Å) and *A*-O-*B* bond angle (123.59 ° → 124.16 °) increases with increasing the Cu and Ru contents, nevertheless, *A*-O bond length and *B*-O-*B* bond angle follow the opposite trend. (*ii*) The XPS measurements reveal divalent electronic state of Cu, Zn and O while trivalent electronic state of Ru and mixed valency of Fe prevails in the spinel lattice. Such elemental configuration is consistent with the effective magnetic moment obtained experimentally from the CW law corresponding to the cationic distribution evaluated from the Rietveld refinement of XRD data. (*iii*) FiM ordering in the investigated system is realized due to the different magnetic moments of each cation at *A* and *B* sites and their different temperature dependency leads to varying ordering temperatures and exchange interactions. The FiM ordering temperature for ZFRO system is 12.73 K, which shifts to higher temperature side (18.13 K) with the substitution of Cu, while it drops to 14.08 K upon increasing the Ru content in the CZFR1.5O system. Nevertheless, 20 atomic percentage of Cu substitution in ZFRO induces SR ordering beyond the T_{SG} (at ≃ $6T_{FiM}$) due to the intrasublattice FM exchange interaction. (*iv*) Data acquired for temperature dependent ac susceptibility at several frequencies ($\chi_{ac}(f, T)$) reveals a prominent frequency dispersion across the T_{SG} which fits well with the two empirical scaling laws: the VFL and PL. The linear variation of the experimental data ($Ln\ \tau$ *vs.* $1/(T - T_0)$ and $Ln\ \tau$ *vs.* $Ln\ [(T - T_{SG})/T_{SG}]$), confirm cluster SG state with the characteristic freezing temperature T_{SG} = 17.77 K and 14 K with the exponent zv = 8.43 and 8.41 for CZFRO and CZFR1.5O, respectively. (*v*) In case of CZFRO system, the real and imaginary components of $\chi_{ac}(T)$ show an additional transition for $T > T_{SG}$ owing to the slowly fluctuating SR FiM clusters prevail in the PM regime. (*vi*) The slow dynamics of the glassy clusters below T_{SG} are further supported by the analysis of Mydosh parameter Ω = 0.009 (0.0119) and the time (t) decay of thermoremanent magnetization study resulting in the magnetic viscosity S = 17.77 emu mol^{-1} (8.65 emu mol^{-1}) for CZFRO (CZFR1.5O), respectively. (*vii*) We employed the HTSE technique to determine the symmetric exchange coupling (J) between the spins which results in J/k_B = −1.09 K, 0.35 K and −0.71 K for the ZFRO, CZFRO and CZFR1.5O systems, respectively, clearly portraying the strengthening of intra sub-lattice FM interactions due to the dilute incorporation of the *JT* active Cu^{2+}. (*viii*) Furthermore, the field variation of the order parameters obtained from the dc magnetization $\chi_{hf-ZFC}(H, T)$ data for CZFRO is consistent with the SR ordering explained on the basis of non-mean-field theory. Combining the field variations of both the dc and ac order parameters, and the results obtained from the heat-capacity analysis, we established a detailed magnetic phase diagram in the $H-T$ plane for these interesting spinels.

Chapter 5

Magnetic Exchange Interactions in Cu-ZnFe$_2$O$_4$ Magnetoceramics

In this chapter we mainly focus on the role of magnetic exchange interaction and electronic structure of few intermediate compositions between the two end compounds $ZnFe_2O_4$ and $CuFe_2O_4$. In the very first section we provide a detailed literature review on the magnetic and structural properties of the above two end compounds along with their intermediate compositions. We also focus on the gaps in literature pertaining to the magnetic and electronic structure of the proposed systems and how the current research objectives fulfil such gaps. Key novelty of this chapter is that we employ the well-known Néel's expression for ferrimagnets to reveal the magnitude of exchange coupling with systematic substitution of Jahn−Teller active divalent Cu within the spinel lattice.

5.1. Introduction and Objectives:

This section discusses about physical properties of the two end compounds: $CuFe_2O_4$ and $ZnFe_2O_4$, illustrates their importance and also provide the motive in choosing these compounds. Copper ferrite ($CuFe_2O_4$), often called cuprospinel, is a well-studied system in the literature because of its tunable tetragonal to cubic crystal structure transition (T^*) owing to the Jahn−Teller effect below its ferrimagnetic ordering (T_{FiM} ~ 507±20 °C, although significant disparities in the T_{FiM} values are found in the literature) [266-269]. Numerous methods are implemented by researchers to tune the degree of tetragonality at room temperature, such as quenching to low temperatures, slowly cooling from sintering point, applying high pressure, and varying the chemical stoichiometry by replacing the B and A site cations with other transition metals [270-279]. In all these cases, the proportion of divalent copper atoms on the tetrahedral A sites to that of the octahedral B sites decides the stability of the tetragonal structure [280]. On the other hand, these spinels under reduced dimensions play an important role in industrial applications such as filters in electromagnetic interference, gas-sensors [281,282], catalysts [283-285], microwave devices [286], hydrogen energy [287], and magneto-electronics [288]. Several reports suggested the following cationic distribution in this compound: $(Cu_xFe_{1-x})_A[Cu_{1-\eta-x}Fe_{1+\eta+x}]_BO_4$ with the degree of inversion x lying between 0 (inverse-spinel) and 1 (normal-spinel) [279,289,290].

It is a very challenging task to maintain the stoichiometric proportion of the cations in this compound using conventional heat-treatment conditions at the synthesis level because of the formation of CuO as secondary phase due to which one always observes deviation from exact stoichiometry leading to η ~ 0.04±0.01 [291]. Thermal kinetics of Cu are quite inimitable in spinel lattice, for example, Cu^{2+} exhibits a high migration rate above 400 °C (with low activation energy $E_a \leq 0.1$ eV) so that they swiftly reorder in the lattice leading to fractional inverse-spinel structure (approximately 0.85 Cu^{2+} ions on the octahedral sites) [292]. Thus, the rate of cooling (either rapid or slow) plays an important role in deciding the crystal structure in the bulk form whether it is cubic or tetragonal. Moreover, the oxygen deficiency in this system is quite unfavorable to the formation of tetragonal structure, which in turn affects the phase transition temperature and magnetic ordering [293]. Nevertheless, the end compound $x = 1$ ($ZnFe_2O_4$) exhibits a normal spinel structure and low-temperature antiferromagnetic ordering with Néel temperature of ~ 10 K [135,137,294-297]. In this compound, both *A* and *B* sites contain divalent Zn and trivalent Fe ions with a general formula $(ZnFe)_x[ZnFe]_{2-x}O_4$, in which the magnetic ordering strongly depends on the stoichiometry/state of chemical order and the site occupancy of cations [137,220,298,299] The cations at *B* sites are positioned at the junctions of the tetrahedron, in which each corner is shared by two tetrahedral. If we consider the tetrahedron as a single entity, then the *B* sites of the spinel structure can be described as face-centred-cubic configuration of molecules similar to the pyrochlore structure and some intermetallic Laves-phases. In such a case, one can expect unusual magnetic behavior in the system such as geometrical frustration, spin-liquid state, Griffiths phase, reentrant spin-glass behavior with unusual ground states, negative magnetization, and bipolar exchange-bias [147,175,240,300-302]. Although the physical properties of Zn-substituted $CuFe_2O_4$ have been extensively investigated, studies related to its compositional dependence of magnetic ordering temperature, exchange interactions, and anisotropy studies in bulk $Cu_{1-x}Zn_xFe_2O_4$ system are still lacking in the literature.

The majority of today's research activity on this system is intensive on the nanostructures and thin films forms of the compounds to explore their potential applications in industries, especially in the renewable energy sector [267,303,304]. Also, a systematic correlation of the change in the electronic and crystal structure of bulk grain sized $Cu_{1-x}Zn_xFe_2O_4$ magneto-ceramics is scarce in the literature. Recent numerical calculations by Salmi *et al.* reported the variation in the exchange interactions ($J_{AA}(x)$, $J_{BB}(x)$, and $J_{AB}(x)$), long-range ordering temperature, and critical exponent (γ) for various compositions of $Cu_{1-x}Zn_xFe_2O_4$ using the high temperature series expansion studies linked with the Padé approximation [305]. Therefore, in the current work, we focus our study on magnetic behavior and exchange interactions between the temperature range 1.9 K and 900 K of various levels of Zn diluted $CuFe_2O_4$ bulk grain size compounds under different measurement protocols along with a systematic correlation of these results with the crystal structure, electronic properties, and morphology. Detailed methodology, experimental results and their discussion, and the analysis are presented below.

5.2. Experimental Details:

This section elaborates the experimental steps followed for the synthesis and preliminary characterizations obtained in connection with the concepts already discussed in Chapter 2. The standard solid-state-reaction method was employed to synthesize the bulk samples of $Cu_{1-x}Zn_xFe_2O_4$. For this, we used copper oxide (CuO), zinc oxide (ZnO), and ferric oxide (Fe_2O_3) as precursors. First, stoichiometric proportions of these compounds are mixed in a ball-milling machine using a tungsten-carbide jar and ethanol as milling medium. Milling was carried out by using tungsten-carbide balls of 10 mm diameter in which the ratio of the weight of the balls to powder is maintained as 5:1. Adequate amount of ethanol was also added as the milling medium so that the balls would rotate (with 150 rpm speed for 10 h) freely without any friction.

The solution was then dried in an oven and calcined at 900 °C for 4 h in air. The calcined powder was made into 13 mm diameter pellets using a hydraulic press and sintered at 1050 °C for 8 h in air. These pellets were further reground and sintered at the same temperature for multiple times to avoid the formation of any secondary phases. This procedure is employed for the synthesis of almost all the compositions; however, Cu rich samples are heat treated at slightly lower temperatures. The crystal structure and phase purity of the compounds are examined by performing the x-ray diffraction (XRD) experiments using Rigaku based x-ray diffractometer (Model: TTRAX III) with Cu-Kα radiation (λ = 1.54056 Å). In order to investigate the microstructure of the samples, we used Field Emission Scanning Electron Microscope, FESEM (Model: Sigma-Zesis with extra high tension EHT 2 KV) and a Transmission Electron Microscope (TEM, JEOL JEM-2100 operated under secondary electron mode with 200 keV potential). These studies reveal the bulk grain size of the investigated composition with an average grain size of ~ 15.768 μm (x = 0.4). The selected area electron diffraction (SAED) pattern further supports the formation of cubic crystal structure consistent with the x-ray diffraction studies. The SAED pattern for the composition x = 0.4 agrees well with the cubic phase determined from the x-ray diffraction studies. The bright-field, high resolution transmission electron micrograph (HRTEM) reveals the uniform lattice spacing of ~ 3.28±0.01 Å consistent with the interplanar spacing (d_{220}) determined from the x-ray diffraction analysis discussed below. Electronic structure and elemental analysis was performed by x-ray photoelectron spectroscopy (XPS) from Thermo Fisher Scientific 250Xi and Energy Dispersive Spectroscopy, EDAX from Zeiss (Model GEMINI 300). Temperature dependence of the magnetization measurements are performed using a physical property measurement system, PPMS from Quantum Design (Model: DynaCool), which is capable of reaching the low temperatures down to 1.9 K from 300 K and a maximum dc magnetic field of 90 kOe. For the high-temperature (until 900 K) magnetization measurements, we used VSM oven accessory separately. In the subsequent sections we provide a meticulous analysis of the experimental results pertaining to the XRD, XPS and magnetization data.

5.3. Results and Discussion:

5.3.1. Elemental Analysis:

Figure 5.1 shows the XPS spectra (photoelectron intensity *vs.* binding energy) of all the individual elements for x = 0.4 composition. Here, the adventitious carbon (C-1*s* peak at 284.8 eV) was used as a charge reference to calibrate the Cu-2*p*, Zn-2*p*, and Fe-2*p* core level intensity spectra. The Zn-2*p* core level spectrum (figure 5.1(a)) exhibits two sharp symmetrical peaks centred at 1020.96 eV and 1044.03 eV, without any signature of satellite peaks. The binding energy separation between these peaks is Δ ~ 23.06 eV confirms the divalent oxidation state of Zn [146]. On the other hand, the Cu-2*p* core level spectrum is deconvoluted into four peaks: two main peaks centred at 933.65 eV and 953.56 eV and two satellite peaks at 941.1 eV and 961.48 eV (figure 5.1(b)). The observed value of spin-orbit splitting between two main peaks is approximately 19.91 eV, confirming the divalent oxidation state of Cu, which is further supported by the observation of the broad satellite peak at 941.1 eV [151]. Figure 5.1(c) shows the Fe-2*p* core level spectrum

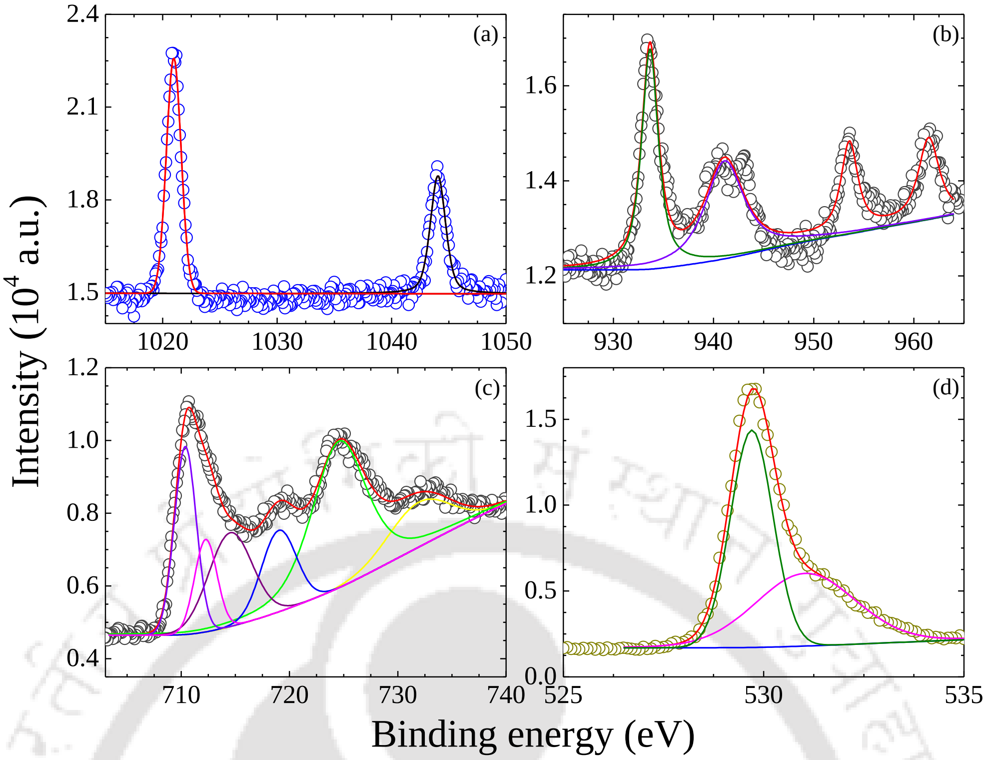

Figure 5.1: X-ray photoelectron spectra of (a) Zn-2*p*, (b) Cu-2*p*, (c) Fe-2*p*, and (d) O-1*s* for the composition $x = 0.4$.

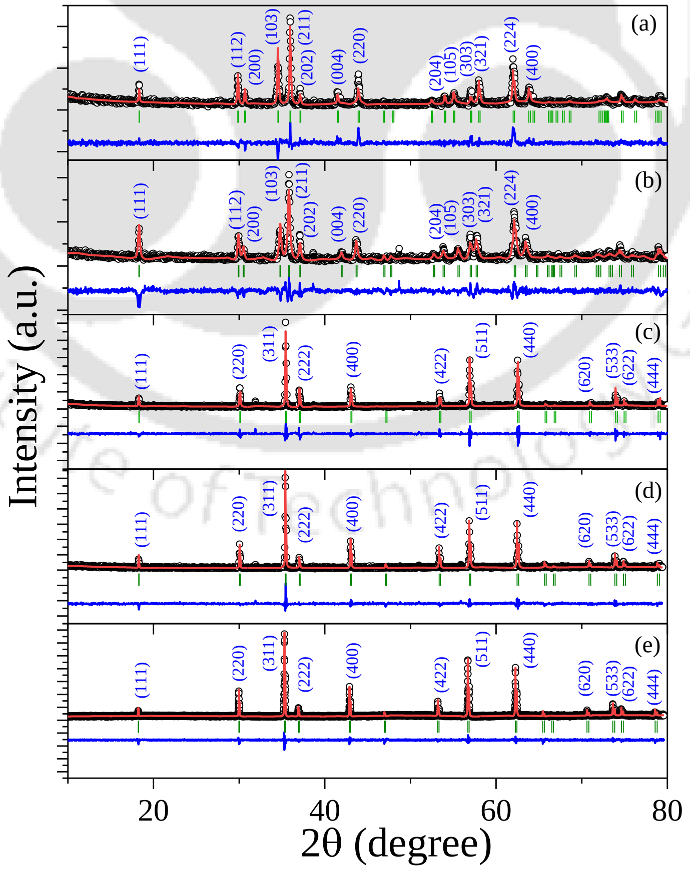

Figure 5.2: X-ray diffraction spectra and their corresponding Rietveld refinement patterns of various compositions (a) $x = 0$, (b) $x = 0.05$, (c) $x = 0.1$, (d) $x = 0.2$, (e) $x = 0.6$ of $Cu_{1-x}Zn_xFe_2O_4$.

that consists of minimum of six peaks to deconvolute. The four main peaks are centred at 710.10 eV (P_1), 712.3 eV (P_2), 719.01 eV (P_3), and 724.6 eV (P_4), and two broad satellite peaks are located at 714.6 eV (S_1) and 732.46 eV(S_2). The peak centred around 710 eV in the 2$p_{3/2}$ core level regime can be assigned to Fe^{2+}, while the peak at 712 eV is associated with Fe^{3+} [148,149]. Moreover, the observed values of spin-orbit splitting $\Delta(P_3 - P_1) \sim 9$ eV and $\Delta(P_4 - P_2) \sim 12$ eV further confirms the mixed (divalent and trivalent) oxidation state of "Fe". These results are consistent with the results obtained from the EDAX measurements.

5.3.2. Structural Characterization:

Figure 5.2 shows the XRD patterns recorded at room temperature for various compositions of Cu$_{1-x}$Zn$_x$Fe$_2$O$_4$ ($0 \leq x \leq 0.6$) system along with the corresponding Rietveld refinement data obtained using the *FullProf* program. The XRD pattern for undoped and moderately diluted Zn compositions (x = 0 and x = 0.05) corresponds to the tetragonal crystal structure of space group $I4_1/amd$ with lattice parameters $a = b$ = 8.243 Å and c = 8.699 Å. The degree of tetragonal distortion abruptly decreases as the Zn dilution level increases in CuFe$_2$O$_4$. For $0.1 \leq x \leq 0.6$, all the compounds exhibit a change in the crystal structure from the tetragonal to cubic phase of space group $Fd{-}3m$. Figure 5.3 depicts the variation of the lattice parameters (a and c) as a function of composition (x), which divulges a step increase in the lattice parameter above 10 atomic percent of the Zn level beyond which it remains almost constant at 8.424 Å up to x = 0.6. The bond angles between the ions A-O-B and A-O-A follows a completely opposite trend, and the A-O bond length was found to remain constant at ~ 2 Å (figure 5.4). Such variations occurring in the unit cell dimensions are consistent with different ionic radius of the Cu^{2+} (0.57 Å), Zn^{2+} (0.6 Å) and Fe^{3+} (0.49 Å) ions on A sites as compared to the B site occupied cations Cu^{2+} (0.73 Å), Fe^{2+} (0.78 Å) and Fe^{3+} (0.55 Å). Nevertheless, it is very interesting to note that the trivalent Fe occupies the tetrahedral A sites with either low spin or high spin states for different compositions (x) along with part of divalent Cu, whereas both the divalent and trivalent Fe along with most of divalent Cu reside on the octahedral B sites and the divalent Zn occupies only the

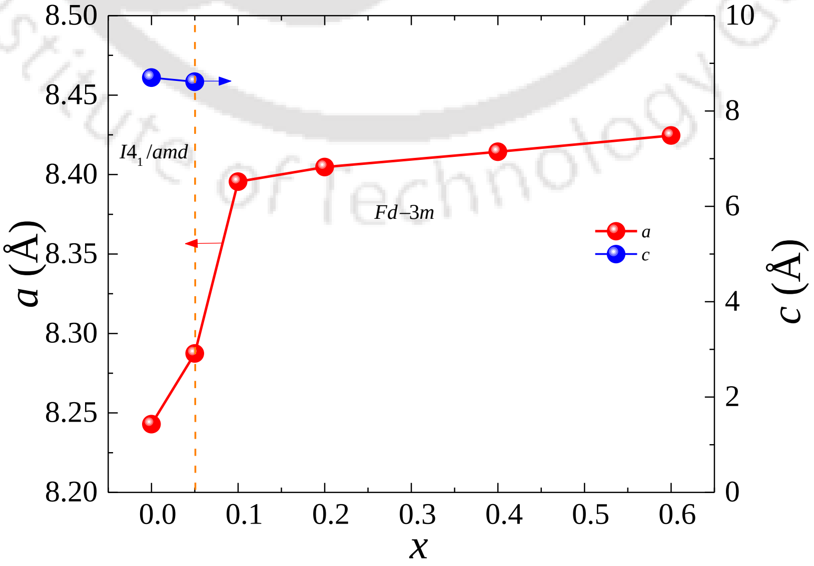

Figure 5.3: Composition variation of the lattice parameters (a and c) obtained from the Rietveld refinement patterns of Cu$_{1-x}$Zn$_x$Fe$_2$O$_4$.

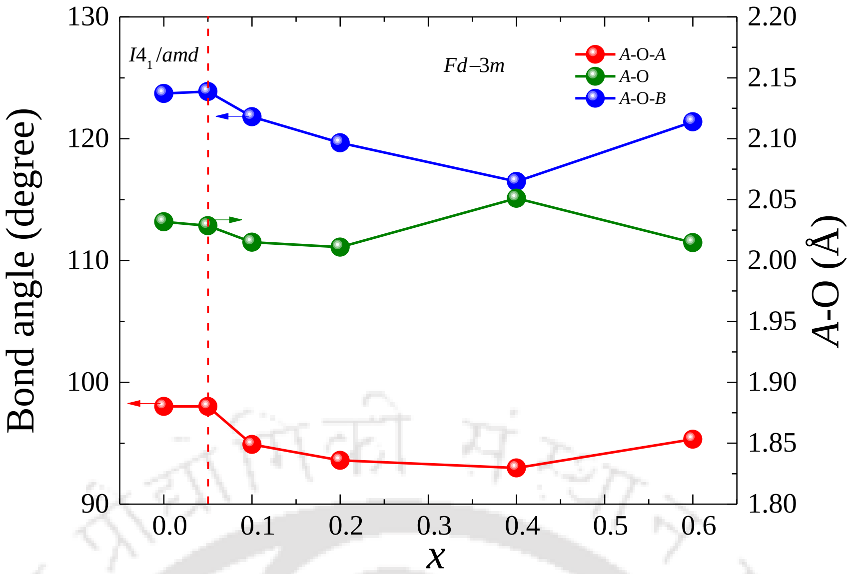

Figure 5.4: Variation of the bond angle between the cations *A*-O-*B* (blue sphere) and *A*-O-*A* (red sphere) plotted on L.H.S scale and bond-length *A*-O plotted on R.H.S scale as a function of composition of $Cu_{1-x}Zn_xFe_2O_4$.

Table 5.1: The list of crystallographic parameters obtained from the XRD data and their corresponding Rietveld refinement data for different compositions of $Cu_{1-x}Zn_xFe_2O_4$.

Composition (*x*)	*a* (Å)	*b* (Å)	*c* (Å)	*A*-O (Å)	*A*-O-*A* (°)	*A*-O-*B* (°)
0	8.243	8.243	8.699	2.032	98.02	123.71
0.05	8.287	8.287	8.613	2.028	98.03	123.87
0.1	8.395	8.395	8.395	2.015	94.9	121.8
0.2	8.405	8.405	8.405	2.011	93.6	119.67
0.4	8.414	8.414	8.414	2.051	92.97	116.49
0.6	8.425	8.425	8.425	2.015	95.33	121.39

tetrahedral *A* sites forming a mixed spinel structure in this interesting spinel. Table 5.1 summarizes all the parameters obtained from the refinement process.

5.3.3. DC Magnetization:

Figures 5.5(a)−5.5(c) show the temperature dependence of dc magnetic susceptibility ($\chi(T)$) recorded under zero-field-cooled (ZFC) and field-cooled (FC, *H* @500 Oe) protocols. In these measurements, the data were recorded under warming condition from 1.9 K to 300 K after cooling it from the room temperature. Both χ_{ZFC} and χ_{FC} curves exhibit bifurcation below T_{irr} ~ 300K (83.7 K), for $x = 0$ (0.4). Such thermal irreversibility is prominent at low-measuring fields which occurs due to the magneto-crystalline anisotropy, beyond T_{irr} the magnetic moment gradually decreases and approaches a minimum of 5.66 emu mol^{-1}Oe^{-1}

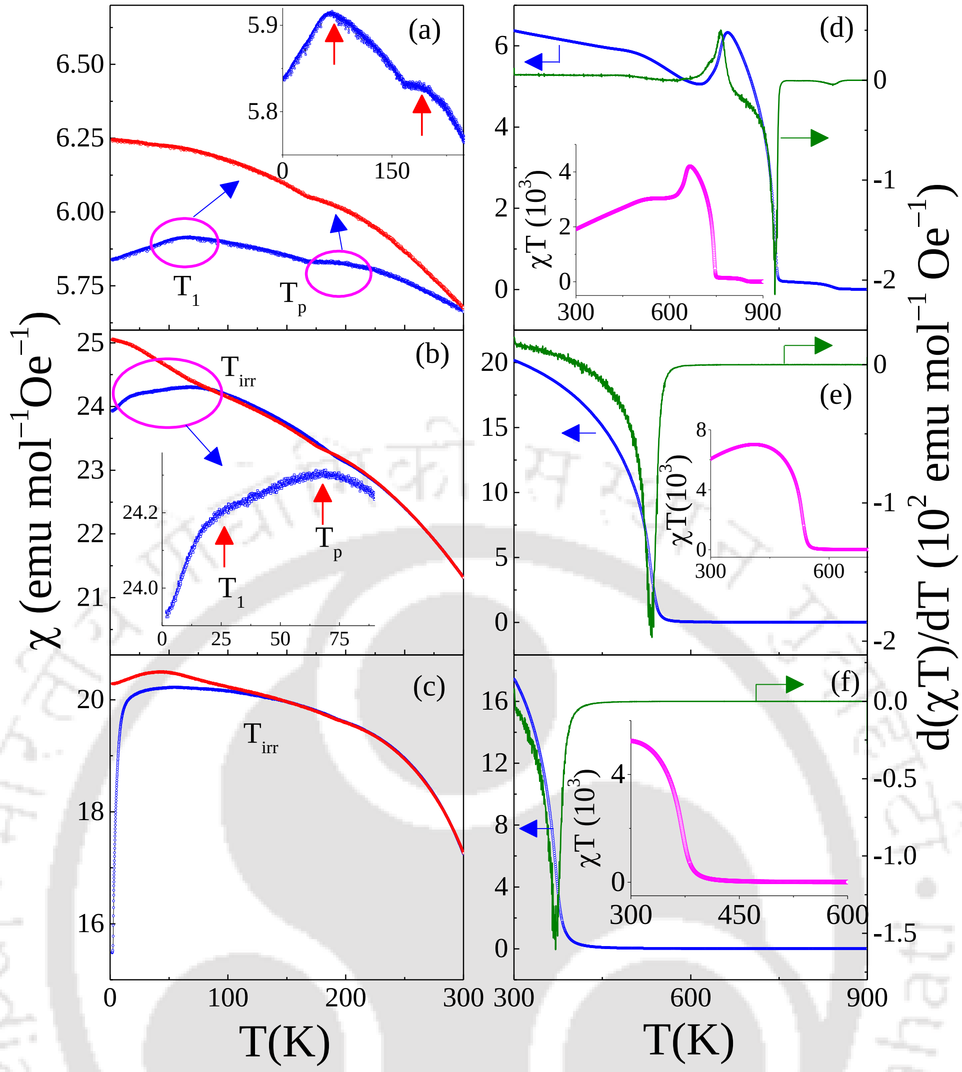

Figure 5.5: Temperature variation of the dc magnetic susceptibility $\chi(T)$ measured under both zero-field-cooled (ZFC) and field-cooled (FC) conditions for different compositions (a) x = 0, (b) 0.4 and (c) 0.6 between the temperatures 1.9 K and 300 K (the insets of figure (a) and (b) clearly depicts the low temperature transitions T_P and T_1). Figure (d), (e) and (f) shows the $\chi(T)$ plots (L.H.S scale) recorded at high temperatures from 300 K to 900 K under warming condition. Whereas, the R.H.S scale shows the temperature dependence of $\partial(\chi T)/\partial T$ and insets represents temperature variation of χT.

(21.31 emu mol^{-1}Oe^{-1}) for x = 0 (0.4), respectively at 300 K. Moreover, upon close examination of $\chi_{ZFC}(T)$ one can notice a fine transition at T_1 = 66 K (27 K) below the maximum in χ_{ZFC} at T_P = 194 K (68 K) for x = 0 (0.4); however, as the compositions increase both T_P and T_1 gradually smears-off (figure 5.5(c)). This system shows ferrimagnetic behavior similar to the parent compound CuFe$_2$O$_4$ due to the unequal magnetic moment of the magnetic cations. In order to precisely estimate the exact magnetic ordering temperature, we performed the high-temperature magnetic measurements separately under the warming condition from 300 K to 900 K in the presence of the external magnetic field (500 Oe). Figure 5.5(e) shows the $\chi(T)$ plot of x = 0.4, where the susceptibility drops to zero across 550 K. In order to estimate the ordering temperature precisely, we plotted the differential magnetic susceptibility of the function χT with respect to T because the temperature dependence of $\partial(\chi T)/\partial T$ is analogous to the thermal variation of the heat capacity C_p (~ A

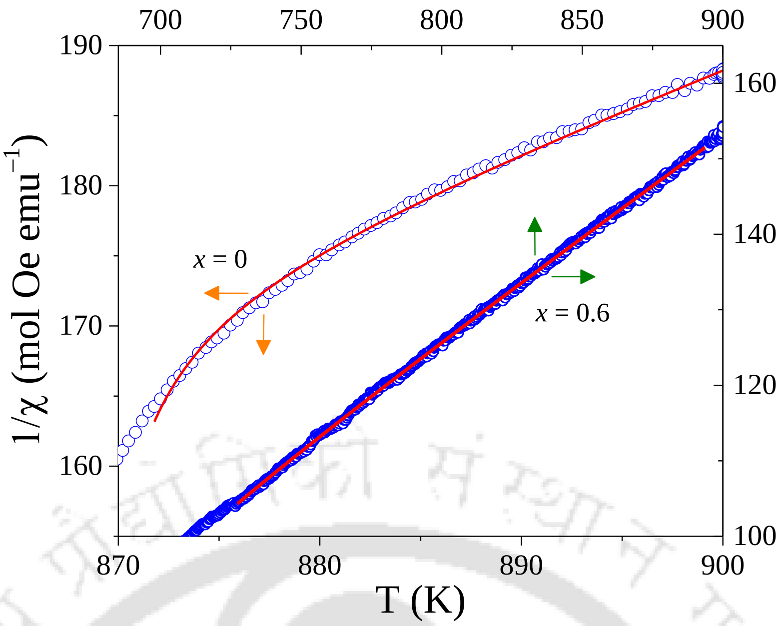

Figure 5.6: Temperature dependence of inverse paramagnetic susceptibility $\chi^{-1}(T)$ and the corresponding fitting (solid red lines) to the Néel's expression for ferrimagnets for the compositions x = 0 and 0.6.

$\partial(\chi T)/\partial T$). Also, typically, the order to disorder transition in ferri/antiferromagnets occurs at a temperature few percent lower than the usual transition. Thus, instead of considering the minimum in the $\chi(T)$ plot, we took the temperature corresponding to the minimum in the $\partial(\chi T)/\partial T$ *vs.* T plot as the exact ordering temperature. The LHS and RHS scales of figures 5.5(d)−5.5(f) show the temperature variation of χ and sharp minimum in derivative plots at 534.3 K corresponding to the ferrimagnetic Néel temperature (T_{FiM}) of the investigated system for x = 0.4, which is less than the undoped case 743 K (figure 5.5(d)). For x = 0.6, as shown in figure 5.5(f), still lower T_{FiM} (= 370.5 K) was observed.

5.3.4. Ferrimagnetic Néel Temperature and Exchange Constant:

In order to estimate the effective magnetic moment μ_{eff} of the compound, we have plotted the thermal variation of inverse paramagnetic susceptibility $\chi^{-1}(T)$ obtained from the $\chi_{\mathrm{ZFC}}(T)$ data in the paramagnetic regime ($T > T_{\mathrm{FiM}}$). Accordingly, the $\chi^{-1}(T)$ (for $T > T_{\mathrm{FiM}}$) data are fitted with the Curie−Weiss law $\chi = C/(T - \theta)$ with $C = N\mu_{\mathrm{eff}}^2/3k_{\mathrm{B}}$, $\mu^2 = g^2 J(J + 1)\mu_{\mathrm{B}}^2$, θ is the Curie−Weiss temperature, g is the Landé factor, and J is the total angular momentum. For x = 0.4, the magnitudes of C (= 3.318 emu K mol^{-1}Oe^{-1}) and θ (= 426.8 K) are evaluated from the slope and intercepts of the $\chi^{-1}(T)$ line. Using the magnitudes of g = 2, C, and θ we have evaluated the μ_{eff} = 5.15 μ_{B}/*f.u.*, which is consistent with the theoretically estimated value of 5.02 μ_{B}/*f.u.* according to the cationic distribution $(\mathrm{Cu_{0.12}Zn_{0.40}Fe_{0.48}})_A[\mathrm{Cu_{0.48}Fe_{1.52}}]_B\mathrm{O_4}$ [85,267,292,306-309]. For a precise understanding of the exchange interactions, we fitted the χ^{-1} *vs.* T data (for $T > T_{\mathrm{FiM}}$) with the Néel's expression for ferrimagnets as follows:

$$(1/\chi) = (T/C) + (1/\chi_0) - [\sigma_0/(T - \theta)] \qquad (5.1)$$

The scattered symbols shown in figure 5.6 signify the experimental χ^{-1} *vs.* T data, whereas the solid lines

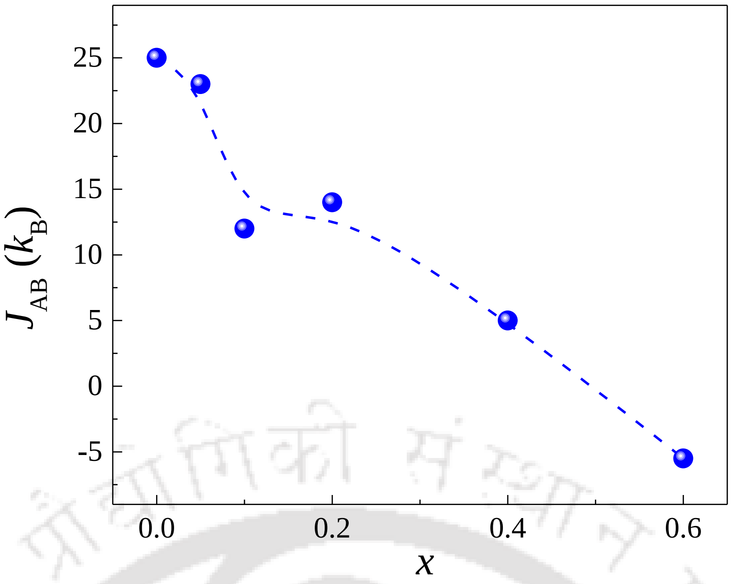

Figure 5.7: Composition dependence of the exchange constants J_{AB} for the system Cu$_{1-x}$Zn$_x$Fe$_2$O$_4$.

Table 5.2: The list of parameters obtained after fitting the Néel's expression (equation (5.1)) for ferrimagnets with the temperature dependence of inverse paramagnetic susceptibility data. The parameter J represents the exchange constant. Whereas the C, μ_{eff} and Θ denotes Curie constant, effective magnetic moment and Curie−Weiss temperature, respectively. σ_0 and χ_0 are the constants.

x	C (emu K/mol-Oe)	$1/\chi_0$ (emu^{-1} mol Oe)	σ_0 (mol Oe K/emu)	Θ (K)	μ_{eff} (μ_B/$f.u.$)	J_{AA} (k_B)	J_{BB} (k_B)	J_{AB} (k_B)
0	1.83	−299	46.17	867	3.82	−2130	−40.2	25
0.05	2.01	−248.78	30.86	831.5	4.01	−2154	−33.2	23
0.10	2.42	−160	409.15	800.12	4.39	−2217	−20.6	12
0.20	3.1	−107.07	87.08	787.63	4.97	−2444	−13.8	14
0.40	4.21	−72	186.74	734.74	5.80	−3055	−9.06	5
0.60	3.76	−84	488.4	625.68	5.48	−3939	−10.41	−5.5

represent their corresponding fits (for x = 0 and 0.6). In equation (5.1), C represents the Curie constant, θ is the Curie−Weiss temperature, σ_0 and χ_0 are constants, and $T_a = C/\chi_0$ is the asymptotic Curie temperature (−547.2 K and −315.8 K for the compositions x = 0 and x = 0.6, respectively). Usually, the asymptotic Curie temperature represents the strength of the magnetic exchange coupling between the tetrahedral A site spins and the remaining cations occupying the octahedral B sites. Using the fitted parameters obtained from the Néel's expression for ferrimagnets, we have determined the molecular field constants and exchange constants (J_{AA}, J_{BB}, and J_{AB}). A detailed composition dependent analysis of exchange interaction ($J(x)$) reveals that J_{AB}/k_B (~ 25 K for x = 0) is ferromagnetic in nature, and it is the main dominant exchange interaction in comparison to the other two exchange constants (J_{AA} and J_{BB}), though, J_{AB} decreases significantly with

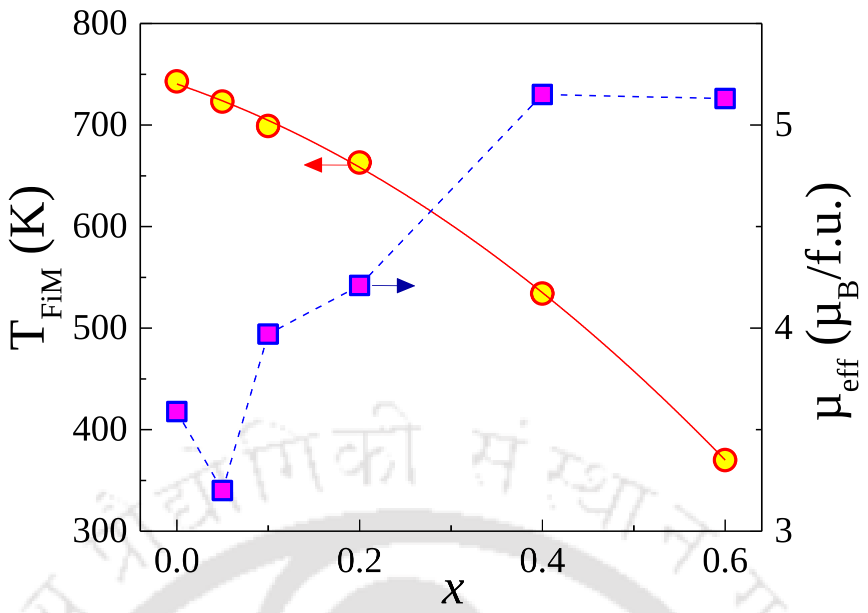

Figure 5.8: Compositional variation of the Néel temperature $T_{FiM}(x)$ and effective magnetic moment $\mu_{eff}(x)$. The red line is the quadratic fitting to the T_{FiM} values obtained for different compositions.

increasing the composition ($J_{AB}/k_B \sim -5.5$ K for $x = 0.6$) (figure 5.7). At very high compositions, these interactions are antiferromagnetic in nature (−ve J_{AB}) consistent with the AFM ordering of the end compound ZnFe$_2$O$_4$ ($x = 1$). Table 5.2 lists all the physical parameters obtained from the Néel fits of the $\chi^{-1}(T)$ data measured under the ZFC condition for all the six compositions. With an increase in x, the A site gets diluted, hence magnetization of A sublattice becomes too small. Also, the interaction between B cations becomes weaker due to competing exchange interaction on B sites, finally leading to a canted spin structure [310]. Nevertheless, for very dilute dispersion of Zn ($x \leq 0.05$), the system stables in the next lower symmetry tetragonal crystal structure of space group $I4_1/amd$, which influences the exchange interactions significantly.

Figure 5.8 shows the variation of ordering temperature and the effective magnetic moment plotted as a function of composition ($T_{FiM}(x)$ and $\mu_{eff}(x)$). We noticed continuous decrease of T_{FiM} with increasing the Zn content following the trend $T_{FiM} = y_0 + b_1 x + b_2 x^2$ with intercept $y_0 = 740.42$ K and the constants $b_1 = -306.73$, $b_2 = -517.84$. However, the magnitudes of μ_{eff} increases progressively from 3.2 μ_B/*f.u.* to 5.15 μ_B/*f.u.*, with increasing x from 0.05 to 0.4, respectively. In the case of tetragonally distorted compositions, μ_{eff} essentially decreases with increasing x, which is apparent due to the increase of the nonmagnetic Zn ions. For the compositions with the stable cubic structure, μ_{eff} increases initially and then decreases beyond x_c (= 0.4). Such a variation is consistent with the anisotropy calculations discussed below.

5.3.5. *M−H* Hysteresis Loop and Magnetic Anisotropy:

Figure 5.9 shows the magnetization *vs.* field (*M−H*) magnetic hysteresis loops of the composition x = 0.4 measured at different temperatures between 2 K and 300 K. These loops quickly saturate with the negligible coercive field. In order to probe the anisotropy of the system, we measured the isotherms of *M−H* at different temperatures (as shown in the inset of figure 5.9) and employed the law of approach to saturation

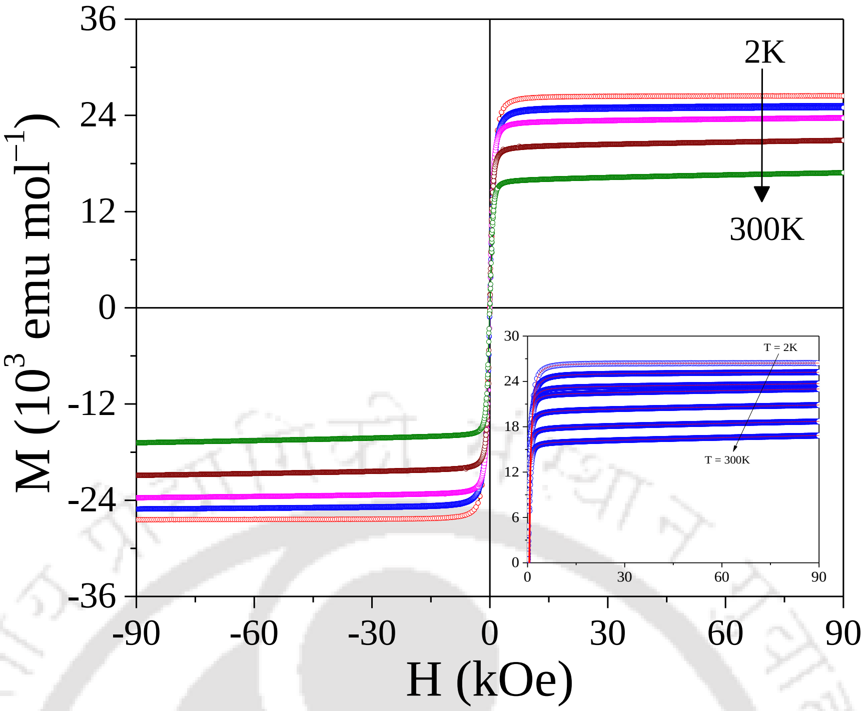

Figure 5.9: Magnetization versus field ($M-H$) hysteresis loops recorded at different temperatures (2 K ≤ T ≤ 300 K) for the composition x = 0.4 under ZFC condition. The inset shows the $M-H$ isotherms recorded in the first quadrant (from 0 to 90 kOe) at different temperatures.

(LAS) technique [311-313]. The virgin magnetization isotherm curves obtained from the experiments are fitted with the mathematical expression of LAS (equation (5.2) given below). According to LAS, near the saturation magnetization (M_S), the magnetic moment of the samples can be expressed as follows:

$$M = M_S\left(1 - \frac{a}{H} - \frac{b}{H^2}\right) + \chi H \tag{5.2}$$

In the above equation, the term a/H is linked with the structural defects, whereas the magneto-crystalline anisotropy of the material is defined by the b/H^2 term, and the last term χH represents the paramagnetic behavior of the system. The value of b in equation (5.2) is given as $b = \frac{8}{105}\frac{K_1^2}{\mu_0^2 M_S^2}$, where K_1 represents the cubic anisotropy constant and M_S being the saturation magnetization. The corresponding anisotropy field H_K for a cubic crystal with easy direction along the [100] direction has been calculated using the relation $H_K = 2K_1/\mu_0 M_S$. The solid lines in the inset of figure 5.9 represent the best fit obtained using equation (5.2) to the experimental data points shown as scattered symbols. At T = 2 K, the magnitude of K_1 and H_K are 1.616 × 10^6 erg/cc and 5.49 kOe, respectively, which decreases drastically with increasing the temperature. From figure 5.10, we noticed that the temperature variation of K_1 and H_K parameters decrease monotonically with increasing the temperature. These magnitudes of K_1 and H_K are consistent with the previously reported data on and slightly larger than the case of nanoparticles, for example, K_1 ~ 1.8 × 10^5 erg/cc (at T = 4.2 K) for $CuFe_2O_4$ nanostructures [289] and two orders greater than (K_1 = 7.2 × 10^4 erg/cc, H_K = 1.97 kOe) the case of magnesium ferrites aerogels [220]. Interestingly, the results obtained from the current study are

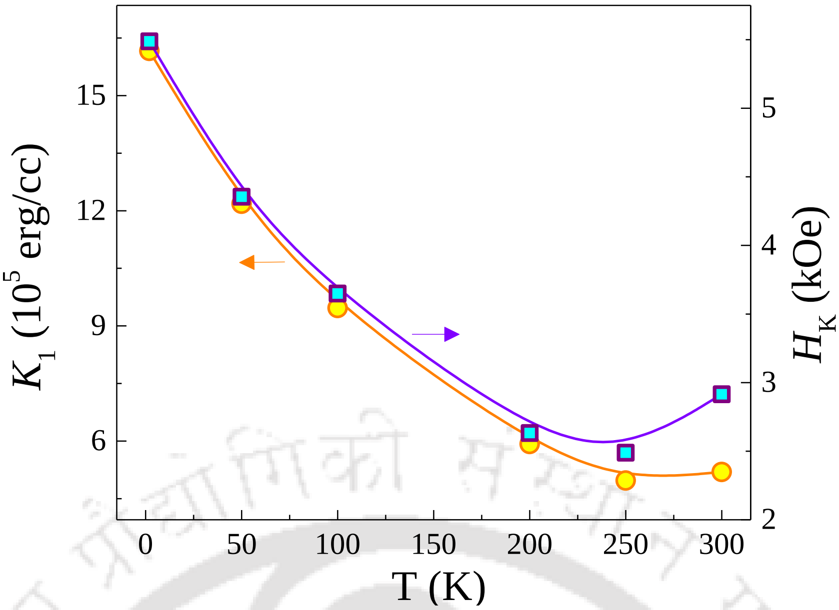

Figure 5.10: Temperature variation of the cubic anisotropy parameter, $K_1(T)$ and the anisotropy field $H_K(T)$ for the composition $x = 0.4$.

comparable to $K_1 = 2.23 \times 10^6$ erg/cc reported by Rondinone *et al.* for $CoFe_2O_4$ nanoparticles of size 8.5 nm using Mössbauer spectroscopy [314]. In the case of Zn-substituted cobalt ferrite, nanoparticles coated with triethylene glycol $K_1 \sim 7.1 \times 10^4$ erg/cc and $H_K \sim 1.9$ kOe, which are significantly lower than the current results [315].

Figure 5.11 shows the temperature variation of the saturation magnetization $M_S(T)$ of $x = 0.4$, which shows a decreasing trend with increasing the temperature. Normally, the spontaneous magnetization in spinel ferrites arises due to the difference in the magnetic moments of cations, which are distributed in the octahedral and tetrahedral sites. The saturation magnetization (M_S) is found to be 2.86 μ_B/*f.u.* at 300 K, which increases to 4.73 μ_B/*f.u.* at 2 K. In figure 5.11, the dotted line represents linear extrapolation of the experimental data, which intersects the temperature axis at 767.74 K (T^*); this value is well above the T_{FiM} (= 534 K), representing that high-field susceptibility is still non-zero till T^*. Although the nonlinear behavior of $M\text{−}H$ loop disappears due to the increasing thermal fluctuations above T_{FiM}, which is typical to the paramagnets, the magnetic moment does not approach exactly to zero value until the measurement temperature approaches T^* [316]. For $x = 0.4$, the magnitude of M_S is found to be ~ 16.08×10^3 emu mol^{-1} (67 emu g^{-1}) at room temperature, which is higher than that of the ball milled prepared nanostructured $CuFe_2O_4$ (26.3 emu g^{-1}) [317], bulk $CuFe_2O_4$ (33.1 emu g^{-1}) [318], nanostructured $CuFe_2O_4$ (37.98 emu g^{-1}) [319], and $CuFe_2O_4$ nanorods (8.35 emu g^{-1}) [320]. For a detailed understanding of the role of Zn dilution on the low temperature magnetic behavior, we measured the virgin $M\text{−}H$ isotherms (as shown in figure 5.12) at $T = 2$ K for various compositions in the range $0 \le x \le 0.6$. It has been observed that the magnitude of M_S increases progressively with increasing x from $x = 0$ to $x = 0.4$ as shown in figure 5.13 (for $T = 2$ K (300 K) M_S increases from 1.64 (1.41) μ_B/*f.u.* to 4.73 (2.86) μ_B/*f.u.*). Such an increase in M_S with the Zn content in $CuFe_2O_4$ may be ascribed

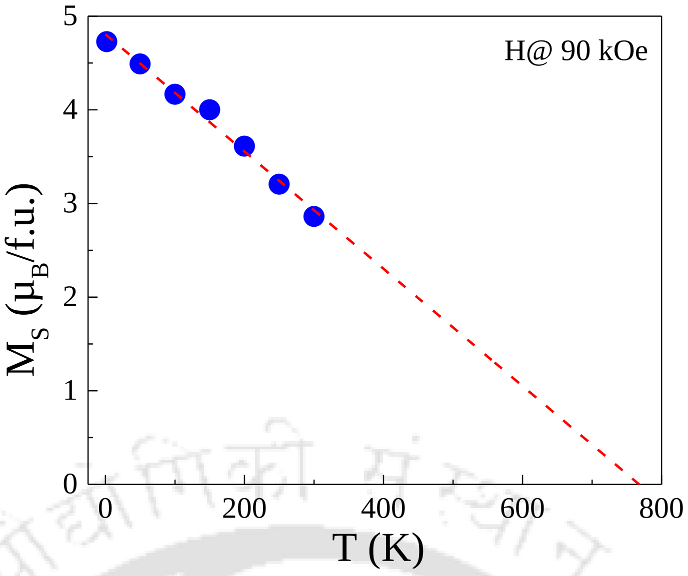

Figure 5.11: Temperature dependence of saturation magnetization $M_S(T)$ obtained from the isothermal magnetization curves (measured till H = 90 kOe) for the composition x = 0.4. The dotted line represents the linear extrapolation.

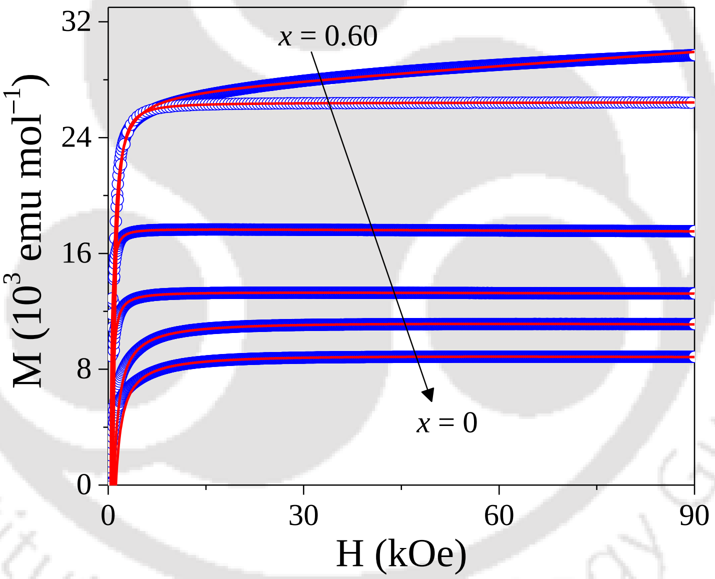

Figure 5.12: Isothermal magnetization (M−H) curves recorded at 2 K for different compositions ($0 \leq x \leq 0.6$) measured in the first quadrant (from 0 to 90 kOe) under ZFC condition.

due to the increase of divalent Fe fraction at the *B* site and a significant increase in the canting angle (triangular Yafet−Kittle angle) between the magnetic ions [321]. But beyond 40 atomic %, it decreases due to competing exchange interaction among the canted spin arrangements on the *B* site [310]. This variation is in well agreement with the variation of exchange constants with composition.

Interestingly, the compositional dependence of anisotropy field $H_K(x)$ and cubic anisotropy constant $K_1(x)$ exhibits very higher magnitudes ~ 1.6 × 10^6 erg/cc and 5.5 kOe, respectively, for x_c (at T = 2 K), but falls beyond it, which is in consonance with the compositional variations of M_S and μ_{eff}. Following a tiny

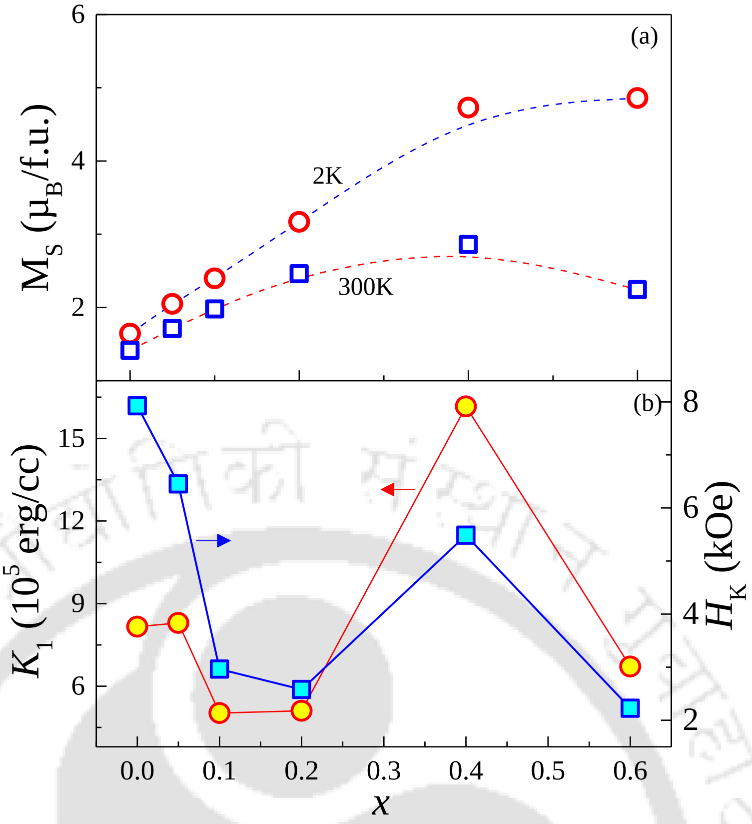

Figure 5.13: (a) Composition dependence of the saturation magnetization $M_S(x)$ for T = 2 K and 300 K, and (b) cubic anisotropy constant $K_1(x)$ (L.H.S.) and the anisotropy field $H_K(x)$ for T = 2 K (R.H.S.).

deviated approach in calculating *b* (in equation (5.2)) for tetragonal systems, the obtained results are consistent with the fact that any change in the crystal structure (from tetragonal to cubic crossover in the present case) is accompanied by a large change in the magneto-crystalline anisotropy of the system [322,323]. Similar trend has been observed in the case of Zn diluted CuFe$_2$O$_4$ thin films and other Zn diluted systems [310,324-326]. It is well known that in cubic crystals, the higher order anisotropy constants are negligible because of the crystal-symmetry, in turn, leading to a smaller value of anisotropy energy and hence anisotropy constant as compared to the lower symmetry-crystals such as tetragonal structure, which is clearly reflected in our measurements across x_p. The compositional variations of K_1 and H_K in the present case are in line with that of μ_{eff} and M_S. The high value of K_1 in the vicinity of x_c can be attributed to the most stable canted spin configuration of the system.

5.4. Summary:

In this section we provide salient features of the important results presented in this chapter on the Cu$_{1-x}$Zn$_x$Fe$_2$O$_4$ ($0 \leq x \leq 0.6$) system. The electronic structure probed by the x-ray photoelectron spectroscopy reveals the divalent oxidation state of both Cu and Zn in which the 2*p* orbitals exhibit doublet corresponding to 2$p_{3/2}$ and 2$p_{1/2}$ with spin-orbit splitting Δ ~ 19.91 eV and 23.06 eV, respectively, whereas the core level spectrum of Fe-2*p* exhibits Δ ~ 9 eV and 12 eV corresponding to the doublet 2$p_{3/2}$ and 2$p_{1/2}$ of divalent and trivalent Fe, respectively. The crystal structure analysis provides evidence for morphotropic phase boundary between the compositions x = 0.05 and 0.10 across which the crystal structure changes from the tetragonal ($I4_1/amd$) to cubic ($Fd{-}3m$) phase. This structural change leads to a step change in the bond angle (A-O-A and A-O-B) and slight change in the bond length (A-O). Nonetheless, under the dilute limit ($x \leq 0.05$), the investigated system stabilizes in next lower symmetry space group $I4_1/amd$ and influences the magnetic exchange interactions significantly. Detailed temperature and field dependence of magnetization studies reveal that all the compositions orders ferrimagnetically and undergoes transition at low temperatures, which smears-off as the Zn concentration increases. Ferrimagnetic ordering temperature decays quadratically ($T_{\mathrm{FiM}} = y_0 + b_1 x + b_2 x^2$) with increasing composition. On the contrary, μ_{eff} and M_{S} increase from 3.59 μ_{B}/*f.u.* (x = 0) to 5.15 μ_{B}/*f.u.* (x = 0.4) and 1.64 μ_{B}/*f.u.* (x = 0) to 4.73 μ_{B}/*f.u.* (x = 0.4), respectively. Furthermore, magnetization results demonstrate that the ferromagnetic exchange interaction, J_{AB}, between Jahn−Teller active Cu and Fe is dominant for lower and intermediate compositions as compared to J_{AA} and J_{BB}, whereas for higher compositions, J_{AB} becomes negative, implying the onset of strong antiferromagnetic correlations at B sites. On the basis of the evidence gathered from XPS and magnetization data, we conclude that the system exhibits the following complex mixed spinel cationic distribution: $(\mathrm{Cu}_{(1-x)/5}\mathrm{Zn}_x\mathrm{Fe}_{4(1-x)/5})_A[\mathrm{Cu}_{4(1-x)/5}\mathrm{Fe}_{2-4(1-x)/5}]_B\mathrm{O}_4$. Using the low temperature $M{-}H$ isotherms and the law of approach to saturation, we have estimated the cubic anisotropic constant (K_1) and anisotropy field (H_{K}) in which the structural change from tetragonal to cubic is accompanied by a large change in the magneto-crystalline anisotropy. Both the parameters $K_1(x)$ and $H_{\mathrm{K}}(x)$ exhibit decreasing trend with anomalous change across the critical composition x_c = 0.4 ($K_1 \sim 8.2 \times 10^5$ erg/cc (x = 0) to 1.6×10^6 erg/cc (x = 0.4), and $H_{\mathrm{K}} \sim$ 7.9 kOe (x = 0) to 5.5 kOe (x = 0.4)). For a particular composition, the temperature variation (2 K $\leq T \leq$ 300 K) of these parameters, $K_1(T)$ and $H_{\mathrm{K}}(T)$ show a continuously decreasing trend until 250 K and starts increasing beyond this point.

Chapter 6

Dynamical Electron Hopping and Dipole Relaxation in Cu-ZnFe$_2$O$_4$

This chapter presents to us the dielectric studies concerning to the series of systems considered for exploration in Chapter 5. The initial section describes the introductory ideas, aims and objectives behind this work. Next it presents a brief description on the experimental part in line with the previous chapter. Later sections deal with a comprehensive analysis of the dielectric/impedance characterization parameters. Interestingly, the interpretation presented in these sections could establish a strong interlinkage between the important conclusions derived here with its magnetic counterpart (Chapter 5).

6.1. Introduction, Motivation and Objectives:

Spinel (AB_2O_4) compounds whose crystal symmetry departs from the cubic to other Bravais lattices due to the Jahn−Teller (*JT*) distortion in the AO_4 tetrahedron have gained considerable interest because of their remarkable magnetic properties [302,327,328]. Novel magnetic phenomena such as multiferroic, exchange-bias, low-T spin liquid ground states, re-entrant glassy behavior driven by geometric/orbital magnetic frustration and spontaneous dimerization are some of the key features that are observed in systems having *JT* active elements [147,302,329]. Spinels such as Mn_3O_4, $CuFe_2O_4$, $NiCr_2O_4$, $CuCr_2O_4$ and $ZnMn_2O_4$ exhibit distortion in the crystal structure as a consequence of *JT* effect [267,327,330-332]. Tuning such structural distortion by site specific substitution with either magnetic or nonmagnetic elements in the spinel lattice is a well-known strategy to probe the cooperative phenomena like orbital, charge, spin, and lattice degrees of freedom in strongly correlated electron systems [267,309,333-335]. Among the above mentioned systems, $CuFe_2O_4$ (CFO) widely known as cuprospinel or copper ferrite is a well-studied compound due to its unique change in the crystal structure from the high-temperature cubic phase (8.392 Å [291]) to the low-temperature tetragonal phase (a ~ 8.243 Å and c ~ 8.699 Å [2]) along with its ferrimagnetic Néel temperature (T_{FiM}) variation (between 710 and 780 K) and semiconducting behavior [278,336]. Owing to such unique properties, CFO in its bulk form as well as in the form of nanostructures have evolved as a promising material for numerous applications in various sectors such as gas sensors [282], catalysts [284], microwave devices [286], magneto-electronics [288], hydrogen production [287], and spintronics [328]. A recent study by Alghamdi *et al.* revealed that $Cu_{1-x}Zn_xFe_2O_4$ ferrite systems can be utilized as prospective material in temperature sensors for magnetic resonance imaging thermometry [337]. On the other hand, the end compound (x = 1) i.e. franklinite $ZnFe_2O_4$ (ZFO) is also an equally promising candidate like the CFO system except that it exhibits low temperature antiferromagnetic (AFM) properties with Néel temperature T_N ~ 10 K. Moreover, ZFO displays cubic pyrochlore structure in which amendment of cations on both *A* and *B* sites form corner sharing tetahedra and suitable dilutions in ZFO largely affect the *B*−*B* super-exchange interactions [2,338].

However, the physical properties of Zn substituted CFO in the form of either single crystals or polycrystalline bulk grain size systems are seldom noticed in the literature, rather most of the work is concentrated on the nanostructures and thin films of these oxides [292,310,339,340]. Among the little available literature on bulk $Cu_{1-x}Zn_xFe_2O_4$ systems, the frequency dependent dielectric dispersion study by Verma *et al.* reveals that Zn and Mg dispersion in CFO shows cubic crystal structure at room temperature with their dielectric spectroscopy studies revealing an anomaly across 493 K [267]. These authors reported two different regimes (high frequency regime and low frequency regime) in which the ac conductivity follows linear behavior linked with the Jonscher's power law (JPL) of hopping of localized charged states. Another report on the Cu-Zn mixed solid solutions by Ravinder reported that the carrier mobility (μ) and concentration (n) obtained from the thermoelectric power measurements can be tuned from $\mu = 1.19 \times 10^{-8}$ cm^2 V^{-1}s^{-1} ($n = 28.3 \times 10^{22}$ cm^{-3}) to 3×10^{-8} cm^2 V^{-1}s^{-1} ($n = 8.8 \times 10^{22}$ cm^{-3}) with Zn substitution at both the end concentrations $x = 0$ and 1 in $Cu_{1-x}Zn_xFe_2O_4$ [341]. Interestingly, these two parameters ($\mu(T)$ and $n(T)$) show very clear anomaly across the ferrimagnetic ordering temperature of CFO. Similar anomalies are reported in case of temperature dependence of initial permeability ($\mu'(T)$) studies in the solid solutions of $Cu_{1-x}Zn_xFe_2O_4$ ferrites along with the Hopkinson type variation across T_{FiM} [342]. Despite such numerous reports available on the $Cu_{1-x}Zn_xFe_2O_4$ system, a detailed dielectric relaxation studies, temperature dependence of ac conductivity and modulus spectroscopy over a wide temperature interval is still missing in the literature. Such gaps will be filled in this current work. In the present comprehensive dielectric spectroscopy study we focus on the changes occurring in dynamical ac conductivity driven by grain and grain boundary relaxations along with a systematic correlation with the magnetic ordering and structural phase transitions for different compositions of $Cu_{1-x}Zn_xFe_2O_4$.

6.2. Materials and Methodology:

In line with the experimental procedure described in Chapter 5, bulk samples of $Cu_{1-x}Zn_xFe_2O_4$ ($0 \leq x \leq 0.6$) were prepared through standard solid state reaction route using the precursors zinc oxide (ZnO), copper oxide (CuO) and ferric oxide (Fe_2O_3) powders. Stoichiometric proportions of these powders were mixed by means of a FRITSCH based ball-milling machine (with zirconia jar) using ethanol as milling medium for 10 h at 150 rpm speed. The solution was dried, calcined, pelletized, re-grinded and sintered between the temperatures 900 °C and 1050 °C, for lower and intermediate Zn compositions, respectively. The detailed synthesis procedure has been reported elsewhere [2]. The electronic structure and elemental analysis was carried out by x-ray photoelectron spectroscopy (XPS) measurements from Thermo Fisher Scientific ESCALAB 250Xi. A detailed analysis of XPS data and crystal structure particulars (obtained from Rigaku x-ray (Cu-Kα) diffractometer, Model-TTRAX III) are reported previously [2]. Our analysis reveals divalent nature of the Zn and Cu along with the signatures of mixed-valent Fe states (2+ and 3+) for all compositions. The crystal structure remains mostly cubic except for $x \leq 0.05$ where tetragonal crystal structure is stable. The liquid nitrogen based low-temperature (from 77 to 320 K) dielectric spectroscopy measurements were performed using the impedance analyzer from Wayne-Kerr Electronics Pvt. Ltd. (model 1J6530B) which is capable of reaching frequencies up to 20 MHz from 20 Hz with a 1 V ac peak-to-peak amplitude. Whereas, for the high temperature (from 323 to 823 K) dielectric measurements we used Solartron (Model SI1260A) impedance analyzer which is capable of reaching frequencies from 10 μHz to 30 MHz with the 100 mV ac peak-to-peak amplitude of the electric field with ±40 V DC bias voltage capability. For these measurements silver electrodes are deposited on either side of the cylindrical pellet to form a parallel-plate capacitor geometry which is a perfect electrode configuration to measure the dielectric measurements.

6.3. Results and Discussion:

6.3.1. Dielectric Relaxation:

First we discuss the low-temperature dependence of the relative dielectric permittivity ϵ_R and Loss tangent (tan δ) at several frequencies (figure 6.1) for a specific composition x_c = 0.4 of bulk polycrystals of $Cu_{1-x}Zn_xFe_2O_4$ (this critical composition (x_c) has been chosen since, across x_c, the $Cu_{1-x}Zn_xFe_2O_4$ system incline towards the dominant AFM ordering from the ferrimagnetic side as reported earlier) [2]. The insets of figures 6.1(a) and 6.1(b) represent the corresponding frequency dependencies at temperatures between 77 and 320 K. Our system shows a relatively high magnitude of ϵ_R (~ 1935) with moderate losses (tan δ ~ 1.3) at room temperature in the intermediate frequency range 1−5 kHz reflecting the higher polarizability of the

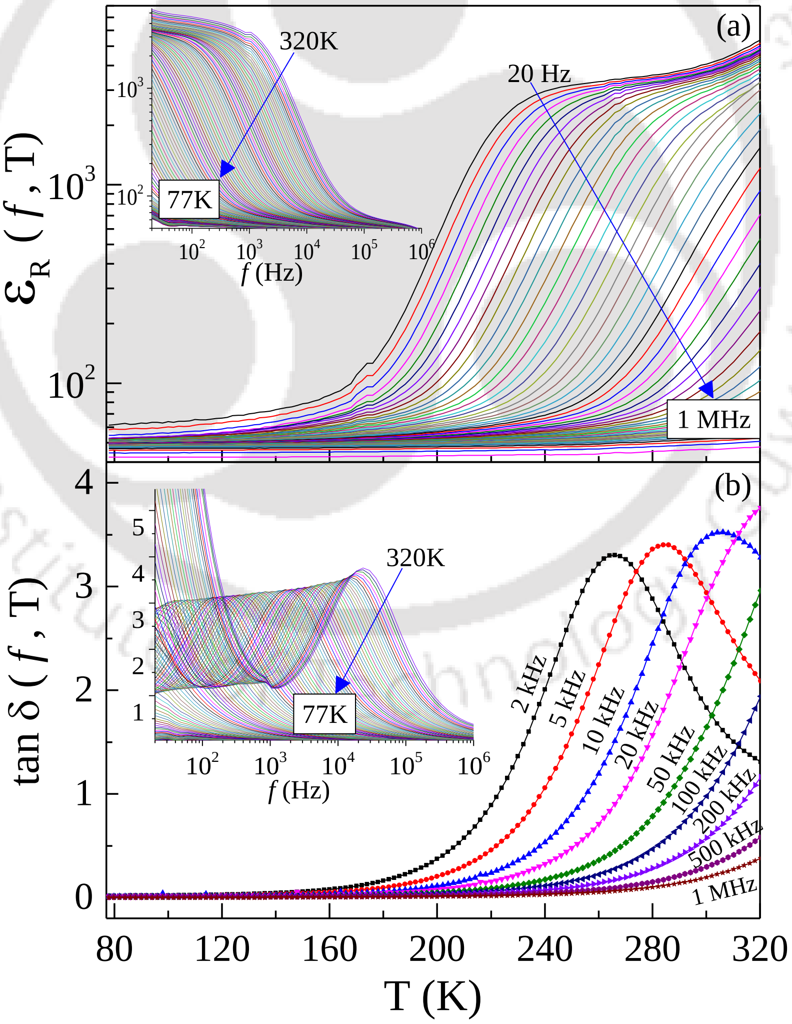

Figure 6.1: Temperature dependence of the relative dielectric permittivity ϵ_R obtained at several frequencies from 20 Hz to 1 MHz (figure (a)) and loss tangent (tan δ) from 2 kHz to 1 MHz (figure (b)) for the composition x_c = 0.4. The insets show the corresponding frequency dependencies at temperatures between 77 K and 320 K.

system. These values are considerably higher than the previously reported values for both the two end compounds CFO (ϵ_R ~ 856) and ZFO (ϵ_R ~ 100) at 300 K and for f = 5 kHz [267,343,344]. Further, higher values of ϵ_R (> 4 × 10^3) are noticed with lowering of frequency up to f = 20 Hz with significant loss in the system as is expected in case of ferrites due to the interfacial and dipolar polarizations which are highly temperature dependent [345-347]. Nevertheless, at higher measurement temperatures (323 K $\leq T \leq$ 823 K) and high frequencies (which will be discussed later) further higher magnitudes of ϵ_R is noticed which might be due to the evaporation of Zn^{2+} ion that escape from the lattice by acquiring thermal energy and resulting in oxygen vacancies followed by the formation of Fe^{2+} ions [267,348]. This scenario is obvious in the present system as evident from the XPS spectra where the signatures of divalent Fe are obtained which is in-line with the previous study [2]. It is interesting to note that a broad hump noticed between 200 and 230 K at low-frequencies shift to the higher temperature side with drastic decrease in its magnitude at higher measuring frequencies which is consistent with the temperature dependent loss tangent (tan δ) clearly revealing the presence of dielectric relaxation (figure 6.1(b)). As the oscillating dipoles are directly coupled to the applied external oscillating field one can expect maximum absorption of the energy and reaching a peak maximum

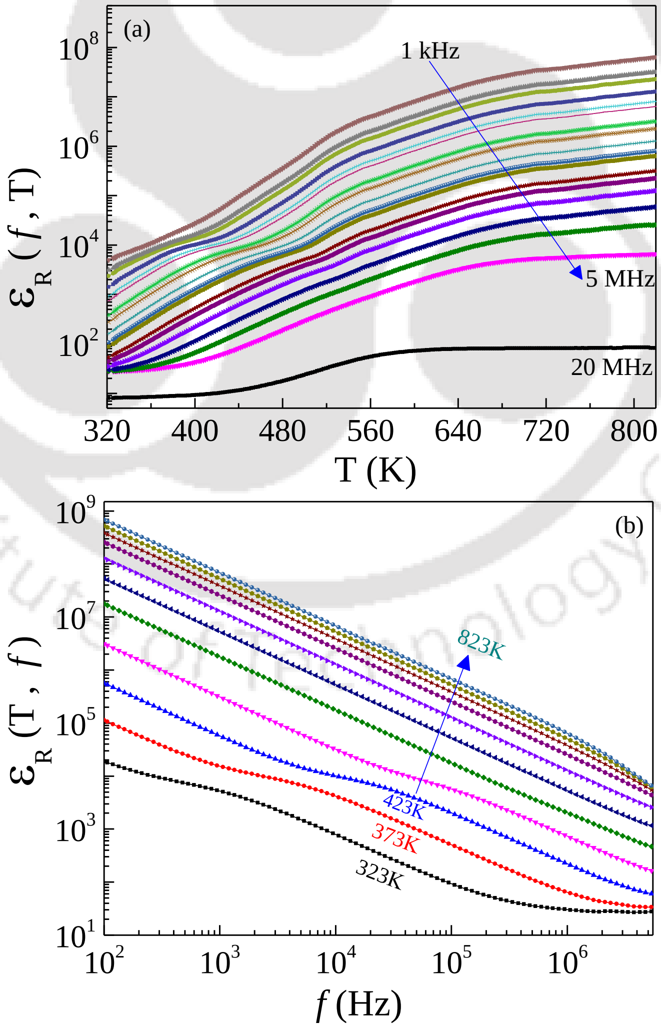

Figure 6.2: Variation of the measured relative dielectric permittivity ϵ_R (a) with temperature at frequencies between 1 kHz and 20 MHz and (b) with frequency at various temperatures between 323K and 823K, for x_c.

in tan δ. The low frequency dispersion of loss-tangent also represents heat dissipation caused by the domain wall motion, since it follows the applied electric field [349].

Considering the conduction process to be a result of hopping of charge carriers, the dielectric relaxation takes place when the hopping frequency of the charge carriers becomes roughly equivalent to that of the frequency of the externally applied electric field. In the present case one can clearly notice the shift of peak in tan δ towards the higher temperature side due to thermal activation of such hopping charge carriers (mostly dipolar kind) resulting in increase of the hopping rate which is usually noticed in most of the ferrites in bulk form [267,345]. Here one cannot rule out the influence of interfacial loss and the loss from grain boundary conductivity at lower frequencies, yet at higher frequencies these losses are negligible resulting in drastic falloff of ϵ_R [350-352]. The frequency dependencies of dielectric permittivity ($\epsilon_R(T, f)$) and loss tangent (tan $\delta(T, f)$) for various temperatures between 77 and 320 K are shown in the insets of figures 6.1(a) and 6.1(b). The decrease of $\epsilon_R(T, f)$ with increasing frequency can be explained by the well-known Koop's phenomenological theory, which assumes that the dielectric is a Maxwell−Wagner inhomogeneous type medium consisting of conducting grains separated by highly resistive grain boundaries (in later sections we provide further evidence for higher grain boundary resistance than that of grain using the analysis based on Nyquist plots) [352-354]. The inset of figure 6.1(b) contains the dispersion in tan δ at several temperatures representing distinct relaxation process occurring in the system. Here the peak frequencies (ω_p) denote the dipolar relaxation frequencies whose temperature dependence is given by the below relation (equation (6.1)) through which one can probe the activation energy of the dipoles:

$$\omega_{\mathrm{p}} = \omega_0 \, exp\left(\frac{-E_{\mathrm{D}}}{k_{\mathrm{B}}T}\right) \tag{6.1}$$

In the above equation ω_0 is the pre-exponential factor, E_D is the activation energy, k_B is the Boltzmann's constant and T is the temperature [355]. From the slope of logarithmic plots of $Ln\ \omega_p$ versus $1/T$ we obtained E_D = 264 meV. Following the Verwey and de-Boer electronic conduction mechanism in the ferrites, the peak in loss tangent can occur when the hopping frequency of electrons between Fe^{2+} and Fe^{3+} is equivalent to the frequency of applied electric field (i.e. the resonance condition $\omega\tau = 1$ is satisfied) [356-358]. We believe that the same state of charge transfer mechanism may arise in the present case at low temperatures.

On the other hand, the high temperature (323 K $\leq T \leq$ 823 K) behavior of $\epsilon_R(f, T)$ is quite unique which shows (figure 6.2(a)) a plateau region over a wide temperature range at high frequencies (5 to 20 MHz). However, $\epsilon_R(f, T)$ displays a uniformly increasing trend for all the frequencies below 5 MHz with increasing the temperature, the magnitude of ϵ_R is as high as 56.8 × 10^6 at 800 K for f = 1 kHz. While the frequency dependence of ϵ_R exhibits decreasing trend almost linearly (6500 for 5 MHz) with increasing the frequency as shown in figure 6.2(b). These magnitudes are much higher than those found for bulk CFO (ϵ_R ~ 450 at 500 K) prepared via chemical co-precipitation route [267]. Recent studies reported ϵ_R ~ 2500 at 673 K in case of bulk ZFO system synthesized by solid state reaction method which is the end compound in present case whose ϵ_R values are larger in comparison to the literature data [343].

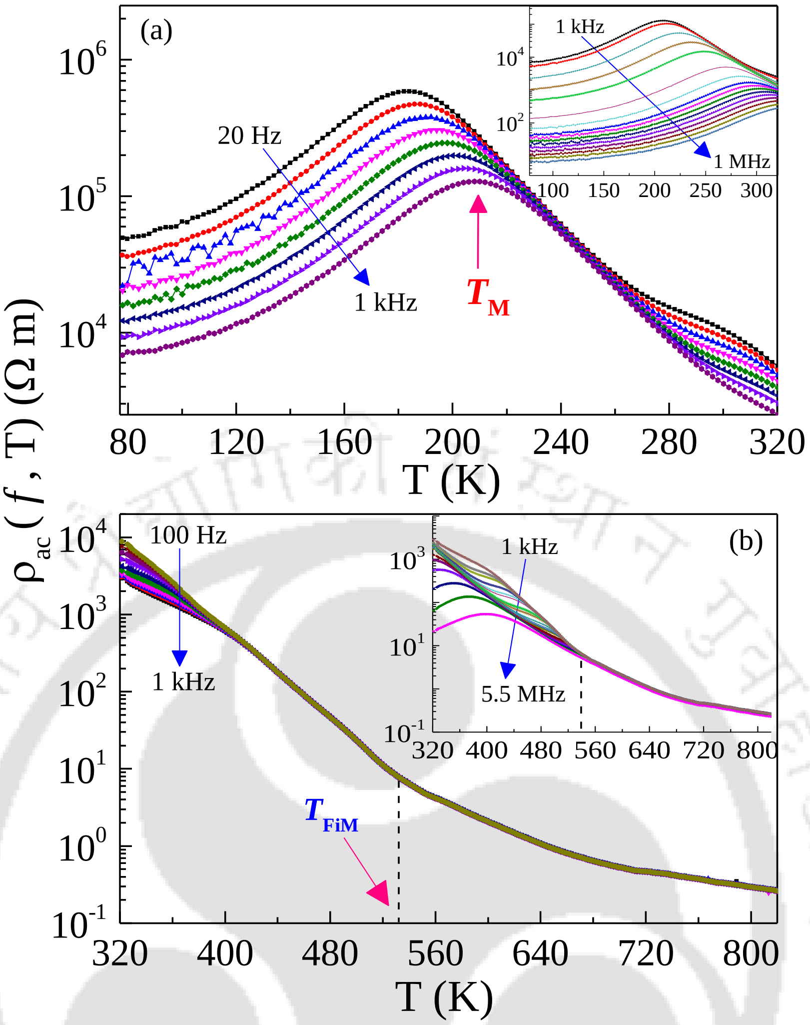

Figure 6.3: Temperature variation of ac resistivity (a) in the low temperature region 77 K ≤ T ≤ 320 K and (b) in the high temperature region 323 K ≤ T ≤ 823 K. The main panels show the data obtained for $f \leq 1$ kHz and the insets show the same for $f \geq 1$ kHz for the composition x_c.

6.3.2. Arrhenius and Variable Range Hopping Conduction:

In order to precisely understand the ac conductivity mechanism a detailed analysis of the temperature dependence of ac resistivity ($\rho_{ac}(f, T)$) is presented below. The main panels in figures 6.3(a) and 6.3(b) show the variation of $\rho_{ac}(f, T)$ for two different temperature regimes from 77 to 320 K and 323 to 823 K, respectively measured between f = 20 Hz and 1 kHz. Whereas, the insets of figures 6.3(a) and 6.3(b) shows the variation of $\rho_{ac}(f, T)$ measured at high frequencies above 1 kHz up to MHz range. At low temperatures $\rho_{ac}(f, T)$ exhibits cusp like behavior for all frequencies in which the peak maximum of ρ_{ac} (T_M = 208 K, for f = 1 kHz) shifts systematically towards the higher temperature side (T_M = 350 K, for f = 1 MHz) which is associated with the transition noticed in the temperature dependence of magnetization (figure 6.4). It is interesting to note that at higher temperatures all the $\rho_{ac}(f, T)$ merged into one single curve (dotted lines in figure 6.3(b)) across the ferrimagnetic Néel temperature, T_{FiM} (= 534.3 K) [2].

Generally, depending on the available sites in a crystal structure different kinds of jump lengths are

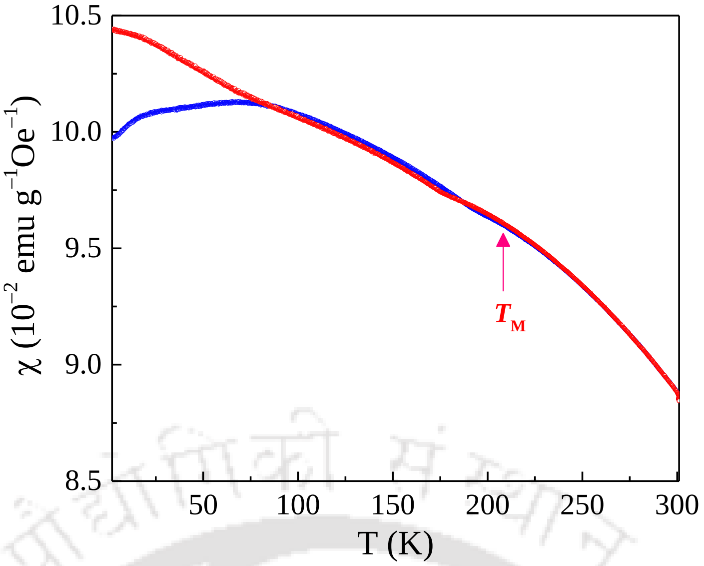

Figure 6.4: Temperature variation of the dc magnetic susceptibility $\chi(T)$ measured at a constant magnetic field H = 500 Oe under zero-field-cooled ZFC (blue) and field-cooled FC (red) conditions for x_c = 0.4. T_M represents the transition temperature due to change in the magnetic ordering.

categorized based on the potential barriers and reorientational arrangements of the ions which leads to different frequency as well as temperature dependence of conductivity (σ_{ac}). Thus in order to study the underlying hopping mechanism, we first verified the Arrhenius relation given below because this mechanism provides at least one or two very well-defined activation energies that belong to the causal hopping processes which are normally preserved over wide range of frequencies [359].

$$\sigma_{ac}T = \sigma_0\, exp\left(\frac{-E_A}{k_B T}\right) \tag{6.2}$$

The slope and intercept of the plots of $Ln\ \sigma_{ac}T$ *vs.* 1000/T for the high temperature (425−500 K) regions yields the magnitudes of pre-exponential term σ_0 ~ 7.976 × 10^7 K Ω^{-1}m^{-1} and 4.338 × 10^6 K Ω^{-1}m^{-1} for f = 1 kHz and 5 MHz, respectively, and the activation energy of conduction electrons E_A ~ 656 and 495 meV for f = 1 kHz and 5 MHz, respectively. But for the low temperature (250−300 K) region the experimental conductivity data deviates from the fitting line indicating the existence of different conduction mechanism. Therefore, we used the variable-range hopping (VRH) conduction mechanism to describe the temperature dependence of conductivity by means of the equation given below [360-363].

$$\rho_{ac}(T) = \rho_0\, exp\left(\frac{T_0}{T}\right)^n \tag{6.3}$$

Here, the parameter ρ_0 is the pre-exponent factor, 'n' is the exponent and T_0 is the characteristic temperature coefficient (usually the magnitude of n decides the nature of the hopping process; if it is equal to −1/4 then the conduction process occurs through the Mott's VRH mechanism). These parameters were extracted from the intercepts and slopes of the logarithmic variation of ρ_{ac} versus $T^{-1/4}$ plots as shown in figure 6.5 where the red solid lines represent the linear fits (of equation (6.3)) to the experimental data points (scattered circles).

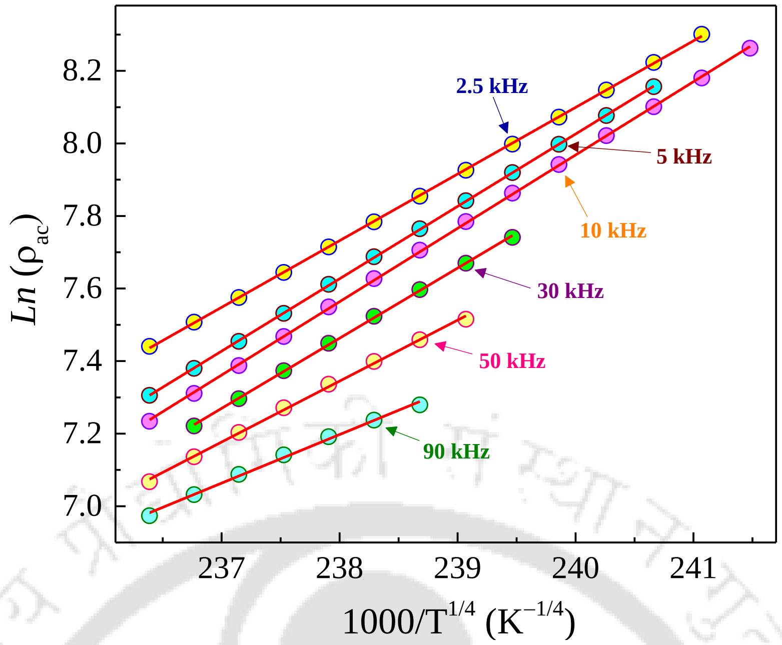

Figure 6.5: Logarithmic variation of ρ_{ac} with temperature [$Ln\ \rho_{ac}$ *vs.* $T^{-1/4}$] of x_c for some selected frequencies.

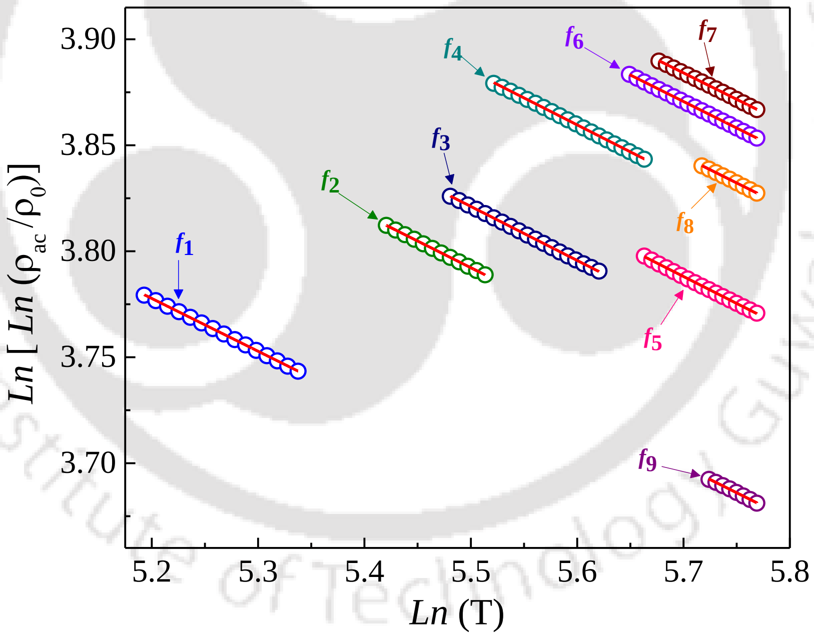

Figure 6.6: Variation of double logarithmic function of ρ_{ac}/ρ_0 with $Ln\ T$ for some selected frequencies f_1 = 20 Hz, f_2 = 200 Hz, f_3 = 500 Hz, f_4 = 1 kHz, f_5 = 2.5 kHz, f_6 = 5 kHz, f_7 = 10 kHz, f_8 = 30 kHz and f_9 = 50 kHz, for x_c.

In order to confirm this, we used the ρ_0 values obtained from figure 6.5 and plotted the double logarithm plots of (ρ_{ac}/ρ_0) as a function of $Ln\ T$ for several frequencies (shown in figure 6.6). Consequently, the magnitude of the slopes obtained from the above graphs were found to be ~ −0.25, affirming the validity of equation (6.3) and thus providing substantial evidence to Mott's VRH mechanism of charge transport in the investigated system in the low temperature regime. Usually, this model is widely adopted to describe the conductivity in strongly disordered systems where the charge-carriers are tightly localized. Nevertheless, in high entropy spinel oxides the occurrence of VRH at higher temperatures is quite possible when the ionization energy of the substituent element is high enough to substantiate such type of conductivity. Yet, in the present case, for temperatures beyond $T_{\rm M}$ we have calculated the hopping energy of activation from the modified temperature dependence of ac conductivity relation is:

$$\sigma_{\rm ac} = \sigma_0 \; exp\,[-B/(T^{1/4})] \tag{6.4}$$

In the above equation $B = 4E_{\rm A-VRH}/(k_{\rm B}T^{3/4})$ and $E_{\rm A-VRH}$ is the hopping activation energy [364,365]. From the mathematical fits of the experimental data to the above expression we have evaluated the activation energies of hopping of charge carriers at a specific temperature within the grains ($E_{\rm G}$) and grain boundaries ($E_{\rm GB}$) (as shown in the figure 6.7). Here, the increasing slope regions of the two semi-circles in Nyquist plot (discussed later) provides us the selected frequency values to calculate the equivalent activation energies. Figure 6.7 shows the frequency variation of the magnitudes of $E_{\rm GB}$ and $E_{\rm G}$ (at 300 K) which increases progressively following a quadratic variation ($y_0 + b_1 f + b_2 f^2$) with increasing f. The corresponding parameters being y_0 (= 119.3 meV) and constants b_1 (= 1.43 × 10^{-5}) and b_2 (= −3 × 10^{-9}) for the grain boundary case and y_0 (= 38.2 meV), b_1 (= 7.55 × 10^{-8}) and b_2 (= −9.5 × 10^{-14}) for that of the grain counterpart. At room temperature the average activation energies are found to be $E_{\rm GB}$ = 131.1 meV and $E_{\rm G}$ = 52.2 meV for $x_{\rm c}$ = 0.4, suggesting the highly resistive nature of the former than the latter. Moreover, the temperature variation of activation energy $E_{\rm A-VRH}$ (corresponding to the Grain contribution) at 1 kHz frequency is depicted in the inset of figure 6.7 which varies linearly with temperature from 114.6 meV (T = 250 K) to 131 meV (T

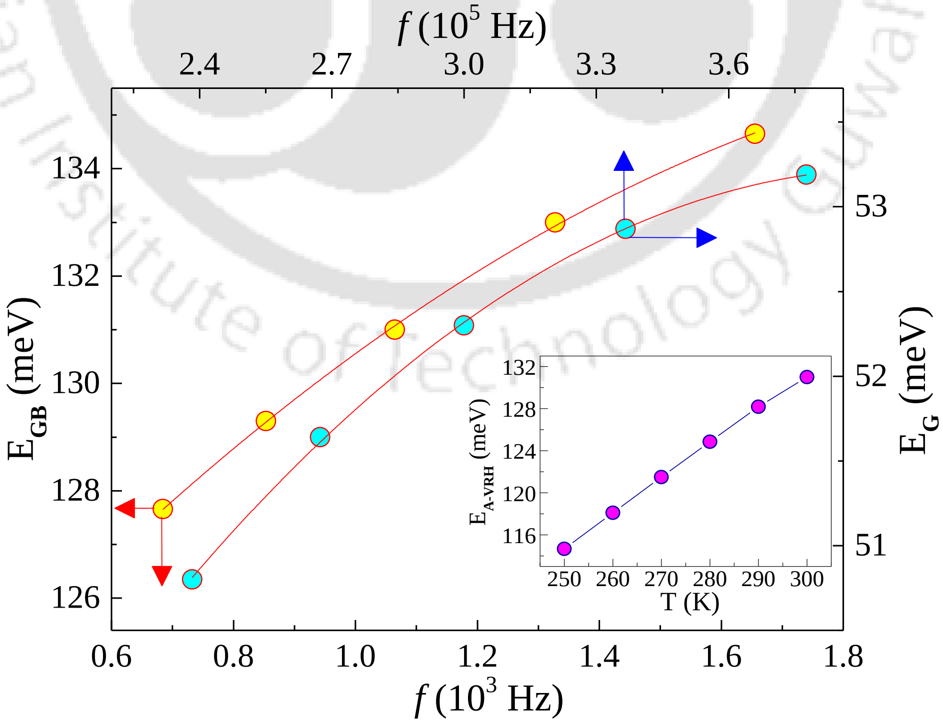

Figure 6.7: Activation energies for grain boundary ($E_{\rm GB}$) and grain ($E_{\rm G}$) obtained for the corresponding frequencies at T = 300K for the composition $x_{\rm c}$. The inset shows the variation of $E_{\rm A-VRH}$ with temperature at 1 kHz.

= 300 K). Similar trend of $E_{\mathrm{A-VRH}}$ has been reported by Zheng *et al.* on the spinel $\mathrm{Ni_{0.5}Zn_{0.5}Fe_2O_4}$ magnetoceramic system in which the localized polarons, LPs (originating from intrinsic oxygen = 300 K). Similar trend of $E_{\mathrm{A-VRH}}$ has been reported by Zheng *et al.* on the spinel $\mathrm{Ni_{0.5}Zn_{0.5}Fe_2O_4}$ vacancy) dominate the overall conductivity of the system; such LPs are responsible for the VRH hopping in this system. For all the temperatures below 235 K till 130 K, the LPs get frozen which are usually active at temperatures above 235 K [365]. However, in our case the presence of small and large polarons (for x = 0, 0.05) and reorientation of localized electrons (for $x \geq x_c$) play major roles for the conduction process (this aspect is discussed in later sections).

Compounds with lower and intermediate compositions (where tetragonal distorted systems of space group $I4_1/amd$ are expected to be more) show less average activation energies (figure 6.13) as compared to the systems with cubic-spinel symmetry ($Fd{-}3m$) which saturates at 130 meV for higher compositions ($0.1 \leq x \leq 0.6$). These results are in consonance with the magnetization data reported previously in these systems [2]; for example, the parameters such as effective magnetic moment μ_{eff}, anisotropy field (H_K) and anisotropy constant (K_1) shows similar trend as that of dielectric data with increasing the composition.

6.3.3. Concept of Polaron:

On the other hand, the frequency dependence of ac conductivity $\sigma_{\mathrm{ac}}(T, f)$ for $\mathrm{Cu_{0.6}Zn_{0.4}Fe_2O_4}$ system are shown in figure 6.8(a) (between 77 and 320 K) and figure 6.8(b) (between 323 and 823 K). These plots exhibit two frequency-independent plateaus at low and mid-frequency regions with a clear discontinuity between these regions achieving higher conductivity in the high frequency dispersion region for 150 K $< T \leq$ 423 K. The plateau regions completely disappeared and a single frequency independent plateau appears throughout the complete frequency range for $T \geq$ 523 K. The origin of frequency dependence of conductivity lies in the relaxation phenomena arising due to the mobile charge carriers. Generally, at low frequencies, there exists a frequency independent plateau region (dc conductivity σ_{dc}); the charge conduction process occurs through inestimable paths of long-range translational motion of the charge carriers. Such behavior is explained on the basis of Funke's jump relaxation model [366,367]. According to this model, the electrons undergo successful hopping to their neighboring vacant sites at low frequencies (with long time period) and lead to the long-range translational motion of charge carriers which contributes to the dc conductivity [367]. While the frequency dependent behavior of conductivity is explained on the basis of JPL which is given by:

$$\sigma_{\mathrm{ac}}(\omega) = \sigma_{\mathrm{dc}} + A\omega^s \tag{6.5}$$

where ω (= $2\pi f$) represents the angular frequency, σ_{dc} is the frequency independent part of the conductivity. The coefficient A and exponent s are temperature and material intrinsic property dependent constants [368-369]. It is well known that the term $A\omega^s$ characterizes all the dispersion phenomena derivable from the magnitude of exponent (s). Usually, the magnitude of 's' lies any value between zero and unity popularly known as universal dielectric response (UDR), yet examples for which $s > 1$ do exist [370]. From figure 6.8, it is clear that after the dc plateau region only one dispersion region appears at high frequencies.

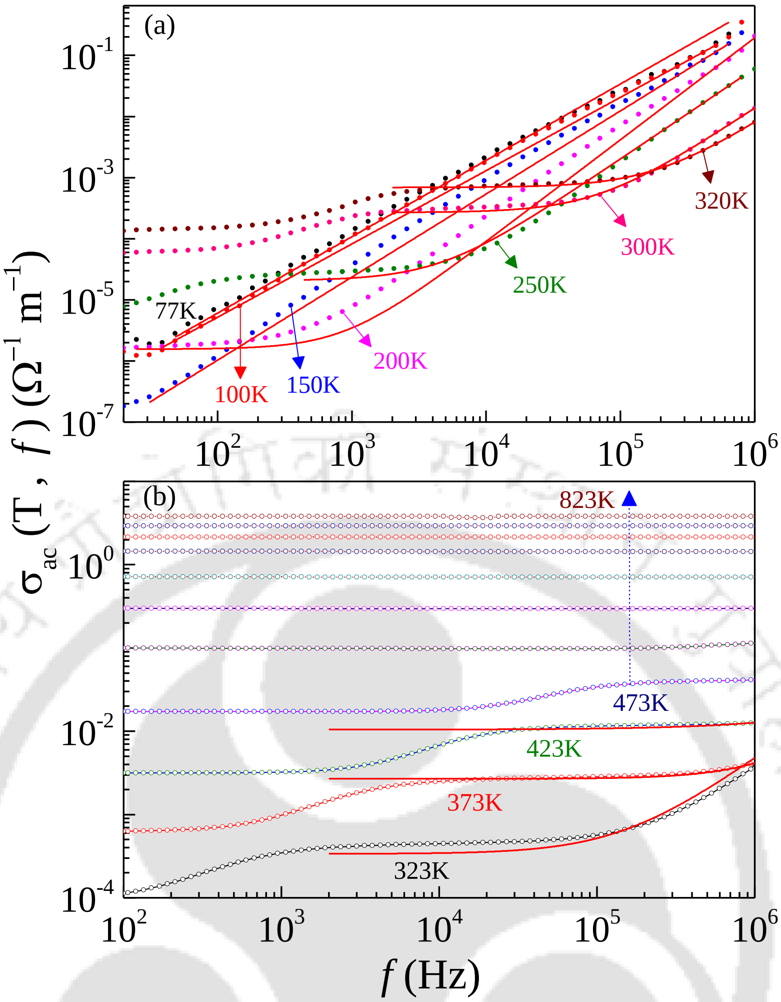

Figure 6.8: Frequency dependence of ac conductivity of x_c composition measured at different temperatures (a) from 77 K to 320 K and (b) from 323 K to 823 K. The solid red lines are the fitting of the data to Jonscher's Power Law.

In order to probe the underlying conduction mechanism, we have fitted the $\sigma_{ac}(T, f)$ data to the equation (6.5). The experimental data points are represented by the scattered solid circles in figure 6.8(a) and by hollow circles in figure 6.8(b), while the solid red lines represent the best fit to the data using the equation (6.5). The temperature variation of the frequency exponent s for different levels of Zn dilution are shown in figure 6.9 where, the hollow symbols representing the $s(x, T)$ values are obtained from the JPL fits to the corresponding conductivity data. For the undoped and moderate substitution levels of Zn (x = 0.05), the magnitude of s lies between 0.6 and 0.8 and decreases progressively as the temperature increases from 150 to 320 K preceded by the increasing trend. These results are in good agreement with the non-overlapping small polaron tunneling (NSPT) mechanism followed by the correlated barrier hopping (CBH) of large polarons as well at higher temperatures [371-373]. Nonetheless for higher compositions ($0.4 \leq x \leq 0.6$), magnitude of s is mostly within the range $1 < s < 2$ (follows Double Power Law), corresponding to localized/reorientational hopping motion of charge carriers [366,374]. Thus, the conduction in the Zn rich samples can be attributed to the back and forth electron hop between the localized states in permanent or induced dipoles present in the system.

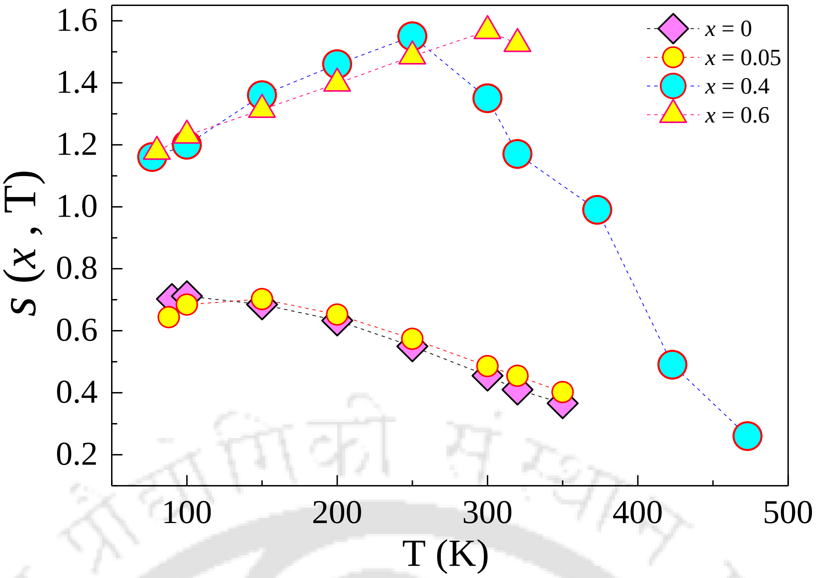

Figure 6.9: Frequency exponent (*s*) values obtained from JPL fit at different temperatures.

For x_c, the magnitude of *s* increases initially from 1.16 (for T = 77 K) to a maximum value of 1.55 at peak temperature T_S = 250 K, then decreases to 0.26 (T = 473 K) and becomes insignificant beyond 473 K. This behavior is in accordance with the analysis of Nyquist plots acquired at different temperatures. Similar trends are observed for all the compositions with shifting of T_S to lower temperatures with decreasing *x*. For any particular (moderate) frequencies T_S is associated with the short-range to long-range hopping of the charge carriers having diverse relaxation times with varied composition, such behavior matches well with the modulus plot (M'' *vs.* *f*) results discussed below.

6.3.4. Temperature Dependence of Complex Modulus Spectra:

To probe the exact capacitive dielectric relaxation process and contributions of space charge injection, electrode polarization and separating the local behavior of electrode effect we performed the complex dielectric modulus spectroscopy from the real (Z') and imaginary (Z'') parts of impedance (Z) using the relations $M' = \omega C_0 Z''$ and $M'' = \omega C_0 Z'$ [375-380]. The frequency dependence of real and imaginary components of the modulus spectra ($M'(T, f)$ and $M''(T, f)$), for x_c = 0.4 between 77 and 320 K are shown in figure 6.10. For all the temperatures, we noticed two broad humps indicating the presence of multiple dielectric relaxation processes. Moreover, a continuous dispersion has been noticed in M' values with the increase of frequency and finally saturates at a maximum asymptotic value on approaching the high frequency regime (figure 6.10(a)). Such tendency of saturation suggests the short-range mobility of charge carriers and lack of the restoring force leading to low-mobility of charge carriers in the presence of an induced electric field [381]. Also, very small value of M' in the low frequency range supports the argument that the conduction phenomena is due to long-range mobility of charge carriers with negligible electrode polarization contribution [382]. These observations are supported by the $M''(T, f)$ plots as well, as shown in figure 6.10(b)

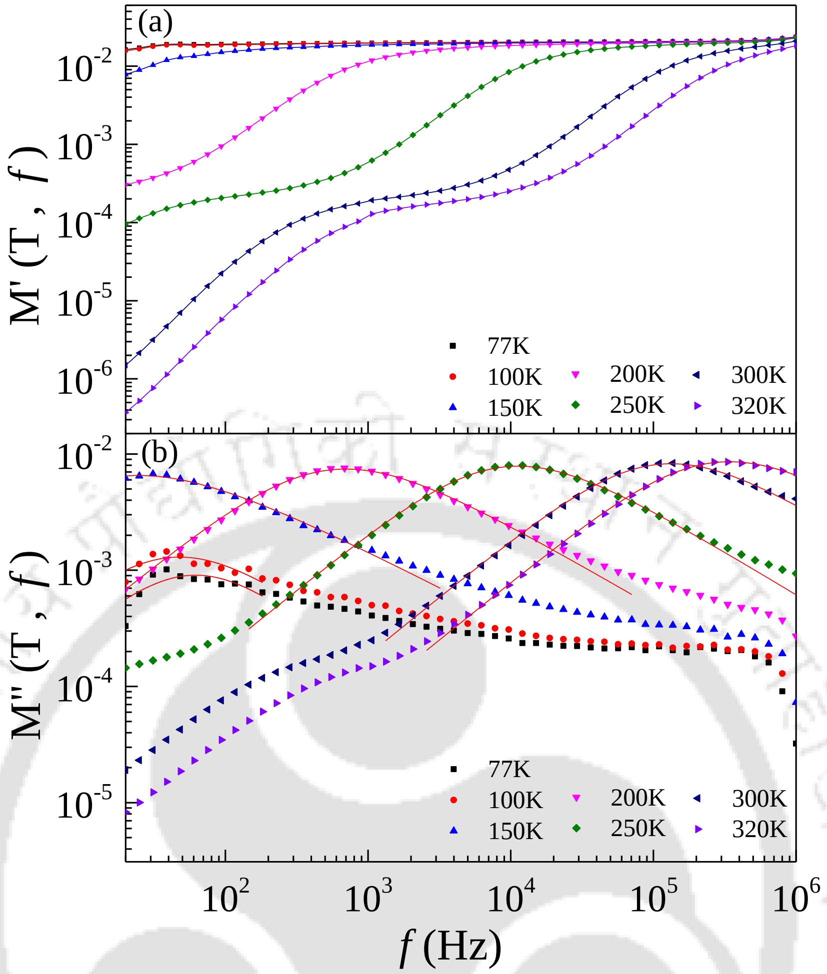

Figure 6.10: Variation of (a) real part and (b) imaginary part of modulus spectra with frequency measured at temperatures between 77 K and 320 K for x_c = 0.4.

which comprises of two types of relaxation processes ascribed to the grain boundary and grain contributions (low frequency peak is attributed to the grain boundary relaxation).

Following the below expression (equation (6.6) involving the Laplace transformation of the complexelectric modulus (M^*), we analyzed the frequency dependence of M'' data as given below.

$$M^* = M_\infty \left[1 - \int_0^\infty e^{-jft} \left(\frac{d\varphi}{dt}\right) dt\right] \tag{6.6}$$

In the above equation (6.6), M_∞ (= ϵ_∞^{-1}) is the inverse of the high frequency asymptotic value of the real part of dielectric permittivity, ϵ_∞, while the relaxation function $\varphi(t)$ provides information related to the time evolution of the electric field (**E**) within the compound [383,384]. It is clear that the asymmetric nature of the plots in figure 6.10(b) provide signatures of non-exponential behavior of the electrical modulus described by a non-exponential decay function and the parameter β representing the Kohlrausch−Williams−Watts (KWW) parameter which is expressed as [385,386]:

$$\varphi(t) = exp\left[-\left(\frac{t}{\tau_0}\right)^{\beta}\right] \tag{6.7}$$

where τ_0 is the characteristic relaxation time. Usually, the stretched exponential parameter decreases with upsurge in the relaxation time distribution [387]. In the above relation, β lies in the range $0 < \beta < 1$ and it characterizes the degree of departure from the linearity (as β approaches unity the system exhibits Debye relaxation). Whereas, $\beta \rightarrow 0$ relates to the extent of interaction between the ions that takes place in the system. Following to the modified analysis of KWW function by Bergman we performed the mathematical fitting approach which allowed direct assessment of modulus plots in the frequency domain as follows [387]:

$$M''(f) = \frac{M''_{max}}{\left[(1-\beta)+(\beta/(1+\beta))\left[\beta\left(\frac{f_{max}}{f}\right)+\left(\frac{f}{f_{max}}\right)^{\beta}\right]\right]} \tag{6.8}$$

Here M''_{max} is the peak value in the imaginary part of M^* with corresponding frequency f_{max}. The red solid lines in figure 6.10(b) represents the nonlinear fitting of the above equation with the experimentally obtained modulus data for the current investigated system. Table 6.1 shows the corresponding parameters extracted from the fitting. The values of β are found in between 0.65 and 0.92 suggesting that non-Debye type relaxation process prevails in this system (for all the measurement temperatures from 77 to 150 K). Moreover, the absolute value of M''_{max} increases with increase of the temperature (as shown in figure 6.10(b)) which is a common behavior, yet here in the present case the peaks shift to lower f side with increasing the measurement temperature from 77 to 150 K, but M''_{max} shift to higher f side for $T > 150$ K. Such anomalous change noticed in the low temperature regime is consistent with the conducting behavior inferred from the Nyquist plot in the same temperature range as discussed below. The frequencies below the M''_{max} corresponds to the range in which the charge carriers are mobile for long-distances mostly within the grain boundaries, whereas, the frequency range above the M''_{max} are linked to the localization of the charge carriers within a potential well of grains which undergo only short-range oscillations [388].

Table 6.1: The list of parameters obtained at several temperatures by fitting the modified KWW function [equation (6.8)] to the frequency dependent modulus (M'') data. The parameter M''_{max} is the maximum value on imaginary modulus axis corresponding to the relaxation frequency (f_{max}), τ_0 is the relaxation time, whereas, β is the stretched exponent.

T (K)	M''_{max} (10^{-3})	f_{max} (Hz)	τ_0	β
77	1	39	25.7 ms	0.92
100	1.6	38	26.9 ms	0.84
150	6.7	31	32.2 ms	0.65
200	7.5	685	1.46 ms	0.72
250	8.1	10742	93 μs	0.75
300	8.4	122450	8.17 μs	0.76
320	8.6	294429	3.4 μs	0.74

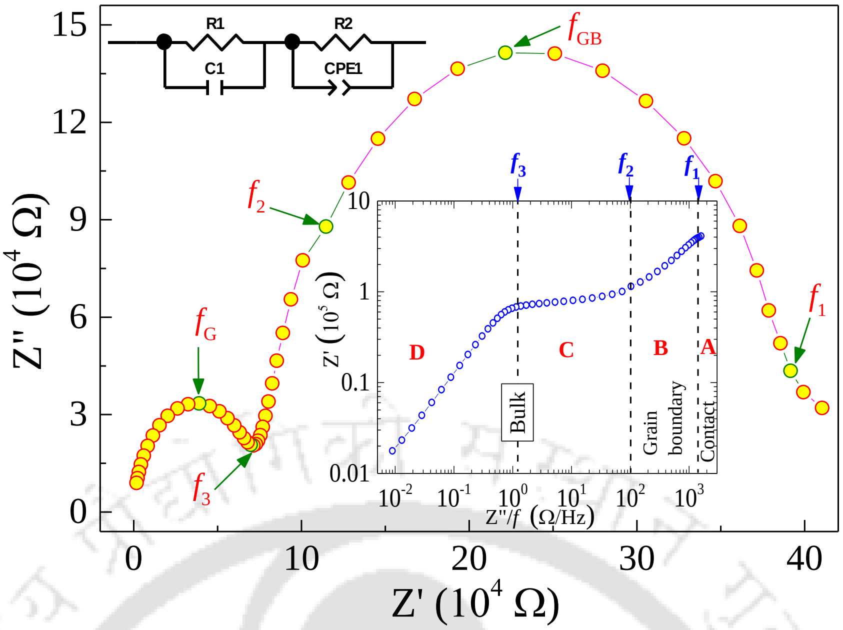

Figure 6.11: Nyquist plot of the composition x_c measured at room temperature. The inset at the top-left-corner represents the equivalent electrical circuit (obtained from the Z−view software) best-fitting with the Z'' *vs.* Z' data points. Another inset (at the centre) shows the alternative representation of the main panel data as Z' *vs.* Z''/f. The symbols f_1, f_2, f_3, f_{GB}, and f_G represents the frequencies 30 Hz, 900 Hz, 15 kHz, 300 Hz, and 90 kHz, respectively.

6.3.5. Nyquist Plot Analysis and Activation Energy:

Figures 6.11 and 6.12 presents the Nyquist plots (also popularly known as Cole−Cole plots), at 300 K (and for different temperatures) for x_c which shows three distinct semicircles with tails at the initial and terminal points indicative of overlapped semicircles. Usually, the smaller radius semicircle corresponds to the high frequency regions from the contribution of grains, while the higher radius semi-circles are of low frequency region due to the grain boundary contribution which are consistent with the brick-layer model for a polycrystalline sample [366]. The inset of the figure 6.11 represents Z' versus Z''/f of the data shown in the main panel. Using this illustration one can clearly distinguish four different linear dielectric responses corresponding to the contacts, grain boundaries, and bulk grains contribution as indicated by segments marked by A, B, C, and D with the borderline frequencies f_1 = 30 Hz, f_2 = 900 Hz, f_3 = 15 kHz [389,390]. Therefore, the linear region A represents the dielectric response from the contact, which contributes to the low-frequency tail of the Nyquist plot near the initial points in the main panel, indicating that the contact response can be neglected. The linear region B presents the dielectric response from the grain boundaries, which contributes to the main body of the Nyquist plot, indicating that the low frequency relaxation is a Maxwell−Wagner type of relaxation caused by grain boundaries. The remaining sections C and D are, therefore, arising from the bulk dielectric contributions [390,391]. This indicates that there are two bulk dielectric relaxations present in this sample. Since the peak frequency observed in the frequency dependence of tan δ lies between f_2 and f_3, one can conclude that the dipolar relaxation is prominent in bulk grains, whereas, the relaxation of grains belong to region D. Thus, in the main panel of the Nyquist plot shown in

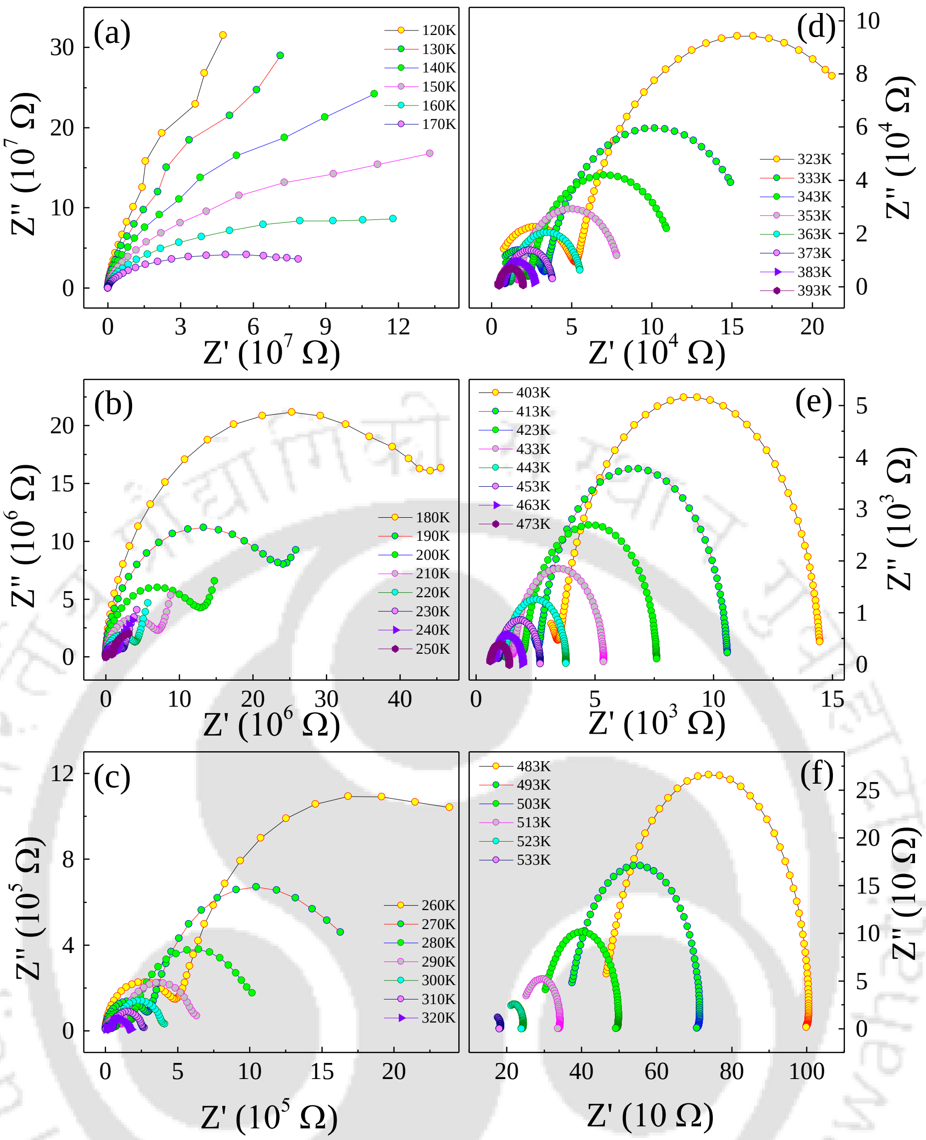

Figure 6.12: (a)−(f) Nyquist plots for the composition x_c = 0.4 at different temperatures from 120 K to 533 K.

figure 6.11, the peak frequencies f_G (= 90 kHz) and f_{GB} (= 300 Hz) correspond to the grain and grain boundary relaxations, respectively which are in-line with the modulus plots. From the relation $\omega_m = 1/RC$; where R is the length of the semi-circle along Z′−axis, we have calculated the grain (grain boundary) capacitance and resistance to be 28.687 pF (1.83 nF) and 63 kΩ (301 kΩ), respectively, signifying the very high resistive nature of the grain boundaries. Besides, it can be observed that the centre of both the semicircles lie above the real axis (depressed semicircles), indicating non-Debye type dielectric relaxation [379].

It is well known fact that the Nyquist plots can be represented by an equivalent electrical circuit consisting of suitable combination of resistance and capacitance network depending on best fit of the model with the experimental data. In the equivalent circuit for polycrystalline Cu$_{0.6}$Zn$_{0.4}$Fe$_2$O$_4$ system (shown as the inset at top-left-corner of figure 6.11 as obtained from the Z−view software) one branch is the parallel *RC* connection related with the sample intrinsic characteristics like interior of the grains and the other branch of the circuit

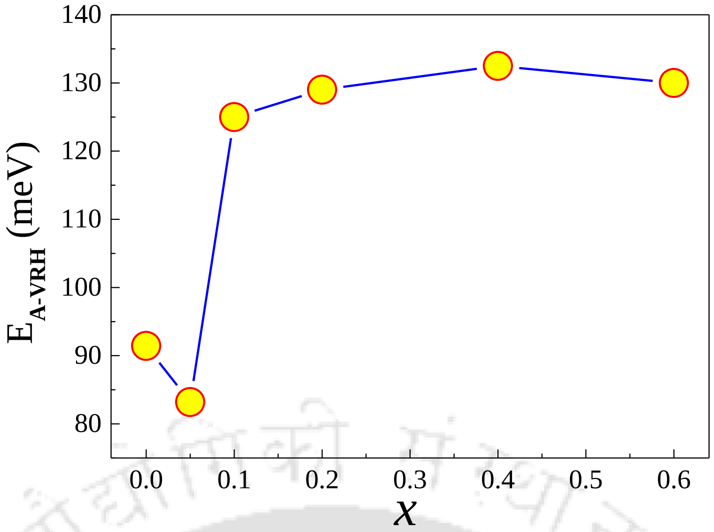

Figure 6.13: Composition variation of $E_{\mathrm{A-VRH}}$ for $Cu_{1-x}Zn_xFe_2O_4$ at room temperature.

corresponds to the interface/grain boundaries [379]. In the present case, one of the two resistive elements is connected with a constant phase element further confirming non-Debye type relaxation response. The absence of a third resistive element confirms negligible contribution from the electrode/contact. We have also performed a detailed temperature variation of Nyquist plots for x_c as shown in the series of figures 6.12(a)−6.12(f), it is interesting to see that for T < 170 K, the bigger semi-circle's magnitude drastically decreases and completely vanishes at low temperatures inferring less resistive grain boundary contribution, but, for T > 473 K, the contribution from grain vanishes, henceforth this indicates the dominance of highly resistive grain boundary network. Upon further rise in the measurement temperature, the magnitude of relaxation time decreases continuously suggesting that the hopping is completely driven by thermal activation process.

6.4. Summary:

A detailed study on dielectric relaxation and ac conductivity of the bulk polycrystalline $Cu_{1-x}Zn_xFe_2O_4$ ($0 \leq x \leq 0.6$) systems has been conducted successfully over a wide temperature interval (77 to 823 K). Our results demonstrated that for a critical composition $x_c = 0.4$, the system displays frequency dispersion in the relative dielectric permittivity $\epsilon_R(T, f)$ and exhibits giant magnitude of ϵ_R with activation energy ~ 264 meV of the dipolar relaxation process. For moderate frequencies at low temperatures, our results validate that the system exhibits VRH of charge carriers while thermally activated Arrhenius like behavior is prevalent at high temperatures. For $x_c = 0.4$, $E_A = 656$ meV (425−500 K) corresponding to Arrhenius like behavior, while $E_{\mathrm{A-VRH}} = 114.6$−131 meV (between 250 and 300 K). We also analyzed the dielectric data in the complex modulus formalism ($M^*(f, T)$) in which two types of relaxation peaks are noticed corresponding to the short-range oscillations of the charge carriers within the potential well of grains and long-range movement of charge carriers across the grain boundaries. The frequency dependence of ac conductivity of the investigated system has been analyzed using the JPL relation: $\sigma_{ac}(\omega) = \sigma_{dc} + A\omega^s$. Based on the magnitudes of the frequency exponent '*s*' we conclude that for $x < x_c$, σ_{ac} follows UDR whereas, for $x \geq x_c$, σ_{ac} follows Jonscher's Double Power Law at lower temperatures. From the temperature dependence of '*s*', it is revealed that the σ_{ac} for low compositions $x < x_c$ (≤ 0.05) follows small polaron tunnelling (NSPT) and CBH model involving large polarons. Whereas, for $x \geq x_c$ the conduction takes place through reorientational hopping of electrons back and forth between the localized states, except for very high temperatures ($T > 400$ K) where thermally activated conduction of electrons succeed.

The depressed semi-circles of the Nyquist plots and lower values of non-exponential parameter (β) from modified KWW function fits to modulus plots suggest the non-Debye relaxation process with a widespread distribution of relaxation times with temperatures. The frequency variation of the activation energies pertaining to the grain and grain boundaries $E_G(f)$ and $E_{GB}(f)$ follow a quadratic variation ($y_0 + b_1 f + b_2 f^2$) with increasing frequency with $y_0 = 38.2$ and 119.3 meV, respectively. At room temperature the average activation energies are $E_{GB} = 131.1$ meV and $E_G = 52.2$ meV for $x_c = 0.4$, suggesting the highly resistive nature of the overall system. A detailed analysis of composition dependence of activation energy E_{A-VRH} (x) reveals that the tetragonally ($I4_1/amd$) distorted systems ($x \leq 0.05$) show less E_{A-VRH} values as compared to those of cubic-spinel symmetry ($Fd{-}3m$) systems which saturates at 130 meV for $0.1 \leq x \leq 0.6$. These results are in consonance with the temperature dependent magnetic susceptibility data reported previously on these systems.

Chapter 7
Conclusions and Prospective of Future Work

This chapter concludes the key outcomes of this thesis work and also paves way for the possible future aspects of this work. In this work we successfully synthesized different Zn-based spinel pyrochlore ferrite systems and investigated their magnetic properties relying on both the dc and ac measurements. Additional support to this study is provided by means of the neutron diffraction, heat capacity and impedance spectroscopy measurements. Below we summarize the important results presented in the different chapters. In the end we discuss about the future scopes that can be derived from this work.

7.1. Conclusions:

Based on the results obtained in Chapter 3 we conclude that the exact cationic distribution of the tetragonal spinel $Zn_{0.8}Cu_{0.2}FeMnO_4$ to be $(Zn_{0.8}{}^{2+}Cu_{0.2}{}^{2+})_A[Fe_{0.4}{}^{2+}Fe_{0.6}{}^{3+}Mn^{3+}]_BO_{4-\delta}$. Analysis of the magnetization data (both dynamical susceptibility and dc magnetization), heat capacity C_p, and neutron diffraction measurements reveal a complex SR ordering without any LR ordering. For $T > 250$ K, the magnetic susceptibility data fits to the Curie−Weiss law which yields the Weiss temperature (θ) $\simeq$ 185 K, signifying very high and dominant FM coupling with the exchange constant $J/k_B = 17$ K. The high-spin states of Cu^{2+} (*A* site) and Fe^{2+} (*B* site), together with the trivalent *B* site ions Mn^{3+} and Fe^{3+} in their low-spin states, lead to the effective magnetic moment $\mu_{eff} = 5.13\ \mu_B$. The saturation magnetization obtained from the *M vs. H* data at $T = 2$ K concludes the ground state spin arrangement: $(Cu^{2+}\downarrow)_A[Fe^{2+}\uparrow, Fe^{3+}\downarrow, Mn^{3+}\uparrow]_B$, which gives evidence that FM clusters interact antiferromagnetically at low temperatures. The typical scaling laws (VFL and PL) fit to the ac susceptibility data (χ'') confirm cluster SG state with an unresolved transition around 9 K. The C_p *vs.* T results obtained in the temperature range 2 K to 200 K for $H = 0$ and $H = 90$ kOe do not show any peak characteristic of LR ordering. However, for $T < 9$ K, C_p follows nearly linear variation with T^2 which is typical of SLs. These results are further in agreement with the neutron diffraction measurements obtained below 9 K and at room temperature. We introduced a new approach to investigate the SL state with the help of thermoremnanent magnetization studies which reveals weakening inter-cluster interaction with increase in temperature.

Chapter 4 follows a different approach to introduce frustration in ZFO by diluting the magnetic interaction with incorporation of low moment ions (Cu^{2+} and Ru^{3+}). The slow spin dynamics of cluster SG spinel $Zn(Fe_{1-x}Ru_x)_2O_4$ investigated in detail along with the effect of *JT* active spin=1/2, Cu^{2+} ions at *B* sites shows the absence of LR ordering. Measurements based on the dynamical ac susceptibility ($\chi_{ac}(f, T)$) and subsequent analysis using the empirical scaling laws reveal the presence of cluster SG state below T_{SG} (17.77 K ($x = 0.5$) and 14 K ($x = 0.75$)). Yet, the analysis of temperature dependent high-field dc susceptibility, χ_{hf} (2 kOe $\leq H \leq$ 20 kOe, T) provides evidence for Gabay−Toulouse type mixed-phase (coexistence of SG and FiM) behavior. Further, in the case of $Cu_{0.2}Zn_{0.8}FeRuO_4$ system, slowly fluctuating magnetic clusters persist even above the short-range T_{FiM}, and their volume fraction vanishes completely across ~ $6T_{\mathrm{FiM}}$. Such feature corresponds to the dominant intra-sublattice FM interaction arising from the *B* site dilution with Cu^{2+} ions. However, the AFM coupling is predominant in $ZnFeRuO_4$ and $Cu_{0.2}Zn_{0.8}Fe_{0.5}Ru_{1.5}O_4$ systems. Detailed variation of the LR and SR phases mapped in the $H{-}T$ plane is the key outcome of this work.

In Chapter 5, we executed a detailed study on the crystal structure, electronic and magnetic properties in Zn diluted cuprospinel for some selected compositions. The chemical composition determined from the XPS, XRD and magnetization results to be: $(Cu_{(1-x)/5}Zn_xFe_{4(1-x)/5})_A[Cu_{4(1-x)/5}Fe_{2-4(1-x)/5}]_BO_4$. More importantly, a systematic variation of exchange interactions across the percolation limits is the major consequence of this work. Our analysis shows that the Cu doping plays a key role that alters the dominant interaction to FiM from AFM (as in ZFO). Upon complete substitution of Zn by Cu, the structural change (cubic to tetragonal) enhances magnetic anisotropy in the system simultaneously raising the T_{FiM} drastically. A detailed field and temperature dependent analysis based on the saturation magnetization and anisotropy parameters (derived using the Law of Approach to Saturation) provide a better insight on the dominant coupling strengths. The system approaches AFM configuration beyond $x_c = 0.4$ (i.e. $J_{AB} \sim -5.5\ k_B$ for $x = 0.6$) where it possesses very high anisotropy field $H_K \geq 5.5$ kOe with cubic anisotropy constant $K_1 \geq 1.6 \times 10^6$ erg/cc for x_c.

Further, we extend our study to the dynamical response of localized electron hopping and dipole relaxation in bulk polycrystals of the Cu-$ZnFe_2O_4$ composites. Our analysis of $\rho_{ac}(T, f)$ provide evidence of the Mott's variable range hopping of charge transport between the localized states below room temperature, however, thermally-activated Arrhenius like behavior is noticed at high temperatures. The electric modulus spectroscopic studies ($M^*(f, T)$) reveals two distinct types of relaxation phenomena: (*i*) the short-range oscillations of the charge carriers within the potential well of grains and (*ii*) the long-range movement of charge carriers across the grain boundaries, both of the Non-Debye type. The study based on the Jonscher's power law reveals that the ac conductivity follows small-polaron tunneling followed by the correlated-barrier-hopping mechanism for dilute Zn concentration (< 10 %). However, for $x \geq x_c$ (40%) reorientational hopping mechanism is predominant, and for $T > 400$ K, the thermally activated Arrhenius-type conduction of charge carriers is prevalent in this spinel system. Interestingly, the lower symmetry tetragonal systems ($x \leq 0.05$) exhibit less activation energy values as compared to the cubic systems. Composition dependent tunability of the impedance parameters are in consonance with the magnetization counterpart discussed above.

A schematic diagram of the important conclusions derived in this thesis work is given below (figure 7.1).

7.2. Prospective of Future Work:

Though the above results provide a comprehensive analysis specifically regarding the magnetic, heat capacity and electrical behavior on few Zn-based spinel ferrites, still we find possible extensions of this work as listed below.

(i) We plan to study the phonon dynamics and optical properties of the bulk systems of $Zn_{0.8}Cu_{0.2}FeMnO_4$ and $Zn_{0.8}Cu_{0.2}FeRuO_4$ at low temperatures which is expected to give clarity on the underlying spin-liquid and spin-glass states reported in the Chapters 3 and 4.

(ii) One can also plan to carry out the Neutron diffraction measurements on the $Cu_{1-x}Zn_xFe_2O_4$ series of systems to reveal on both the high and low temperature magnetic anisotropy, disorder and transitions.

(iii) In correlation to Chapter 6, Magneto-Dielectric measurements on Cu-$ZnFe_2O_4$ systems is expected to reveal their applicability in magneto-electronic devices.

(iv) We also plan to compare the results obtained in this thesis work with the characterizations performed on the nanostructures of the above discussed compounds to probe the probable size and surface effects.

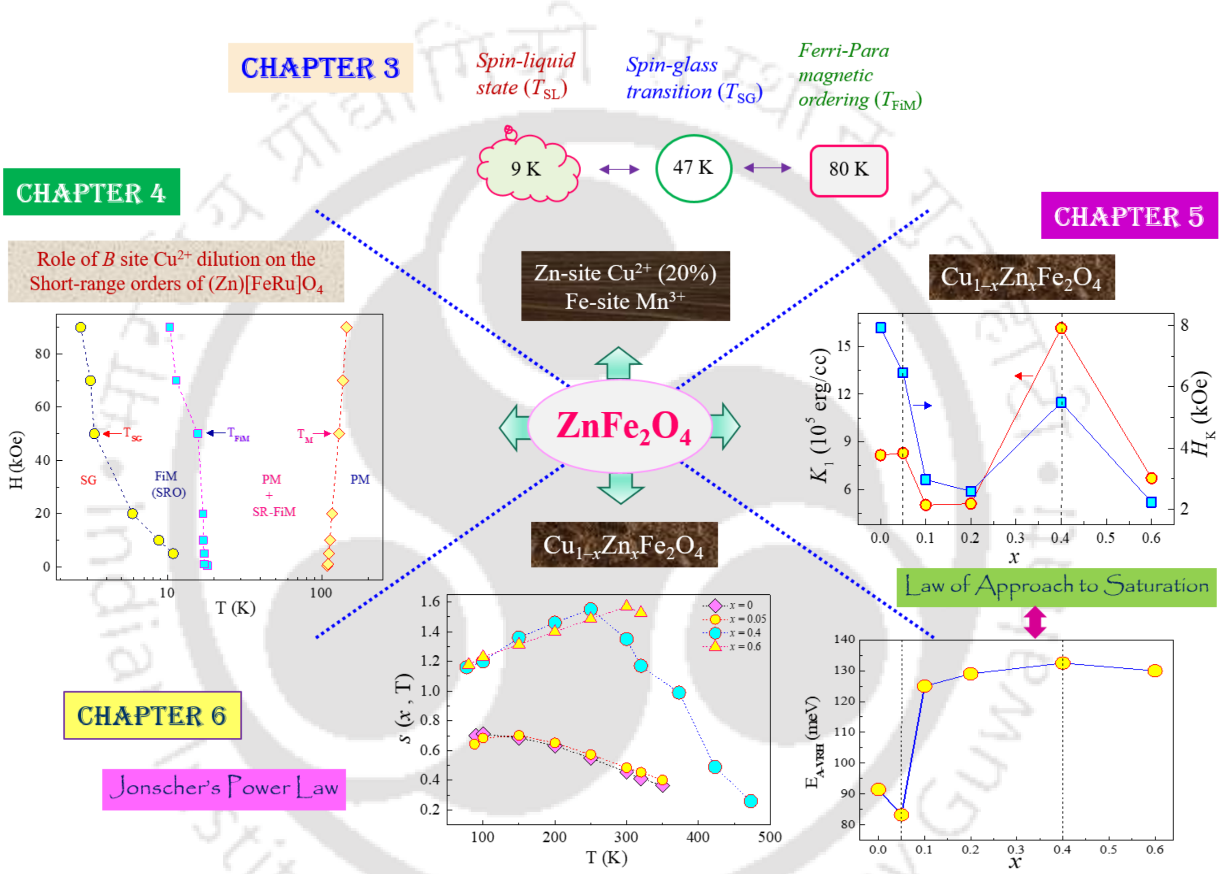

Figure 7.1: Schematic diagram of the important conclusions derived in this thesis work.

Bibliography

1. T. A. Kaplan, *Phys. Rev.* **119**, 1460 (1960).
2. S. K. Jena, D. C. Joshi, Z. Yan, Y. Qi, S. Ghosh, and S. Thota, *J. Appl. Phys.* **128**, 073908 (2020).
3. P. Pramanik, D. C. Joshi, M. Reehuis, A. Hoser, J.-U. Hoffmann, R. S. Manna, T. Sarkar, and S. Thota, *J. Phys.: Condens. Matter* **32**, 245801 (2020).
4. S. K. Jena, D. C. Joshi, S. Ghosh, K. Dasari, and S. Thota, *J. Phys. D: Appl. Phys.* **54**, 425303 (2021).
5. A. Ghasemi, M. Mousavinia, *Ceram. Int.* **40**, 2825 (2014).
6. X. Wu, W. Chen, W. Wu, H. Li, C. Lin, *J. Electron. Mater.* **46**, 199 (2017).
7. S. Thota, V. Narang, S. Nayak, S. Sambasivam, B. C. Choi, T. Sarkar, M. S. Andersson, R. Mathieu, and M. S. Seehra, *J. Phys.: Condens. Matter* **27**, 166001 (2015).
8. G. Srinivasan and M. S. Seehra, *Phys. Rev. B* **28**, 1 (1983).
9. E. Maniv, R. A. Murphy, S. C. Haley, S. Doyle, C. John, A. Maniv, S. K. Ramakrishna, Y.-L. Tang, P. Ercius, R. Ramesh, A. P. Reyes, J. R. Long, and J. G. Analytis, *Nat. Phys.* **17**, 525 (2021).
10. D. Sherrington, *Phys. Rev. Lett.* **111**, 227601 (2013).
11. Y. K. Tsui, C. A. Burns, J. Snyder, and P. Schiffer, *Phys. Rev. Lett.* **82**, 3532 (1999).
12. J. Khatua, M. Gomilšek, J. C. Orain, A. M. Strydom, Z. Jagličić, C. V. Colin, S. Petit, A. Ozarowski, L. Mangin-Thro, K. Sethupathi, M. S. R. Rao, A. Zorko, and P. Khuntia, *Commun. Phys.* **5**, 99 (2022).
13. C. Castelnovo, R. Moessner, and S. L. Sondhi, *Nature* **451**, 42 (2008).
14. Q. Zhao, Z. Yan, C. Chen, and J. Chen, *Chem. Rev.*, **117 [15]**, 10121 (2017).
15. V. Tsurkan, H.-A. K. v. Nidda, J. Deisenhofer, P. Lunkenheimer, A. Loidl, *Phys. Rep.* **926**, 1–86 (2021).
16. W. H. Bragg, “The Structure of the Spinel Group of Crystals,” *Philos. Mag.* **30 [176]**, 305–15 (1915).
17. S. Nishikawa, “Structure of Some Crystals of the Spinel Group,” *Proc. Math. Phys. Soc. Tokyo* **8**, 199–209 (1915).
18. K. E. Sickafus and J. M. Wills, *J. Am. Ceram. Soc.* **82 [12]**, 3279–92 (1999).
19. J. Sugiyama, T. Atsumi, A. Koiwai, T. Sasaki, T. Hioki, S. Noda, and N. Kamegashira, *J. Phys.: Condens. Matter* **9**, 1729 (1997).
20. T. Omata, N. Ueda, N. Hikuma, K. Ueda, H. Mizoguchi, T. Hashimoto, and H. Kawazoe, *Appl. Phys. Lett.* **62**, 499 (1993).
21. M. S. Seehra, V. Singh, and S. Thota, *J. Appl. Phys.* **110**, 113907 (2011).
22. L. Minervini, R. W. Grimes, and K. E. Sickafus, *J. Am. Ceram. Soc.* **83 [8]**, 1873 (2000).
23. J. Shamblin, M. Feygenson, J. Neuefeind, C. L. Tracy, F. Zhang, S. Finkeldei, D. Bosbach, H. Zhou, R. C. Ewing, and M. Lang, *Nat. Mater.* **15**, 507 (2016).
24. J. S. Gardner, M. J. P. Gingras, J. E. Greedan, *Rev. Mod. Phys.* **82**, 53 (2010).
25. M. A. Subramanian and A. W. Sleight, *in Handbook on the Physics and Chemistry of Rare Earths*, edited by K. A. Gschneidner and L. Eyring Elsevier Science, New York, p. 225, (1993).
26. V. Tsurkan, H.-A. K. v. Nidda, J. Deisenhofer, P. Lunkenheimer, A. Loidl, *Phys. Rep.* **926**, 1–86 (2021).
27. R. Moessner and A. P. Ramirez, *Phys. Today* **59 [2]**, 24 (2006).
28. N. Tristan, J. Hemberger, A. Krimmel, H-A. K. v. Nidda, V. Tsurkan, and A. Loidl, *Phys. Rev. B* **72**, 174404 (2005).
29. L. Balents, *Nature* **464**, 199 (2010).
30. J. Villain, *Z. Phys. B* **33**, 31 (1979).
31. R. Moessner and J. T. Chalker, *Phys. Rev. Lett.* **80**, 2929 (1998).
32. A. P. Ramirez, *in Handbook of Magnetic Materials*, edited by K. H. J. Buschow (Elsevier, New York), Vol. **13**, (2001).
33. S. E. Palmer and J. T. Chalker, *Phys. Rev. B* **62**, 488 (2000).
34. H. Ueda, H. A. Katori, H. Mitamura, T. Goto, and H. Takagi, *Phys. Rev. Lett.* **94**, 047202 (2005).
35. S.-H. Lee, C. Broholm, W. Ratcliff, G. Gasparovic, Q. Huang, T.H. Kim, and S.-W. Cheong, *Nature* **418**, 856 (2002).
36. A. P. Ramirez, A. Hayashi, R. J. Cava, R. Siddharthan, and B. S. Shastry, *Nature* **399**, 333 (1999).
37. S. T. Bramwell and M. J. P. Gingras, *Science* **294**, 1495 (2001).
38. Y. Yamashita and K. Ueda, *Phys. Rev. Lett.* **85**, 4960 (2000).
39. O. Tchernyshyov, R. Moessner, and S. L. Sondhi, *Phys. Rev. Lett.* **88**, 067203 (2002).
40. B. Bernu, P. Lecheminant, C. Lhuillier, and L. Pierre, *Phys. Rev. B* **50**, 10048 (1994).
41. P. W. Anderson, *Mater. Res. Bull.* **8**, 153 (1973).
42. J. Wen, S.-L. Yu, S. Li, W. Yu, and J.-X. Li, *npj Quantum Mater.* **4**, 12 (2019).
43. P. A. Lee, N. Nagaosa, and X.-G. Wen, *Rev. Mod. Phys.* **78**, 17–85 (2006).
44. S. Yamashita, Y. Nakazawa, M. Oguni, Y. Oshima, H. Nojiri, Y. Shimizu, K. Miyagawa, and K. Kanoda, *Nat. Phys.* **4**, 459 (2008).
45. K. T. Law and P. A. Lee, *Proc. Natl. Acad. Sci. U.S.A.*, **114 [27]**, 6996 (2017).
46. M. Yamashita, N. Nakata, Y. Senshu, M. Nagata, H. M. Yamamoto, R. Kato, T. Shibauchi, and Y. Matsuda, *Science* **328**, 1246 (2010).
47. M. Klanjšek, A. Zorko, R. Žitko, J. Mravlje, Z. Jagličić, P. K. Biswas, P. Prelovšek, D. Mihailovic, and D. Arčon, *Nat. Phys.* **13**, 1130 (2017).
48. N. Read, S. Sachdev, *Phys. Rev. B* **42**, 4568 (1990).
49. T. Senthil, M. P. A. Fisher, *Phys. Rev. B* **62**, 7850 (2000).
50. S. A. Kivelson, D. S. Rokhsar, J. P. Sethna, *Phys. Rev. B Condens. Matter.* **35**, 8865 (1987).

51. G. Baskaran, Z. Zou, P. W. Anderson, *Solid State Commun.* **63**, 973 (1987).
52. V. Kalmeyer and R. B. Laughlin, *Phys. Rev. B* **39**, 11879 (1989).
53. R. B. Laughlin and Z. Zou, *Phys. Rev. B* **41**, 664 (1990).
54. H. Yao and S. A. Kivelson, *Phys. Rev. Lett.* **99**, 247203 (2007).
55. G. Gorohovsky, R. G. Pereira, and E. Sela, *Phys. Rev. B* **91**, 245139 (2015).
56. S. T. Bramwell and M. J. Harris, *J. Phys.: Condens. Matter* **32**, 374010 (2020).
57. L. Pauling, *J. Am. Chem. Soc.* **57**, 2680 (1935).
58. S. V. Isakov, R. Moessner, and S. L. Sondhi, *Phys. Rev. Lett.* **95**, 217201 (2005).
59. D. I. Khomskii, *Nat. Commun.* **3**, 904 (2012).
60. M. J. Harris, S. T. Bramwell, P. C. W. Holdsworth, and J. D. M. Champion, *Phys. Rev. Lett.* **81**, 4496 (1998).
61. R. Edberg, L. Ø. Sandberg, I. M. B. Bakke, M. L. Haubro, L. C. Folkers, L. Mangin-Thro, A. Wildes, O. Zaharko, M. Guthrie, A. T. Holmes, M. H. Sørby, K. Lefmann, P. P. Deen, and P. Henelius, *Phys. Rev. B* **100**, 144436 (2019).
62. L. Bovo, C. M. Rouleau, D. Prabhakaran, and S. T. Bramwell, *Nat. Commun.* **10**, 1219 (2019).
63. M. E. Brooks-Bartlett, S. T. Banks, L. D. C. Jaubert, A. Harman-Clarke, and P. C. W. Holdsworth, *Phys. Rev. X* **4**, 011007 (2014).
64. H. D. Zhou, S. T. Bramwell, J. G. Cheng, C. R. Wiebe, G. Li, L. Balicas, J. A. Bloxsom, H. J. Silverstein, J. S. Zhou, J. B. Goodenough, and J. S. Gardner, *Nat. Commun.* **2**, 478 (2011).
65. T. Fennell, O. A. Petrenko, B. Fåk, S. T. Bramwell, M. Enjalran, T. Yavors'kii, M. J. P. Gingras, R. G. Melko, and G. Balakrishnan, *Phys. Rev. B* **70**, 134408 (2004).
66. J. Snyder, J. S. Slusky, R. J. Cava, and P. Schiffer, *Nature* **413**, 48 (2001).
67. M. J. Harris, S. T. Bramwell, D. F. McMorrow, T. Zeiske, and K. W. Godfrey, *Phys. Rev. Lett.* **79**, 2554 (1997).
68. B. C. d. Hertog and M. J. P. Gingras, *Phys. Rev. Lett.* **84**, 3430 (2000).
69. M. J. P. Gingras and B. C. d. Hertog, *Can. J. Phys.* **79**, 1339 (2001).
70. R. B. Laughlin, *Rev. Mod. Phys.* **71**, 863 (1999).
71. T. Sakakibara, T. Tayama, Z. Hiroi, K. Matsuhira, and S. Takagi, *Phys. Rev. Lett.* **90**, 207205 (2003).
72. S. Petit, E. Lhotel, B. Canals, M. C. Hatnean, J. Ollivier, H. Mutka, E. Ressouche, A. R. Wildes, M. R. Lees, and G. Balakrishnan, *Nature Phys.* **12**, 746 (2016).
73. I. A. Ryzhkin, *J. Exp. Theor. Phys.* **101**, 481 (2005).
74. Z. Fang, N. Nagaosa, K. S. Takahashi, A. Asamitsu, R. Mathieu, T. Ogasawara, H. Yamada, M. Kawasaki, Y. Tokura, K. Terakura, *Science* **302**, 92 (2003).
75. A. Yu. Kitaev, *Ann. Phys.* **303**, 2 (2003).
76. P. J. Ford, *Contemp. Phys.* **23 [2]**, 141 (1982), Taylor & Francis.
77. J. A. Mydosh, *Rep. Prog. Phys.* **78**, 5 (2015).
78. S. Kundu, T. Dey, A. V. Mahajan, and N. Büttgen, *J. Phys.: Condens. Matter* **32**, 115601 (2019).
79. S. Wu and Z. Cai, arXiv:1807.04792 **[quant-ph]**, DOI: https://doi.org/10.48550/arXiv.1807.04792.
80. M. T. Wolfinger, S. Will, I. L. Hofacker, R. Backofen, and P. F. Stadler, EPL **74**, 726 (2006).
81. Z. Zhang, *J. Mater. Sci. Technol.* **44**, 116 (2020).
82. T. J. Bullard, M. A. Susner, K. M. Taddei, J. A. Brant, and T. J. Haugan, *Sci. Rep.* **11**, 11355 (2021).
83. J. R. L. de Almeida, D. J. Thouless, *J. Phys. A* **11**, 983 (1978).
84. D. Fiorani, S. Viticoli, J. L. Dormann, J. L. Tholence, and A. P. Murani, *Phys. Rev. B* **30**, 2776 (1984).
85. S. Thota and M. S. Seehra, *J. Appl. Phys.* **113**, 203905 (2013).
86. R. N. Bhowmik, R. Ranganathan, *J. Magn. Magn. Mater.* **248**, 101 (2002).
87. S. R. Vieira, F. D. Nobre, F. A. d. Costa, *J. Magn. Magn. Mater.* **210**, 390 (2000).
88. A. Kumar, S. D. Kaushik, V. Siruguri, and D. Pandey, *Phys. Rev. B* **97**, 104402 (2018).
89. K. H. Fischer, *J. Phys. B Condens. Matter* **60**, 151 (1985).
90. C. Lupo and F. Ricci-Tersenghi, *Phys. Rev. B* **97**, 014414 (2018).
91. S. F. Edwards and P. W. Anderson, *J. Phys. F: Met. Phys.* **5**, 965 (1975).
92. K. Binder and A. P. Young, *Rev. Mod. Phys.* **58**, 801 (1986).
93. D. Sherrington and S. Kirkpatrick, *Phys. Rev. Lett.* **35**, 1792 (1975).
94. G. Parisi, *Phys. Rev. Lett.* **43**, 1754 (1979).
95. M. Mezard, G. Parisi, Virasoro, A. Miguel, *"Spin Glass Theory and Beyond: An Introduction to the Replica Method and its Applications"*, World Scientific Press (1987), DOI: https://ui.adsabs.harvard.edu/link_gateway/1987sgtb.book.....M/doi:10.1142/027.
96. W. Tang, J. Li, J, Zhao, W. Zhang, F. Yan, X. Guo, *IEEE Electron. Device Lett.* 36, 950 (2015).
97. A. Manohar, V. Vijayakanth, S. V. P. Vattikuti, K. H. Kim, *Ceram. Int.* **49**, 4365 (2023).
98. K. Samatha, H. Vijeth, S. Raghavendra, *J. Energy Storage* **52**, 104871 (2022).
99. Y. Zhang, J.-P. Zhou, Q. Liu, S. Zhang, C.-Y. Deng, *Ceram. Int.* **40**, 5853 (2014).
100. R. A. Pawar, S. S. Desai, S. M. Patange, S. S. Jadhav, K. M. Jadhav, *Physica B Condens. Matter* **510**, 74 (2017).
101. N. Chaiyo, B. Boonchom, N. Vittayakorn, *J. Mater. Sci.*, **45**, 1443 (2010).
102. A. D. McNaught and A. Wilkinson, IUPAC. *Compendium of Chemical Terminology, 2nd ed. (the "Gold Book")*, Blackwell Scientific Publications (1997).
103. P. Gabbott, "Principles and Applications of Thermal Analysis", *Blackwell Publishing Ltd.* (2008).
104. K.S. Cole and R.H. Cole, *J. Chem. Phys.*, **9**, 341 (1941).

105. S. J. L. Kang, "Sintering, Densification, Grain growth & Microstructure", *Elsevier* (2005).
106. W. H. Bragg and W. L. Bragg, "The reflection of X-rays by crystals", *Proceedings of the Royal Society of London. Series A, Containing Papers of a Mathematical and Physical Character* (1913).
107. R. A. Young, *The Rietveld method*, **5**, 1 (1993).
108. R. A. Young, *"The Rietveld Method", Oxford University Press* (1995).
109. J. F. Moulder, *Handbook of X-Ray Photoelectron Spectroscopy: A Reference Book of Standard Spectra for Identification and Interpretation of XPS Data* (1992).
110. J. J. Shea, *IEEE Electr. Insul. Mag.* **19**, 73 (2003).
111. P. S. Bagus, E. S. Ilton, and C. J. Nelin, *Surf. Sci. Rep.* **68**, 273 (2013).
112. J. Clarke and A. I. Braginski, *The SQUID Handbook* (2005).
113. R. L. Fagaly, *Rev. Sci. Instrum.* **77**, 101101 (2006).
114. S. Ran, *Gravity Probe B: Exploring Einstein's Universe with Gyroscopes-Einstein NASA*, p. 26 (2004).
115. S. Shapiro, *Phys. Rev. Lett.* **11**, 80 (1963).
116. M. Buchner, K. Höfler, B. Henne, V. Ney, and A. Ney, *J. Appl. Phys.* **124**, 161101 (2018).
117. S. H. Liao and Y. K. Su, *Sens. Actuator B-Chem.* **238**, 66 (1997).
118. J. A. Mydosh, "Spin Glasses: an experimental introduction", Taylor & Francis, London, Washington, DC (1993).
119. Physical Property Measurement System, Heat Capacity Option User's Manual (Quantum Design, 2010).
120. J. S. Hwang, K. J. Lin, and C. Tein, *Rev. Sci. Instrum.* **68**, 94 (1997).
121. G. L. Squires, *"Introduction to the Theory of Thermal Neutron Scattering"*, Cambridge University Press, Cambridge, U.K. (1978).
122. S. W. Lovesey, *"Theory of Neutron Scattering from Condensed Matter"*, **vol. 2**, Clarendon Press, Oxford (1984).
123. T. Chatterji, "Neutron scattering from magnetic materials", Elsevier (2005).
124. N. J. Kidner, B. J. Ingram, Z. J. Homrighaus, T. O. Mason, and E. J. Garboczi, *MRS Online Proc. Libr. Arch.* **756**, (2003).
125. B. Fe and O. Nb, *Phys. B Phys. Condens. Matter* **406**, 3470 (2011).
126. O. S. Doroshkevych, A. V. Shylo, O. V. Saprukina, I. A. Danilenko, T. E. Konstantinova, and L. A. Ahkozov, *World J. Condens. Matter Phys.* **2**, 1 (2012).
127. P. Electrochemistry, C. Elements, C. Equivalent, and C. Models, *Appl. Note AC* **286**, R491 (2010).
128. J. R. Macdonald and W. B. Johnson, *in Impedance Spectrosc. Theory, Exp. Appl. Second Ed.* (2005), pp. 1-26.
129. A. P. Ramirez, *Annu. Rev. Mater. Sci.* **24**, 453-480 (1994).
130. C. Broholm, G. Aeppli, G. P. Espinosa, and A. S. Cooper, *Phys. Rev. Lett.* **65**, 3173 (1990).
131. I. S. Hagemann, Q. Huang, X. P. A. Gao, A. P. Ramirez, and R. J. Cava, *Phys. Rev. Lett.* **86**, 894 (2001).
132. J. S. Helton, K. Matan, M. P. Shores, E. A. Nytko, B. M. Bartlett, Y. Yoshida, Y. Takano, A. Suslov, Y. Qiu, J.-H. Chung, D. G. Nocera, and Y. S. Lee, *Phys. Rev. Lett.* **98**, 107204 (2007).
133. P. W. Anderson, *Phys. Rev.* **102**, 1008 (1956).
134. F. K. Lotgering, *J. Phys. Chem. Solids* **27**, 139 (1966).
135. W. Schiessl, W. Potzel, H. Karzel, M. Steiner, G. M. Kalvius, A. Martin, M. K. Krause, I. Halevy, J. Gal, W. Schäfer, G. Will, M. Hillberg, and R. Wäppling, *Phys. Rev. B* **53**, 9143 (1996).
136. S. Nakashima, K. Fujita, K. Tanaka, K. Hirao, T. Yamamoto, and I. Tanaka, *Phys. Rev. B* **75**, 174443 (2007).
137. K. Kamazawa, Y. Tsunoda, H. Kadowaki, and K. Kohn, *Phys. Rev. B* **68**, 024412 (2003).
138. Y. Yamada, K. Kamazawa, and Y. Tsunoda, *Phys. Rev. B* **66**, 064401 (2002).
139. C. Cheng, *Phys. Rev. B* **78**, 132403 (2008).
140. P. Pramanik, S. Singh, M. RoyChowdhury, S. Ghosh, V. Sathe, K. M. Rabe, D. Vanderbilt, M. S. Seehra, and S. Thota, *Phys. Rev. B* **104**, 014433 (2021).
141. J. K. Dey, A. Chatterjee, A.-C. Dippel, O. Gutowski, M. v. Zimmermann, S. Majumdar, and S. Giri, *Phys. Rev. Materials* **5**, 014410 (2021).
142. S. M. Disseler, Y. Chen, S. Yeo, G. Gasparovic, P. M. B. Piccoli, A. J. Schultz, Y. Qiu, Q. Huang, S. W. Cheong, and W. Ratcliff, *Sci. Rep.* **5**, 17771 (2015).
143. H. Chang, I.-Y. Hwang, J.-H. Chung, J. R. Stewart, W. Higemoto, and Y. Miyake, *Phys. Rev. B* **97**, 014406 (2018).
144. J. Rodríguez-Carvajal, Recent advances in magnetic structure determination by neutron powder diffraction, *Phys. B: Condens. Matter.* **192**, 55 (1993).
145. V. F. Sears, in *International Tables for Crystallography*, edited by A. J. C. Wilson (Kluwer Academic Publishers, Dordrecht/Boston/London), **Vol. C**, 383 (1995).
146. F. Hai-Bo, Y. Shao-Yan, Z. Pan-Feng, W. Hong-Yuan, L. Xiang-Lin, J. Chun-Mei, Z. Qin-Sheng, C. Yong-Hai, and W. Zhan-Guo, *Chin. Phys. Lett.* **24**, 2108 (2007).
147. P. Pramanik, S. Thota, S. Singh, D. C. Joshi, B. Weise, A. Waske, and M. S. Seehra, *J. Phys.: Condens. Matter* **29**, 425803 (2017).
148. V. M. Goldschmidt, *Laws Cryst. Chem. Naturwissenschaften* **14**, 477 (1926).
149. M. Mullet, V. Khare, and C. Ruby, *Surf. Interface Anal.* **40**, 323 (2008).
150. S. K. Jena, T. Sarkar, M. RoyChowdhury, B. Weise, Y. Qi, and S. Thota, *J. Phys.: Condens. Matter* **34**, 405801 (2022).
151. J. G. Jolley, G. G. Geesey, M. R. Hankins, R. B. Wright, and P. L. Wichlacz, *Appl. Surf. Sci.* **37**, 469 (1989).
152. G. V. Lecomte, H. v. Löhneysen, and E. F. Wassermann, *Z. Phys. B. Condens. Matter* **50**, 239 (1983).

153. C. A. M. Mulder, A. J. van Duyneveldt, and J. A. Mydosh, *Phys. Rev. B* **23**, 1384 (1981).
154. P. Bag, P. R. Baral, and R. Nath, *Phys. Rev. B* **98**, 144436 (2018).
155. S. Ghara, B.-G. Jeon, K. Yoo, K. H. Kim, and A. Sundaresan, *Phys. Rev. B* **90**, 024413 (2014).
156. C. Tien, C. H. Feng, C. S. Wur, and J. J. Lu, *Phys. Rev. B* **61**, 12151 (2000).
157. J. Souletie and J. L. Tholence, *Phys. Rev. B* **32**, 516(R) (1985).
158. M. RoyChowdhury, M. S. Seehra, P. Pramanik, S. Ghosh, T. Sarkar, B. Weise, and S. Thota, *J. Phys.: Condens. Matter* **34**, 275803 (2022).
159. L. B. Mendelsohn, F. Biggs, and J. B. Mann, *Phys. Rev. A* **2**, 1130 (1970).
160. M. E. Fisher, *Phil. Mag.* **7**, 1731 (1962).
161. V. Narang, D. Korakakis, and M. S. Seehra, *J. Magn. Magn. Mater.* **368**, 353 (2014).
162. N. Mottaghi, M. S. Seehra, J. Shi, M. Jain, and M. B. Holcomb, *J. Appl. Phys.* **128**, 073903 (2020).
163. V. Markovich, I. Fita, A. Wisniewski, D. Mogilyansky, R. Puzniak, L. Titelman, C. Martin, and G. Gorodetsky, *Phys. Rev. B* **81**, 094428 (2010).
164. H. L. Tsay, Y. C. Chen, S. S. Weng, C. F. Chang, and H. D. Yang, *Phys. Rev. B* **59**, 636 (1999).
165. V. Hardy, Y. Bréard, and C. Martin, *Phys. Rev. B* **78**, 024406 (2008).
166. G. L. Ferreira-Fraga, L. A. Borba, and P. Pureur, *Phys. Rev. B* **74**, 064427 (2006).
167. R. Kannan and M. S. Seehra, *Phys. Rev. B* **35**, 6847 (1987).
168. S. Ghosh, D. C. Joshi, P. Pramanik, S. K. Jena, S. Pittala, T. Sarkar, M. S. Seehra, and S. Thota, *J. Phys.: Condens. Matter* **32**, 485806 (2020).
169. H.-J. Schmidt, A. Lohmann, and J. Richter, *Phys. Rev. B* **84**, 104443 (2011).
170. Y. Zhang, Q. Shi, J. Schliesser, B. F. Woodfield, and Z. Nan, *Inorg. Chem.* **53**, 10463 (2014).
171. A. P. Ramirez, G. P. Espinosa, and A. S. Cooper, *Phys. Rev. Lett.* **64**, 2070 (1990).
172. A. P. Ramirez, B. Hessen, and M. Winklemann, *Phys. Rev. Lett.* **84**, 2957 (2000).
173. S. Nakatsuji, Y. Nambu, H. Tonomura, O. Sakai, S. Jonas, C. Broholm, H. Tsunetsugu, Y. Qiu, and Y. Maeno, *Science* **309**, 1697 (2005).
174. N. Tsujii and H. Kitazawa, *J. Phys.: Condens. Matter* **19**, 145245 (2007).
175. S. Nayak, K. Dasari, D. C. Joshi, P. Pramanik, R. Palai, A. Waske, R. N. Chauhan, N. Tiwari, T. Sarkar, and S. Thota, *J. Appl. Phys.* **120**, 163905 (2016).
176. S. D. Tiwari and K. P. Rajeev, *Phys. Rev.* B **72**, 104433 (2005).
177. S. Pakhira, C. Mazumdar, R. Ranganathan, S. Giri, and M. Avdeev, *Phys. Rev. B* **94**, 104414 (2016).
178. A. Bhattacharyya, S. Giri, and S. Majumdar, *Phys. Rev. B* **83**, 134427 (2011).
179. N. Khan, P. Mandal, and D. Prabhakaran, *Phys. Rev. B* **90**, 024421 (2014).
180. B. Maji, K. G. Suresh, and A. K. Nigam, *J. Phys.: Condens. Matter* **23**, 506002 (2011).
181. V. K. Anand, D. T. Adroja, and A. D. Hillier, *Phys. Rev. B* **85**, 014418 (2012).
182. D. X. Li, Y. Shiokawa, Y. Homma, A. Uesawa, A. Dönni, T. Suzuki, Y. Haga, E. Yamamoto, T. Honma, and Y. Ōnuki, *Phys. Rev. B* **57**, 7434 (1998).
183. P. Granberg, P. Svedlindh, P. Nordblad, L. Lundgren, and H. S. Chen, *Phys. Rev. B* **35**, 2075 (1987).
184. D. Chu, G. G. Kenning, and R. Orbach, *Phys. Rev. Lett.* **72**, 3270 (1994).
185. M. Godinho, A. Carvalho, M. Noguès, J. L. Dormann, and M. Seqqat, *J. Magn. Magn. Mater.* **133**, 457 (1994).
186. R. Lamouri, L. Fkhar, E. Salmani, O. Mounkachi, M. Hamedoun, M. A. Ali, A. Benyoussef, and H. Ez-Zahraouy, *Appl. Phys. A* **126**, 325 (2020).
187. N. Sivakumar, A. Narayanasamy, J.-M. Greneche, R. Murugaraj, and Y. S. Lee, *J. Alloys Compd.* **504**, 395 (2010).
188. V. G. Harris, A. Geiler, Y. Chen, S. D. Yoon, M. Wu, A. Yang, Z. Chen, P. He, P. V. Parimi, X. Zuo, C. E. Patton, M. Abe, O. Acher, and C. Vittoria, *J. Magn. Magn. Mater.* **321**, 2035 (2009).
189. Y. F. Chen, D. Spoddig, M. Ziese, *J. Phys. D: Appl. Phys.* **41**, 205004 (2008).
190. A. B. Gadkari, T. J. Shinde, P. N. Vasambekar, *IEEE Sens. J.* **11**, 849 (2011).
191. S. Jauhar, S. Singhal, *Ceram. Int.* **40**, 11845 (2014).
192. M. Rethinasabapathy, A. T. E. Vilian, S. K. Hwang, S.-M. Kang, Y. Cho, Y.-K. Han, J.-K. Rhee, and Y. S. Huh, *J. Power Sources* **483**, 229170 (2021).
193. M. Bohra, V. Alman, R. Arras, *Nanomaterials* **11**, 1286 (2021).
194. C. J. O'Brien, Z. Rák, D. W. Brenner, *J. Phys.: Condens. Matter* **25**, 445008 (2013).
195. S. J. Stewart, I. A. Al-Omari, F. R. Sives, and H. M. Widatallah, *J. Alloys Compd.* **495**, 506 (2010).
196. H. M. Gobara, I. M. Nassar, A. M. A. E. Naggar, and G. Eshaq, *Energy* **118**, 1234 (2017).
197. C. E. Patton, C. A. Edmondson, and Y. H. Liu, *J. Appl. Phys.* **53**, 2431 (1982).
198. C. M. Srivastava, S. N. Shringi, M. J. Patni, and S. M. Joglekar, *Bull. Mater. Sci.* **6**, 7 (1984).
199. A. K. M. Zakaria, M. A. Asgar, S.-G. Eriksson, F. U. Ahmed, S. M. Yunus, and H. Rundlöf, *J. Magn. Magn. Mater.* **265**, 311 (2003).
200. A. K. M. Zakaria, M. A. Asgar, *J. Alloys Compd.* **396**, 44 (2005).
201. P. Schiffer, A. P. Ramirez, K. N. Franklin, and S-W. Cheong, *Phys. Rev. Lett.* **77**, 2085 (1996).
202. F. Mila, *Phys. Rev. Lett.* **81**, 2356 (1998).
203. B. Canals, C. Lacroix, *Phys. Rev. Lett.* **80**, 2933 (1998).
204. P. Schiffer, A. P. Ramirez, D. A. Huse, and A. J. Valentino, *Phys. Rev. Lett.* **73**, 2500 (1994).

205. P. Schiffer, A. P. Ramirez, D. A. Huse, P. L. Gammel, U. Yaron, D. J. Bishop, and A. J. Valentino, *Phys. Rev. Lett.* **74**, 2379 (1995).
206. J. Vannimenus, G. Toulouse, *J. Phys. C: Solid State Phys.* **10**, L537 (1977).
207. H. Mamiya, N. Tsujii, N. Terada, S. Nimori, H. Kitazawa, A. Hoshikawa, and T. Ishigaki, *Phys. Rev. B* **90**, 014440 (2014).
208. T. Murata, Y. Kozuka, M. Uchida, and M. Kawasaki, *J. Appl. Phys.* **118**, 193901 (2015).
209. S. Takita, H. Suzuki, K. Tomiyasu, K. Kamazawa, and T. Watanabe, *J. Phys.: Conf. Ser.* **592**, 012108 (2015).
210. G. H. Wannier, *Phys. Rev.* **79**, 357 (1950).
211. R. Ballou, E. Lelièvre-Berna, B. Fåk, *Phys. Rev. Lett.* **76**, 2125 (1996).
212. Z. Y. Meng, T. C. Lang, S. Wessel, F. F. Assaad, and A. Muramatsu, *Nature* **464**, 847 (2010).
213. K. Tomiyasu, K. Kamazawa, *J. Phys. Soc. Jpn.* **80**, SB024 (2011).
214. Y. Ying, L. Wang, W. Li, L. Qiao, J. Zheng, J. Yu, W. Cai, L. Jiang, S. Che, L. Zhang, and L. Ling, *J. Supercond. Nov. Magn.* **31**, 3553 (2018).
215. K. L. S. Rodríguez, S. J. Stewart, P. M. M. Zélis, G. A. Pasquevich, and C. E. R. Torres, *J. Alloys Compd.* **752**, 289 (2018).
216. J. J. M. Quintero, C. E. R. Torres, and L. A. Errico, *J. Alloys Compd.* **741**, 746 (2018).
217. T. Watanabe, S. Takita, K. Tomiyasu, and K. Kamazawa, *Phys. Rev. B* **92**, 174420 (2015).
218. T. Usa, K. Kamazawa, H. Sekiya, S. Nakamura, Y. Tsunoda, K. Kohn, and M. Tanaka, *J. Phys. Soc. Jpn.* **73**, 2834 (2004).
219. P. W. Anderson, *Phys. Rev.* **115**, 2 (1959).
220. H. H. Hamdeh, J. C. Ho, S. A. Oliver, R. J. Willey, G. Oliveri, and G. Busca, *J. Appl. Phys.* **81**, 1851 (1997).
221. G. F. Goya, H. R. Rechenberg, *J. Magn. Magn. Mater.* **196**, 191 (1999).
222. M. A. Hakim, M. M. Haque, M. Huq, and P. Nordblad, *Phys. B: Condens. Matter* **406**, 48 (2011).
223. M. Á. Cobos, P. de la Presa, I. Puente-Orench, I. Llorente, I. Morales, A. García-Escorial, A. Hernando, and J. A. Jiménez, *Ceram. Int.* **48**, 12048 (2022).
224. T. Suzuki, Y. Aikawa, T. Katsufuji, *J. Phys. Soc. Jpn.* **74**, 863 (2005).
225. J. Strečka, M. Jaščur, *J. Magn. Magn. Mater.* **272**, 987 (2004).
226. K. Kamazawa, S. Katano, Y. Tsunoda, *Phys. B: Condens. Matter* **345**, 96 (2004).
227. C. Cheng, C.-S. Liu, *J. Phys.: Conf. Ser.* **145**, 012028 (2009).
228. V. Zviagin, M. Grundmann, R. Schmidt-Grund, *Phys. Status Solidi B* **257**, 1900630 (2020).
229. C. E. R. Torres, F. Golmar, M. Ziese, P. Esquinazi, and S. P. Heluani, *Phys. Rev. B* **84**, 064404 (2011).
230. H. Mamiya, N. Terada, T. Furubayashi, H. S. Suzuki, and H. Kitazawa, *J. Magn. Magn. Mater.* **322**, 1561 (2010).
231. A. Hassadeea, T. Jutarosagaa, W. Onreabroya, *Procedia Eng.* **32**, 597 (2012).
232. M. S. Anwar, F. Ahmed, B. H. Koo, *Acta Mater.* **71**, 100 (2014).
233. S. Akhter, D. P. Paul, S. M. Hoque, M. A. Hakim, M. Hudl, R. Mathieu, and P. Nordblad, *J. Magn. Magn. Mater.* **367**, 75 (2014).
234. M. Lakshmi, K. V. Kumar, K. Thyagarajan, *J. Nanostruct. Chem.* **5**, 365 (2015).
235. B. Alshahrani, H. I. ElSaeedy, S. fares, A. H. Korna, H. A. Yakout, M. I. A. A. Maksoud, R. A. Fahim, M. Gobara, and A. H. Ashour, *J. Mater. Sci.: Mater. Electron.* **32**, 780 (2021).
236. L. Yang, Z. Wang, B. Zhai, Y. Shao, Z. Zhang, Y. Sun, and J. Yang, *Ceram. Int.* **39**, 8261 (2013).
237. A. R. Tanna, U. N. Trivedi, M. C. Chhantbar, and H. H. Joshi, *Indian J. Phys.* **87(11)**, 1087 (2013).
238. I. Pollini, *Phys. Rev. B* **50**, 2095 (1994).
239. A. V. Humbe, J. S. Kounsalye, S. B. Somvanshi, and K. M. Jadhav, *Mater. Adv.* **1**, 880 (2020).
240. P. Pramanik, S. Ghosh, P. Yanda, D. C. Joshi, S. Pittala, A. Sundaresan, P. K. Mishra, S. Thota, and M. S. Seehra, *Phys. Rev. B* **99**, 134422 (2019).
241. R. N. Bhowmik, R. Ranganathan, R. Nagarajan, *J. Magn. Magn. Mater.* **299**, 327 (2006).
242. K. D. Strooper, *Phys. Status Solidi A* **39**, 431 (1977).
243. J. K. Srivastava. S. Ramakrishnan, V. R. Marathe, G. Chandra, R. Vijayaraghavan, J. A. Kulkarni, V. S. Darshane, and S. Singh, *J. Appl. Phys.* **61**, 3622 (1987).
244. M. Gabay, G. Toulouse, *Phys. Rev. Lett.* **47**, 201 (1981).
245. M. D. Mukadam, S. M. Yusuf, P. Sharma, S. K. Kulshreshtha, and G. K. Dey, *Phys. Rev. B* **72**, 174408 (2005).
246. D. N. H. Nam, R. Mathieu, P. Nordblad, N. V. Khiem, and N. X. Phuc, *Phys. Rev. B* **62**, 8989 (2000).
247. P. Bag, K. Somesh, R. Nath, *J. Magn. Magn. Mater.* **497**, 165977 (2020).
248. T. Mori, H. Mamiya, *Phys. Rev. B* **68**, 214422 (2003).
249. J. L. Dormann, L. Bessais, D. Fiorani, *J. Phys. C: Solid State Phys.* **21**, 2015 (1988).
250. M. S. Seehra, K. L. Pisane, *J. Phys. Chem. Solids* **93**, 79 (2016).
251. V. Singh, M. S. Seehra, J. Bonevich, *J. Appl. Phys.* **105**, 07B518 (2009).
252. A. Malinowski, V. L. Bezusyy, R. Minikayev, P. Dziawa, Y. Syryanyy, and M. Sawicki, *Phys. Rev. B* **84**, 024409 (2011).
253. J. Lago, S. J. Blundell, A. Eguia, M. Jansen, and T. Rojo, *Phys. Rev. B* **86**, 064412 (2012).
254. P. J. Baker, T. Lancaster, S. J. Blundell, M. L. Brooks, W. Hayes, D. Prabhakaran, and F. L. Pratt, *Phys. Rev. B* **72**, 104414 (2005).
255. C. Sow, D. Samal, P. S. A. Kumar, A. K. Bera, and S. M. Yusuf, *Phys. Rev. B* **85**, 224426 (2012).

256. S. S. Rathore, S. Vitta, *Sci. Rep.* **5**, 9751 (2015).
257. M. Svedberg, S. Majumdar, H. Huhtinen, P. Paturi, and S. Granroth, *J. Phys.: Condens. Matter* **23**, 386005 (2011).
258. C. Nayek, S. Samanta, K. Manna, A. Pokle, B. R. K. Nanda, P. S. Anil kumar, and P. Murugavel, *Phys. Rev. B* **93**, 094401 (2016).
259. S. Pakhira, C. Mazumdar, A. Basu, R. Ranganathan, R. N. Bhowmik, and B. Satpati, *Sci. Rep.* **8**, 14870 (2018).
260. Y. Tabata, T. Waki, H. Nakamura, *Phys. Rev. B* **96**, 184406 (2017).
261. F. Wang, J. Zhang, Y. Chen, G. Wang, J. Sun, S. Zhang, and B. Shen, *Phys. Rev. B* **69**, 094424 (2004).
262. P. M. Shand, A. L. Meyer, M. Streicher, A. Wilson, T. Rash, M. W. Roth, T. E. Kidd, and L. H. Strauss, *Phys. Rev. B* **85**, 144432 (2012).
263. A. Durán, A. M. Arévalo-López, E. Castillo-Martínez, M. García-Guaderrama, E. Moran, M. P. Cruz, F. Fernández, and M. A. Alario-Franco, *J. Solid State Chem.* **183**, 1863 (2010).
264. N. P. Raju, M. Dion, M. J. P. Gingras, T. E. Mason, and J. E. Greedan, *Phys. Rev. B* **59**, 14489 (1999).
265. E. F. Westrum, D. M. Grimes, *J. Phys. Chem. Solids* **3**, 44 (1957).
266. V. K. Lakhani, K. B. Modi, *J. Phys. D: Appl. Phys.* **44**, 245403 (11pp) (2011).
267. K. Verma, A. Kumar, D. Varshney, *Curr. Appl. Phys.* **13**, 467 (2013).
268. I. Onyszkiewicz, J. Pietrzak, *phys. stat. sol. (a)* **73**, 641 (1982).
269. H. Nagata, T. Miyadai, S. Miyahara, *IEEE Trans. Magn.* September 1972. Intermag Conference.
270. H. Ohnishi, T. Teranishi, *J. Phys. Soc. Jpn.* **16**, No. 1, 35 (1961).
271. T. Yamadaya, T. Mitui, T. Okada, *J. Phys. Soc. Japan* **17**, 1897 (1962).
272. A. Kyono, Y. Nakamoto, M. Sakata, and M. Kato, *Photon Factory Activity Report* **32 B**, 2014 (2015).
273. R. S. Yadav, I. Kuřitka, J. Vilcakova, J. Havlica, J. Masilko, L. Kalina, J. Tkacz, M. Hajdúchová, and V. Enev, *J. Mater. Sci: Mater. Electron* **28**, 6245 (2017).
274. M. A. Amer, T. Meaz, A. Hashhash, S. Attalah, and F. Fakhry, *J. Alloys Compd.* **649**, 712 (2015).
275. S. J. Stewart, R. C. Mercader, G. Punte, J. Desimoni, G. Cernicchiaro, and R. B. Scorzelli, *Hyperfine Interactions* **156/157**, 89 (2004).
276. D. Prabhu, A. Narayanasamy, K. Shinoda, B. Jeyadeven, J. M. Greneche, and K. Chattopadhyay, *J. Appl. Phys.* **109**, 013532 (2011).
277. S. J. Stewart, M. J. Tueros, G. Cernicchiaro, and R. B. Scorzelli, *Solid State Commun.* **129**, 347 (2004).
278. K. J. Kim, J. H. Lee, S. H. Lee, *J. Magn. Magn. Mater.* **279**, 173 (2004).
279. B. J. Evans, S. S. Hafner, *J. Phys. Chem. Solids* **29**, 1573 (1968).
280. K. H. Maria, S. Choudhury, M. A. Hakim, *J. Bangladesh Acad. Sci.* **34**, No. 1, 1 (2010).
281. E. R. Kumar, R. Jayaprakash, G. S. Devi, and P. S. P. Reddy, *Sens. Actuator B* **191**, 186 (2014).
282. Z. Sun, L. Liu, D. Jia, and W. Pan, *Sens. Actuator B* **125**, 144 (2007).
283. B. Sreedhar, A. S. Kumar, D. Yada, *Tetrahedron Lett.* **52**, 3565 (2011).
284. S. C. Yang, W. N. Su, S. D. Lin, J. Rick, J. H. Cheng, J. Y. Liu, C. J. Pan, D. G. Liu, J. F. Lee, T. S. Chan, H. S. Sheu, and B. J. Hwang, *Appl. Catal. B: Environmental* **106**, 650 (2011).
285. A. S. Kumar, B. Thulasiram, S. B. Laxmi, V. S. Rawat, and B. Sreedhar, *Tetrahedron* **70**, 6059 (2014).
286. R. Peymanfar, F. Azadi, Y. Yassi, *Proceedings* **2**, 1155 (2018).
287. M. A. Haija, A. I. Ayesh, S. Ahmed, and M. S. Katsiotis, *Appl. Surf. Sci.* **369**, 443 (2016).
288. K. Ali, J. Iqbal, T. Jan, D. Wan, N. Ahmad, I. Ahamd, and S. Z. Ilyas, *J. Magn. Magn. Mater.* **428**, 417 (2017).
289. J. Z. Jiangdag, G. F. Goyaddag, H. R. Rechenbergddag, *J. Phys.: Condens. Matter* **11**, 4063 (1999).
290. R. Zhang, Q. Yuan, R. Ma, X. Liu, C. Gao, M. Liu, C. Jia, and H. Wang, *RSC Adv.* **7**, 21926 (2017).
291. X.X. Tang, A. Manthiram, J. B. Goodenough, *J. Solid State Chem.* **79**, 250 (1989).
292. N. Najmoddin, A. Beitollahi, H. Kavas, S. M. Mohseni, H. Rezaie, and J. Åkerman, M. S. Toprak, *Ceram. Int.* **40**, 3619 (2014).
293. H. M. O'Bryan Jr., H. J. Levinstein, R. C. Sherwood, *J. Appl. Phys.* **37**, 1438 (1966).
294. D. M. Grimes, E. F. Westrum, *J. Appl. Phys.* **29**, 384 (1958).
295. J. M. Hastings, L. M. Corliss, *Phys. Rev.* **102**, 1460 (1956).
296. S. Ligenza, *Phys. Stat. Sol. B* **75**, 315 (1976).
297. B. Boucher, R. Buhl, M. Perrin, *Phys. Stat. Sol.* **40**, 171 (1970).
298. K. L. S. Rodríguez, S. J. Stewart, P. M. M. Zélis, G. A. Pasquevich, and C. E. R. Torres, *J. Alloys Compd.* **752**, 289 (2018).
299. S. A. Oliver, H. H. Hamdeh, J. C. Ho, *Phys. Rev. B* **60**, 3400 (1999).
300. J. S. Gardner, B. D. Gaulin, S.-H. Lee, C. Broholm, N. P. Raju, and J. E. Greedan, *Phys. Rev. Lett.* **83**, 211 (1999).
301. A. Keren, J. S. Gardner, *Phys. Rev. Lett.* **87**, 177201 (2001).
302. S. Thota, M. Reehuis, A. Maljuk, A. Hoser, J.-U. Hoffmann, B. Weise, A. Waske, M. Krautz, D. C. Joshi, S. Nayak, S. Ghosh, P. Suresh, K. Dasari, S. Wurmehl, O. Prokhnenko, and B. Büchner, *Phys. Rev. B* **96**, 144104 (2017).
303. X. Hu, Z. Zhu, Z. Li, L. Xie, Y. Wu, and L. Zheng, *Sens. Actuator B* **264**, 139 (2018).
304. A. Chapelle, I. E. Younsi, S. Vitale, Y. Thimont, T. Nelis, L. Presmanes, A. Barnabé, and P. Tailhades, *Sens. Actuator B* **204**, 407 (2014).
305. S. Salmi, R. Masrour, A. El Grini, K. Bouslykhane, A. Hourmatallah, N. Benzakour, and M. Hamedoun, *Chin. Phys. Lett.* **35**, No. 1, 017501 (2018).

306. S. Nayak, S. Thota, D. C. Joshi, M. Krautz, A. Waske, A. Behler, J. Eckert, T. Sarkar, M. S. Andersson, R. Mathieu, V. Narang, and M. S. Seehra, *Phy. Rev. B* **92**, 214434 (2015).
307. S. Thota and M. S. Seehra, *J. Appl. Phys.* **118**, 129901 (2015).
308. M. U. Rana, M. Islam, T. Abbas, *Mater. Chem. Phys.* **65**, 345 (2000).
309. N. K. Thanh, T. T. Loan, L. N. Anh, N. P. Duong, S. Soontaranon, N. Thammajak, and T. D. Hien, *J. Appl. Phys.* **120**, 142115 (2016).
310. A. C. Nawle, A. V. Humbe, M. K. Babrekar, S. S. Deshmukh, and K. M. Jadhav, *J. Alloys Compd.* **695**, 1573 (2017).
311. S. Chakrabarty, A. Dutta, M. Pal, *J. Alloys. Compd.* **625**, 216 (2015).
312. S. V. Komogortsev, R.S. Iskhakov, *J. Magn. Magn. Mater.* **440**, 213 (2017).
313. J. F. Herbst, F. E. Pinkerton, *Phys. Rev. B* **57**, 10733 (1988).
314. A. J. Rondinone, A. C. S. Samia, Z. J. Zhang, *Appl. Phys. Lett.* **76**, 3624 (2000).
315. R. Topkaya, A. Baykal, A. Demir, *J. Nanopart. Res.* **15**, 1359 (2013).
316. U. Kurtan, R. Topkaya, A. Baykal, and M. S. Toprak, *Ceram. Int.* **39**, 6551 (2013).
317. G. F. Goya, H. R. Rechenberg, *Nanostruct. Mater.* **10 [6]**, 1001 (1998).
318. G. F. Goya, H. R. Rechenberg, J. Z. Jiang, *J. Magn. Magn. Mater.* **218**, 221 (2000).
319. H. Jiao, G. Jiao, J. Wang, *Synth. React. Inorg. M.* **43**, 131 (2013).
320. T. G. Altincekic, I. Boz, A. Baykal, S. Kazan, R. Topkaya, and M. S. Toprak, *J. Alloys Compd.* **493**, 493 (2010).
321. M. U. Rana, M. Ul-Islam, I. Ahmad, and T. Abbas, *J. Magn. Magn. Mater.* **187**, 242 (1998).
322. S. V. Andreev, M. I. Bartashevich, V. I. Pushkarsky, V. N. Maltsev, L. A. Pamyatnykha, E. N. Tarasov, N. V. Kudrevatykh, and T. Goto, *J. Alloys Compd.* **260**, 196 (1997).
323. N. T. Malafaev, A. A. Murakhovskii, J. A. Popkov, *J. Magn. Magn. Mater.* **89**, 8 (1990).
324. C. Choodamani, B. Rudraswamy, G. T. Chandrappa, *Ceram. Int.* **42**, 10565 (2016).
325. M. Sundararajan L. J. Kennedy, U. Aruldoss, Sk. K. Pasha, J. J. Vijaya, and S. Dunn, *Mater. Sci. Semicond. Process.* **40**, 1 (2015).
326. M. Zahraei, A. Monshi, M. del P. Morales, D. S. Gahrouei, M. Amirnasr, and B. Behdadfar, *J. Magn. Magn. Mater.* **393**, 429 (2015).
327. A. Chatterjee, J. K. Dey, S. Majumdar, A.-C. Dippel, O. Gutowski, M. v. Zimmermann, and S. Giri, *Phys. Rev. Mater.* **3**, 104403 (2019).
328. D. Odkhuu, T. Tsevelmaa, D. Sangaa, N. Tsogbadrakh, S. H. Rhim, and S. C. Hong, *Phys. Rev. B* **98**, 094408 (2018).
329. J. D. Dunitz, L. E. Orgel, *J. Phys. Chem. Solids* **3**, 318 (1957).
330. F. Guillou, S. Thota, W. Prellier, J. Kumar, and V. Hardy, *Phys. Rev. B* **83**, 094423 (2011).
331. M. Ptak, M. Maczka, A. Gągor, A. Pikul, L. Macalik, and J. Hanuza, *J. Solid State Chem.* **201**, 270 (2013).
332. P. Patra, I. Naik, H. Bhatt, and S. D. Kaushik, *Physica B Condens. Matter* **572**, 199 (2019).
333. V. Manikandan, V. Kuncser, B. Vasile, S. Kavita, S. Vigneselvan, and R. S. Mane, *J. Magn. Magn. Mater.* **476**, 18 (2019).
334. S. A. Mazen, M. H. Abdallah, B. A. Sabrah, and H. A. M. Hashem, *Phys. Status Solidi A* **134**, 263 (1992).
335. E. R. Kumar, R. Jayaprakash, G. S. Devi, and P. S. P. Reddy, *Sens. Actuators B* **191**, 186 (2014).
336. A. M. Balagurov, I. A. Bobrikov, M. S. Maschenko, D. Sangaa, and V. G. Simkin, *Crystallogr. Rep.* **58**, 710 (2013).
337. N. A. Alghamdi, J. H. Hankiewicz, N. R. Anderson, K. F. Stupic, R. E. Camley, M. Przybylski, J. Żukrowski, and Z. Celinski, *Phys. Rev. Appl.* **9**, 054030 (2018).
338. C. Yao, Q. Zeng, G. F. Goya, T. Torres, J. Liu, H. Wu, M. Ge, Y. Zeng, Y. Wang, and J. Z. Jiang, *J. Phys. Chem. C* **111**, 12274 (2007).
339. S. B. Kale, R. M. Borade, J. S. Kounsalye, A. V. Raut, S. R. Nimbhore, and K. M. Jadhav, *J. Phys.: Conf. Ser.* **1644**, 012012 (2020).
340. W. Pan, F. Gu, K. Qi, Q. Liu, and J. Wang, *Mater. Chem. Phys.* **134**, 1097 (2012).
341. D. Ravinder, *J. Alloys Compd.* **291**, 208 (1999).
342. K. H. Maria, S. Choudhurya, M. A. Hakim, *Int. Journal of Phy. and Appl.* **3**, 23 (2011).
343. D. Mohanty, P. Mallick, S. K. Biswal, B. Behera, R. K. Mohapatra, A. Behera, S. K. Satpathy, *Mater. Today* **33**, 4971 (2020).
344. G. Umapathy, G. Senguttuvan, L. J. Berchmans, V. Sivakumar, *J. Mater. Sci: Mater. Electron.* **27**, 7062 (2016).
345. N. Sivakumar, A. Narayanasamy, N. Ponpandian, and G. Govindaraj, *J. Appl. Phys.* **101**, 084116 (2007).
346. N. Ponpandian and A. Narayanasamy, *J. Appl. Phys.* **92**, 2770 (2002).
347. N. Sivakumar, A. Narayanasamy, N. Ponpandian, J.-M. Greneche, K. Shinoda, B. Jeyadevan, and K. Tohji, *J. Phys. D: Appl. Phy.* **39**, 4688 (2006).
348. C. P. Rana, J. S. Baijal, P. Kishan, *J. Less Common Met.* **106**, 257 (1985).
349. K. Ali, A. Bahadur, A. Jabbar, S. Iqbal, I. Ahmad, and M. I. Bashir, *J. Magn. Magn. Mater.* **434**, 30 (2017).
350. N. Rezlescu, E. Rezlescu, *Phys. Status Solidi A* **23**, 575 (1974).
351. J. T. S. Irvine, A. Huanosta, R. Velenzuela, and A. R. West, *J. Am. Ceram. Soc.* **73**, 729 (1990).
352. C. G. Koops, *Phys. Rev.* **83**, 121 (1951).
353. P. Lunkenheimer, V. Bobnar, A. V. Pronin, A. I. Ritus, A. A. Volkov, and A. Loidl, *Phys. Rev. B* **66**, 052105 (2002).
354. K.W. Wanger, *Ann. Phys. (Leipz.)* **40**, 817 (1913).
355. N. Ponpandian, P. Balaya, A. Narayanasamy, *J. Phys.: Condens. Matter* **14**, 3221 (2002).
356. D. G. Chen, X. G. Tang, Q. X. Liu, Y. P. Jiang, C. B. Ma, and R. Li, *J. Appl. Phys.* **113**, 214110 (2013).

357. R. S. Yadav, I. Kuřitka, J. Vilcakova, P. Urbánek, M. Machovsky, M. Masař, and M. Holek, *J. Phys. Chem. Solids* **110**, 87 (2017).
358. E. J. W. Verwey, P. W. Haayman, *Physica* **8**, 979 (1941).
359. N. E. Rajeevan, R. Kumar, D. K. Shukla, P. P. Pradyumnan, S. K. Arora, and I. V. Shvets, *Mater. Sci. Eng. B* **163**, 48 (2009).
360. D. Joshi, S. Thota, S. Nayak, D. Harish, P. Mahesh, A. Kumar, D. Pamu, and M. Qureshi, *J. Phys. D: Appl. Phys.* **47**, 435305 (2014).
361. R. Hill, *Phys. Status Solidi A* **34**, 601 (1976).
362. N. Mott, *Conduction in Non-Crystalline Materials (Oxford University Press, UK)*, 835 (1993).
363. D. Yu, C. Wang, B. L. Wehrenberg, and P. Guyot-Sionnest, *Phys. Rev. Lett.* **92**, 216802 (2004).
364. C. Ang, J. R. Jurado, Z. Yu, M. T. Colomer, J. R. Frade, and J. L. Baptista, *Phys. Rev. B* **57**, 11858 (1998).
365. H. Zheng, W. Weng, G. Han, and P. Du, *J. Phys. Chem. C* **117**, 12966 (2013).
366. N. Ortega, A. Kumar, P. Bhattacharya, S. B. Majumder, and R. S. Katiyar, *Phys. Rev. B* **77**, 014111 (2008).
367. R. T. George, D. C. Joshi, S. Nayak, N. Tiwari, R. N. Chauhan, P. Pramanik, T. A. Dar, S. Ghosh, and S. Thota, *J. Appl. Phys.* **123**, 054101 (2018).
368. A. P. Almond, A. R. West, R. J. Grant, *Solid State Commun.* **44**, 277 (1982).
369. D. C. Joshi, P. Pramanik, M. K. Warshi, S. Ghosh, A. Meher, K. Dasari, S. Thota, *J. Phys. Chem. Solids* **130**, 154 (2019).
370. J. C. Dyre, T. B. Schrøder, *Rev. Mod. Phys.* **72**, 873 (2000).
371. R. K. Panda, R. Muduli, S. K. Kar, D. Behera, *J. Alloy Compd.* **615**, 899 (2014).
372. A. Radoń, D. Łukowiec, M. Kremzer, J. Mikuła, and P. Włodarczyk, *Materials* **11**, 735 (2018).
373. T. L. Rao, M. K. Pradhan, S. Singh, and S. Dash, *J. Mater. Sci.: Mater. Electron.* **31**, 4542 (2020).
374. K. Funke, *Prog. Solid State Chem.* **22**, 111 (1993).
375. R. Richert, H. Wagner, *Solid State Ion.* **105**, 167 (1998).
376. J. Liu, C-G Duan, W-G Yin, W. N. Mei, R. W. Smith, and J. R. Hardy, *J. Chem. Phys.* **119**, 2812 (2003).
377. A. K. Pradhan, T. K. Nath, S. Saha, *Mater. Res. Express* **4**, 076107 (2017).
378. Z. Imran, M. A. Rafiq, M. Ahmad, K. Rasool, S. S. Batool, and M. M. Hasan, *AIP Adv.* **3**, 032146 (2013).
379. M. B. Hossen, A. K. M. A. Hossain, *J. Adv. Ceram.* **4**, 217 (2015).
380. S. Upadhyay, D. Kumar, O. M. Prakash, *Bull. Mater. Sci.* **19**, 513 (1996).
381. K. P. Padmasree, D. K. Kanchan, A. R. Kulkami, *Solid State Ion.* **177**, 475 (2006).
382. B. V. R. Chowdari, R. Gopalkrishnnan, *Solid State Ion.* **23**, 225 (1987).
383. I. M. Hodge, C. A. Angell, *J. Chem. Phys.* **67**, 1647 (1977).
384. P. B. Macedo, C. T. Moynihan, R. Bose, *Phys. Chem. Glass.* **13**, 171 (1972).
385. K. L. Ngai, *J. Non-Cryst. Solids* **203**, 232 (1996).
386. J. Hazarika, A. Kumar, *Synth. Met.* **198**, 239 (2014).
387. R. Bergman, *J. Appl. Phys.* **88**, 1356 (2000).
388. B. Deka, S. Ravi, A. Perumal, and D. Pamu, *Ceram. Int.* **43**, 1323 (2017).
389. Q. J. Li, S. Q. Xia, X. Y. Wang, W. Xia, Y. Yu, Y. M. Cui, J. Zhang, J. Zheng, C. Cheng, Y. D. Li, H. Wang, S. G. Huang, and C. C. Wang, *J. Alloys Compd.* **616**, 577 (2014).
390. J. C. C. Abrantes, J. A. Labrincha, J. R. Frade, *Mater. Res. Bull.* **35**, 727 (2000).
391. O. Bidault, M. Maglione, M. Actis, M. Kchikech, B. Salce, *Phys. Rev. B* **52**, 4191 (1995).